NUMERICAL ANALYSIS OF A BRUSHLESS PERMANENT MAGNET DC MOTOR USING COUPLED SYSTEMS

HLA NU PHYU
(B. Eng.(Electrical Power),Y.T.U)

A THESIS SUBMITTED
FOR THE DEGREE OF DOCTOR OF PHILOSOPHY
DEPARTMENT OF ELECTRICAL & COMPUTER ENGINEERING
NATIONAL UNIVERSITY OF SINGAPORE
2004

Acknowledgments

I wish to express my gratitude to my supervisor, Dr. M. A. Jabbar from Department of Electrical and Computer Engineering, National University of Singapore for his guidance, advice, support and encouragement for this research work. I am grateful to my co-supervisor Dr. Liu Zhejie from Data Storage Institute for his suggestions and help to this work in all possible aspects.

I am also greatly indebted to Dr. Bi Chao, Research Scientist from the Data Storage Institute for the experimental set up. I wish to thank Lab officers, Mr.Y. C. Woo and Mr.M. Chandra from Electrical Machine and Drives Laboratory for their support and assistance in the Lab where I carried out my research work. Many thanks to my colleagues: Mr. Nay Lin Htun Aung for his smart ideas and suggestions concerning with FEM analysis, Ms. Dong Jing for her constant support and helping hands for programming work, Mr. Krishna Manila for his support, patience and valuable discussion for both hardware and software implementation for experiments.

I would like to express my most heartfelt thanks and gratitude to my family, who have always provided me with constant support, concern and prayers. Finally, to my husband, San Yu, I express my deepest gratitude. Without his understanding, kindness and sacrifices, the dream would never have come to reality.

Contents

Summary

This thesis deals with the modeling, simulation and performance analysis of the brushless permanent magnet DC (BLDC) motors using numerical methods. The primary objective is to develop efficient and practical procedures based on numerical techniques to analyze the steady state and dynamic performances of BLDC motors.

Dynamic model of the BLDC motor is developed using time stepping finite element method. In this model, nonlinear electromagnetic field, circuit equations and motion equations are formulated in time domain and solved simultaneously in each time steps. Due to the direct coupling of the transient electromagnetic field, circuit and motion, the solutions can take into account the eddy current effect, the saturation effect, the rotor movement, the non-sinusoidal quantities and high order harmonics of the electromagnetic fields which are very difficult to include using analytical approaches and traditional finite element method (FEM). Proposed dynamic model is used to investigate the transient analysis of the BLDC motor at step voltage variation, load torque changing and locked rotor condition.

The analysis of the steady state performance of nonlinear electromagnetic systems using time stepping FEM requires very long computational times. An improved steady state model is proposed using time stepping FEM combined with two dimensional FEM. In this model, current fed two dimensional FEM is used as a pre-computation stage for the time stepping solver. Using the proposed steady state model, the transient solver can be started with initial conditions quite close to the steady state solution and it can reduce the time spent in reaching a steady state solutions. In addition, the non-sinusoidal quantities, high-order harmonic and rotor motion which are very difficult to take into account in the traditional steady state analysis using the FEM can be included. Steady-state model is used for the calculation of steady-state current, cogging torque and back-emf in time domain and determination of torque-speed characteristics of the BLDC motor.

BLDC motors cannot work without the electronic controllers. In order to analyze the motor with a controller as an actual system, a new approach to couple the time stepping FEM with closed-loop control structure is implemented. Cascaded speed and current hysteresis control loop structures is used. By coupling the control loop features with the time stepping FEM, the stator windings could be fed with the actual input voltages to the time stepping FEM model. In addition, motor operations under transient conditions can be controlled instantaneously as an actual motor-controller system. Using this new scheme, application characteristics of the HDD spindle motors are investigated. Important features of the spindle motor at starting such as spin-time, starting torque and starting current under no load and loaded conditions are analyzed. Computational analysis of the run-up performance of a spindle motor is investigate. It is found that the proposed model works satisfactorily when it is used to simulate the motor drive under real transient conditions with voltage, current and speed limits.

In order to determine the accuracy and validation of the proposed dynamic and steady state model, DSP based BLDC motor test stand is implemented. Simple and reliable methods of motor performance measurements are presented. A new approach for detecting the motor starting sequences for controller is developed. The good agreement of the computational results with the experimental results indicates that developed numerical models are useful and applicable to analyze the static and dynamic behaviours of the BLDC motor.

List of Figures

List of Tables

List of Symbols

H	magnetic field intensity
B	magnetic flux density
A	magnetic vector potential
J	current density
B_r	the remanence flux density
ν	magnetic relucitvity
σ	electric conductivity
μ_0	magnetic permeability in the free space
μ	magnetic permeability
H_c	the coercivity
T_e	electromagnetic torque
T_L	load torque
D,	damping coffcient
ω	angular velocity
Δt,	time step length
θ_m	rotor angle in mechanical degree

E	electric field intensity
i_s	stator phase current
S	total cross-sectional area of the stator winding one turn per one coil side
t	time
V	stator phase voltage
R	total stator phase resistance
e	backemf
i_s	stator phase current
L_σ	end winding inductance
Ω^+, Ω^-	total cross-section area of ” go “ and ” return “ side of stator windings

Chapter 1

Introduction

1.1 Permanent Magnet Motors

Permanent magnets (PM) have been used in electrical machine applications almost from the beginning of the development of these machines as replacements for wound field excitation systems. The availability of high-energy permanent magnets and advances in power electronics are leading to a large diffusion of permanent magnet machines in a variety of applications [1]-[2]. In general, permanent magnet motors are broadly classified into:

- **Brushed DC motor (or) PMDC commutator motor:** The construction of a permanent magnet DC motor(PMDC) is similar to a DC conventional motor with the electromagnetic excitation system replaced by permanent magnets. A PMDC commutator motor can be compared with a separately excited DC motor. The only difference is in the excitation flux in the airgap: for PMDC commutator motor excitation flux is constant whilst for a separately excited DC motor's excitation flux can be controlled. The structures of a conventional DC motor and a PMDC commutator motor are shown in Fig. 1.1.

- **Brushless permanent magnet motor:** Brushless permanent magnet motor falls into two principal classes: Bushless DC motor (BLDC)and Permanent magnet synchronous motor (PMSM).

The PMSM owes its origin to the replacement of the exciter of the wound synchronous machine with a permanent magnet. PMSMs are fed with three phase currents in sinusoidal shape and operate on the principle of a magnetic rotating field. All phase windings conduct current at a time with phase differences. The structures of a PMSM is shown in Fig. 1.2.

The BLDC owes its origin to an attempt to invert the brush DC machine to remove the need for the commutator and brush gear. BLDC is fed with rectangular or trapezoidal shape current waveforms shifted by 120 electrical degree one from another. Electronic commutation is done by the rotor position sensors and electronic controller where armature current is precisely synchronized with the rotor frequency and instantaneous position. Only two phases are conducting at any given instant of time. Basic configuration and characteristic of BLDC motor are presented more in detail at next section.

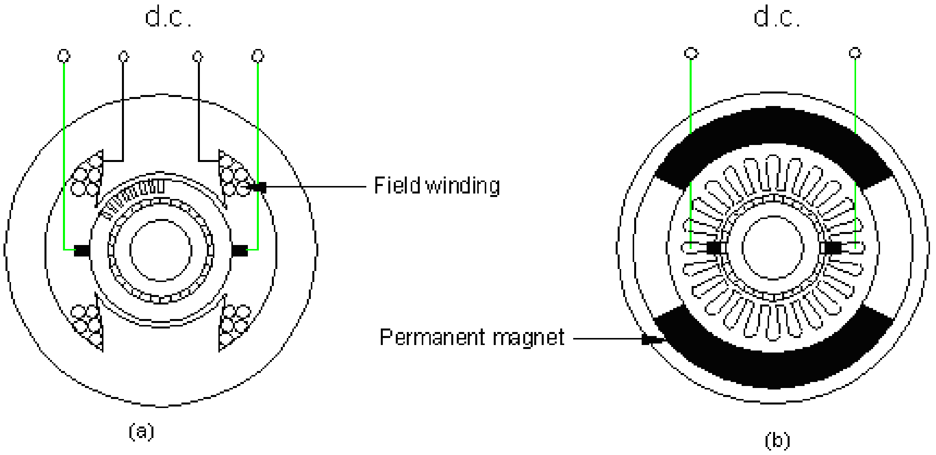

Figure 1.1: Typical configurations of a DC motor and a PMDC commutator motor

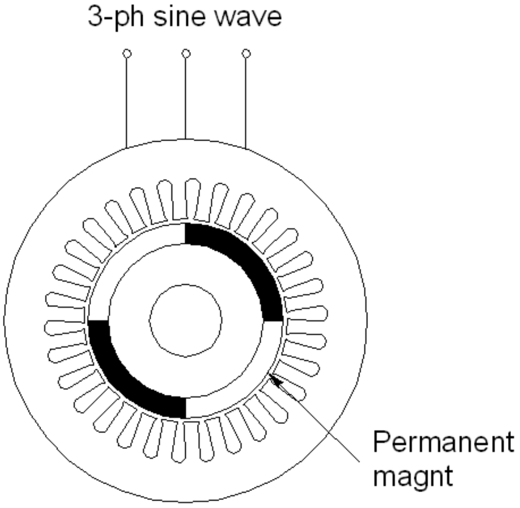

Figure 1.2: Typical configuration of a PMSM

1.2 Brushless Permanent Magnet DC Motors

Until recently, conventional DC motors have been the dominant drive system because they provide easily controlled motor speed over a wide range, rapid acceleration and deceleration, convenient control of position, and lower product cost. However, technical advances in permanent magnet materials, in high power semiconductor transistor technology, and in various rotors position-sensing devices have made using BLDC motor a viable alternative. The developments and applications of the BLDC motors have been greatly accelerated by improvements in permanent magnet materials, especially rare-earth magnets. Brushless motors are smaller, lighter and have higher efficiency and power density compared to traditional DC motors because of lack of field windings, commutators and brushes. Additionally, the brushless design offers increased motor speed range because the motor speed is not limited by the arcing at the commutator as in brushed DC motors. Therefore, BLDC motors are highly demanded in clean, explosive environments such as aeronautics, robotics, electric vehicles, food and chemical industries, and have a wide variety of applications in the area of HDD drives, servo drives and variable speed drives.

1.2.1 Basic Configurations of BLDC motors

There are several different configurations of BLDC motors for different applications. Three basic configurations of the permanent magnet BLDC motor are inner rotor, outer rotor and axial gap disc designs, with many different winding pattern as well as many different pole configurations [3]. The magnets may be in strips, arcs or discs of various shapes and they may or may not be pre-magnetized.

Inner rotor motor configuration is nearly the same as the classical AC synchronous motor or the induction motor. The stator is similar to that of the three-phase induction motor. The advantage of interior type is its high torque/inertia ratio. Hence it is widely used in servo systems, requires rapid acceleration and deceleration of the load and the torque/inertia ratio should be as high as possible. Most inner rotor motors have multiple phases in an effort to reduce the starting problems associated with single phase motors. The stators may have salient pole or distributed windings. Fig. 1.3 illustrates a three phase four salient pole inner rotor type BLDC motor.

If the application requires constant speed at medium to high speed it may take more sense to use an exterior-rotor configuration with the rotating member on the outside of the wound stator. This type is used in fans, blowers and computer hard disk drive spindle motor. Fig. 1.4 shows the cross-section of a typical motor of exterior- rotor type. The most important application for the exterior-rotor motor is the spindle motor used in computer hard disk drives. This application requires a very uniform and constant speed and the high inertia of the exterior rotor is an advantage in achieving this.

There are other applications such as record players, VCR players, CD players and floppy disc drives for computers which have a different set of requirements. These type of motor should be rotated at relatively low speed. It has been common to design axial-gap or pancake motors for many of these applications. Fig. 1.5 is axial field type BLDC motor. The main advantages of these motors are their low cost, their flat shape and smooth rotation with zero cogging.

The choice of motor type is the most fundamental design decision, because of the relatively high cost of magnets, together with issues related to packaging, magnet retention, and winding. However, to date, it has not been determined which configuration should be used to maximize the power density, efficiency and quietness of a motor [4]. To thoroughly investigate permanent magnet BLDC motor technology, it is necessary to study the relative merits of each configuration in terms of the power density, efficiency and noise/vibration levels.

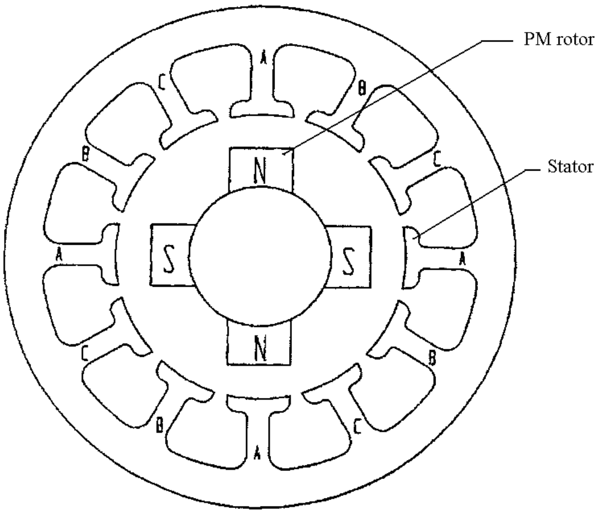

Figure 1.3: Multiphase inner rotor BLDC motor configuration

1.2.2 Characteristics of BLDC Motors

A BLDC motor cannot work without the electronic controller. The terminal voltages on the windings of each phase are controlled by the power electronic switches. The phase windings are energized in sequence by the switching elements in the inverter which are controlled by shaft position sensors. Thus stator magnetomotive force (mmf) runs ahead rotor mmf keeping a constant angular displacement. The basic components of the BLDC motor drive system are: a rectifier, an inverter, a

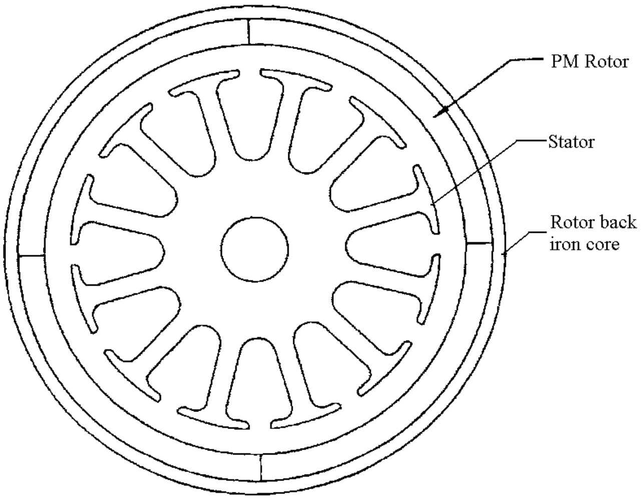

Figure 1.4: Exterior rotor BLDC motor configuration

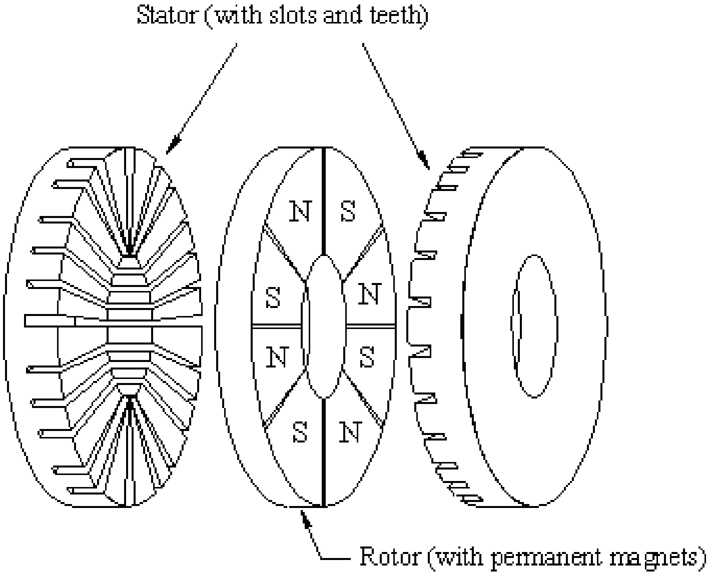

Figure 1.5: Axial field type BLDC motor configuration

PM motor, rotor position sensors and a controller as shown in Fig. 1.6. ***Rectifier***:

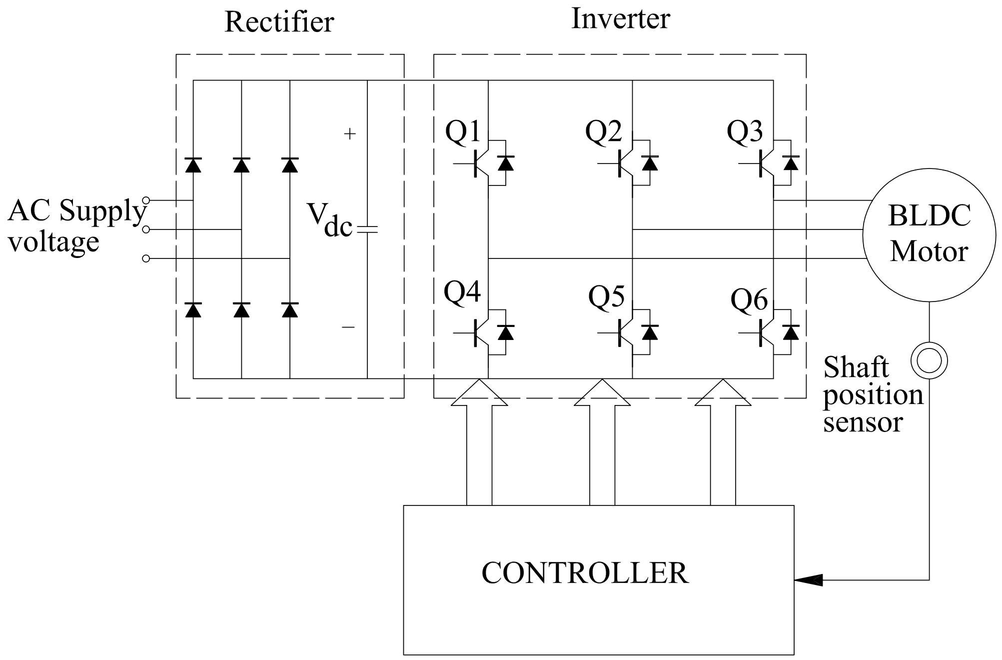

Figure 1.6: Basic components of the BLDC motor drive

The electrical energy can be a DC source, such as a battery, or an alternating current AC source. Rectifier converts the AC line voltage into DC bus voltage.

Inverter: Inverter includes the power semiconductor switches and their current sensors and protection circuitry. The inverter circuit diagram is shown in Fig. 1.7 for the wye and the delta connections. In square wave operation, there are normally two transistors conducting at any one time. Transistors in the inverter receive conduction commands from a system of logic which is synchronized with the rotor position sensors [3]. Fig. 1.8 shows the sequence of switching transistors for the corresponding current wave form for wye connection.

Rotor position sensors : Position sensors detect the position of the rotating magnets and send logic codes to a commutation decoder which activates the firing circuits of semiconductor switches feeding power to the stator winding of the drive motor. A unidirectional torque is produced via the interaction between the

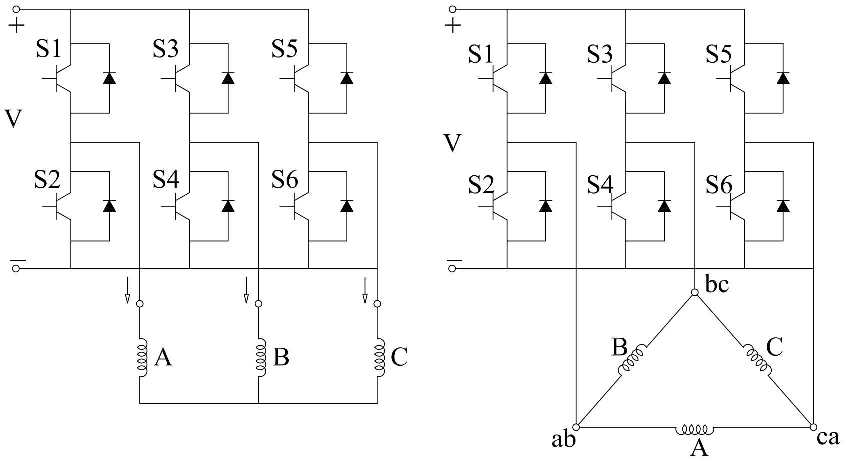

(a) Wye connection

(b) Delta connection

Figure 1.7: Inverter-fed armature circuits of BLDC motors

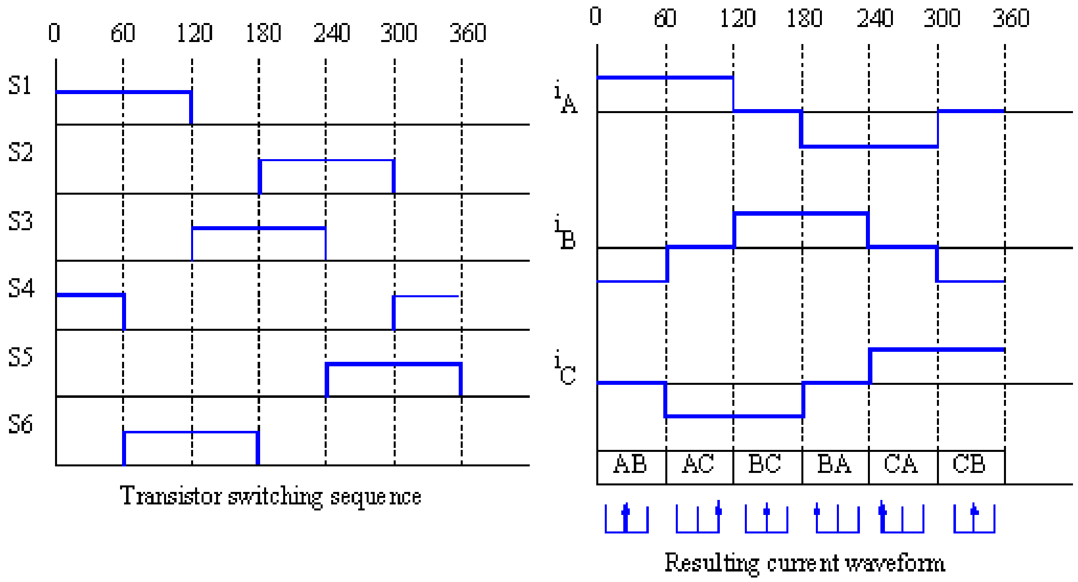

Transistor switching sequence

Resulting current waveform

Figure 1.8: Transistor switching sequences and corresponding current waveforms

permanent magnets and currents flowing through the winding. Generally, rotor position sensing in commercial brushless DC motor is done by resolvers, optical position sensors and hall-effect transducer. Hall sensors are mostly used BLDC motor drives.

The various shaft position sensors seem straightforward enough in themselves, and yet in the marketplace there has been concern with the use of brushless motors in many applications because of the need for these devices. On the other hand, it is widely stated that there are no brushes or commutator to affect reliability. However, these must be replaced by a shaft position transducer, with additional electronic circuitry and an interconnecting cable. These components inevitably add to the cost, and may decrease the reliability because they are relatively fragile and, unless they are properly protected, they may be susceptible to damage or maloperation for high temperatures, dusts, oil, vibration and shock, etc., and even from electrical interference. It is not surprising that there has been much effort in recent years to eliminate the need for the shaft position transducer. This is called sensorless control. Sensorless motors are applicable in refrigerators, air conditioners and especially in hard disk drives [5].

PM motor: Different configurations and magnetic excitations for particular applications are as mentioned in the section 1.2.1.

Controller: The main task of the controller is to decode shaft position sensor's input data, to control the supplied voltage to inverter, to operate control loop such as speed and position. Actually, the power circuit of the electronic controller is a switchmode circuit. The only means of controlling such circuits is to control the timing of the gate signals that turn the power transistors on and off. These low-level timings must be controlled to meet a set of high-level functional requirements. The state of the art for BLDC motors calls for a single chip controller that could be used for low-cost applications. Most of the recent

DSP controller board contains all of the active functions required to implement a full featured open-loop, three or four phases motor control system.

1.3 Magnetic Materials

Good knowledge of materials used in the construction of a permanent magnet motor is important in the design and operating conditions of the machine. Different material qualities offer various design possibilities and application choices [6]. In general, magnetic circuit should be optimized in accordance with the characteristics of the materials chosen. Generally, two groups of materials are used in the magnetic circuit:

- Hard magnetic materials (permanent magnet) and
- Soft magnetic materials

The magnetic flux density versus magnetic field strength curve, the hysteresis loop, is used in the characterization of these materials. A soft magnetic material is one in which the hysteresis loops are narrow. For narrow loops, the normal magnetization curve is a good approximation and is often used to characterize the material. Another type of material that is characterized by a broad hysteresis loop is called hard magnetic material.

1.3.1 Hard magnetic materials (Permanent magnets)

Permanent magnets can produce magnetic flux in an airgap with no dissipation of electric power. The basic operational characteristic of permanent magnet is given by its demagnetization curve in the second quadrant of $B - H$ plane as shown in Fig. 1.9. When a permanent magnet has been magnetized, it remains magnetized even the applied field intensity is decreased to zero. The magnetic field density at this point is called the remanence flux density B_r. If a reverse magnetic field intensity is applied, the flux density decreases. If the reverse magnetic field is large enough, the flux density become zero. The field intensity at this value is called the coercivity H_c. The operating point of the permanent magnet is the intersection point of a $B - H$ curve of the external magnetic circuit (load line) and the demagnetization curve of a permanent magnet. The operation point moves along the demagnetization curve with changes in the external magnetic field. The absolute value of the product of the flux density B and the field intensity H at each point along the demagnetization curve can be represented by the energy product [7] and this quantity is one of the indexes of the strength of the permanent magnet.

For the modern high energy permanent magnets, the demagnetisation curve at ambient temperature is linear. It only shows a noticeable bent at higher temperatures. The result is that the operating point of the modern rare-earth permanent magnets can easily be designed to be within the linear area of the demagnetisation curve. This is one of the major advantages of the modern high energy permanent magnets over the conventional permanent magnets in the designs for engineering applications. The effect of armature field on the permanent magnets is either magnetizing or demagnetizing. Since the demagnetizing curve of some permanent magnets has a knee, there is a limit to the maximal allowable armature field.

Proper selection of magnetic materials is important from both economics as well as performance considerations. There are basically three different types of permanent magnet which are used in PM motors:

- Alnico
- Ceramics (Ferrites) and
- Rare-earth materials, i.e Sm-Co and Nd-Fe-B.

Typical demagnetisation characteristics of these three types is shown in Fig. 1.10.

Alnico- The main advantages of Alnico are its high magnetic remanent flux density, Br and low temperature coefficients. These advantages allow quite a high air gap flux density and high operating temperatures [2]. But coercive force is very low and the demagnetization curve is extremely non-linear. When the coercivity is low and two opposing magnetic poles locate at a close distance, the poles can weaken each other. Therefore, an Alnico magnet is used after being magnetized lengthwise. It is very easy not only to magnetize but also to demagnetize this magnet. Alnico dominated the PM industry from the mid 1940s to about 1970 when ferrites became the most widely used materials.

Ferrite- A ferrite has a higher coercive force than that of Alnico, but at the same time has a lower remanent magnetic flux density. Temperature coefficients are relatively high. The maximum service temperature is 400 degree C. The main advantages of ferrites are their low cost and very high electric resistance, which means no eddy-current losses in the PM volume. Ferrite magnets are most economical in fractional horsepower motors and may show an economic advantage over Alnico up to about 7.5kW.

Rare- earth permanent magnet materials- The first generation of rare-earth magnet is based on the composition SmCo5 and invented in the 1960s has been commercially produced since the early 1970s. Smco5 has the advantage of high remanent flux density, high coercive force, high-energy product, linear demagnetization curve and low temperature coefficient. It is well suited to build motors with low volume and consequently high specific power and low moment of inertia. NdFeB is another type of rare earth magnets. It has the highest B*H product among all the permanent magnet materials currently available. The maximum service temperature is 150 degree C. This indicates that the use of NdFeB will result in the smallest and the most powerful motor design.

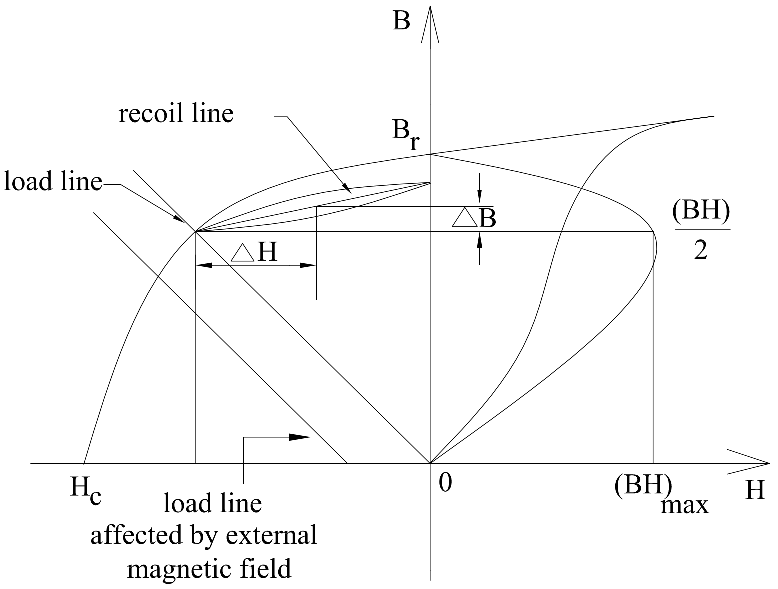

Figure 1.9: Demagnetization curve of PM

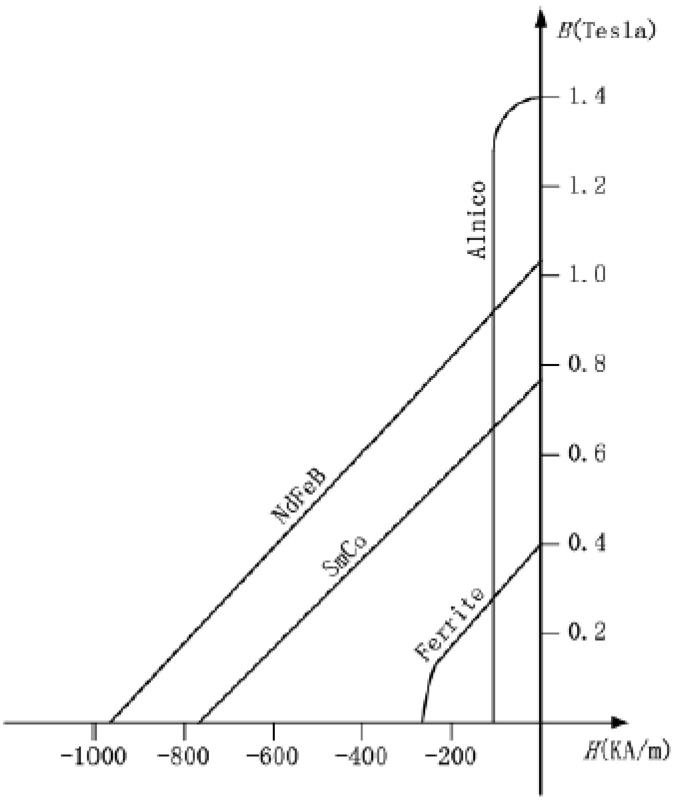

Figure 1.10: Characteristic of permanent magnet materials

1.3.2 Soft magnetic materials

Desirable properties of the soft magnetic material that can be used in PM motors are high saturation flux density, high permeability, low coercive field strength and low specific conductivity. Low coercivity is required to minimize hysteresis losses; generally, in brushless motors, the armature core experiences an alternating flux as well as high-frequency flux variation due to PWM. In high frequency applications the eddy currents are minimized by using thinner laminations and high-resistive steels. There have been great improvements in the quality of electrical steels over the last 20 years. This has been made possible by improved manufacturing techniques and a better understanding of factors which control magnetic properties. For effective use of soft magnetic material, the desire is to have the operating point in the middle of the magnetization curve. Saturation of the soft magnetic material should be avoided, otherwise, an appreciable percentage of the useful energy provided by the permanent magnet for use in air-gap would be lost.

1.4 Computational Analysis of Electrical Machines

Prediction of electrical machine performance is necessary for the evaluation of machine designs. Various methods of analysis have been employed to model the electrical machines and to predict their performance accurately at the design stage. Generally, **experimental methods, analytical methods and numerical methods** are used out to predict the performance and design of the electrical machines.

Experimental methods require building hardware prototypes or scaled models and results obtained from tests and conducted on these models are used to predict the performance of the actual devices and also to enable hardware changes to be made in order to meet specifications. These methods prove to be expensive, cumbersome, and time consuming. Further, often only terminal quantities could be measured owing to the non-availability of sophisticated sensors and instrumentation.

Analytical methods are computationally quick and simple to use. They can give a good view over the influence of machine parameters on the performances for machines with relative ease. However, analytical methods are limited to techniques applicable to linear isotropic media. Only constant values of permeability and conductivity for magneto static and eddy current problems and constant dielectric permittivity for electrostatic problems can be used. Several simplifications of the formulation and associated boundary conditions are required in view of the limitations on available solution techniques. Modelling of non-linearity is not possible except for simple problems where transformation methods could be used.

Due to the advent of digital computer and subsequent advances in computing power and storage devices, it has become practical to use **numerical methods** to compute the performance of the electrical machines. For complex geometrical shapes, with varying materials characteristics and often mixed boundary conditions, numerical methods offer the best and often the most economical solution. In order to obtain a good method for various engineering problems, many numerical methods have been developed such as finite difference method, boundary element method, moment method and finite element method (FEM)[8]. Among these methods, FEM is widely used in performance analysis of the electrical machines because it is feasible for a wide rage of application and can be used for solving both linear and nonlinear problems, static and dynamic problems, 2D and 3D problems.

1.4.1 Analysis of electrical machines using FEM

Electrical machines have their behaviours governed by the electromagnetic fields which flow in them; the fields, in turn, obey Maxwell's equations. The solution of many practical electromagnetic field problems can only be undertaken by applying numerical methods. Before such a solution can be undertaken, it is important that a correct mathematical model be established for the problem considered. In the analysis of electrical machines, different types FEM model are applied based on the various electromagnetic field behaviour of the problem.

In general, electromagnetic fields in low frequency application can be identified as: time independent static and quasi-static. Static field is a field which is excited by DC currents or voltages. If a DC voltage is applied, the DC current depends on the voltage and DC resistance of the circuit. No induced effects such as eddy currents or induced voltages are present in the model. In a static model, the flux is constant in time and thus the reluctivities are constant as well [9]. A quasi-static field can be divided into time invariant and time-varying fields with or without involving the eddy currents. In the time invariant cases, the field solution does not depend on the time-derivative term in the differential equations. It can be regarded as a static field for a particular instant of time. The calculation of the field is performed for a certain instant of time and therefore the flux density and the resulting inductances are calculated for this specific instant of time. In such cases, magneto-static FEM is used to analyze the behaviour of electromagnetic field.

In the time varying quasi-static field, the eddy currents are involved and have to be considered, a time derivative term appears in the differential equations. The varying field generates induced voltages and currents. The eddy currents also influences the field. Each form of time variation can be modelled either in the time domain or in the frequency domain. When the field is periodic with one or a limited number of frequencies, it is more efficient to perform a field calculation in the frequency domain. For the case in which the field is oscillating at one frequency and assume all field quantities,imposed sources and boundary conditions vary sinusoidally with time, time harmonic complex eddy current FEM is used. Strictly speaking, in the complex eddy current FEM, all material properties are assumed to be linear and constant in time. However, for non-linear material, an effective material characteristic could be used [10]-[12]. This characteristic gives a sinusoidal averaged value in terms of rms value of the field quantity. Indeed, the non-linear time harmonic analysis seeks to include the effects of nonlinearities like saturation and hysteresis on the fundamental of the response, while ignoring higher harmonic content[13].

In the time harmonic complex eddy current model, the simulation based on the field concepts. The behaviour of the machine is determined directly by the distribution of magnetic fields and current density. Rotor rotation effect cannot be included hence motion equations could not be taken into account in the system of equations. Non-sinusoidal quantities also cannot be included. Therefore, this model can apply in the steady state analysis of machines. Many researchers have studied the performance of BLDC motors using complex eddy current FEM [14]-[23]. The great majority of machines are used in applications when important feature is the steady state performances. Although almost all applications of machines have definite steady state requirements, an increasing number of applications place great emphasis on dynamic performance, so that mathematical and experimental techniques are needed to investigate dynamic features. It frequently happens that a machine with excellent steady state characteristics cannot be used because it is unsatisfactory in dynamic operation and vice versa.

In order to determine the transient behaviour of the electromagnetic devices that are activated by a voltage or current source which may be time dependent, it is needed to analyze in time domain. In this case, time stepping FEM is appropriate to use in the analysis of electrical machines [24]-[26]. In the time stepping FEM analysis, the equations for the stator and rotor fields are written in their own coordinate systems. The solutions of the two field equations are matched with each other in the air gap. The rotor rotation is accomplished by rotating the FEM meshes of the rotor. The circuit equations which describe the supply and control system and motion equations are directly coupled together to the field equations. Both the transient performance and the steady state performance of the machine in time domain can be studied accurately, particularly when non-sinusoidal quantities and high-order space and time harmonics are to be considered.

Although three dimensional (3D) finite element analysis is required to accurately model the 3D effect such as end winding effects, in practice these are accounted for analytically, by appropriate modification of 2D finite element predicted parameter values [27]-[29]. Compared with 3D technique, the 2D FEM has the advantages of simple mesh generation, short computing time and small computer storage requirement especially in studying of transient conditions where rotor movement is needed to include. Therefore, in practical applications, it is highly desirable a 2D model.

1.5 Literature Review

Due to the advent of high energy permanent magnets and sophisticated electronic controllers, brushless permanent magnet DC motor is getting more and more popular in a wide range of applications, which include machine tools, robotics, aerospace generators, actuators, industrial drives and electric vehicles. The majority of work has been done on the analytical design approach based on the equivalent circuits model (a-b-c model), state space model and lump parameter model [30]-[39]. Nehl at el [31] developed a-b-c phase variable model with the back-emf represented as a Fourier series and P. Pillay [40] also developed a-b-c model to study both steady state and transient characteristics of the BLDC motor. Y.P. Liu, D. Howe, T.S. Birch and D.M.H. Matthews [41] proposed the dynamic model of the BLDC motor with a-b-c reference frame. In these models, the motor voltage equation, current equations, and torque equation are written in the a-b-c reference frame. The switching devices are also represented by circuit model. The main advantage of this model is that no assumptions are required regarding constant speed operation. However, the saturation effect, the eddy current effect and permanent magnet characteristic cannot be taken into account in the system of solution. M M Elmissiry and S Chari [42] investigates the dynamic performance of a class of an axial-flux, permanent magnet brushless DC drive using state space model. In this study, the motor dynamic equations are written on state-space form. In deriving the dynamic equations, the rotor flux density distribution is assumed to be invariant with the operating conditions but material saturation effect is neglected. Mathematical model of the drive is presented and two cases of dynamic operation; motor start-up and the sudden change of the applied voltage are considered.

Based on the above research works, it can be concluded that although the analytical methods are fast and flexible in computation, they cannot be accurate in the conditions that involve complex configuration and eddy current effect. Modelling of nonlinearity was not possible except for simple problems where transformation methods could be used. Due to the complexity of the BLDC motor geometries, control techniques and eddy current phenomena in magnetic field of the motor, the simulation of electromagnetic fields and their effects by numerical models is suitable as an appropriate engineering tool. Among the numerical methods, finite element method(FEM) is by far the most efficient and popular method and it has been extensively used in performance analysis of the BLDC motors. Generally, research works have been done by FEM modelling in electrical machines can be classified as: magneto-static approach, frequency domain approach and time stepping approach. The common parameters and performance indicators of the BLDC motor in steady states such as calculation of winding inductances [43], cogging torque [44]- [49], back-emf [50], iron losses [51]-[52] and prediction of the new motor design [53]- [57]

have been done by using magneto-static FEM and the frequency domain FEM. However, the precision of these two FEM models are limited by the concept of the equivalent circuit. Non-sinusoidal quantities cannot be included. FEM mesh cannot rotate according to the rotor positions; hence motion equations cannot be taken into account in the system of equations. In addition, eddy current effect cannot be included in magneto-static FEM model. Hence, it is concluded that magneto-static FEM and complex eddy current FEM model are limited to use in the steady state analysis of machines.

The advance in time-stepping finite element method in recent years, it is now possible to overcome these difficulties by coupling the external circuit and rotor movement with the internal electromagnetic field into the system of equations. The time stepping FEM is finding increasing popularity in the analysis of induction machines [58]- [64]. S. L. Ho and H. L. Li [65] used time-stepping FEM in the modelling of permanent magnet synchronous machines. Jinyun Gan [66] proposed a new PM brushless DC machine with a unique feature of flux regulation and analyze the motor performance by using time stepping FEM method. Analysis of the exterior rotor BLDC motor takes into account the eddy current effect in solid rotor steel shell by time stepping FEM has been proposed by Seung-Chan Park at el [67]. Transient analysis of a new outer-rotor BLDC motor at both normal and flux weakening operations by using circuit-field-torque coupled time stepping finite element method has been presented at [68]. It can be found that by using time stepping FEM in machines modelling, the stator current, the load angle, torque and force can be directly computed. Many assumptions such as neglecting material non-linearities, eddy current effect, rotor motion and high order harmonics which are essential when using equivalent circuit model, frequency domain FEM model, are no longer necessary.

One of the difficulties in the modelling of the time-stepping FEM is developing the methods of rotor rotation. In the time stepping FEM model, the external circuit equations and the internal field equations are needed to couple with the rotor movement and solved simultaneously at each time steps. C. W. Chan and H. L. Li [69] reported a multislice time stepping FEM model including rotor rotation. They developed special technique required for the mesh generation for the movement of the rotor mesh and stator mesh in the multislice model. B. I. Kwon and K. I. Woo [70] proposed new moving mesh technique of rotor rotation for studying the steady state and dynamic behaviour of the permanent magnet motors. In this technique, pseudo-stationary approximation method is used to couple the motion equations with circuit and field equations. S. J. Salon and M. J. Lee [71] suggested moving band technique to study the induction motor analysis. They proposed one moving band between stator and rotor mesh and when the rotor is rotated according to the time step; only moving band meshes are needed to mesh again. Chuntin Mi [72] established a new moving mesh technique to calculate the iron losses of the synchronous motor in transient conditions. In establishing the meshes for the analysis, the rotor is moved and positioned at each time step such that it does not disturb the integrity of the mesh structure as it moves. The initial meshes of the stator and the rotor are generated first. The air gap is divided into two parts and the first half is for the stator and the other half is for rotor. A stator mesh and rotor mesh share the same boundary at the middle of the air gap. The inner stator circumference and outer rotor circumference of the air gap are divided into equal steps so that their nodes coincide. To provide for rotor movement, the time step has been chosen so that the angle or length of each step is equal to the interval between two neighboring nodes along the mid air gap. As a consequence, the time step cannot be chosen arbitrary. Step size is fixed throughout the whole process. That is the main disadvantage of this technique.

S. L. Ho, W. N. Fu [73] reported simple and reliable moving mesh technique in the analysis of induction motor. The air gap is divided into three layers; two layers belong to the stator mesh and the rest layer belongs to the rotor mesh. The stator mesh and the rotor mesh are generated separately and connected by the periodic boundary condition. When the rotor is rotated, only boundary conditions and node numbers need to be changed. Stator mesh and rotor mesh are unchanged. In this thesis, moving mesh technique developed by W. N. Fu is adopted in the simulation of rotor rotation.

BLDC motors cannot work without the electronic controllers and their control methods are complicated compared with traditional DC motors. The phase windings are energized in sequence by the switching elements in the inverter which are controlled by shaft position sensors. The impressed voltages comprised of a series of pulses of varying widths and the stator phase currents are non-sinusoidal. High order harmonics in the currents and in the magnetic field will have significant effects upon the motor output torque and corresponding motor performances. In order to simulate precisely both steady state and dynamic performance of the motor, characteristic of the inverter circuit and its control loop feature must be included as a coupled system. However, few studies have reported the effects of control loop feature in the performance analysis of a BLDC motor. Hui Tan [74] simulated time stepping FEM model to study the steady state analysis of a multipole brushless DC motor including with control loop feature in the system. W. N. Fu, Z. J. Liu and C. Bi [75] proposed the performance analysis of disk dive spindle motor using time stepping FEM with current loop control and PWM switching strategies. G. H. Jang [76] proposed nonlinear time-stepping finite element analysis of the magnetic field considering the switching action of pulse width modulation (PWM), which controls the average voltage applied to the motor. It can be found that all of these works which have included of coupling the time stepping FEM with current loop control were applied only to study the steady state analysis of the motor. In the BLDC motor, the torque is directly proportional to the winding currents and speed of the motor can be controlled by measuring the stator phase voltage applied to the motor. Therefore cascaded current and speed control scheme is suitable for the purpose of rapid response. In this work, cascaded speed and current closed loop control is implemented in order to simulate both static and dynamic performances of the BLDC motor.

1.6 Scope of the Thesis

This thesis deals with the modeling, simulation and performance analysis of a BLDC motor using numerical methods. The primary objective is to develop an efficient and practical procedure based on numerical techniques to analyze the steady state and dynamic performances of BLDC motors. In order to achieve these objectives, the following modelling techniques, numerical methods and experimental set up are developed in this thesis.

- Dynamic model of the BLDC motor is developed using two dimensional time stepping finite element method. In this model, the electromagnetic field equations, motion equations and circuit equations are formulated in time domain and solved simultaneously at each time steps. 3D effects i.e end winding effects are taken into account using empirical formulae. The eddy current effect, the saturation effect, the skin effect, the rotor movement, the non-sinusoidal quantities and nonlinear electric circuit systems with semiconductor converters are included in the system of equations.

- Time stepping finite element method combined with current fed two dimensional FEM is used to develop the steady state model of the BLDC motor. In this steady state model, current fed two dimensional FEM is used as a pre-computation stage for time domain model. By using the proposed model, extensive computation time to reach to steady state using time stepping FEM alone can be eliminated. In addition, non-sinusoidal quantities, high-order harmonic and rotor rotation which are very difficult to take into account in the steady state analysis using the traditional finite element method can be included.

- A new approach to couple the time stepping FEM with control loop feature is implemented. Speed loop cascaded with hysteresis current controller is used in this control loop application. This approach provides simple and efficient ways to analyze the BLDC motor as an actual motor-controller drive system.
- Experimental test stand for exterior rotor BLDC motor is developed using DS1104 controller board. Both software and hardware set up for HDD spindle motor is implemented.
- Performance analysis of the BLDC motor are simulated using proposed steady state and dynamic models. Application characteristics of the HDD spindle motor are studied using the time stepping FEM coupled with control loop feature. Important features of the spindle motor at starting conditions under no load and loaded conditions are investigated. Optimization of the motor run-up performances at starting and normal running conditions are analyzed. Simulation results are verified with experimental results.

1.7 Outlines of the Thesis

Contents of the thesis are organized in the following:

Chapter 1 discusses the basic ideas of the numerical techniques in electrical machines, configuration and characteristic of the BLDC motor and the main objectives of the thesis.

Chapter 2 presents numerical modelling of the BLDC motor using conventional FEM. Procedures to develop the mathematical models of BLDC motor in magneto-static FEM are described.

Chapter 3 presents the modelling of a BLDC motor in time domain. Detailed procedures and formulations by using time stepping finite element method are presented. Modeling technique to reduce the starting period in studying the steady state performance in time stepping model is described.

In Chapter 4, software and hardware implementation of the DSP based experimental set up for exterior rotor BLDC motor-controller system is presented. Experimental procedures to measure the motor speed with various supply voltages, motor back-emf, stator currents under load and no load conditions and motor transients are described. Experimental constraints under hardware and software limitations are discussed.

Chapter 5 deals with the performance analysis of the BLDC motor using developed numerical models. The steady state performances of a BLDC motor in no load and load conditions are described. Dynamic conditions of step voltage variation, load torque changing and locked rotor condition are investigated.

In chapter 6, the application characteristics of the exterior rotor BLDC motors using developed numerical models are presented. The starting processes of the spindle motor with voltage, current and speed limits are investigated by coupling with current-speed cascaded closed loop control structure. Optimization of spindle motor performance under starting and normal running conditions are analyzed.

Chapter 7 provides the discussions and conclusions of this work.

Chapter 2

Computational Analysis of a BLDC Motor

2.1 Introduction

It is important to predict accurately the steady state and dynamic performances of the proposed design of a BLDC motor in order to avoid the design misjudgment that can prove costly once the motor is manufactured. Traditionally, equivalent circuits and lumped parameter models have been used to calculate the performance of BLDC motors and to conduct the design with idealized and simplified physical representation. However, it is difficult to use the traditional analytical method to calculate their characteristics taking into account the effect of magnetic saturation, complex configuration, eddy currents and external circuits at the same time. Basically, electrical machines are electromechanical converters and their behaviours can be described by electromagnetic fields. Using Maxwell's equations, all of the electromagnetic fields can be expressed by partial differential equations. To solve these partial differential equations, numerical methods have been recognized as practical and accurate tools. Among numerical methods, finite element method has been proved to be an accurate tool to compute the electromagnetic field distribution and has been extensively used for solving field related problems [77]-[81].

In this chapter, the finite element analysis for the two-dimensional electromagnetic field problems is presented. The finite element model for static magnetic field calculation is derived. Proposed static FEM model is used to develop the steady state model of a BLDC motor.

2.2 Finite Element Analysis

In the finite element analysis, the partial differential equations modelling the field problems are transformed into energy-related functionals. Approximate solutions are then sought to the field problems that minimize these functionals. By this procedure, a detailed modelling of the geometry of the field region is possible, and the results obtained are found to be accurate. In brief, general procedures of the finite element method are as follows [82]-[85]:

1. Define the boundary value problem by partial differential equations (Mathematical formulations of the physical model)

2. Represent the variational formulation of the partial differential equations in terms of energy-related functionals

3. Discretize the problem domain with sub-regions called 'elements'

4. Choose the trial function for each elements in terms of nodal values of the elements and interpolating functions

5. Derive the element matrix equations using the principle of weighted residual or the variational principle

6. Assemble the element matrix equations

7. Impose the boundary conditions into the system of equations

8. Solve the system of equations to obtain the discretized function values on every node

Detailed descriptions of the procedures listed above will be discussed in next sections. These procedures are leading to the solution of the electromagnetic problems of BLDC motors. In this work, under-slung type hard disk drive spindle motor (exterior rotor type BLDC) is used as a working example to study the finite element analysis of the BLDC motor. Fig. 2.1 shows the physical model of the BLDC motor to be analyzed.

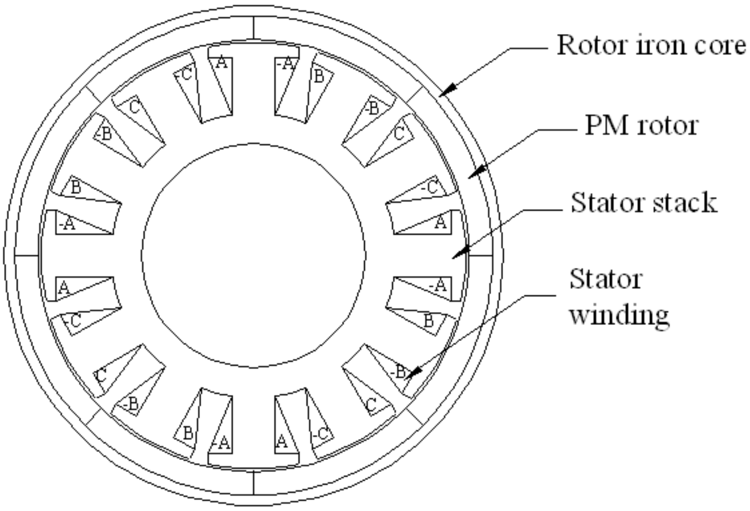

Figure 2.1: BLDC motor configuration

2.2.1 Mathematical formulations of the physical model

The nonlinear magneto-static field in an electric machine can be described by the following Maxwell's equations

$$\nabla \times H = J \tag{2.1}$$

$$B = \mu H \tag{2.2}$$

The magnetic vector potential A is defined as

$$B = \nabla \times A \tag{2.3}$$

Substituting equations (2.1) into (2.2), we get

$$\nabla \times \frac{B}{\mu} = J \tag{2.4}$$

$$\nabla \times \frac{1}{\mu} (\nabla \times A) = J \tag{2.5}$$

$$\nabla \times \nu(\nabla \times A) = J \tag{2.6}$$

where A is the axial component of the magnetic vector potential, ν is the reluctivity of the material and J is the current density. In the analysis of electric machines, it is common practice to evaluate the field solution in two dimensions only so that the current density and magnetic vector potential have only z-direction components. This analysis is valid for most cases because the air gap between the rotor and the stator in an electric machine is so small that over a considerable range in the axial direction of the machine, except the end regions, the magnetic field is virtually two-dimensional. Furthermore, two dimensional FEM requires much less computing power, storage and computer time usage compared to the three dimensional FEM [86]. In this mathematical model, it is assumed that the eddy current on the stator laminations and rotor back iron are neglected. Therefore, for a problem domain or region, the equation (2.6) in two dimensional X-Y planes becomes,

$$\frac{\partial}{\partial x}\left(\nu \frac{\partial A_z}{\partial x}\right) + \frac{\partial}{\partial y}\left(\nu \frac{\partial A_z}{\partial y}\right) = -J_z \tag{2.7}$$

The above equation (2.7) is Poisson equation considering only the current source excitation. In this For permanent magnet BLDC motor, the mathematical model for permanent magnets is required. There are two possibilities of the modeling of permanent magnet materials:

- Magnetisation vector model and
- Current sheet approach.

Although these two models have different starting points, they both result in the same set of equations [10]. In this work, magnetization vector model is used.

Magnetization vector model

According to the magnetization phenomenon of the permanent magnet, the characteristic of a permanent magnet can be shown as shown in Fig. 2.2 where B_r is the remanence flux density and H_c is the coerecitivity. The relationship between magnetic flux density and magnetic field intensity can be given by

$$B = \mu_0(H + M) \tag{2.8}$$

$$B = \mu_0\{(1 + \chi)H + M_r\} \tag{2.9}$$

$$B = \mu_0\{\mu_r H + M_r\} \tag{2.10}$$

$$B = \mu H + \mu_0 M_r \tag{2.11}$$

Hence

$$H = \nu\,(B - \mu_0 M_r) \tag{2.12}$$

we have

$$\nabla \times H = J \tag{2.13}$$

Substitute equation (2.12) into equation (2.13),

$$\nabla \times \{\nu\,(B - \mu_0 M_r)\} = J \tag{2.14}$$

$$\nabla \times (\nu B) - \nabla \times \nu\mu_0 M = J \tag{2.15}$$

Therefore, the field equation for two-dimensional magneto-static analysis of permanent magnet is

$$\nabla \times (\nu B) = J + \nabla \times \nu\mu_0 M_r \tag{2.16}$$

$$\nabla \times (\nu B) = J + J_m \tag{2.17}$$

where $J_m = \nabla \times \nu\mu_0 M_r$, which is the equivalent current density of the permanent magnet.

According to the equations (2.7) and (2.17), the mathematical model of the prototype BLDC motor can be represented as

$$\frac{\partial}{\partial x}\left(\nu\frac{\partial A}{\partial x}\right)+\frac{\partial}{\partial y}\left(\nu\frac{\partial A}{\partial y}\right)=-J+J_m \tag{2.18}$$

where ν is the reluctivity of the material, J_0 is the applied source current density, J_m is the equivalent current density of the permanent magnet, ω is the angular frequency, σ is the conductivity of the material. The first term of the right hand side of the equation represents for the applied source region (the stator conductor region)and the last term represents for the permanent magnet region. After we got the mathematical formulation of the physical model, according to the FEM procedures as mentioned before, it is needed to discretize the physical model into small sub-regions or finite elements to derive the finite element equations for elements using variational principle or method of weighted residuals.

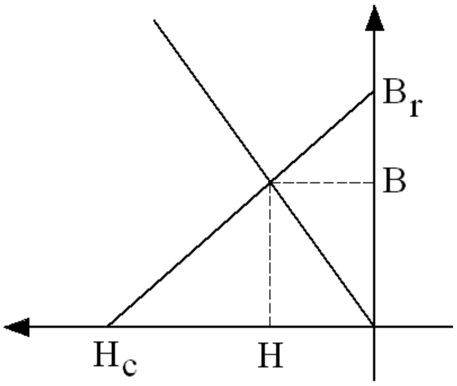

Figure 2.2: Characteristic of a permanent magnet material

2.2.2 Discretization of the problem domain

Domain discretization is one of the most important steps in FEM. Most of the time necessary for the finite element method is spent for domain discretization or mesh generation. The size of the elements, in other words the dimension or number of the elements decides length of computing time and storage of computer memory.

Since the fineness of the mesh has major effect on the accuracy of the solution. Understanding the nature of the field is useful in determining the mesh densities of the various places in a machine. Generally where the field is changing rapidly,the mesh density should be higher. The shapes, sizes and the configurations of the elements can be of many different types. Fig. 2.3 shows examples of various shapes of elements that can be used. Triangular elements are widely used because these elements are easy to fit in the domain sub-divisions.

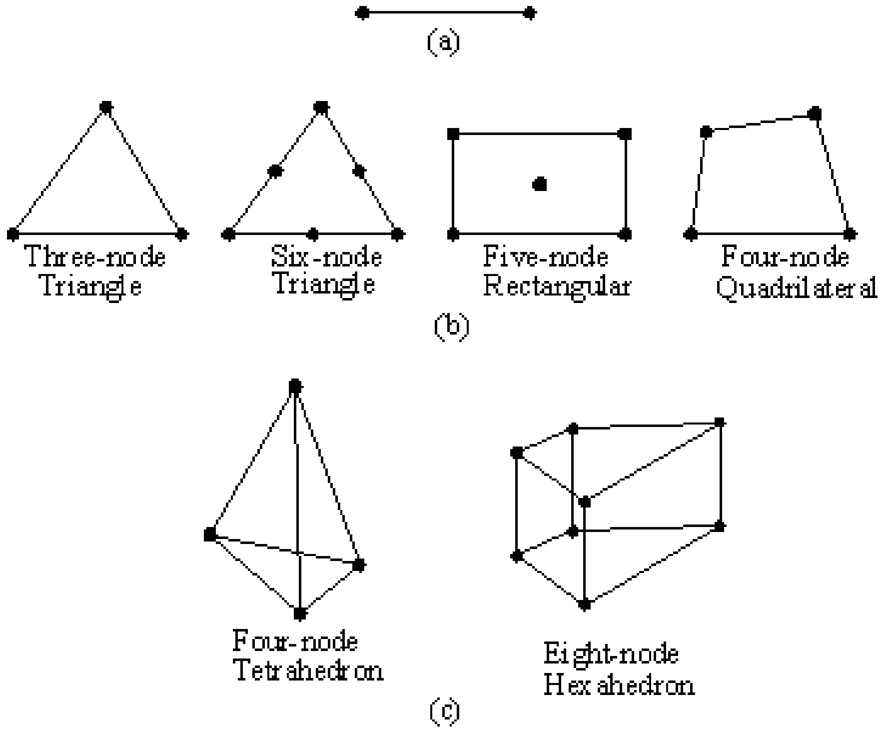

Figure 2.3: Typical finite elements (a) One-dimensional (b) Two-dimensional (c) Three-dimensional

After dividing the problem domain into finite elements, an interpolation or shape function for the distribution of the unknown function in each element is derived. The choice of the geometry of the element and the form of the approximating function to represent the behaviour of field variables within each element are both extremely important. Mostly, a polynomial series is used to represent the shape of the element since the polynomial is easy to manipulate. Let us consider a triangle element with vertex i, j and k as shown in Fig. 2.4. The vertices are nodes at which

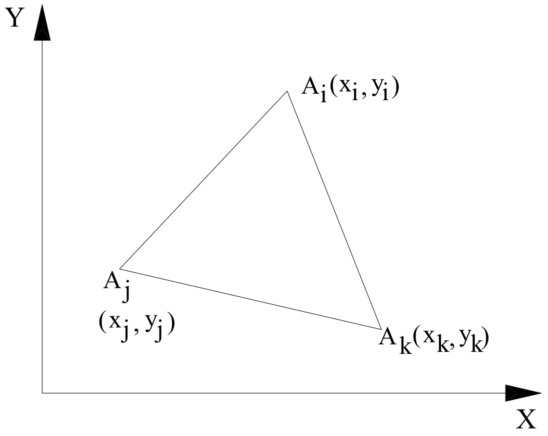

Figure 2.4: A triangular element

the unknown vector potentials will eventually be calculated. Assume the potential varies linearly in the element. With this approximation, a linear polynomial function, as a trial function, at any point in the triangle can be expressed as

$$A = C_1 + C_2x + C_3y \tag{2.19}$$

where C_1, C_2 and C_3 are constants to be determined. At vertex i, j and k of the triangle as shown in Fig. 2.4, we have $x = x_i, x_j, x_k$ and $y = y_i, y_j, y_k$. At these points, A must be equal to A_i, A_j and A_k so that

$$C_1 + C_2x_i + C_3y_i = A_i \tag{2.20}$$

$$C_1 + C_2x_j + C_3y_j = A_j \tag{2.21}$$

$$C_1 + C_2x_k + C_3y_k = A_k \tag{2.22}$$

Solving equations (2.20), (2.21) and (2.22) by using Kramer's rule, we have

$$A = \frac{(a_i + b_ix + c_iy)A_i + (a_j + b_jx + c_jy)A_j + (a_k + b_kx + c_ky)A_k}{2\Delta} \tag{2.23}$$

where Δ is the area of the triangle, $a_i = x_jy_k - x_ky_j$, $b_i = y_j - y_k$ and $c_i = x_k - x_j$.

Equation (2.23) can be represented as,

$$A = \sum_{i=1}^{m} N_i(x, y)A_i \tag{2.24}$$

Writing the nodal potential in the element in the matrix form,

$$A = (N_i, N_j, N_k) \begin{pmatrix} A_i \\ A_j \\ A_k \end{pmatrix} \tag{2.25}$$

$$N_i = \frac{1}{2\Delta} \left[(x_j y_k - x_k y_j) + (y_j - y_k)\, x + (x_k - x_j)\, y \right] = (a_i + b_i x + c_i y)/2\Delta \tag{2.26}$$

$$N_j = \frac{1}{2\Delta} \left[(x_k y_i - x_i y_k) + (y_k - y_i)\, x + (x_i - x_k)\, y \right] = (a_j + b_j x + c_j y)/2\Delta \tag{2.27}$$

$$N_k = \frac{1}{2\Delta} \left[(x_i y_j - x_j y_i) + (y_i - y_j)\, x + (x_j - x_i)\, y \right] = (a_k + b_k x + c_k y)/2\Delta \tag{2.28}$$

where m are nodes in the element and N_i are the shape functions for the triangular element because they only depend on the position of the nodes and dimensions or "shape" of the element and have nothing related with the node values. These shape functions are linear. These functions have the following important properties:

1. $N_i = 1$ at node i and is 0 at all other nodes.
2. The sum of all shape functions at any point in the triangle is 1.

FEM mesh of the exterior rotor BLDC motor geometry is as shown in Fig. 2.5.

2.2.3 Derivation of the element matrix equations

The variational approach and the weighted residual approach are used to derive the element matrix equations. Both principles force the error between the real and the approximate solution to approach zero. The variational method is based on the equivalent functional of the governing equation. The weighted residual method is based on the operator equation directly. In this respect, the weighted residual method is a more general and more universally applicable method than the variational approach because to apply it the variational principle need not be known. In fact, there are a number of practical cases in which the variational expression does not exist and the weighted residual method can be applied. Based

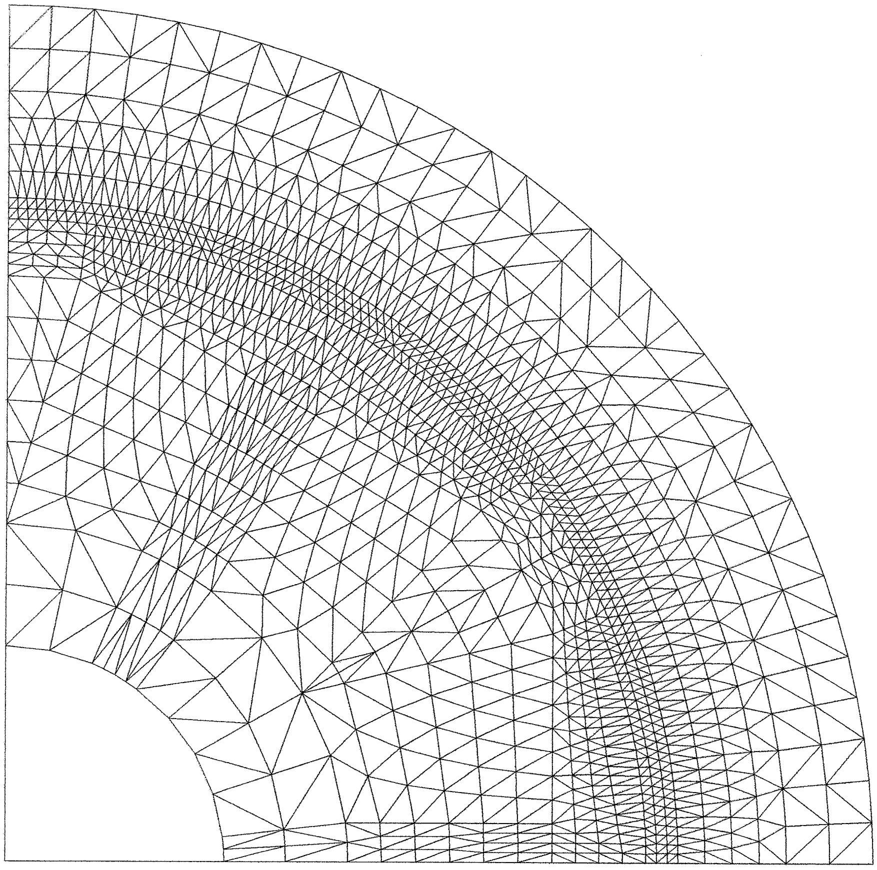

Figure 2.5: FEM mesh of the exterior rotor BLDC motor

on the choice of different weighting functions, basic functions and the approach to discretization, different weighted residual methods are formulated. In this work, the Galerkin's method is employed for the FE formulation. This is a particular weighted residual method for which the weighting functions are the same as the shape functions. The method of weighted residuals can be stated simply as follows. Our objective is to approximate the solution to an operator equation. An operator equation $L(x) = 0$; in the region Ω with boundary condition C. If we substitute an approximate solution $\hat{x}$ into an operator equation, the residual R can be obtained because $x = \hat{x}$.

$$L(\hat{x}) = R \tag{2.29}$$

Choose the weighing function W and set the integral of the multiplication of weighing function and a residual to zero.

$$\iint_{\Omega} WR = 0 \tag{2.30}$$

According to the Galerkin's method, substituting an approximation $\hat{A}$ for A into the mathematical model of the BLDC motor (equation (2.18)), the residual R is

$$R = \frac{\partial}{\partial x}\left[\nu \frac{\partial \hat{A}}{\partial x}\right] + \frac{\partial}{\partial y}\left[\nu \frac{\partial \hat{A}}{\partial y}\right] + J_0 - J_m \tag{2.31}$$

if we multiply with the weighting function W and set the integral to zero over the domain area Ω,

$$\begin{aligned} &\iint_{\Omega} W\left(\frac{1}{\mu}\frac{\partial^2 \hat{A}}{\partial x^2} + \frac{1}{\mu}\frac{\partial^2 \hat{A}}{\partial y^2}\right) dxdy \\ &- \iint\limits_{\Omega} WJ_0 dxdy = \iint_{\Omega} WJ_m dxdy \end{aligned} \tag{2.32}$$

For the sake of clarity and simplicity, Galerkin's formulation of the permanent magnet will be discussed in next section. In this section, we are concentrated on Galerkin's formulation of the first three terms of the left hand side of the equation (2.32). Rewrite the equation (2.32) eliminating the term represents the permanent magnet as follow.

$$\iint_{\Omega} W \left(\frac{1}{\mu}\frac{\partial^2 \hat{A}}{\partial x^2} + \frac{1}{\mu}\frac{\partial^2 \hat{A}}{\partial y^2} \right) dxdy = \iint\limits_{\Omega} W J_0 dxdy \tag{2.33}$$

Integrating the first term by parts,

$$\iint_{\Omega} W \left(\frac{1}{\mu}\frac{\partial^2 \hat{A}}{\partial x^2} + \frac{1}{\mu}\frac{\partial^2 \hat{A}}{\partial y^2} \right) dxdy = \iint_{\Omega} \frac{1}{\mu} \left(\frac{\partial W}{\partial x}\frac{\partial \hat{A}}{\partial x} + \frac{\partial W}{\partial y}\frac{\partial \hat{A}}{\partial y} \right) dxdy - \oint_{C} \frac{1}{\mu} W \frac{\partial \hat{A}}{\partial \hat{n}} dc \tag{2.34}$$

Substitute the equation (2.34) into equation (2.33), we get

$$\begin{aligned} &\iint_{\Omega} \frac{1}{\mu} \left(\frac{\partial W}{\partial x}\frac{\partial \hat{A}}{\partial x} + \frac{\partial W}{\partial y}\frac{\partial \hat{A}}{\partial y} \right) dxdy - \oint_{C} \frac{1}{\mu} W \frac{\partial \hat{A}}{\partial \hat{n}} dc \\ &= \iint_{\Omega} W J_o dxdy \end{aligned} \tag{2.35}$$

We can break the surface integrals into summations over small areas. First order triangular element is used to discretize the whole region. Domain discretization and derivation of element shape functions have been shown in section (2.2.2). Hence, we get

$$\begin{aligned} &\sum_{M} \left\{ \frac{1}{\mu^e} \iint_{\Omega} \frac{\partial W^e}{\partial x}\frac{\partial A^e}{\partial x} + \frac{\partial W^e}{\partial y}\frac{\partial A^e}{\partial y} \right\} dxdy - \frac{1}{\mu^e}\frac{\partial A}{\partial \hat{n}} \oint\limits_{c} W^e dc \\ &= J_o \iint_{\Omega_e} W^e dxdy \end{aligned} \tag{2.36}$$

where M is the number of triangular elements. The line integral of the above equation (2.36) needs to be evaluated over elements which have a side in common with the boundary of the problem. Normally, this integral is simply set to zero implying that $\frac{\partial \hat{A}}{\partial \hat{n}} = 0$ [10].

According to Galerkin's method, the weighting function is the same as the element shape function, hence,

$$W^e = \begin{pmatrix} N_i^e \\ N_j^e \\ N_k^e \end{pmatrix} \tag{2.37}$$

Taking derivatives of equation (2.23) with respect to x and y

$$\frac{\partial \hat{A}}{\partial x} = \frac{1}{2\Delta}(b_i^e, b_j^e, b_k^e) \begin{pmatrix} \hat{A}_i \\ \hat{A}_j \\ \hat{A}_k \end{pmatrix} \tag{2.38}$$

$$\frac{\partial \hat{A}}{\partial y} = \frac{1}{2\Delta}(c_i^e, c_j^e, c_k^e)\begin{pmatrix} \hat{A}_i \\ \hat{A}_j \\ \hat{A}_k \end{pmatrix} \tag{2.39}$$

Taking derivatives of equations (2.26), (2.27) and (2.28) with respect to x and y

$$\frac{\partial W^e}{\partial x} = \frac{1}{2\Delta}\begin{pmatrix} b_i^e \\ b_j^e \\ b_k^e \end{pmatrix} \tag{2.40}$$

$$\frac{\partial W^e}{\partial y} = \frac{1}{2\Delta}\begin{pmatrix} c_i^e \\ c_j^e \\ c_k^e \end{pmatrix} \tag{2.41}$$

Substitute equations (2.38), (2.39), (2.40) and(2.41) into the first term on the left hand side of the equation (2.36),

$$\begin{gathered} \frac{1}{\mu^e}\iint_{\Omega_e}\left(\frac{\partial W^e}{\partial x}\frac{\partial \hat{A}^e}{\partial x} + \frac{\partial W^e}{\partial y}\frac{\partial \hat{A}^e}{\partial y}\right) dxdy = \\ \frac{1}{4\mu^e\Delta}\begin{pmatrix} b_i^2 + c_i^2 & b_ib_j + c_ic_j & b_ib_k + c_ic_k \\ b_ib_j + c_ic_j & b_j^2 + c_j^2 & b_jb_k + c_jc_k \\ b_ib_k + c_ic_k & b_jb_k + c_jc_k & b_k^2 + c_k^2 \end{pmatrix}\begin{pmatrix} \hat{A}_i \\ \hat{A}_j \\ \hat{A}_k \end{pmatrix} \end{gathered} \tag{2.42}$$

The above coefficient matrix is sometimes referred to as the stiffness matrix S in the finite element analysis. Its size is NxN, where N is the number of nodes. The material of the elements and element structure determines the items in the stiffness matrix.

The forcing function (right hand side of the equation (2.36))becomes

$$J_0 \iint\limits_{\Omega_e} W^e dxdy = J_0 \iint_{\Omega_e} \frac{(a_i + b_ix + c_iy)}{2\Delta} dxdy = J_0 \frac{(a_i + b_i\bar{x} + c_y\bar{y})}{2\Delta} \tag{2.43}$$

where $\bar{x}$ and $\bar{y}$ are the coordinates of the triangle.

$$\bar{x} = \frac{1}{3}(x_i + x_j + x_k) \tag{2.44}$$

Substituting the values we found for a_i, b_i and c_i,

$$\bar{y} = \frac{1}{3}(y_i + y_j + y_k) \tag{2.45}$$

Assuming that J_0 is constant over the triangle we get

$$\frac{a_i + b_i\bar{x} + c_i\bar{y}}{2} = \frac{\Delta}{3} \tag{2.46}$$

Therefore, the element matrix equations for the equation (2.36) is

$$\frac{1}{4\mu^e\Delta}\begin{pmatrix} b_i^2+c_i^2 & b_ib_j+c_ic_j & b_ib_k+c_ic_k \\ b_ib_j+c_ic_j & b_j^2+c_j^2 & b_jb_k+c_jc_k \\ b_ib_k+c_ic_k & b_jb_k+c_jc_k & b_k^2+c_k^2 \end{pmatrix}\begin{pmatrix}\hat{A}_i\\ \hat{A}_j\\ \hat{A}_k\end{pmatrix} = J_0^e\frac{\Delta}{3}\begin{pmatrix}1\\1\\1\end{pmatrix} \tag{2.47}$$

2.2.3.1 Galerkin's formulation for the permanent magnet

Using Galerkin's method, the field equation (2.32) of two dimensional magnetostatic analysis of permanent magnet can be represented as,

$$\iint_\Omega W\left(\frac{1}{\mu}\frac{\partial^2\hat{A}}{\partial x^2}+\frac{1}{\mu}\frac{\partial^2\hat{A}}{\partial y^2}\right)dxdy = \iint_\Omega WJ_m dxdy \tag{2.48}$$

where $J_m = \nabla\times\nu\mu_0 M$, hence we get

$$\iint_\Omega(\nabla\times v(\nabla\times A)).Wdxdy - \iint_\Omega(\nabla\times(v\mu_o M).Wdxdy = 0 \tag{2.49}$$

Rearranging the equation (2.49)

$$\iint_\Omega \nabla\times(v\nabla\times A - v\mu_o M)\cdot Wdxdy = 0 \tag{2.50}$$

As before, we choose the weighting function W to be the same as the element shape function, N. We now integrate by parts. Using the vector identity

$$(\nabla\times F)\cdot G = \nabla\cdot(F\times G) + F\cdot(\nabla\times G) \tag{2.51}$$

and with

$$F = v\nabla\times A - v\mu_o M \tag{2.52}$$

and $G = N$. Therefore,

$$\begin{aligned}\iint_\Omega(\nabla\times(v\nabla\times A) - v\mu_o M)\cdot Ndxdy = \\ \iint(v\nabla\times A - v\mu_o M)\cdot(\nabla\times N)dxdy \\ +\iint\nabla\cdot((v\nabla\times A - v\mu_o M)\times N)dxdy\end{aligned} \tag{2.53}$$

The last term of the equation (2.53) can be written as a line integral using the stroke's theorem.

$$\iint\nabla\cdot(v\nabla\times A - v\mu_o M)\times NdS = \oint_C\{(v\nabla\times A - v\mu_o M)\times N\}\cdot\hat{n}dC \tag{2.54}$$

Ignore the line integral, the equation (2.54) becomes

$$\iint_{\Omega} \nu(\nabla\times A)\cdot(\nabla\times N)dxdy = \iint_{\Omega} \nu\mu_o M(\nabla\times N)dxdy \tag{2.55}$$

For two dimensional case, A and J have only z components and M has only x and y components. Substituting the curl of the weighting function in the first term on the right hand side of equation (2.55) we obtain

$$\iint_{\Omega} \nu\left(\frac{\partial A}{\partial x}\frac{\partial N}{\partial x} + \frac{\partial A}{\partial y}\frac{\partial N}{\partial y}\right)dxdy = \iint_{\Omega}\left(\nu\mu_o\left(M_x\frac{\partial N}{\partial y} - M_y\frac{\partial N}{\partial x}\right)\right)dxdy \tag{2.56}$$

The term representing the permanent magnet is

$$\iint_{\Omega} \nu\mu_o\left(M_x\frac{\partial N}{\partial y} - M_y\frac{\partial N}{\partial x}\right)dxdy \tag{2.57}$$

But

$$\frac{\partial N_i}{\partial x} = \frac{b_i}{2\Delta} \tag{2.58}$$

$$\frac{\partial N_i}{\partial y} = \frac{c_i}{2\Delta} \tag{2.59}$$

Substituting equations (2.58) and (2.59) into equation (2.57), we get

$$\iint_{\Omega} \frac{\nu\mu_o}{2\Delta}\left(M_x\begin{pmatrix} c_i \\ c_j \\ c_k \end{pmatrix} - M_y\begin{pmatrix} b_i \\ b_j \\ b_k \end{pmatrix}\right)dxdy \tag{2.60}$$

Therefore, according to the equations (2.47) and (2.60) the final global finite element matrix equations for the BLDC motor is

$$\begin{aligned} &\frac{1}{4\mu^e\Delta}\begin{pmatrix} b_i^2+c_i^2 & b_ib_j+c_ic_j & b_ib_k+c_ic_k \\ b_ib_j+c_ic_j & b_j^2+c_j^2 & b_jb_k+c_jc_k \\ b_ib_k+c_ic_k & b_jb_k+c_jc_k & b_k^2+c_k^2 \end{pmatrix}\begin{pmatrix} \hat{A}_i \\ \hat{A}_j \\ \hat{A}_k \end{pmatrix} \\ &= J_0^e\frac{\Delta}{3}\begin{pmatrix} 1 \\ 1 \\ 1 \end{pmatrix} + \frac{\nu\mu_o}{2\Delta}\left(M_x\begin{pmatrix} c_i \\ c_j \\ c_k \end{pmatrix} - M_y\begin{pmatrix} b_i \\ b_j \\ b_k \end{pmatrix}\right) \end{aligned} \tag{2.61}$$

2.2.4 Assembling of element matrix equation

All element equations of the problem domain are needed to be assembled to form a system of matrix equations. The principle for assembling the element matrices into a system matrix is based on the property of compatibility. It means that at every node the nodal values of the unknown function of each element are the same no matter where the node belongs to. In the assembly process all the elements matrices are simply added to form the global matrix. We go through each element and add the (i j) terms of the stiffness and mass matrices to the corresponding (i j) terms in the global matrix. The resulting global matrix will be sparse, symmetric and singular. The procedures for assembling the system matrix of the problem are as follows. For simplicity, the problem domain containing three elements is considered as shown in Fig. 2.6. If is coefficient matrix for element e. The contribution of each element can be summarized as shown in Table 2.1. After assembling, the final global matrix $[K]$ will be

$$\begin{bmatrix} K11 & K12 & K13 & K14 & K15 \\ K21 & K22 & K23 & K24 & K25 \\ K31 & K32 & K33 & K34 & K35 \\ K41 & K42 & K43 & K44 & K45 \\ K51 & K52 & K53 & K54 & K55 \end{bmatrix}$$
$$= \begin{bmatrix} K_{11}^{1} & K_{12}^{1} & K_{13}^{1} & 0 & 0 \\ K_{12}^{1} & K_{22}^{1}+K_{22}^{2}+K_{22}^{3} & K_{23}^{1}+K_{23}^{2} & K_{24}^{3} & K_{25}^{2}+K_{25}^{3} \\ K_{13}^{1} & K_{23}^{1}+K_{23}^{2} & K_{33}^{1}+K_{33}^{2} & 0 & K_{53}^{2} \\ 0 & K_{24}^{3} & 0 & K_{44}^{3} & K_{45}^{3} \\ 0 & K_{25}^{2}+K_{25}^{3} & K_{53}^{2} & K_{45}^{3} & K_{55}^{3} \end{bmatrix} \tag{2.62}$$

In practical case, one node can only connect with the other limited nodes through several elements so that there exists a great number of zero elements in the matrix. Hence, the resulted stiffness matrix is symmetric and sparse. The diagonal elements of the matrix are positive and dominant, and all the values of the sequent sub-determinant are positive. Therefore, the system matrix is a positive definite matrix.

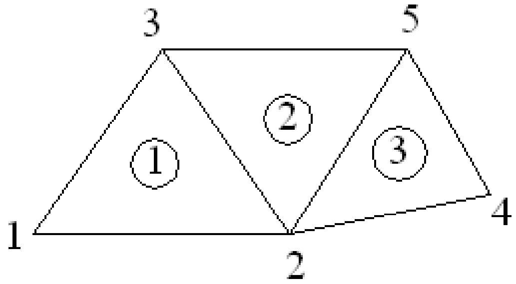

Figure 2.6: Problem domain containing three triangular elements

Table 2.1: Element contribution

Element No	Contribution nodes	K_{ii}^e	K_{jj}^e	K_{kk}^e	K_{ij}^e	K_{ik}^e	K_{jk}^e
Element 1	1,2,3	K_{11}^1	K_{22}^1	K_{33}^1	K_{12}^1	K_{13}^1	K_{23}^1
Element 2	2,5,3	K_{22}^2	K_{55}^2	K_{33}^2	K_{25}^2	K_{23}^2	K_{53}^2
Element 3	2,4,5	K_{22}^3	K_{44}^3	K_{55}^3	K_{24}^3	K_{25}^3	K_{45}^3

2.2.5 Imposing the boundary conditions

Specific boundary conditions are needed to be imposed upon the system of equations. In most applications the electromagnetic field is an infinitely extending space. In these applications, boundaries are used to simplify the finite element model and approximate the magnetic vector potential at nodal points. In fact, the correct and appropriate application of the boundary condition is the key to define the field problems and to allow an accurate solution in an efficient way. For example, rotary electrical machines have identical pole pitches or sometimes half pole pitches. Boundaries due to symmetry greatly reduce the size of the finite element matrix. In General, boundary conditions can be classified into three types.

- Dirichlet boundary condition
- Neumann boundary condition and
- Cyclic or periodic boundary condition.

Dirichlet boundary condition sets the unknown function to a known function on the boundary of the differential problem. This boundary condition is imposed by assigning the specific values to the vectors on the boundary. The most common use of Dirichlet boundary conditions is to define magnetic vector potential, $A = 0$ along a boundary to keep flux from crossing the boundary. Fig. 2.7 shows in a typical example the application of the Dirichlet boundary condition of an electromagnetic field of a BLDC motor. It is sometimes called the boundary condition of first kind.

Neumann boundary condition is the next important boundary condition for field problems. Here the known value of the derivative of the unknown function in the normal direction of the boundary is prescribed. If the derivative in the normal direction is constant, lines of constant potential can pass the outer boundary of the studied domain. Usually, $\frac{\partial A}{\partial n} = 0$ is defined along a boundary to force flux to pass the boundary at exactly a 90 degree angle to the boundary. The most important property of this type of boundary condition is that by knowing symmetries of the field, and applying the Neumann boundaries there, the numerical model can be reduced to obtain the same solution of the problem. In this way, the problem size, the time to prepare the field problem and the computational efforts can be reduced significantly. On the other hand, if less than the complete geometry has to be defined and discretised, a higher accuracy is achievable for the overall solution of the problem without extra effort. Therefore, particular attention must be paid to this boundary condition.

Periodic boundary condition can be applied in the rotating electrical machines, not only using symmetries in the geometry but also symmetry in the magnetic field distribution. This type of periodic boundary condition has the form:

$$kA_1(x) + A_2(x) = m \tag{2.63}$$

Under load conditions, the air gap field of an electrical machine repeats itself every pole pitch. This field periodicity can be used to define another type of boundary condition to reduce the size of the numerical model. The local potentials in such boundaries depend on the solution of the field problem and thus inherently occur always in pairs. One boundary is computed and the opposite one is linearly linked to this value. In Fig. 2.8 the dotted lines indicate the pairs of the boundaries.

After determining which boundary conditions have to be used for a particular problem, treatment of boundary conditions can be included in the formulation of the system of equations. For example, if the problem subject to the Dirichlet boundary condition, the nodal value of those nodes located on the boundary are known. The known value must be removed to the right hand side of the matrix equation. The system matrix and the column vector of the right hand side of the equation are needed to modify as follows. Consider the following the global matrix equation.

$$\begin{bmatrix} k_{11} & \cdots & k_{1m} & \cdots & k_{1N} \\ \vdots & \vdots & \vdots & \vdots & \vdots \\ k_{m1} & \cdots & k_{mm} & \cdots & k_{mN} \\ \vdots & \vdots & \vdots & \vdots & \vdots \\ k_{N1} & \cdots & k_{Nm} & \cdots & k_{NN} \end{bmatrix} \begin{bmatrix} A_1 \\ \vdots \\ A_m \\ \vdots \\ A_N \end{bmatrix} = \begin{bmatrix} p_1 \\ \vdots \\ p_m \\ \vdots \\ P_N \end{bmatrix} \tag{2.64}$$

Assuming that the node m is on the Dirichlet boundary and its potential value is A0. Its means that the equation of m row in the simultaneous equations is . Hence, let and is set to . Where N is 1 to i. Diagonal element of mth row is replaced by 1 and other element in the mth column are filled by zero. Then the matrix equation (2.64) is changed to

$$\begin{bmatrix} k_{11} & \cdots & 0 & \cdots & k_{1N} \\ \vdots & \vdots & \vdots & \vdots & \vdots \\ 0 & \cdots & 1 & \cdots & 0 \\ \vdots & \vdots & \vdots & \vdots & \vdots \\ k_{N1} & \cdots & 0 & \cdots & k_{NN} \end{bmatrix} \begin{bmatrix} A_1 \\ \vdots \\ A_m \\ \vdots \\ A_N \end{bmatrix} = \begin{bmatrix} p_1 - k_{1m}A_0 \\ \vdots \\ A_0 \\ \vdots \\ P_N - k_{Nm}A_0 \end{bmatrix} \tag{2.65}$$

If there are several nodes on the Dirichlet boundary, the same procedure will be needed to carried out. Above description shows, the dimension of the column matrix is not reduced by introducing the known potential values of the boundary and the size of the matrix is unchanged. Consequently, the advantage of this method is that the construction of the system matrix is unchanged and the computer program is independent of the specific geometry.

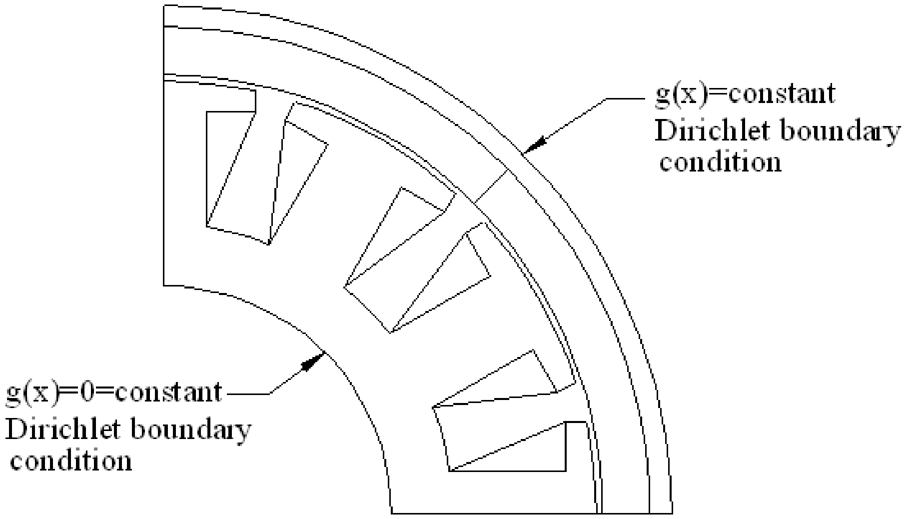

Figure 2.7: Dirichlet boundary condition for the BLDC motor

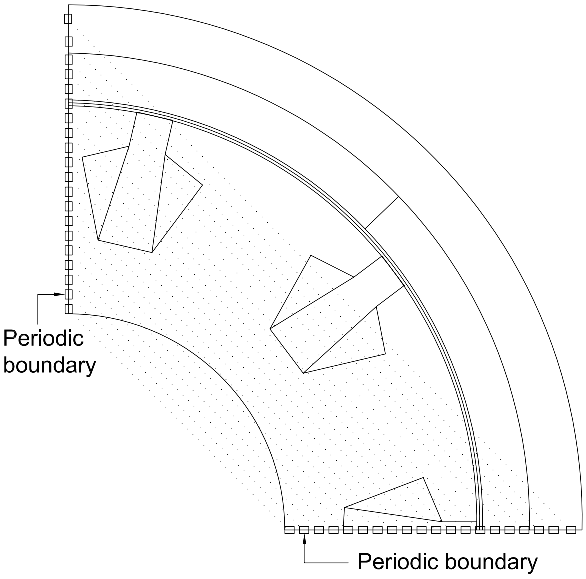

Figure 2.8: Periodic boundary condition applied to the BLDC motor

2.2.6 Numerical solution to nonlinear problems

After enforcing the appropriate boundary conditions and re-assembling the element matrix equations, the set of simultaneous system equations are to be solved. In this BLDC model, the ferromagnetic properties of iron and the demagnetization properties of permanent magnets as well as the voltage versus flux characteristic of the resulting network elements are non-linear. This result in a system of non-linear equations and this system cannot be solved in a closed form. A numerical iteration scheme has to be used to obtain a field solution. Newton Raphson method is widely used in solving the non-linear finite element equations. Newton Raphson algorithm is described in Appendix B. This method is based on derivatives of the function or quantity to be updated, and the procedure yields rapid convergence, with the error in a given step decreasing as the square of the error in the previous step. Therefore, it is one of the quadratic methods.

The application of Newton Raphson's to a nonlinear magnetic finite element problem is as follow. Let us consider two-dimensional nonlinear Poission equation for the magnetic vector potential. The stiffness matrix for a two-dimensional first order triangle is

$$\frac{\nu}{4\Delta}\begin{pmatrix} s_{ii} & s_{ij} & s_{ik} \\ s_{ji} & s_{jj} & s_{jk} \\ s_{ki} & s_{kj} & s_{kk} \end{pmatrix}\begin{pmatrix} A_i \\ A_j \\ A_k \end{pmatrix} = \frac{\Delta}{3}\begin{pmatrix} J_e \\ J_e \\ J_e \end{pmatrix} \tag{2.66}$$

This procedure consists of finding a change in the potential as a result of a change in the reluctivity, which again varies a function of the potential. Since the permeability of the iron and the permanent magnet may be non-linear and field dependent, one cannot obtain the solution to the field problem by solving the matrix equations for the discretized field region only in one iteration. Further, the solution to the problem is piecewise continuous, we cannot determine a priori the permeability in the different subregions or finite elements spanning the iron parts.

Let us assume

$$F_1 = \frac{\nu}{4\Delta} \left[\begin{array}{ccc} s_{ii} & s_{ij} & s_{jk} \end{array} \right] \begin{pmatrix} A_i \\ A_j \\ A_k \end{pmatrix} - \frac{J_e \Delta}{3} \tag{2.67}$$

$$F_2 = \frac{\nu}{4\Delta} \left[\begin{array}{ccc} s_{ji} & s_{jj} & s_{jk} \end{array} \right] \begin{pmatrix} A_i \\ A_j \\ A_k \end{pmatrix} - \frac{J_e \Delta}{3} \tag{2.68}$$

$$F_2 = \frac{\nu}{4\Delta} \left[\begin{array}{ccc} s_{ki} & s_{kj} & s_{kk} \end{array} \right] \begin{pmatrix} A_i \\ A_j \\ A_k \end{pmatrix} - \frac{J_e \Delta}{3} \tag{2.69}$$

For simplicity, we consider the equation (2.67) only to derive the Newton Raphson form because the formulation procedures are the same for the rest equations (2.68) and (2.69). The first step is to find out the derivatives necessary for the Newton Raphson method.

$$\frac{\partial F_1}{\partial A_i} = \frac{\nu}{4\Delta} s_{ii} + \frac{1}{4\Delta} \left[s_{ii} A_i + s_{ij} A_j + s_{ik} A_k \right] \frac{\partial \nu}{\partial A_i} \tag{2.70}$$

$$\frac{\partial F_1}{\partial A_j} = \frac{\nu}{4\Delta} s_{ij} + \frac{1}{4\Delta} \left[s_{ii} A_i + s_{ij} A_j + s_{ik} A_k \right] \frac{\partial \nu}{\partial A_i} \tag{2.71}$$

$$\frac{\partial F_1}{\partial A_k} = \frac{\nu}{4\Delta} s_{ik} + \frac{1}{4\Delta} \left[s_{ii} A_i + s_{ij} A_j + s_{ik} A_k \right] \frac{\partial \nu}{\partial A_i} \tag{2.72}$$

The Newton Raphson form is

$$\frac{\partial F_1}{\partial A_i} \Delta A_i + \frac{\partial F_1}{\partial A_j} \Delta A_j + \frac{\partial F_1}{\partial A_k} \Delta A_k = -F(A_i, A_j, A_k) \tag{2.73}$$

Substituting equations (2.70), (2.71) and (2.72) into the equation (2.73) we get

$$\begin{aligned} & \frac{\nu}{4\Delta} \left[s_{ii} \Delta A_i + s_{ij} \Delta A_j + s_{ik} \Delta A_k \right] + \\ & \frac{1}{4\Delta} \left[s_{ii} A_i + s_{ij} A_j + s_{ik} A_k \right] \left[\frac{\partial \nu}{\partial A_i} \Delta A_i + \frac{\partial \nu}{\partial A_j} \Delta A_j + \frac{\partial \nu}{\partial A_k} \Delta A_k \right] \\ & = -\frac{\nu}{4\Delta} \left[s_{ii} \Delta A_i + s_{ij} \Delta A_j + s_{ik} \Delta A_k \right] + \frac{J_e \Delta}{3} \end{aligned} \tag{2.74}$$

The rest of the equations (2.71) and (2.72) can derive the same procedures as mentioned above.

In the equation (2.74), the term $\frac{\partial \nu}{\partial A}$ can be represented by using the chain rule as

$$\frac{\partial \nu}{\partial A} = \frac{\partial \nu}{\partial B^2} \frac{\partial B^2}{\partial A} \tag{2.75}$$

Where the the term $\frac{\partial B^2}{\partial A}$ can be calculated as follows:

The flux density B can be calculated by using the magnetic vector potential values at the element nodes. For first order elements, we have

$$A = \frac{a_i + b_i x + c_i y}{2\Delta} A_i + \frac{a_j + b_j x + c_j y}{2\Delta} A_j + \frac{a_k + b_k x + c_k y}{2\Delta} A_k \tag{2.76}$$

$$B_x = \frac{\partial A}{\partial y} = \frac{A_i c_i + A_j c_j + A_k c_k}{2\Delta} \tag{2.77}$$

$$B_y = -\frac{\partial A}{\partial x} = -\frac{A_i b_i + A_j b_j + A_k b_k}{2\Delta} \tag{2.78}$$

$$B = \sqrt{B_x^2 + B_y^2} \tag{2.79}$$

$$B^2 = \left(\frac{\partial A}{\partial x}\right)^2 + \left(\frac{\partial A}{\partial y}\right)^2 = \frac{\left(A_i b_i + A_j b_j + A_k b_k\right)^2 + \left(A_i c_i + A_j c_j + A_k c_k\right)^2}{4\Delta^2} \tag{2.80}$$

$$\frac{\partial B^2}{\partial A} = \frac{2b_i \left(A_i b_i + A_j b_j + A_k b_k\right) + 2c_i \left(A_i c_i + A_j c_j + A_k c_k\right)}{4\Delta^2} \tag{2.81}$$

The value of $\frac{\partial \nu}{\partial B^2}$ can be calculated from the typical magnetization curve as shown in Fig. 2.9. For the realization of a numerical solution, the numerical values of the non-linear characteristics of the magnetization curve of the ferromagnetic magnetic material, specified as discrete sets of points, is stored in a file in a computer. Since Newton Raphson method requires a continuous representation of the variables, interpolation procedures are used to generate the required values. Numerous ways of modeling magnetic property curves have been tried out. Different methods of interpolation are available. In the simplest case, one can use a stepwise linear interpolation. The main disadvantage of this method is the discontinuity of the equations required for the evaluation of the Jacobian elements, which adversely affects the convergence of the Newton Raphson's method. In addition, the deviation of the approximated value from the real function is considerable. For greater accuracy, polynomials of higher order can be used. If the first priority is on the continuity of the first and higher derivatives of the equations, a rigid interpolation polynomial of a spline function is used. The main reason for the interest in splines is that they result in a simple formulation. They interpolate exactly at the given data points and have a continuous first and second order derivative. The continuous first derivative makes the method suitable for the Newton iteration. A great advantage of using cubic spline is the fact that this linear system of equations has to be solved only once to obtain the values of the second derivative. For the finite element method, this system of equation has to be solved only once independently of the number of finite elements used in the model of the magnetic circuit. For the practical used of the method a field of 20-25 data samples is sufficient to represent a non-linear ferromagnetic material characteristic. In this work, cubic spline interpolation is used to represent the B-H curve of the stator and rotor irons of the BLDC motor. The development of cubic spline algorithm is shown in Appendix C.

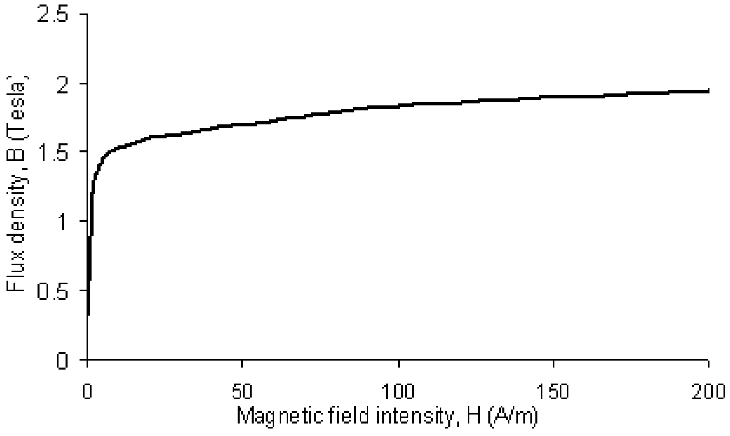

Figure 2.9: Magnetization curve for ferromagnetic material

2.2.7 Solution of the System of Equations

Generally, the methods for solving the linear algebraic equations can be classified into direct methods and iterative methods. Direct methods are supposed to give the exact solution from the theoretical point of view. And the computation time can also be estimated. However, due to the rounding errors produced by computation, the results are still approximate.

Iterative methods have the advantage that the sparseness of the coefficient matrix is utilized. If a problem can be solve by iterative method, the solutions are not affected by the rounding errors. However, the computation time is difficult to be estimated as it is dependent on the initial values used. The over-relaxation iteration and conjugate gradient method are two well known schemes using iterative methods. The matrices resulting from the finite element formulation are sparse and positive definite. Although the number of equations may be large, each equation will have relatively few terms. An efficient method for solving sparse matrix equations resulting from the discretization of boundary value problems is the preconditioned conjugate gradient method. This method combines useful aspects of iterative methods with the desirable characteristics of direct methods. In this work, Incomplete cholesky conjugate gradient method (ICCG) is used to solve the system of equations.

From the mathematical point of view, solution of the system matrix is not a difficult problem. However, in practical cases, as the number of un-knowns are normally in thousands or even in hundreds of thousands, the size of the stiffness matrix is huge. Therefore an effective storage method plays an important role in solving the global system of matrix equations. In the finite element computation, an effective storage scheme means,

- It can store all the information of the stiffness matrix.

- It can use small storage to store the matrix information.

As the stiffness matrix is symmetric, banded and non-zero terms are clustered around the main diagonal, utilizing this characteristics, non-zero storage methods are mostly used in finite element analysis. In this work, one type of the non-zero storage methods called index storage method is used. The index storage method is suitable for solving the linear system of equation by using ICCG algorithm. The structure of the proposed non-zero storage method is as follows.

Consider the m^{th} row of the following global matrix $[K]$.

$$K = \begin{bmatrix} k_{11} & k_{12} & k_{13} & k_{14} & 0 \\ k_{21} & k_{22} & 0 & k_{24} & 0 \\ k_{31} & 0 & k_{33} & k_{34} & k_{35} \\ k_{41} & k_{42} & k_{43} & k_{44} & k_{45} \\ 0 & 0 & k_{53} & k_{54} & k_{55} \end{bmatrix} \tag{2.82}$$

In this method, upper half of the matrix with non-zero terms is needed to store. Detailed procedures are as follows.

1. Arrange the non-zero element column by column in the matrix $[A]$.
2. The corresponding row numbers of each element are stored in the matrix $[IC]$.
3. Meanwhile, the position of each diagonal element in the matrix $[A]$ is stored in matrix $[ID]$.

For example, for the global matrix $[K]$ from the equation (2.82),

$$[A] = \begin{bmatrix} k_{11} & k_{12} & k_{13} & k_{14} & k_{22} & k_{24} & k_{33} & k_{34} & k_{35} & k_{44} & k_{45} & k_{55} \end{bmatrix} \tag{2.83}$$

$$IC = \begin{bmatrix} 1 & 1 & 1 & 1 & 2 & 2 & 3 & 3 & 3 & 4 & 4 & 5 \end{bmatrix} \tag{2.84}$$

$$ID = \begin{bmatrix} 1 & 5 & 7 & 10 & 12 \end{bmatrix} \tag{2.85}$$

In the ICCG iteration, retrieve the element position by using the these two matrices $[IC]$ and $[ID]$; and solve the linear equations according to the algorithm.

2.3 Conclusion

This chapter described two dimensional finite element analysis of the prototype BLDC motor. Mathematical models of the BLDC motor were developed using Maxwell's equations. Basic procedures and modelling techniques of two dimensional finite element method were presented. Proposed FEM model will be used as a pre-computation stage for developing the steady state model of the BLDC motor. In the steady state model, the solutions got from this FEM model are used as initial values for time stepping solver in order to reduce the extensive computation time to reach to the static conditions in time stepping FEM. Modelling of BLDC motors using time stepping finite element will be presented in the next chapter.

Chapter 3

Time Domain Modelling of a BLDC Motor by Coupled Systems

3.1 Introduction

Electrical machines are electromechanical converters and their behaviours can be described by the electromagnetic fields. In turn, electrical machines receive power form external sources through electric circuit. This requires the modelling of electromagnetic field inside the machine to be coupled with electric circuit. In addition, electrical machines are moveable devices. It is important to take into account the interaction of electromagnetic field with mechanical forces and motions. Therefore, a comprehensive modelling of field, circuit and motion of an electrical machine system should be considered together. Moreover, if the machine is in its transient state, transient fields are varied with time. So it is needed to develop the model in time domain.

A method for proper coupling of transient fields, circuits and motion must be such that [86]-[87]:

1. Only terminal voltage (or total terminal current) applied to the device is required as a known input quantity, and total terminal current (terminal voltage) is calculated as an unknown;
2. The transient external circuit equations that represent the electrical sources

and circuit components are coupled to the finite element field equations; and

3. Equations for motion are coupled to the finite element field equations.

The most rigorous way is to allow for time variation of magnetic non-linearity, harmonic effects, rotor rotation and coupling with the external circuit in the time stepping approach. The following sections describe a non-linear time stepping method to analyze the performance characteristics of BLDC motors. A system composed of a BLDC motor, a semiconductor inverter and the control equipment is considered. The proposed mathematical model includes the finite element equations of the electromagnetic field in time domain, the equations which define the connections of windings and inverter elements, the motion equation, and the relations which describes the control systems. A HDD spindle motor (exterior rotor type BLDC motor) is used as a typical example to describe the principles of the proposed method.

3.2 Modelling Techniques

In the time stepping FEM model, the electromagnetic fields represented by Maxwell's equations are coupled with the stator circuit equations and the rotor motion equations and solved simultaneously at each time step. The inputs are stator phase voltages, rotor position, motor geometries and material characteristics; other variables such as magnetic vector potentials for each node of the FEM mesh, stator currents, back-emf, motor torque and the speed are directly calculated. The magnetic field equations of the stator and the rotor are written in their own coordinate systems in time domain. The solution of the two field equations are matched with each other in the air gap. The rotor part of the FEM mesh is rotated at each time step by an angle determined from the motion equation. Hence, the solution of the time stepping model can take into account the complexity of the geometric model, non-linearity, induced eddy currents, the material saturation and the rotor rotation which are very difficult to be considered using analytical methods.

3.3 Mathematical Model of the BLDC Motor

An underslung type hard disk drive spindle motor is used in this model. This is the exterior rotor type permanent magnet BLDC motor. Underslung motors are generally designed for low capacity and low profile hard disk drives. These are mostly used in PC computers. Fig. 3.1 shows the mechanical structure of the underslung type disk drive spindle motor. The configuration of the motor and power electronic circuit to be modelled are shown in Fig. 3.2. Motor specifications are listed in Table A.1. Demagnetization curve of the permanent magnet used in this motor is given in Appendix D. In the proposed model, the terminal voltages on the stator windings of each phase are controlled by power electronic switches according to the control scheme. In this star connected motor, at any moment, there are two phase windings in conducting state and one phase winding in non-conducting state. Typical switching states and input voltage waveforms are shown in Fig. 3.3. Modelling of the BLDC motor in the time stepping FEM can be divided into three main parts:

1. Electromagnetic field modelling
2. Circuit modelling
3. Rotor rotation

Each part yields its own matrix equations. They are coupled and solved simultaneously at each time step.

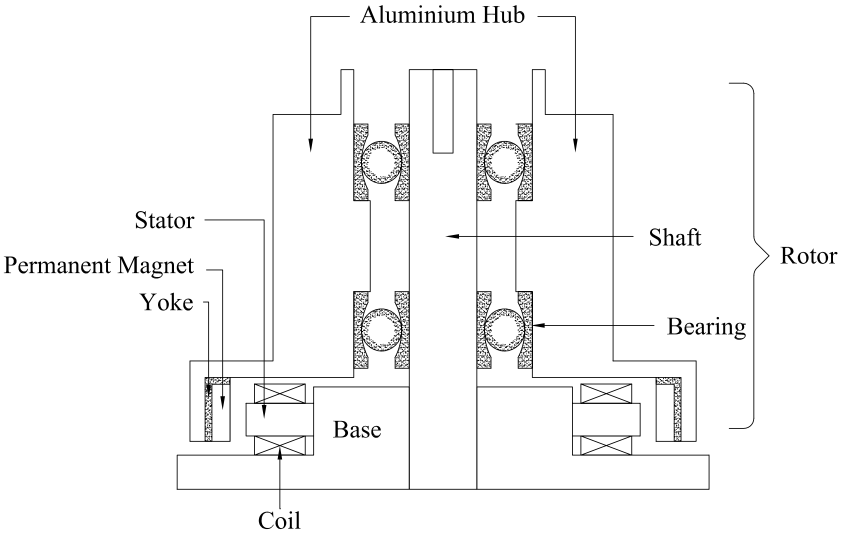

Figure 3.1: Mechanical structure of the motor

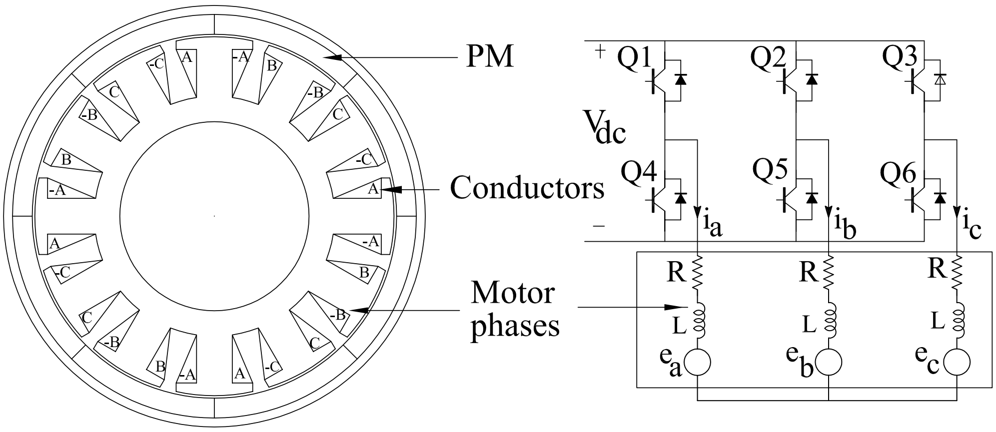

Figure 3.2: BLDC motor configuration and power electronic circuit

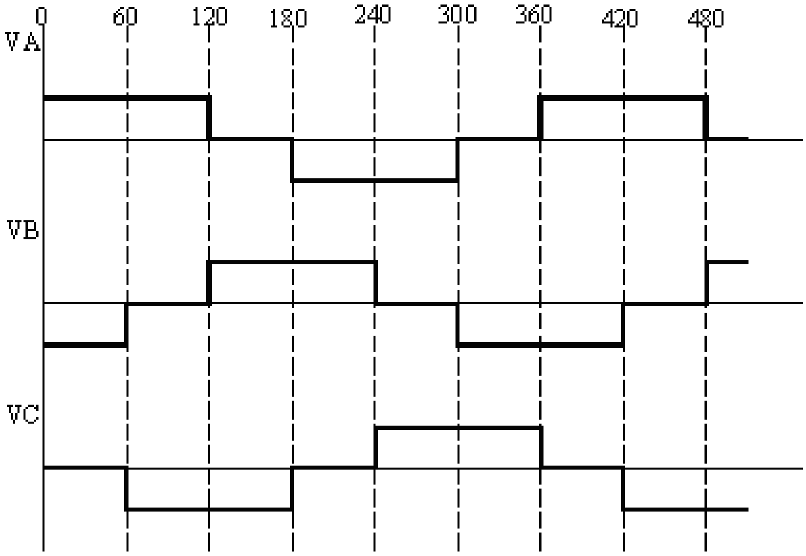

Figure 3.3: Typical input voltage waveforms with respective electrical degrees

3.3.1 Electromagnetic field modelling

Time-dependent electromagnetic field of the BLDC motor can be represented as

$$\nabla \times (\nu \nabla \times A) = J \tag{3.1}$$

where A is the magnetic vector potential, ν is the reluctivity of the material and J is the current density. J and A are assumed to be z direction and independent of z. According to formulation equation (**??**), in the area of the stator conductor, the electromagnetic field equation can be represented as

$$\nabla \times (\nu \nabla \times A) + \frac{i_s}{S} = 0 \tag{3.2}$$

where i_s is the stator phase current and S is the total cross-sectional area of the one turn on one coil side.

In the solid rotor iron core and the laminated stator, there have eddy current effect, the electromagnetic field can be expressed as

$$\nabla \times (\nu \nabla \times A) + \sigma \frac{\partial A}{\partial t} = 0 \tag{3.3}$$

There is no induced electric field produced by time varying magnetic flux in the air gap and the term $\sigma \frac{\partial A}{\partial t}$ is zero. Therefore, the electromagnetic field equation in these areas can be simply represented as

$$\nabla \times (\nu \nabla \times A) = 0 \tag{3.4}$$

There are two models which are commonly used to represent permanent magnets; a magnetization vector model and an equivalent current sheet model. Magnetizing vector method is used in this modelling. Detailed procedures and formulation of magnetization vector method has been given in section (2.2.1.1). According the proposed method, the permanent magnet can be represented as an equivalent magnet current source as

$$\nabla \times (\nu \nabla \times A) = \nabla \times (\nu B_r) \tag{3.5}$$

3.3.1.1 Modelling of eddy current effect on stator lamination

Most of the stator iron cores of BLDC motors are built up out of thin laminations to reduce the eddy current effects. There are many methods and approach to model eddy current effect on stator laminations [88]-[89]. One possible method is to model each discrete lamination and insulation between laminations in the finite element geometry. An alternative is to treat the laminated material as a continuum and derive bulk properties. Bulk lamination modelling is applied to model the stator lamination in this thesis because it is simple, reliable and easy to implement in FEM calculation. David Meeker, developer of Free FEM software named Finite Element Method Magnetic (FEMM) has implemented this bulk approach [13]. Detail modelling technique is as follow.

Consider that the flux can flow through the laminations in a combination of two ways: along the laminations and across the thickness of laminations as shown in Fig. 3.4. Assume the permeability of the iron is isotropic in deriving the bulk lamination model. For the condition where the flux flow along the laminations, the circuit model can be produced as shown in Fig. 3.4. There are two reluctances in the model: one for flux that flows through the iron part of the laminations R_{fe} and another reluctance for flux that flows through the air between laminations, R_{air}.

$$R_{fe} = \frac{L}{\mu_r \mu_o c W} \tag{3.6}$$

$$R_{air} = \frac{L}{\mu_o (1-c) W} \tag{3.7}$$

where L and W are the length and width of the path traversed and c is the fraction of the path filled with iron. Adding these two reluctances in parallel yields

$$R_{ez} = \frac{L}{((1-c)+c\mu_r)\mu_o} W \tag{3.8}$$

Since L and W are arbitrarily chosen, the bulk permeability of the section is

$$\mu_{ez} = ((1-c)+c\mu_r)\mu_o \tag{3.9}$$

For the condition where the flux flow across the thickness of the laminations, circuit model can be described as shown in Fig. Fig. 3.5. In this case, the circuit is two reluctances are in series, as the flux has to cross the insulation and the lamination. These reluctances are

$$R_h = \frac{cL}{\mu_r \mu_o W} \tag{3.10}$$

$$R_a = \frac{(1-c)L}{\mu_o W} \tag{3.11}$$

Adding these two reluctances together in series yields

$$R_{hard} = \left(\frac{c + (1-c)\mu_r}{\mu_r \mu_o} \right) \frac{L}{W} \tag{3.12}$$

Since L and W are arbitrarily chosen, the bulk permeability of the condition is

$$\mu_{hard} = \frac{\mu_r \mu_o}{c + (1-c)\,\mu_r} \tag{3.13}$$

In equation (3.2), the value of bulk permeabilities are substituted. Hence, the electromagnetic field equation (3.2) takes into account the eddy current effect in stator laminations.

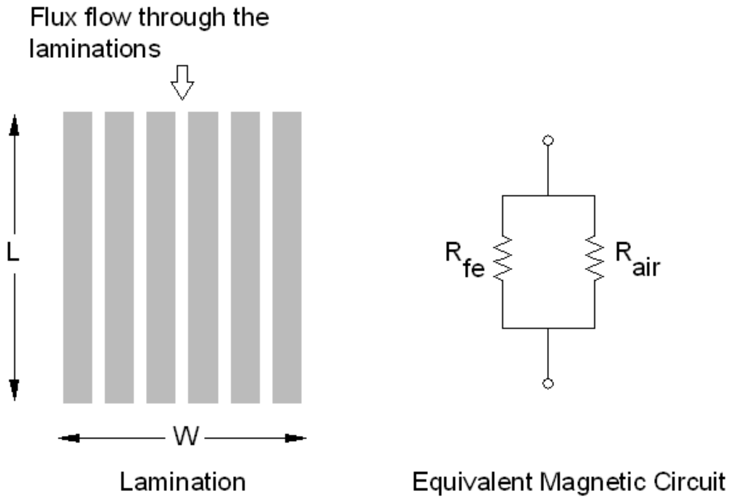

Figure 3.4: Equivalent circuit for flux flow through the laminations

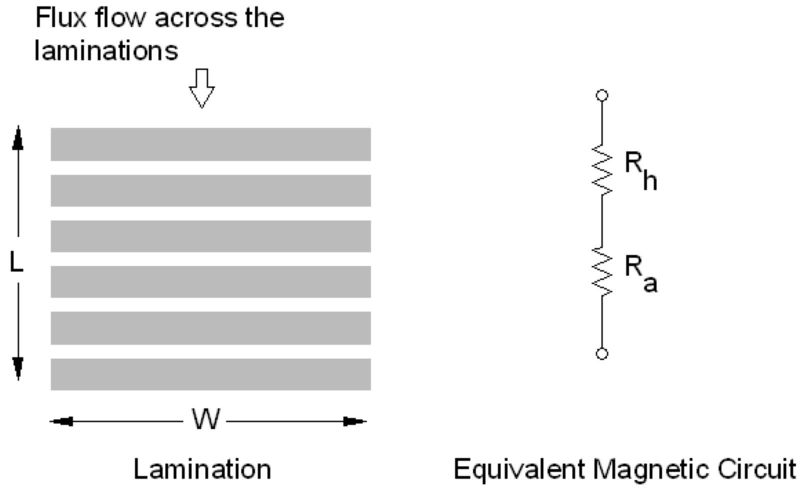

Figure 3.5: Equivalent circuit for flux flow across the thickness of laminations

3.3.2 Modelling of electric circuit

In BLDC motors, the stator windings are connected in delta or star. In both cases, the power electronic circuit and the switching sequence of the transistors remain the same. Since the settling time of the semiconductor devices are shorter than the time step length of the time stepping FEM, the switching devices can be simply represented by the nonlinear resistances corresponding to the forward conduction resistance in the ‘ON’ state and a high resistance to simulate the ‘OFF’ state [90]-[94]. In this model, one of the high speed switching MOSFET model-IRF620 is used as the switching devices. BLDC motor operates on square wave supply and two phases are in operation. Commutation (changing switching states between two phases) takes place every 60 electrical degrees. During this interval the third phase carries no current and is idle. For example, during interval when phase A and phase B are conducting at the same time as shown in Fig. 3.6, the conducting current flows from phase A to phase B and semiconductor switches S1 and S4 will be ’ON’.

The stator winding for one phase can be represented by total stator phase resistance, end winding inductance and induced back-emf voltage as shown in Fig. 3.7. It is assumed that the coil ends are treated as concentrated resistance and inductances elements in this two dimensional model. Hence, the stator phase circuit equation can be expressed in general form as

$$V = Ri_s + L_\sigma \frac{di}{dt} + e \tag{3.14}$$

where R is the sum of ’ON’ state semiconductor resistance and armature winding resistance, V is the stator phase voltage, L_σ are ending winding inductances and e is the induced voltage (back-emf). In this equation, stator phase voltage is input and the output stator current will be calculated by coupling the circuit equation (**??**) with the field equations in the time stepping model. Required parameters such as winding resistance, end winding inductance and back-emf can be determined as describe in next section.

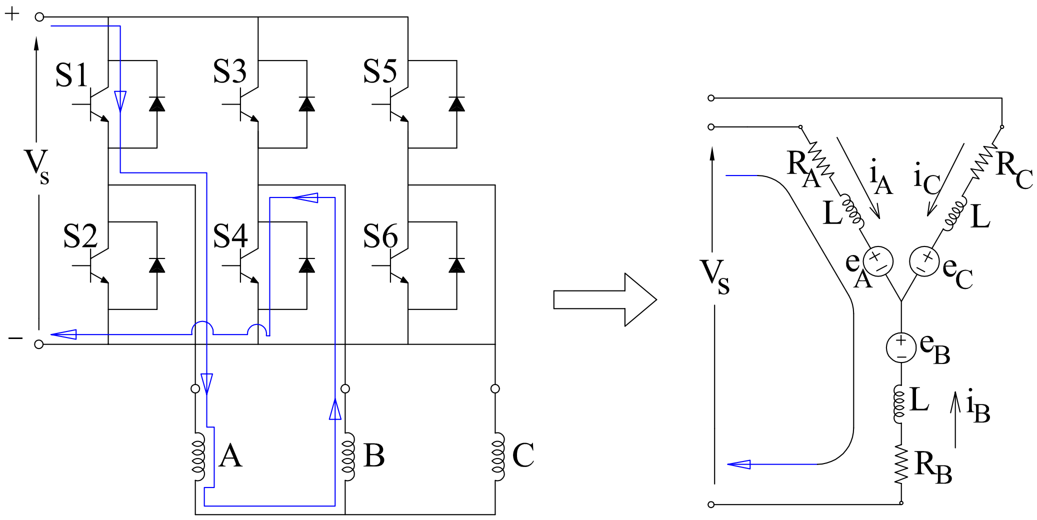

Figure 3.6: The inverter circuit where current flow from phase A to B

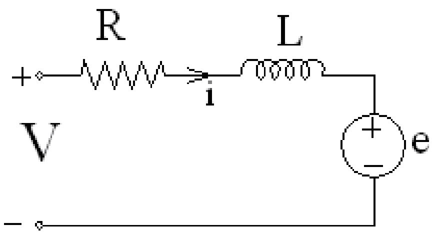

Figure 3.7: Circuit representation of a phase winding

3.3.2.1 Determination of DC winding resistance and Back-emf

The electromagnetic field in an electric machine is governed by Maxwell's equations:

$$\nabla \times E = -\frac{\partial B}{\partial t} \tag{3.15}$$

with the constitute relationship:

$$J = \sigma E \tag{3.16}$$

But

$$B = \nabla \times A \tag{3.17}$$

Substituting equation (3.15) to equation (3.17) yields

$$\nabla \times E = -\frac{\partial\left(\nabla \times A\right)}{\partial t} = -\nabla \times \frac{\partial A}{\partial t} \tag{3.18}$$

or

$$\nabla \times \left(E + \nabla \times \frac{\partial A}{\partial t}\right) = 0 \tag{3.19}$$

According to the Poincare' Theorem, the curl of a gradient is zero, hence we can write

$$E + \frac{\partial A}{\partial t} = -\nabla V \tag{3.20}$$

$$E = -\frac{\partial A}{\partial t} - \nabla V \tag{3.21}$$

where V is a scalar potential. Substituting equation (3.21) into equation (3.16), we get

$$J = \sigma E = \sigma\left(\frac{\partial A}{\partial t} + \nabla V\right) \tag{3.22}$$

In the equation (3.22), the first term of right hand side represents induced electric field intensity per unit length of stator conductor produced by electromagnetic induction (back-emf) and the second term is caused by the effect of charge build up at the conductor end.

If we consider a current carrying conductor of length l, its positive terminal is point a and a negative terminal is point b. If the difference in electric scalar potential between point a and b is V_{ab}, we can write

$$V_{ab} = V_a - V_b = \int_a^b E dl = -\int_a^b \nabla V dl \tag{3.23}$$

In two-dimensional problem ∇V is considered to be constant in z-direction, then equation (3.23) becomes

$$V_{ab} = -\nabla V \cdot l \tag{3.24}$$

$$\nabla V = -\frac{V_{ab}}{l} \tag{3.25}$$

Therefore, the current density for the current carrying conductor for two dimensional field is

$$J = -\sigma\frac{\partial A}{\partial t} + \sigma\frac{V_{ab}}{l} \tag{3.26}$$

Integrating the equation (3.26) over its corresponding cross-sectional area S, we get the total current flowing through the conductor, which is

$$\begin{aligned} I &= \iint\limits_S J dxdy J \\ &= -\sigma \iint\limits_S \frac{\partial A}{\partial t} dxdy + \sigma\frac{V_{ab}}{l}\iint\limits_S dxdy \\ &= -\sigma \iint\limits_S \frac{\partial A}{\partial t} dxdy + \sigma\frac{S}{l}V_{ab} \end{aligned} \tag{3.27}$$

Divided by $\sigma\frac{S}{1}V_ab$ on both sides of the equation (3.27), the terminal voltage v_{ab} across a Z-directed conductor with length l and cross-sectional area S is

$$V_{ab} = \frac{l}{\sigma S}I + \frac{l}{S}\iint\limits_S \frac{\partial A}{\partial t} dxdy \tag{3.28}$$

In the equation (3.28), the first term of the right hand side is the voltage drop across the stator conductor and the last term represents the induced voltage (back-emf) of the conductor. Therefore, DC winding resistance for the conductor can be calculated by

$$R = \frac{Nl}{\sigma S} = \frac{Nl}{4\sigma\pi d^2} \tag{3.29}$$

where N is number of winding per phase, d is the diameter of the wire.

Stator windings are made up by conductors connected in many turns. If we consider a 'go' and 'return' loop of current carrying conductors, back-emf for one phase can be represented as

$$e = \frac{Nl}{S}\left[\iint\limits_{S^+} \frac{\partial A}{\partial t} dxdy - \iint\limits_{S^-} \frac{\partial A}{\partial t} dxdy\right] \tag{3.30}$$

3.3.2.2 End winding inductance

End winding inductance is difficult to calculate accurately with simple formulas because the conformation of end winding is complex and difficult to characterize mathematically in simple terms. Determination of the end winding inductances are different from different winding structures, end winding layers, rotor type etc. Probably the easiest way to determine the end winding inductance for distributed winding type and concentrated winding type are by the following analytical methods. Validity of the analytical results has been verified by experiment and finite element analysis in [3] and [95]-[98].

Determination of end winding inductance for distributed winding:

The inductance is estimated by assuming that the end-windings from the two ends taken together form a circular coil whose diameter d is equal to the chord spanned by the coil, evaluated at the radius of the bottoms of the slots, r_s as shown in Fig. 3.8. But

$$r_s = \frac{D}{2} - d_s \tag{3.31}$$

And coil pitch is τ slot pitches, the coil span in radians is

$$\sigma = \frac{2\pi}{N_s}\tau \tag{3.32}$$

$$d = 2r_s \sin(\frac{\sigma}{2}) \tag{3.33}$$

Therefore, the end winding inductance of one coil L_σ is calculated from the formula

$$L_\sigma = \frac{\mu_0 d N_c^2}{2} \ln\left(\frac{4d}{d_{GMD}} - 2\right) \tag{3.34}$$

where N_s is number of complete coils, N_c is the number of turns per coil, d_{GMD} is the geometric mean distance between the conductors in the coil cross section. If the coil cross-section is assumed square with the area A, then d_{GMD} is taken to be $0.447\sqrt{A}$. The total contribution from the phase windings to the phase inductance can be obtained from the series/parallel combination of the end-winding inductances of the number of coils per phase, each one of which is given by the above equation (3.34). The geometric mean distance is modified to include all conductors of one coil which are assumed to be perfectly coupled in the end windings. With this changes, end winding inductance of the distributed winding structure is

$$L_\sigma = \frac{N_s}{a^2} . \frac{\mu_0 d N_c^2}{2} \ln \left(\frac{4d}{d_{GMD}} - 2 \right) \tag{3.35}$$

where a is the number of parallel paths.

Determination of end winding inductance for concentrated winding:

Most of the hard disk drive spindle motor has used concentrated type winding due to their short end turns and simple structure suitable for high-volume automated manufacturing. The basic idea to determine the end winding inductance for concentrated winding is the same as the distributed winding as mentioned above. However, there a little modification is needed to apply because of the different winding structures. To calculate the end winding inductance of one coil, it is assumed that the end windings are the circular arc as shown in Fig. 3.9. If the stator iron core between the end-coils is removed, the two end-coils from the same coil form a circular loop as shown in Fig. Here, the diameter D_c is approximately equal to the length of the arc segment of the middle of the two adjacent slots. We have

$$\alpha = \frac{2\pi}{N_s} \tag{3.36}$$

Hence

$$D_c = r \times \alpha \tag{3.37}$$

where N_s is the total number of slots. The end winding inductance for one coil is

$$L_e = \frac{\mu_0 D_c N_c^2}{2} \ln \left(\frac{4D_c}{d_{GMD}} - 2 \right) \tag{3.38}$$

where N_c is the number of turns per coil and $d_G MD$ is the geometric mean distance between the conductors in the coil cross-section. The total end winding inductance per phase is obtained by multiplying the number of coils per phase N_{coil} and dividing the a^2, where a is the number of parallel paths as below.

$$L_e = \frac{N_{coil}}{a^2} \cdot \frac{\mu_0 D_c N_c^2}{2} \ln\left(\frac{4D_c}{d_{GMD}} - 2\right) \tag{3.39}$$

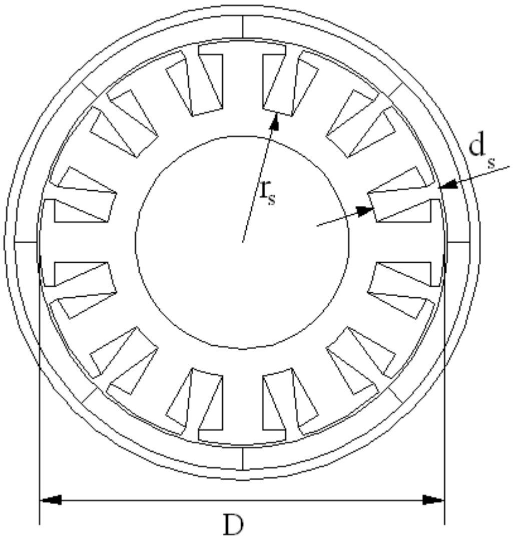

Figure 3.8: Motor geometry for distributed winding inductance calculation

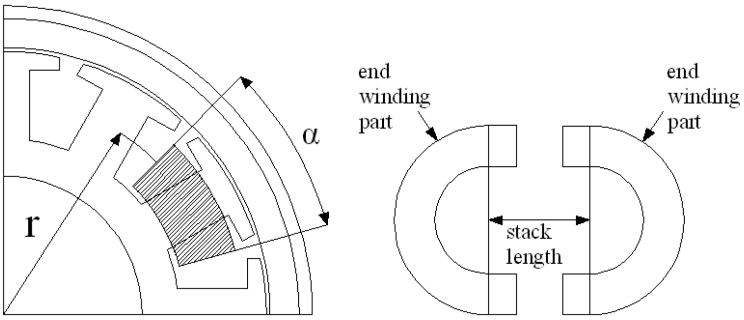

Figure 3.9: Motor geometry for concentrated winding inductance calculation

3.3.3 Modelling of the rotor movement equation

Rotor motion governed by the mechanical equation is given by

$$J_m \frac{d\omega}{dt} = T_e - T_L + D\omega \tag{3.40}$$

where J_m is the total moment of inertia this includes the inertia of the transmission system, the load referred to the motor shaft and the inertia of the rotor; ω is the rotor speed; T_e is the electromagnetic torque, D is the damping coefficient and T_L is the torque required to drive the load referred to the motor shaft including the external load torque, windage torque and friction loads (load caused by the bearings, the system inefficiencies and stiction force caused by the read/write head with the platters in working model BLDC motor). Load torque T_L, damping coefficient D and moment of inertia J_m are necessary to determine prior before the coupling the motion equation with field and circuit equations.

3.3.3.1 Consideration of load torque

It includes friction torque, stiction torque and external load torque. It is known that friction torque occurs from the relative motion between surfaces and it is mainly due to in bearings, lead screws, gear-boxes, slideways, etc. In the prototype motor, stiction force between read/write head and the platters at starting condition is needed to be taken into account. In general, the force required to overcome the surface friction, F_f, for a normally applied load, W, is given by [99]

$$F_f = \gamma W \tag{3.41}$$

where γ is the coefficient of friction; typical values of friction coefficients are given in Table 3.1. The value of coefficient of friction depends on both surfaces. The motor used ball bearings, and therefore friction caused by ball bearings effect is necessary to be considered. The manufacturer can supply a complete data set, but as an indication, the friction torque, T_b for a bearing can be determined using the generally accepted relationship

$$T_b = 0.5 B_L d \mu_b \tag{3.42}$$

where d is the shaft diameter, μ_b is the coefficient of friction for the bearings (Table 3.1) and B_L is the bearing load computed from the radial load, F_r and the axial load, F_a in the bearings; B_L is given by

$$B_{L=}\left(F_r^2+F_a^2\right)^{1/2} \tag{3.43}$$

Table 3.1: Friction coefficients

Material	Friction coefficient	Mechanism	Friction coefficient
Steel on steel	0.58	*Ball bushing*	< 0.001
Steel on steel (greased)	0.15	*Linear bearing*	< 0.004
Aluminium on steel	0.45	*Dove tail slides*	0.2
Copper on steel	0.30	*Gibb ways*	0.5
Brass on steel	0.35	–	–
Plastic on steel	0.15 – 0.25	–	–

3.3.3.2 Determination of rotor inertia

The following method for calculating rotor inertia is based on the assumption that all parts of the rotor rotate around the center of the shaft. For the proposed motor, we shall calculate the inertia of each part separately as shown in Fig. 3.10, then add the parts together for the total rotor inertia. The inertia of the shaft is given by

$$J_{shaft}=2\pi\rho L_{shaft}\left(\frac{D_{shaft}}{2}\right)^4 \tag{3.44}$$

The inertia of the solid rotor iron core is given by

$$J_{iron\_core}=2\pi\rho L_c\left[\left(\frac{D_{ro}}{2}\right)^4-\left(\frac{D_{rm}}{2}\right)^4\right] \tag{3.45}$$

The inertia of the permanent magnet is given by

$$J_{pm}=2\pi\rho L_c\left[\left(\frac{D_{rm}}{2}\right)^4-\left(\frac{D_{ri}}{2}\right)^4\right] \tag{3.46}$$

There are two parts in the aluminium hub; one part has a bigger diameter as shown in Fig. 3.10. Therefore these two parts are considered separately in the calculation of inertia. The inertia of the first part (larger diameter) which is fixed with the permanent magnet and the solid rotor iron core is given by

$$J_{pm} = 2\pi\rho L_c \left[\left(\frac{D_{rm}}{2} \right)^4 - \left(\frac{D_{ri}}{2} \right)^4 \right] \tag{3.47}$$

The inertia of the other part which is the outermost part of the rotor is given by

$$J_{Al\_out} = 2\pi\rho L_{Al\_out} \left[\left(\frac{D_{ro}}{2} \right)^4 - \left(\frac{D_{Al}}{2} \right)^4 \right] \tag{3.48}$$

For the above equations ρ is the density of the material used respectively. Density of the aluminium is 2700kg/m3 and the steel is 7750 kg/m3 (Table 3.2). Densities of the common permanent magnets are also shown in Table 3.3 for reference. In this model, NdFEB magnet is used.

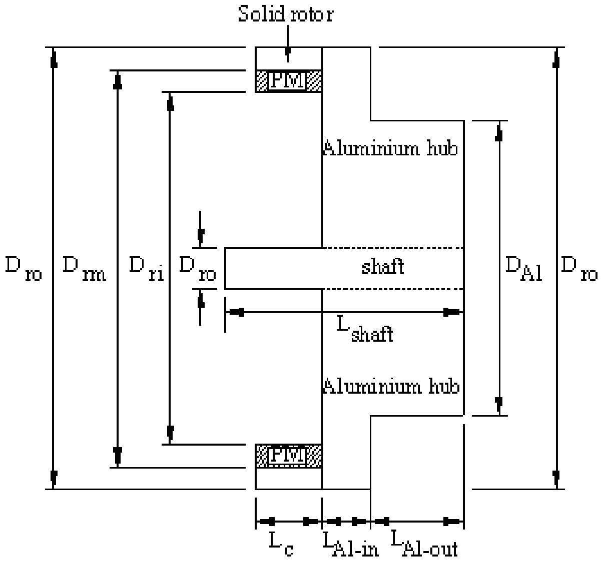

Figure 3.10: Rotor part of the BLDC motor

Table 3.2: Material densities

Material	Lb/in3	g/cm3
Aluminium	0.098	2.7
Brass	0.3	8.3
Bronze	0.295	8.17
Copper	0.322	8.91
Plastic	0.04	1.11
Steel	0.28	7.75
Hardwood	0.029	0.8

Table 3.3: Densities of permanent magnet

Material	Lb/in3	g/cm3
Bonded ferrite	0.134	3.71
Sintered ferrite	0.177	4.9
Alnico	0.264	7.31
Samarium cobalt	0.302	8.35
NdFeB	0.271	7.5

3.4 Mesh Generation and Rotation

Mesh generation for the time stepping FEM should be simple, robust and rotor meshes should be allowed to rotate easily. In this work, simple and reliable moving mesh technique developed by W. N. Fu at el [100] is used for meshing and rotation of the problem domain. The moving mesh technique adopted in this work is described below.

The FEM mesh of the cross-section of the BLDC motor is divided into two parts; the stator and the rotor, with each including a part of the air gap. The air gap is divided into three layers: two upper layers belong to the rotor and the rest layer belongs to the stator. Meshes of the two parts are then generated separately.

Detailed procedure of basic mesh generation composes of the following steps:

1. Generation of the boundary mesh by using the algorithm of reduction of nodes [100].
2. Identification to insert the internal points according to the relative area of elements by using element quality factors.
3. Improvement on the mesh connection and quality by Delaunay method [101]-[102].

In dividing the mesh, triangular elements are used. The algorithm of reduction of point is to reduce the points one by one from every edge. The main idea is the identification of the point which is to be eliminated. To find a suitable point in line L, a new element is created. From the edge L, try to find out the points so that the newly created element has the best quality factor. The quality factor of the triangular elements can be determined by the following formula [103].

$$Q_2 = \frac{4\sqrt{3}\Delta}{(a^2 + b^2 + c^2)} \tag{3.49}$$

where a, b and c are the lengths of the sides of the triangle; and δ is the area of the triangle. The quality factor of a triangle is always greater zero. An equilateral triangle has the best quality factor of 1.

After identification of the points to be reduced, it is needed to justify the new created element that it is reasonable. The following procedures are carried out for justification:

- Check whether the new element is inside the problem domain
- Justify whether any line already exists across the new element
- Make sure it is the new element
- Whether the new element includes any point.

If it satisfies the above conditions, the point can be reduced and a new element is created. If there is no point that satisfies the above procedures, one has to start again from the next edge. Detailed program formulation can be found in reference [100].

For quality improvement, it is needed to create internal points based on the geometrical considerations. It is also necessary to justify where to insert points and how to insert points. In this technique, two approaches have been used.

1. Calculate the element index n as shown below and if the index n is larger than the average value of all the elements, a point is inserted.

$$Index, n = \frac{\Delta_k}{\frac{1}{N}\sum\limits_{i=1}^{N}\Delta_i} \tag{3.50}$$

2. Check the quality factor of each elements and if the quality factor of element is small compared to the average value of the qualification factor of all the element, a point is inserted.

The final step of automatic mesh generation is done by Delaunay method. Further detailed of this method is in references [104]. Delaunay triangulation provides a mesh that is optimal for a given set of points. However, it cannot avoid thin triangles because all points have been fixed. Therefore, a step for mesh smoothing has to be carried out. This is accomplished by replacing each internal node at a new position given by [104]:

$$x^n = (1-\omega)x^0 + \frac{\omega}{N}\sum_{i=1}^{N} x_i \tag{3.51}$$

$$y^n = (1-\omega)y^0 + \frac{\omega}{N}\sum_{i=1}^{N} y_i \tag{3.52}$$

where (x^0, y^0) and (x^n, y^n) is the old and new positions of a given node respectively and (x_i, y_i) are the neighboring node locations. The relaxation factor ω is in the interval of [0, 2] and N is the number of neighboring nodes. This process is activated for several steps until the all of the element quality stop increasing.

Fig. 3.11 and Fig. 3.12 shows separately generated the basic stator mesh and rotor mesh including air gap parts. As shown in Fig. 3.13, the air gap is divided into three layers and the upper two layers belong to the rotor part and the rest layer belongs to the stator part. The inner-most nodes of the rotor mesh and the outer most nodes for the stator mesh are connected by the periodic boundary condition as shown in Fig. 3.14. When the rotor is rotated according to the time step, the shape of the mesh for both the stator and rotor can be kept constant and only the coordinates of the rotor mesh and the periodic boundary condition on the interface are needed to be changed. Therefore, in this moving mesh technique, the stator mesh and the rotor mesh are needed to generate only one time. FEM mesh after rotor is rotated 1000 steps is shown in Fig. 3.15.

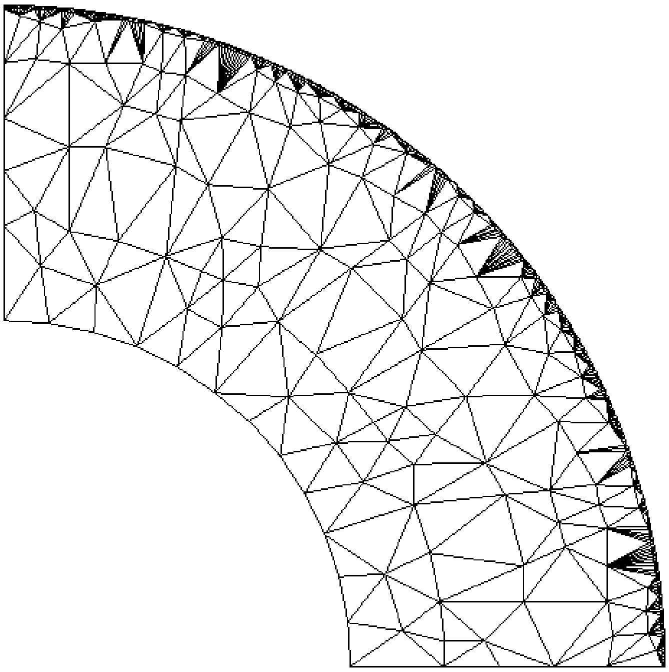

Figure 3.11: Basic stator mesh in including air gap parts

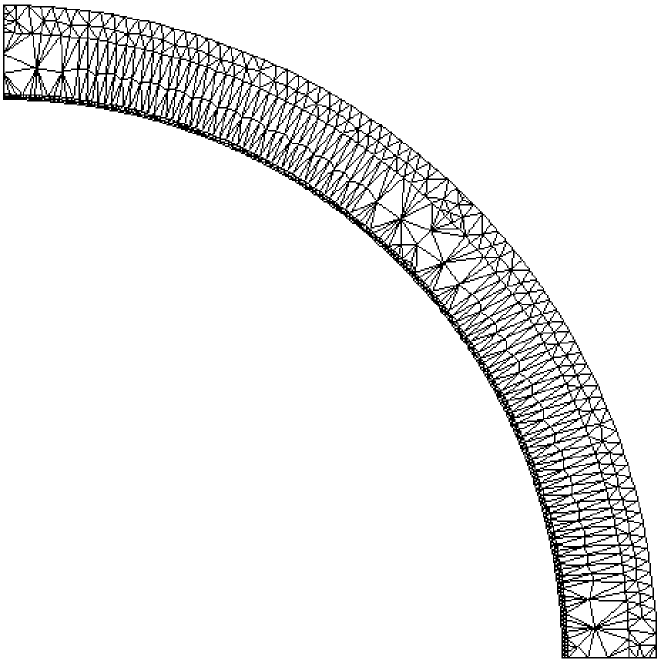

Figure 3.12: Basic rotor mesh including air gap part

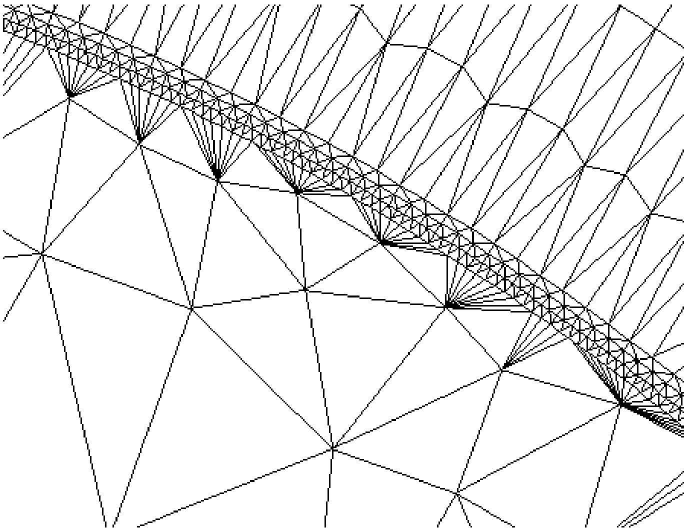

Figure 3.13: FEM mesh at air gap

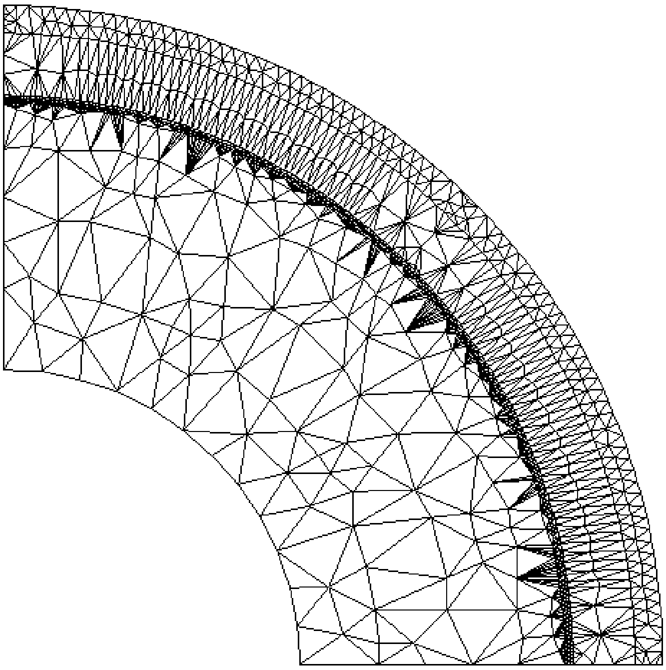

Figure 3.14: FEM mesh before rotor rotation (1899 nodes, 2828 elements)

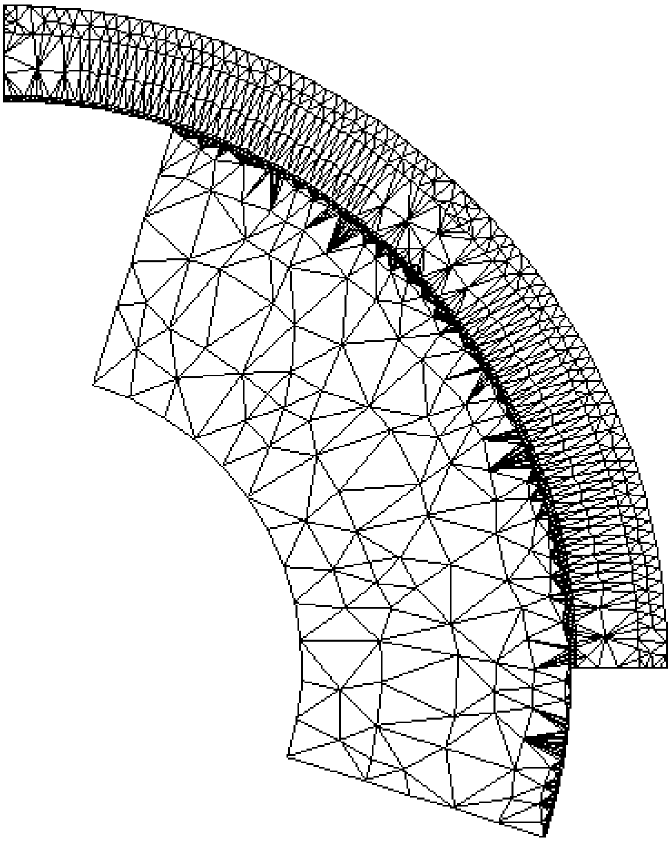

Figure 3.15: FEM mesh after rotation 1000 steps

3.5 Finite Element Formulation in Time Domain

In this proposed model, the Galerkin's method is employed for the finite element formulation. This is the particular weighted residual method for which the weighting functions are the same as the shape functions. According to the Galerkin's method the magnetic vector potential A at each node of the triangular element can be represented as

$$\hat{A} = \sum_{i=1}^{3} N_i A_i \tag{3.53}$$

and the element shape functions, N_i are equal to the weight functions, W_i .

$$W_i = N_i \tag{3.54}$$

where $i = 1, 2, 3$.

Galerkin's formulations for the permanent magnet has been described in section (2.2.3.1). Galerkin's formulations of the magnetic field in iron core and stator conductor region; circuit equations and the motion equation for the proposed modelling of the BLDC motor in time domain are discussed in the following sections.

3.5.1 Galerkin's formulation of the electromagnetic field equation in iron core

The eddy current effect in the iron core of the solid rotor and the laminated stator of the motor cannot be ignored. The field equation (3.3) of the iron core is

$$\frac{\partial}{\partial x}\left(\nu\frac{\partial A}{\partial x}\right) + \frac{\partial}{\partial y}\left(\nu\frac{\partial A}{\partial y}\right) + \sigma\frac{\partial A}{\partial t} = 0 \tag{3.55}$$

According to Galerkin's method, the field equation is multiplied by the weighting function W, choose the approximation solution $\hat{A}$ and set the integral to zero. The equation (3.55) becomes,

$$\iint W\left(\frac{\partial}{\partial x}\left(\nu\frac{\partial \hat{A}}{\partial x}\right) + \frac{\partial}{\partial y}\left(\nu\frac{\partial \hat{A}}{\partial y}\right) dxdy\right) + \iint W\sigma\frac{\partial A}{\partial t} = 0 \tag{3.56}$$

Integrating the left side of the above equation by parts,

$$\iint \nu \left(\frac{\partial W}{\partial x}\frac{\partial \hat{A}}{\partial x} + \frac{\partial W}{\partial y}\frac{\partial \hat{A}}{\partial y} \right) dxdy - \oint \nu W \frac{\partial \hat{A}}{\partial n} dc + \iint W\sigma \frac{\partial A}{\partial t} dxdy = 0 \quad (3.57)$$

These surface integrals may be broken into summations over small areas. The whole domain is replaced with small sub-domains so called finite elements, and integration can easily be performed over the individual elements.

$$\sum_{i=1}^{N} \left\{ \nu^e \iint \frac{\partial W^e}{\partial x}\frac{\partial \hat{A}^e}{\partial x} + \frac{\partial W^e}{\partial y}\frac{\partial \hat{A}^e}{\partial y} dxdy - \nu_e \frac{\partial A^e}{\partial \hat{n}} \int\limits_C W_i^e dC + \sigma \iint W \frac{\partial \hat{A}^e}{\partial t} dxdy \right\} = 0 \quad (3.58)$$

where N is the total number of elements in the domain. The line integral in equation is only employed over elements which have a side common with the boundary C. By imposing the natural boundary condition ,i.e $\frac{\partial A}{\partial \hat{n}} = 0$ this line integral is vanished. Therefore, the equation (3.58) becomes

$$\iint \frac{\partial W^e}{\partial x}\frac{\partial \hat{A}^e}{\partial x} + \frac{\partial W^e}{\partial y}\frac{\partial \hat{A}^e}{\partial y} dxdy + \sigma \iint W \frac{\partial \hat{A}^e}{\partial t} dxdy = 0 \quad (3.59)$$

According to the equation (3.54) , where weighting function W is equal to element shape function N, the equation (3.59) becomes

$$\iint \frac{\partial N^e}{\partial x}\frac{\partial \hat{A}^e}{\partial x} + \frac{\partial N^e}{\partial y}\frac{\partial \hat{A}^e}{\partial y} dxdy + \sigma \iint N \frac{\partial \hat{A}^e}{\partial t} dxdy = 0 \quad (3.60)$$

In matrix form,

$$\sum_e \left[\nu \left[S(t) \right]^e \left\{ \hat{A}(t) \right\}^e + \sigma \left[T \right]^e \left\{ \frac{\partial \hat{A}(t)}{\partial t} \right\}^e \right] = 0 \quad (3.61)$$

where $T_{e,ij} = \iint N_i N_j dxdy = \left\{ \begin{matrix} \frac{\Delta_e}{6} & i = j \\ \frac{\Delta_e}{12} & i \neq j \end{matrix} \right\}$

$S_e = \iint \left(\frac{\partial N_i}{\partial x}\frac{\partial N_j}{\partial x} + \frac{\partial N_i}{\partial y}\frac{\partial N_j}{\partial y} \right) dxdy = \frac{b_i b_j + c_i c_j}{4\Delta_e}$

and Δ_e is the triangular area of the element.

3.5.2 Galerkin's formulation of field equation in the stator conductor area

According to the electromagnetic magnetic field equation of the stator conductor, equation (3.2), the magnetic diffusion equation of the stator conductor area can be represented as

$$\frac{\partial}{\partial x}\left(\nu\frac{\partial A}{\partial x}\right)+\frac{\partial}{\partial y}\left(\nu\frac{\partial A}{\partial y}\right)+\frac{i_s}{s}=0 \tag{3.62}$$

Multiplying by the weighting function, W, and choosing the approximation solution, and setting the integral to zero, we get

$$\iint W\left[\frac{\partial}{\partial x}\left(\nu\frac{\partial A}{\partial x}\right)+\frac{\partial}{\partial y}\left(\nu\frac{\partial A}{\partial y}\right)dxdy\right]+\iint W\frac{i_s}{s}dxdy=0 \tag{3.63}$$

Integrate the first term of the equation (3.63) by parts and neglect the line integral as mentioned in above section, we get

$$\iint \nu\left[\frac{\partial W}{\partial x}\frac{\partial \hat{A}}{\partial x}+\frac{\partial W}{\partial y}\frac{\partial \hat{A}}{\partial y}\right]dxdy+\iint W\frac{i_s}{s}dxdy=0 \tag{3.64}$$

Now break the surface integrals into summations over small areas. First order triangular elements are used to discretize the desired motor geometry. The integral over the entire domain is represented with the summation of the integral over the individual triangles. we can get

$$\sum_{i=1}^{N}\iint \nu^e\left[\frac{\partial W^e}{\partial x}\frac{\partial \hat{A}^e}{\partial x}+\frac{\partial W^e}{\partial y}\frac{\partial \hat{A}^e}{\partial y}\right]dxdy+\iint W^e\frac{i_s}{s}dxdy=0 \tag{3.65}$$

where N is the number of triangular elements. Substituting the equations (3.53) and (3.54) into equation (3.65), the Galerkin's form of the electromagnetic field equation in the stator conductor area is

$$\sum\nolimits_e\iint\left[\nu\left\{\frac{\partial N_i}{\partial x}\frac{\partial\left(\sum\limits_{j=1}^{3}N_jA_j\right)}{\partial x}+\frac{\partial N_i}{\partial y}\frac{\partial\left(\sum\limits_{j=1}^{3}N_jA_j\right)}{\partial y}\right\}\right]dxdy+\iint N_i\frac{i_s}{s}=0 \tag{3.66}$$

Alternatively, in matrix form,

$$\sum_e \left[\nu \left[S_e \right] \{A(t)\}_e + \{Q_e\} \frac{i_s}{s} \right] = 0 \tag{3.67}$$

where $Q_e = \iint N_i dxdy = \frac{\Delta e}{3}$ and
$S_e = \iint \left(\frac{\partial N_i}{\partial x} \frac{\partial N_j}{\partial x} + \frac{\partial N_i}{\partial y} \frac{\partial N_j}{\partial y} \right) dxdy = \frac{b_i b_j + c_i c_j}{4\Delta_e}$.

3.5.3 The stator circuit equation in Galerkin's form

Before combining the stator circuit equation into the global matrix equation, it is necessary to formulate the circuit equation into Galerkin's form. The stator circuit equation as shown in equation (**??**) is

$$V = \frac{l}{s} \left[\iint\limits_{\Omega+} \frac{\partial A}{\partial t} d\Omega - \iint\limits_{\Omega-} \frac{\partial A}{\partial t} d\Omega \right] + Ri + L_\sigma \frac{di}{dt} \tag{3.68}$$

But in Galerkin's form

$$\frac{\partial A}{\partial t} = \sum_{i=1}^{3} N_i \frac{\partial A_i}{\partial t} \tag{3.69}$$

Therefore, the stator circuit equation in Galerkin's form is as shown below:

$$V = \frac{l}{s} \left[\left(\{Q\}^T \left\{ \frac{\partial A}{\partial t} \right\} \right)_{\Omega+} - \left(\{Q\}^T \left\{ \frac{\partial A}{\partial t} \right\} \right)_{\Omega-} \right] + Ri_s + L_\sigma \frac{di_s}{dt} \tag{3.70}$$

3.6 Time Discretization

The field equation in iron cores (3.61), the circuit equation (3.70) and the motion equation (3.31) are time dependent. These equations are needed to discretize in the time domain. The method of time-discretization used is based on the following equation:

$$\beta \left\{ \frac{\partial A}{\partial t} \right\}^{t+\Delta t} + (1-\beta) \left\{ \frac{\partial A}{\partial t} \right\}^{t} = \frac{\{A\}^{t+\Delta t} - \{A\}^{t}}{\Delta t} \tag{3.71}$$

Basically, there are three different types of time discretization.

1. Forward difference type, where the constant value of $(\beta = 0)$

2. Backward difference type, where ($\beta = 1$) and
3. Crank-Nicholson Method, where ($\beta = 1/2$).

In this proposed method, backward difference type is used to discretize the time domain because it has a good convergence rate. Therefore, equation (3.71) becomes

$$\left\{\frac{\partial A}{\partial t}\right\}^{t+\Delta t} = \frac{\{A\}^{t+\Delta t} - \{A\}^{t}}{\Delta t} \tag{3.72}$$

3.6.1 Time discretization of the FEM equation in iron core

The Galerkin formulation of the equation of the iron core

$$\nu[s]\,\{A(t)\} + \sigma\,[T]\left\{\frac{\partial A}{\partial t}\right\} = 0 \tag{3.73}$$

Substituting back ward difference time discretization equation (3.72), into equation (3.73),

$$\nu\,[s]\,\{A\}^{t+\Delta t} + \sigma\,[T]\left[\frac{\{A\}^{t+\Delta t} - \{A\}^{t}}{\Delta t}\right] = 0 \tag{3.74}$$

Rearranging the equation (3.74) yields the following equation in time discretizing model,

$$\frac{\sigma\,[T]\,\{A\}^{t+\Delta t}}{\Delta t} + \nu\,[s]\,\{A\}^{t+\Delta t} = \frac{\sigma\,[T]\,\{A\}^{t}}{\Delta t} \tag{3.75}$$

3.6.2 Time discretization of the FEM equation in stator conductor area

Galerkin's form of the field equation in stator conductor area is

$$\nu\,[S]\,\{A(t)\} + \{Q\}\,\frac{i_s}{s} = 0 \tag{3.76}$$

applying the time discretization equation (3.72),

$$\nu[S][\Delta A]^{t+\Delta t} + \frac{[Q]}{S}\,[\Delta i_s]^{t+\Delta t} = 0 \tag{3.77}$$

3.6.3 Time discretization of the stator circuit equation

In order to discretize the stator circuit equation in time domain, recall the stator circuit in Galerkins form equation (3.70) as follow,

$$V = \frac{l}{s}\left[\left(\{Q\}^T\left\{\frac{\partial A}{\partial t}\right\}\right)_{\Omega^+} - \left(\{Q\}^T\left\{\frac{\partial A}{\partial t}\right\}\right)_{\Omega^-}\right] + Ri_s + L_\sigma\frac{di_s}{dt} \tag{3.78}$$

Rearranging the equation (3.78)

$$\frac{l}{s}\{Q\}\left\{\frac{\partial A}{\partial t}\right\}_{\Omega^+} - \frac{l}{s}\{Q\}\left\{\frac{\partial A}{\partial t}\right\}_{\Omega^-} + L_\sigma\frac{di_s}{dt} = V - R_\sigma i_s \tag{3.79}$$

applying the time discretization equation (3.72),

$$\left\{\frac{di_s}{dt}\right\}^{t+\Delta t} = \frac{\{i_s\}^{t+\Delta t} - \{i_s\}^t}{\Delta t} \tag{3.80}$$

$$\left\{\frac{dA}{dt}\right\}^{t+\Delta t} = \frac{\{A\}^{t+\Delta t} - \{A\}^t}{\Delta t} \tag{3.81}$$

Substituting equations (3.80) and (3.81)into equation (3.79), we obtain the stator circuit equation in time discretization model as

$$\begin{aligned}&\frac{l}{s}\{Q\}\left(\frac{\{A\}^{t+\Delta t} - \{A\}^t}{\Delta t}\right)_{\Omega^+} - \frac{l}{s}\{Q\}\left(\frac{\{A\}^{t+\Delta t} - \{A\}^t}{\Delta t}\right)_{\Omega^-}\\ &+L_\sigma\frac{\{i_s\}^{t+\Delta t} - \{i_s\}^t}{\Delta t} = V_s - R_t i_s^{t+\Delta t}\end{aligned} \tag{3.82}$$

3.6.4 Time discretization of the motion equation

The motion equation (3.31) is discretized according to equation (3.72):

$$\left\{\frac{\partial\omega}{\partial t}\right\}^{t+\Delta t} = \frac{\omega^{t+\Delta t} - \omega^t}{\Delta t} \tag{3.83}$$

$$J\frac{d\omega^{t+\Delta t}}{dt} = T_e - T_f - D\omega \tag{3.84}$$

$$J\frac{\omega^{t+\Delta t} - \omega^t}{\Delta t} = T_e - T_f - D\omega \tag{3.85}$$

3.7 Linearization

In this model, field equations are nonlinear; linearization of these equations are required before they can be combined with other equations of the system in a global matrix equation. In this work, Newton-Raphson procedure is applied to linearize the nonlinear system equations. Cubic spline interpolation algorithm is used to represent the magnetization curves of the ferromagnetic materials.

Newton-Raphson form of the stator conductor field equation after time discretization is given by,

$$\nu[S][\Delta A]_{k+1}^{t+\Delta t} + \frac{[Q]}{S}\,[\Delta i_s]_{k+1}^{t+\Delta t} = -\nu[S][A]_{k}^{t+\Delta t} - \frac{[Q]}{S}\,[\Delta i_s]_{k}^{t+\Delta t} \tag{3.86}$$

in air gap,

$$\nu[S][\Delta A]_{k+1}^{t+\Delta t} = -\nu[S][A]_{k}^{t+\Delta t} \tag{3.87}$$

in laminated stator iron core and solid rotor iron core,

$$\nu[S][\Delta A]_{k+1}^{t+\Delta t} + \frac{\sigma[T]}{\Delta t}\,[\Delta A]_{k+1}^{t+\Delta t} = -\nu[S][A]_{k}^{t+\Delta t} - \frac{\sigma[T]}{\Delta t}\,[\Delta A]_{k}^{t+\Delta t} \tag{3.88}$$

in permanent magnets, the equation is

$$\nu[S][\Delta A]_{k+1}^{t+\Delta t} = -\nu[S][\Delta A]_{k}^{t+\Delta t} + \frac{\nu}{2}(B_{rx}[c_i] - B_{ry}[b_i]) \tag{3.89}$$

and the stator circuit equation is given by

$$\begin{aligned} &{}_{k+1}^{t+\Delta t}R + \frac{L_\sigma}{\Delta t}[\Delta i_s]_{k+1}^{t+\Delta t} + \frac{[Q]}{S}l\frac{[\Delta A]_{k+1}^{t+\Delta t}}{\Delta t} \\ &= -[i_s]_{k}^{t+\Delta t}R - \frac{L_\sigma}{\Delta t}[i_s]_{k}^{t+\Delta t} - \frac{[Q]}{S}l\frac{[A]_{k}^{t+\Delta t}}{\Delta t} + V + \frac{L_\sigma}{\Delta t}[i_s]^{t} + \frac{[Q]}{S}l\frac{[A]^{t}}{\Delta t} \end{aligned} \tag{3.90}$$

Hence, the final global equation in matrix form is

$$\begin{bmatrix} \nu\,[S] & \frac{[Q]}{S} \\ \nu\,[S] + \sigma\frac{[T]}{\Delta t} & 0 \\ \nu\,[S] & 0 \\ \frac{[Q]}{S}\frac{l}{\Delta t} & [R] + \frac{[L_\sigma]}{\Delta t} \end{bmatrix} \begin{bmatrix} \Delta A_{k+1}^{t+\Delta t} & [\Delta i_s]_{k+1}^{t+\Delta t} \end{bmatrix} \tag{3.91}$$

$$= \begin{bmatrix} -\nu[S][A]_k^{t+\Delta t} - \dfrac{[Q]}{S}[\Delta I]_k^{t+\Delta t} \\ \\ -\nu[S][A]_k^{t+\Delta t} - \dfrac{\sigma[T]}{\Delta t}[\Delta A]_k^{t+\Delta t} \\ \\ -\nu[S][\Delta A]_k^{t+\Delta t} + \dfrac{\nu}{2}(B_{rx}[c_i] - B_{ry}[b_i]) \\ \\ -[i_s]_k^{t+\Delta t}R - \frac{L_\sigma}{\Delta t}[i_s]_k^{t+\Delta t} - \frac{[Q]}{S}l\frac{[A]_k^{t+\Delta t}}{\Delta t} + V + \frac{L_\sigma}{\Delta t}[i_s]^t + \frac{[Q]}{S}l\frac{[A]^t}{\Delta t} \end{bmatrix}$$

3.8 Coupling the Rotor Movement with the FEM

After time discretization the motion equation can be represented by

$$\omega^k = \omega^{k-1} + \left(\frac{T_e - T_L}{J}\right) \times \Delta T \tag{3.92}$$

and rotor displacement can be determined by the following equations:

$$\Delta\theta_m = \omega^k \times \Delta T \tag{3.93}$$

$$\theta_m^k = \theta_m^{k-1} + \Delta\theta_m \tag{3.94}$$

where θ_m is the rotor angle. This step is carried out in the post processing process. The procedure is as follows;

- The electromagnetic torque, T_e is calculated using Maxwell stress tensor method.
- The motion equation (3.92) is used after time discretization to calculate the rotor speed.
- The rotor displacement (rotor angle)is calculated according to equations (3.93) and (3.94).

The rotor FEM mesh is moved according to the rotor angle θ_m at every time steps.

3.9 Solving the Global System of Equation

The resulting global matrix equations are symmetric, positive definite and nonzeros terms are clustered around the main diagonal. Hence, for iterative solver, only the upper triangular coefficient matrix with nonzero elements is stored. Index storage method describe in section (2.2.7) is used in this model. At each iteration cycle of Newton Raphson method, the ICCG algorithm is used to solve the large system of equations. Detailed formulations of solving methods are as follow.

The general form of global system of equation (3.91) can be represented as

$$AX + B\frac{\partial X}{\partial t} = P \tag{3.95}$$

where X is the unknown vector to be determined. For this proposed model, the unknown vector X includes the magnetic vector potentials and stator currents. A and B are sparse coefficient matrices. P is a column vector associated with the input voltages. After time discretization using Backward Euler method, the equation (3.95) becomes

$$\left[A^k + \frac{B^k}{(\Delta t)^k}\right] X^k = P^k + \frac{B^k}{(\Delta t)^k} X^{k-1} \tag{3.96}$$

we can represent the equation (3.95) in Newton Raphson method as

$$J^k_n (\Delta X)^k_n = P^k_{n-1} + \frac{B^k_{n-1}}{(\Delta t)^k} X^{k-1} - \left[A^k_{n-1} + \frac{B^k_{n-1}}{(\Delta t)^k}\right] X^k_{n-1} \tag{3.97}$$

where $X^k_n = X^k_{n-1} + (\Delta X)^k_n$; J is the Jacobian matrix and n is the iteration number of the Newton Raphson method.

The initial calue of the solution X^k can be predicted by the backward method

$$X^k_0 = X^{k-1} + \left(\frac{dX}{dt}\right)^{k-1} (\Delta t)^k \tag{3.98}$$

The error of the Newton Raphson method at the n^{th} iteration cycle is

$$(e_{NR})_n = \frac{1}{N_x}\left| P^k_{n-1} + \frac{B^k_{n-1}}{(\Delta t)^k} X^{k-1} - \left[A^k_{n-1} + \frac{B^k_{n-1}}{(\Delta t)^k}\right] X^k_{n-1}\right| \tag{3.99}$$

where e_{NR} is the number of the total unknown values. The iteration of the Newton Raphson method will stop if

$$(e_{NR})_n \leqslant e_{NR-allowed} \tag{3.100}$$

where $e_{NR-allowed}$ is the error tolerance of the Newton Raphson method. Within each cycle of the Newton Raphson method, the ICCG algorithm is used to solve the large system of algebraic equations.

3.9.1 ICCG algorithm for solving the algebraic equations

At each iteration cycle of the Newton Raphson method, the ICCG algorithm is used to solve the set of algebraic equations. In the ICCG algorithm, it is necessary to determine the approximate factorization of the coefficient matrix. The incomplete Cholesky factorization is used in this method in order to reduce the storage and computing time for factorization the matrix. For iterative solver, only the upper triangular coefficient matrix with nonzero elements is needed to be stored. The coefficient matrix of the algebraic equation set can be expressed as

$$J = LL^T + E \tag{3.101}$$

Where E is the error matrix and L is the lower triangular matrix of the incomplete Cholesky factorization. Since the nonzero values of the coefficient matrix are mainly distributed near the matrix diagonal, the conjugate gradient method is used to solve the equation

$$\begin{aligned} & L^{-1} J_n^k L^{-T} L^T \left(\Delta X\right)_n^k \\ & = L^{-1} \left\{ P_{n-1}^k + \frac{D_{n-1}^k}{\left(\Delta t\right)^k} X^{k-1} - \left[C_{n-1}^k + \frac{D_{n-1}^k}{\left(\Delta t\right)^k} \right] X_{n-1}^k \right\} \end{aligned} \tag{3.102}$$

The step by step iteration procedures are carried out according to the following formulations.

$$Q_1 = \left(LL^T\right)^{-1} r_0 \tag{3.103}$$

$$\beta_{m-1} = \frac{r_{m-1}^{T}\left(LL^{T}\right)^{-1} r_{m-1}}{r_{m-2}^{T}\left(LL^{T}\right)^{-1} r_{m-2}} \tag{3.104}$$

$$Q_m = \left(LL^{T}\right)^{-1} r_{m-1} + \beta_{m-1} P_{m-1} \tag{3.105}$$

$$\alpha_m = \frac{r_{m-1}^{T}\left(LL^{T}\right)^{-1} r_{m-1}}{Q_m^{T} J Q_m} \tag{3.106}$$

The iteration process is controlled by a vector r and it can be represented as

$$r = P_{n-1}^{k} + \frac{D_{n-1}^{k}}{(\Delta t)^{k}} X^{k-1} - \left[C_{n-1}^{k} + \frac{D_{n-1}^{k}}{(\Delta t)^{k}}\right] X_{n-1}^{k} - \left[J_n^k\right](\Delta X)_n^k \tag{3.107}$$

The iteration error of the ICCG algorithm can be determined as

$$(e_{ICCG})_n = \frac{1}{N_x}\left|P_{n-1}^{k} + \frac{B_{n-1}^{k}}{(\Delta t)^{k}} X^{k-1} - \left[A_{n-1}^{k} + \frac{B_{n-1}^{k}}{(\Delta t)^{k}}\right] X_{n-1}^{k} - J_n^k(\Delta X)_n^k\right| \tag{3.108}$$

If $(e_{ICCG})_n \leqslant e_{ICCG-tolerance}$ the iteration of the ICCG algorithm is terminated. The block diagram of the solution process is shown in Fig. 3.16.

3.10 Determination of Time Step Size for Time Stepping FEM

In the time stepping method, $\frac{\partial X}{\partial t}$ (X is unknown variable) is substituted by $\frac{\Delta X}{\Delta t}$ approximately. The system equation solved at times $t_1, t_2, ...(t_k = t_k - 1 + \Delta t)$ step by step. The computation precision is dependent directly on the step size Δt. If the step size Δt is too small, a lot of computing time is required. If the step size Δt is too large, the error will be unacceptable. The choice of the step size is thus critical in reaching a compromise between CPU time and acceptable errors [105]. Hence the best way is to adjust the step size automatically within the program. The criteria developed for controlling the time steps depends on a knowledge of the magnitude of the local truncation error [106]. It is necessary to estimate the local truncation error from a knowledge of the numerical solution only and to use this information to control the step selection [107]-[108]. The general form of global system of equation (3.91) can be represented as

$$AX + B\frac{\partial X}{\partial t} = P \tag{3.109}$$

where X is an unknown vector to be evaluated. A and B are coefficient matrices. Equation (3.109) can be further expressed in a more simplified form as

$$\frac{\partial X}{\partial t} = f(X, t) \tag{3.110}$$

Integrating the above equation from t_{k-1} to t_k gives

$$X_k = X_{k-1} + \int_{t_{k-1}}^{t_k} f(X, t)dt \tag{3.111}$$

If Backward Euler's method is used, the approximate solution at the k^{th} step is

$$X_k^* = X_{k-1} + (\Delta t)f\left(X_k^*, t_k\right) \tag{3.112}$$

Equation (3.111) can be expressed by using Talyor's expansion at t_k as

$$X_{k-1} = X_k - (\Delta t)f(X_k, t_k) + \frac{(\Delta t)^2}{2}X''(\xi^*) \tag{3.113}$$

where X_k is the exact solution and X'' is the second derivative of X with respect to t, $t_{k-1} \leqslant \xi^* \leqslant t_k$. Assuming $f(X_k^*, t_k)$ is equal to $f(X_k, t_k)$ and subtracting the equation (3.112) from (3.113), the local truncation error of X by using Backward Euler's method at the k^{th} step is given by

$$\varepsilon^* = X_k - X_k^* = -\frac{(\Delta t)^2}{2}X''(\xi) \tag{3.114}$$

On the other hand, if Euler's method is used at the k^{th} step and its approximate solution $X^{\#}$ is,

$$X_k^{\#} = X_{k-1} + (\Delta t)f(X_{k-1}, t_{k-1}) \tag{3.115}$$

Using as above steps, the local truncation error is

$$\varepsilon^{\#} = X_k - X_k^{\#} = \frac{(\Delta t)^2}{2}X''(\xi^{\#}) \tag{3.116}$$

where X_k is the exact solution at $t_{k-1} \leqslant \xi^{\#} \leqslant t_k$. Subtracting equation (3.114) from (3.115) gives

$$X_k^* - X_k^{\#} = \frac{(\Delta t)^2}{2} X''(\xi^{\#}) + \frac{(\Delta t)^2}{2} X''(\xi^*) \tag{3.117}$$

Assuming $X^{''}(t))$ is continuous, there certainly exists a ξ between $\left[\xi^{\#}, \xi^*\right]$ or $\left[\xi^*, \xi^{\#}\right]$, hence

$$\frac{(\Delta t)^2}{2} X''(\xi^{\#}) + \frac{(\Delta t)^2}{2} X''(\xi^*) = (\Delta t)^2 X''(\xi) \tag{3.118}$$

Assuming $X^{''}(t)$ changes very slowly between a small area $\left[\xi^{\#}, \xi^*\right]$ or $\left[\xi^*, \xi^{\#}\right]$, one obtains $X^{''}\left(\xi^*\right) \approx X^{''}\left(\xi\right)$. Substituting equation (3.118), (3.117) into (3.114), the local truncation error of X using Backward Euler's method is

$$\varepsilon^* \approx (X_k^{\#} - X_k^*)/2 \tag{3.119}$$

The norm of the vector $X = [x_1, x_2, ..., x_N]^T$ is defined as follows;

$$\|X\| = \frac{1}{N}(|x_1| + |x_2| + \cdots + |x_N|) \tag{3.120}$$

where N is the number of unknowns. Thus the norm of ε^* is defined as

$$\varepsilon = \left\| X_k^{\#} - X_k^* \right\| /2 \tag{3.121}$$

where ε is the error indicator.

According to the equations (3.119) and (3.114), the accuracy can be improved by modifying X_k^* as

$$X_k = X_k^* + \varepsilon^* \approx (X_k^{\#} - X_k^*)/2 \tag{3.122}$$

Substituting equations (3.115), (3.112) into equation (3.122), the improved solution is

$$X_k^{\Delta} = X_{k-1} + \frac{\Delta t}{2} \left[f(X_{k-1}, t_{k-1}) + f(X_k, t_k) \right] \tag{3.123}$$

The process of the adjusting step size is summarized as follows:

At the first step

1. Input an initial step size $(\Delta t)^0$.

2. Use Euler's equation (3.115) to obtain the solution X''.

3. use the Backward Euler's equation (3.112) to obtain the solution X^*. This is the approximate solution of X at this step.

4. Check the error ε by (3.121). If ε is larger than the allowed value $\varepsilon_{allowed}$, reduce the step size according to the following equation, then go back to process 2.

$$\Delta t = 0.8\,(\Delta t)^0 \sqrt{\frac{\varepsilon_{allowed}}{\varepsilon}} \tag{3.124}$$

   Where 0.8 is a typical safety factor to ensure the step size is smaller than the allowed value.

5. Calculate $f(X_1, t_1)$ for the next step according to equation (3.112) as

$$f(X_k, t_k) = \frac{\left(X_k^* - X_{k-1}^*\right)}{\Delta t} \tag{3.125}$$

At the k^{th} step

1. Estimate the step size according to the error at the last step. Assume $X''\,(\xi^*)_k \approx X''\,(\xi^*)_{k-1}$. From equation (3.114), we get

$$(\Delta t)_k = 0.8\,(\Delta t)_{k-1} \sqrt{\frac{\varepsilon_{allowed}}{\varepsilon}} \tag{3.126}$$

2. Use Euler's equation (3.115)to obtain the solution $X_k^{\#}$.

3. Use Backward Euler's equation (3.112) to obtain the solution X^*.

4. Check the error by equation (3.121). If error is larger that the allowed value $\varepsilon_{allowed}$, reduce the size according to the equation (3.126) and then go back to the process 2.

5. Calculate $f(X_k, t_k)$ for the next step using the equation (3.125).

If the improved solution given in equation (3.123)is used as the approximate solution of X at each step,$X_k^{\#}$ has to be obtained by solving the Euler's explicit equation (3.115). Simulated result with or without using time step adjusting scheme will be shown in performance evaluation of the motor.

3.11 Conclusion

In this chapter, numerical modelling of the BLDC in time domain was presented. Circuit-field-motion coupled time stepping finite element method was used. Detail procedures of mathematical modelling of the BLDC motor in time varying electromagnetic field, coupling with the non-linear circuit equation and rotor movement equations were described. Circuit equation included real time model of the inverter switches. Although the switches are assumed to be ideal devices, the circuit model developed is flexible enough to incorporate turn 'ON' and 'OFF' times.

An efficient method to generate the FEM mesh and rotate the rotor mesh was presented. Using proposed mesh rotation technique, stator mesh and rotor mesh are needed to generate only one time. When rotor is rotated, minor modification to the nodes on the interface is needed in order to generate the topology of the whole mesh. Hence, the computing time is greatly reduced.

Finite element formulations of mathematical equations of the time varying magnetic field, circuit and motion using Galerkin's method were described. Time dependent FEM equations are discretized by Backward difference method. Since the electromagnetic field of the problem domain are modelled in time varying magnetic field; the eddy current effect, the non-sinusoidal quantities and high order harmonics can all be taken into account in this proposed model. Linearization of the non linear electromagnetic field equations were performed by Newton's Raphson method coupled with cubic spline interpolation. Hence, saturation characteristics of the ferromagnetic materials can be included into the system of equations. Detailed procedures to solve the global system of equations using ICCG algorithm were developed.

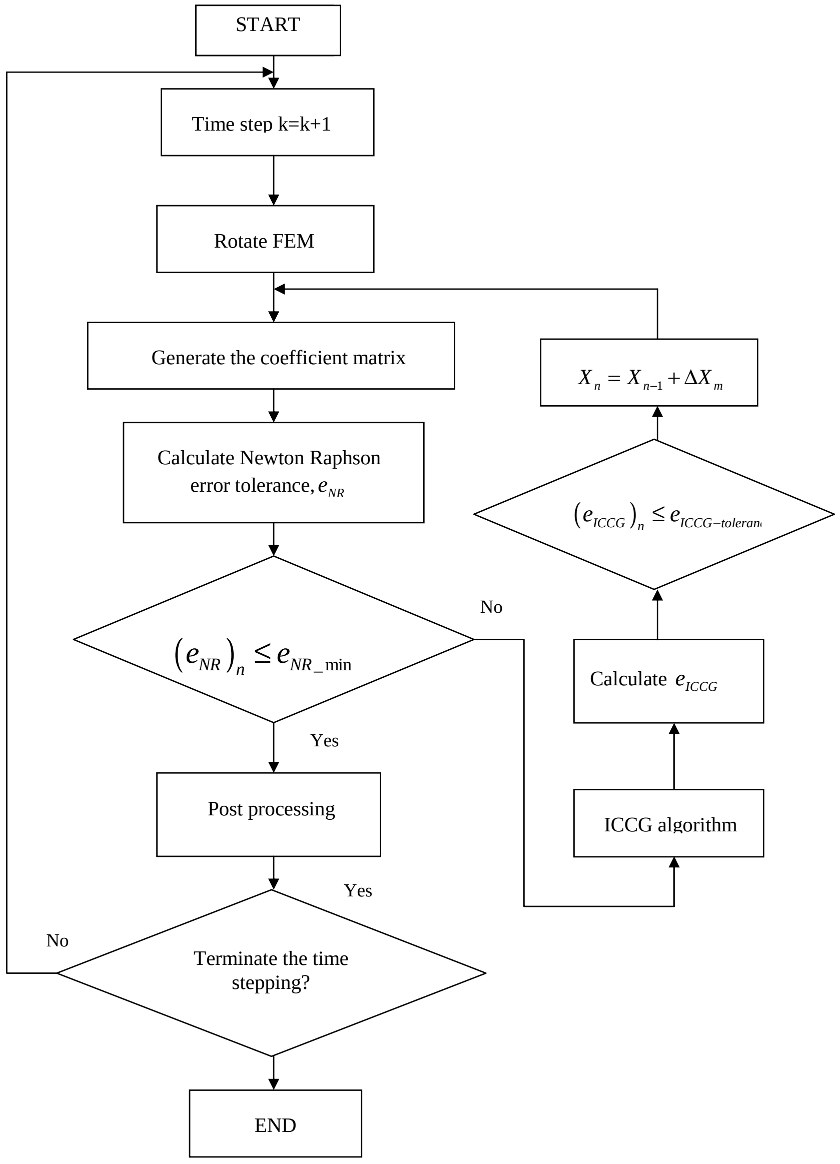

Figure 3.16: Block Diagram of the time stepping solver

Chapter 4

Experimental Implementation of the DSP Based BLDC Motor Drive System

4.1 Introduction

The experimental set up for BLDC motor drive especially for sensorless micro motor type spindle motor is another challenging subject. Owing to certain inherent features of permanent magnet motor with electronic controllers, the standard DC motor test procedures are no longer suitable for BLDC drive system. A simple and reliable test stand for exterior rotor BLDC motor type, HDD spindle motor has developed in this chapter. The test equipments include a 8 poles 12 slots spindle motor, dSpace1104 controller board, six steps IRF620 MOSFET voltage source inverter, incremental encoder and rectified variable DC power supply. Software implementation includes control program algorithm and drive functions based on the DS1104 real time interface. A simple approach to determine the starting switching sequences of the BLDC motor with respective rotor positions has developed. Measuring the motor performances in both steady state and transient are presented.

4.2 Hardware Implementation

The system hardware essentially consists of a spindle motor, a voltage source inverter, rectified variable DC supply, current sensors, an incremental encoder, a DS1104 controller board and a host PC computer. Fig. 4.1 shows the hardware set up in the laboratory and Fig. 4.2 shows the schematic diagram of the hardware equipment. The individual functions and characteristic features of the hardware components are briefly described in following subsections.

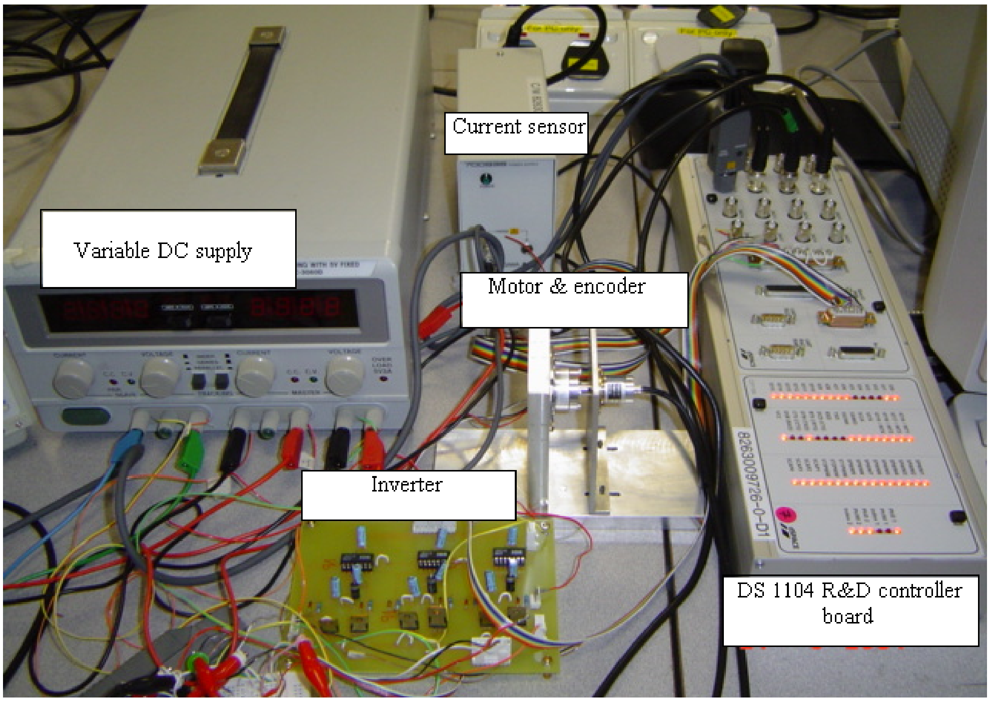

Figure 4.1: Photograph of hardware set up in the Laboratory

4.2.1 The Variable DC supply

The variable DC source is used for supplying the motor and the driving voltage source for the inverter. The spindle motor requires variable power supply ranges from 5V to 12 V whereas the inverter requires 12 V fixed DC supply for driving the MOSFETs and 5V fixed DC supply for MOSFET's drivers.

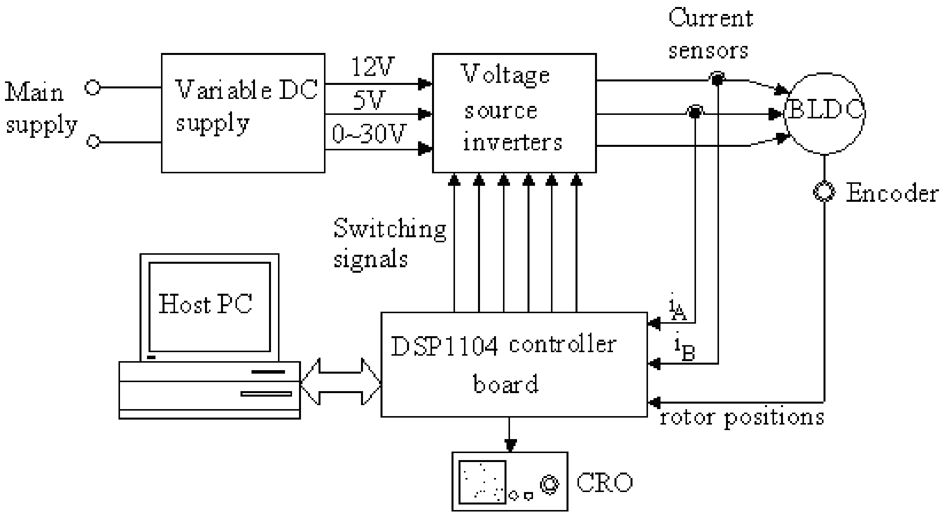

Figure 4.2: Schematic diagram of the hardware equipments

4.2.2 The voltage source inverter

It is well known that an ideal semiconductor device for power switching should exhibit a low forward-voltage drop to reduce forward-conduction losses and a high switching speed to reduce switching losses to a minimum. In addition, the switch should ideally have a zero voltage drop during the on-state while providing infinite resistance in the off-state. In this experimental set up, N-channel 200V, 0.8 ohm static drain-source on resistance, 6A drain current (at 25 C, continuous) IRF620 MOSFET is used to implement the voltage source inverter for the prototype BLDC motor. In the switching of high voltage floating devices (such as MOSFET) within a three phase bridge configuration, the driving voltage to a device must typically be higher than the drain or collector voltage. If a device is referenced to the high side, the required voltage will be greater than the supply. The driving signal is supplied from the logic circuits, which are normally referenced to the ground potential; hence the signals need to be level shifted to the source or emitter of the device. As the voltage across the lower device switches between the two rail voltages, a high-performance level changer and isolation is required. Therefore, in order to ease the design tasks, IR2110 high and low side drivers are used to control one arm of the a MOSFET bridge circuit where the high side is floating with respect to the low side.

The key feature of driver IR2110 is their suitability for applications up to 500V, with a 2A peak output capability and a 25ns switching speed. To protect the system, the device will shut down if an under-voltage is detected on the logic supply; this is critical for safe operation during switching of the circuit. Circuit diagram of hardware implementation of voltage source inverter is shown in Fig. 4.3. The voltage for the high-side driver is provided by the network capacitor C2 and and diode D1. For example, when the MOSFET S1 is on, capacitor C2 is charged via D1. The diode prevents the capacitor from discharging when the device is off and when the voltage of the collector approaches the supply voltage, Vs. The time during which the current can be supplied to the high side driver is limited by the current drain and by the size of the capacitor. A typical value of 1000pF and a current drain of 5mA can be sustained at an operating frequency of up to 10kHz. Detailed specifications of hardware equipment used in this inverter circuit are given in Appendix E.

4.2.3 Spindle motor

An in-hub type 8 pole 12 slots spindle motor is used in this experiment. Principal motor specifications are listed in Table 4.1. Motor is mounted with an incremental encoder to sense the rotor position. Disc platters are used as loads for the motor and mounted on the motor hub the same way used in the hard disk drive. Fig. F.1 shows the hardware set up of the spindle motor with the encoder. Electronic commutation is carried out according to the rotor position and switching sequences of the controller.

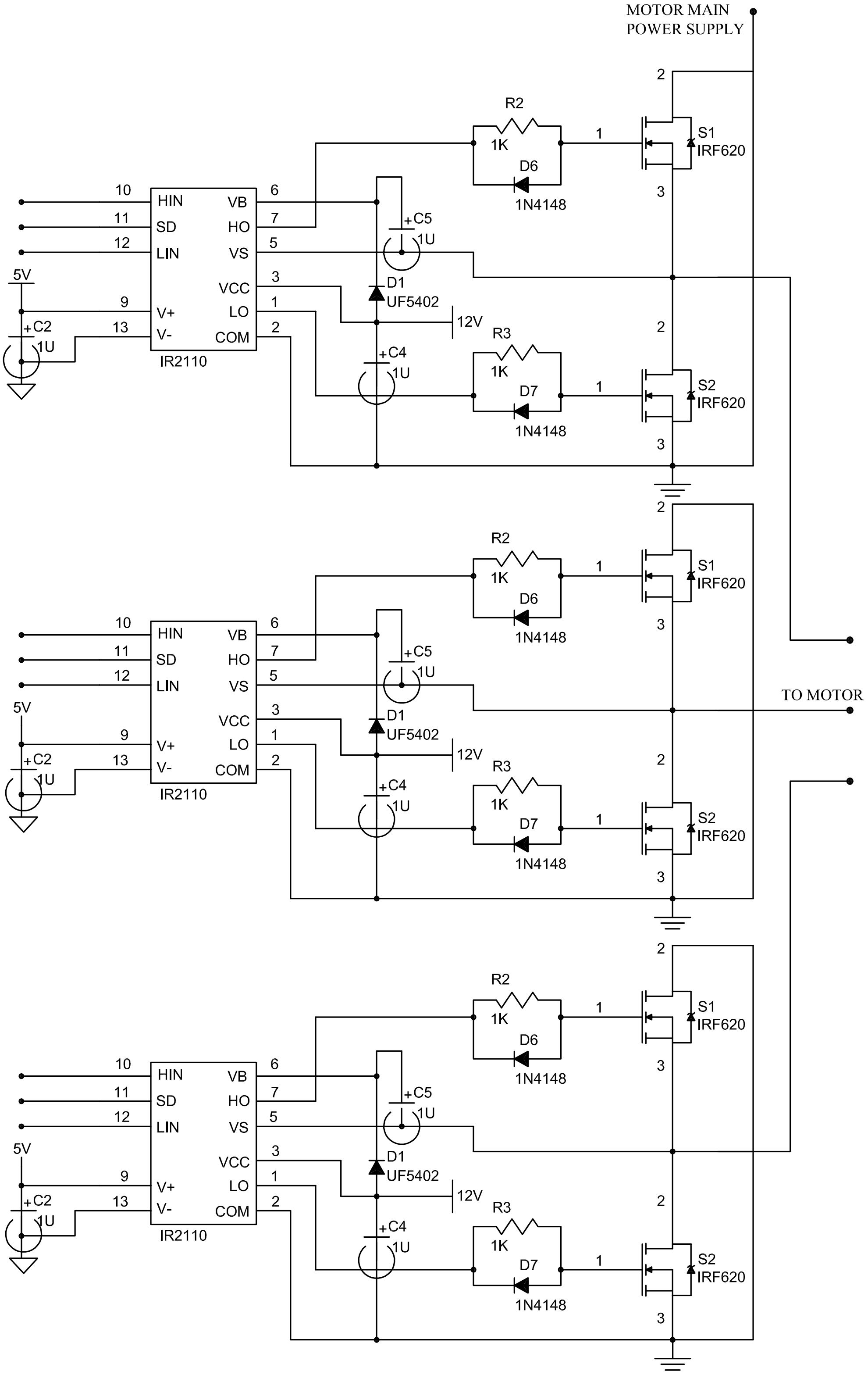

Figure 4.3: Circuit diagram of the voltage source inverter

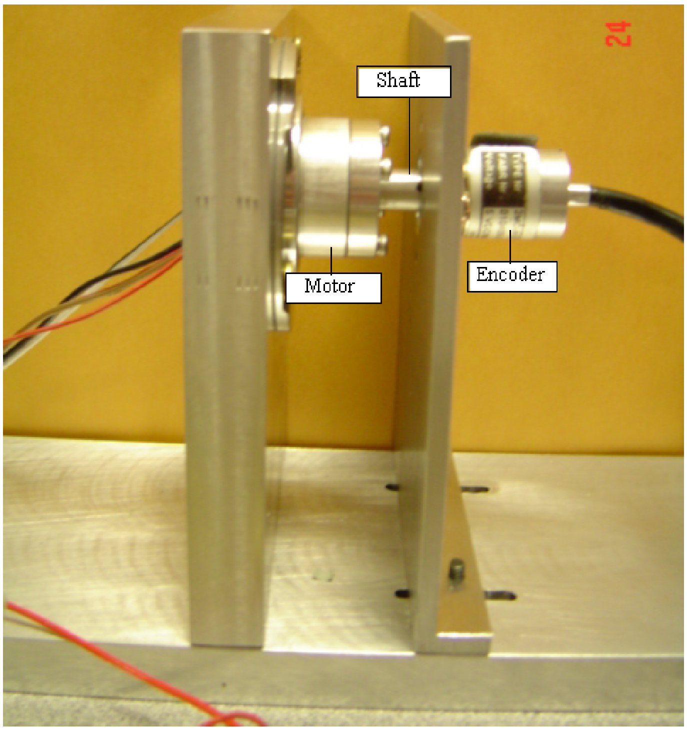

Figure 4.4: Hardware set up for motor and encoder

Table 4.1: Motor specifications

voltage	$12V$
No of poles	8
No of slots	12
Rated speed	$7200rpm$
Stator outside diameter	$28mm$
Rotor outside diameter	$30mm$
Stack length	$4.5mm$
Air gap	$0.2mm$
Magnet	$NdFeB$

4.2.4 Incremental encoder

In hub-type disk drive motors are mostly designed to rotate only two or three disc platters. Therefore, an encoder mounted with this type of spindle motor should have relatively very small holding torque and inertia. In this type, SCANCON incremental encoder, mirco hollow shaft type 2MCH model is used. It has a resolution of 1024 lines per revolution; mass moment of inertia is $0.25gcm^2$ and starting torque is $< 0.005Nm$. Detailed specifications are attached in Appendix F. The output from the encoder is in pulse form and it cannot provide the rotor position at starting. Encoder is the incremental type therefore it is needed to detect the index or home signal. DS1104 encoder interface provides the feature to detect the index signal. Adding an index channel to an incremental encoder allows the encoder to provide absolute rotor position.

4.2.5 DS1104 controller board

DS1104 controller board is specifically designed for the development of high speed multivariable digital controllers and real time simulations in various fields. It is a complete real-time control system based on a 603 PowerPC floating point processor running at 250MHz. For advanced I/O purposes, the board includes a slave-DSP subsystem based on the TMS320F240 DSP microcontroller. For rapid control prototyping, specific interface connectors and connector panels provide easy access to all input and output signals of the board. The DS1104 controller board is designed like a PC expansion card so that it can be inserted into the PCI slot of the PC, together with the PC video card or sound card. Fig. 4.5 shows the overview of the architecture and the functional units of the DS1104. The controller board provides the following features:

Master PPC which is the main processing unit of the board and consists of

- A PowerPC 603e microprocessor with running at 250 MHz, containing 16 kilo-bite L1 data cache and L1 instruction cache
- An interrupt controller
- A 32 MB synchronous DRAM controller

- Timers and
- A PCI interface (5V, 32 bit, 33 MHz).

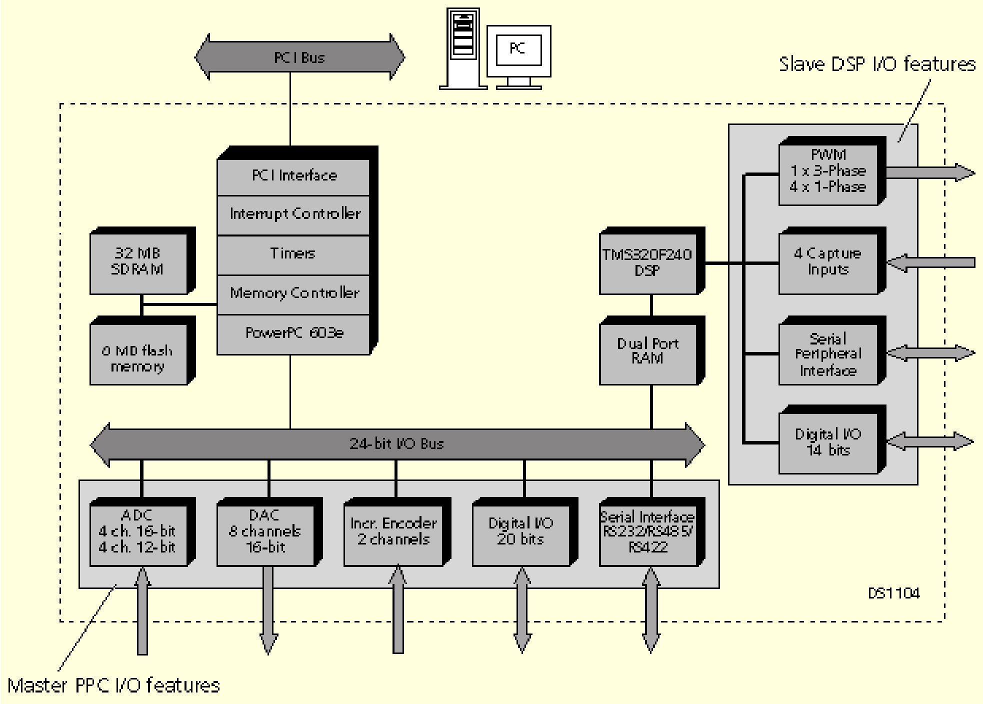

Figure 4.5: Overview of DS1104 Feature

The master PPC controls the I/O features of analog to digital (ADC) unit, digital to analog (DAC) unit, bit I/O unit, incremental encoder interface and serial interface. These features can be fully programmed from the real time interface by simulink or hand coded C program. The ADC units convert the analog feedback signals of 10 V into digital format so that the DSP can read the measured quantity. In this experiment, motor input voltages and stator currents are measured via the ADC converters. Alternatively, DAC units are used for the digital to analog signals of the range of 10 V so that all these signals can be displayed on the oscilloscope.

Bit I/O unit can be used for digital I/O to and from the experiment and real time interface of the DS1104 control board. It contains 20 bit I/O pins. The I/O pins are called IO0.. IO19. The direction of each bit can be selected individually by software control program. In this experiment, bit I/O unit is used as an interface for control program and inverter switching input signals. Bit IO0 to IO5 are used to provide the required six input signals for inverter circuit to switch on the respective MOSFET.

There are two input channels for two digital incremental encoders (Inc1 and Inc2) in the master PPC of the DS1104. Both of theses two encoder interfaces can support single ended TTL and differential signals. It can provide 1.65 MHz maximum encoder line count frequency that means it can measure up to 1,650,000 encoder lines per second. Since the DS1104 perform internally a fourfold subdivision of each encoder line, the board can therefore handle count frequencies of up to 6.6 MHz. The DS1104 is equipped with a 24 bit position counter. Due to the fourfold subdivision of each encoder line, the counter allows to measure up to 222 encoder lines in the range -221...+221-1. The count direction depends on the encoder's rotation direction. The counter can be reset by the encoder's index pulse. Each encoder channel provides an index input. The input is connected to the DS1104 interrupt control unit. The index signal can be extracted and written the position information to the position counters immediately when an index is found. Motor speed can be calculated via encoder interface. In this experiment, "Inc1" incremental encoder interface is used to measure motor speed and sense the rotor position. Interrupt controller provides various hardware and software interrupts. In this work, encoder index signal is extracted by encoder interrupt. Host interface is used for setting up the DS1104, downloading the programs and transferring runtime data to and from the host PC.

The DS1104 is equipped with two memory: global memory and flash memory. Global memory provides 32 MByte synchronous DRAM for experiment. Flash memory provides of 8 Mbyte which is divided by the 4 blocks of 2 Mbyte each. The application for this experiment is very simple therefore global memory is enough to use for real time implementation.

4.3 Software Implementation

Spindle motors are operated in two phases on operation. In order to run the motor in correct direction, it is necessary to switch on the correct and exact two phases of the motor. Therefore, rotor position should be known a prior and then it is required to determine the switching sequences. If the switching sequences are not correct, motor may not run properly. Fig. 4.6 and Fig. 4.7 show typical input phase voltage waveforms and switching states for the motor with a wye connected stator winding. Possible switching sequences are shown in Table 4.2. In practical cases, the motor may start at any of these switching conditions.

Based on these consequences, simple and reliable control program is implemented in this experiment. Firstly, detect the initial rotor position by encoder interface of the DS1104. And then switch on any predefined two phases (for example phases A and B of switching sequence no(1)) and check whether the motor starts to run or not. If the motor rotates as the desired direction, suppose that the proposed switching sequences are the correct sequence to run the motor. If not, move on to another two pairs of switching states and check again. It is needed to test only six steps and one can decide the switching sequence very easily.

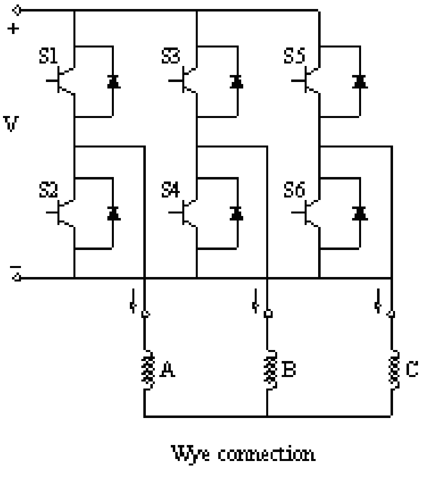

Figure 4.6: Wye connected stator windings

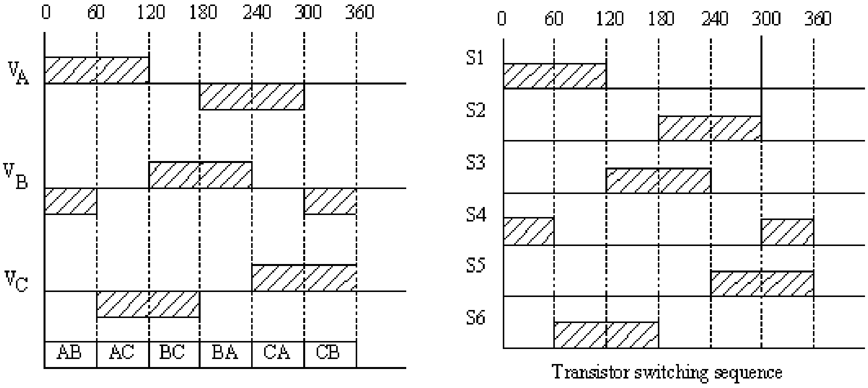

Figure 4.7: Typical input voltage waveform and switching states

Table 4.2: Possible switching sequences

sequence no.1	*sequence no.2*	*sequence no.3*	*sequence no.4*	*sequence no.5*	*sequence no.6*
AB	*AC*	*BC*	*BA*	*CA*	*CB*
AC	*BC*	*BA*	*CA*	*CB*	*AB*
BC	*BA*	*CA*	*CB*	*AB*	*AC*
BA	*CA*	*CB*	*AB*	*AC*	*BC*
CA	*CB*	*AB*	*AC*	*BC*	*BA*
CB	*AB*	*AC*	*BC*	*BA*	*CA*

Bit I/O unit is used to operate the inverter circuit driver ,IR2110 to switch on the respective MOSFET (from S1 to S6). In this experiment, bit IO0 is used to provide the switching signal for high end MOSFET, S1, IO1 is used to provide the switching signal for low end MOSFET, S2 and so on. In other words, if the value of bit IO0 is 1, S1 will be turn on and if bit IO0 is 0, S1 will be turn off. Program flow chart for switching sequence control is given in Fig. 4.8. Main control program and interrupt service routine program flow charts are shown in Fig. 4.9. The entire control program is written in C language.

The execution processes for developed C program into DSP real time interface are as mentioned below. Real time RTILib is used to implement the hand-coded C program. Downloading and starting applications on the real time hardware can be done by the Platform Manager as a batch client. After downloading the program into DSP, the users can easily modify the process variables and control parameters via on line real time interface.

4.4 Measuring Motor Performances

Motor performance can be measured using DS1104 controller board in real time interface and an oscilloscope. The following subsections describe how to measure the motor performances in both transient and steady state conditions.

4.4.1 Rotor position sensing and switching sequence detecting

Rotor position is measured every sampling period of the DSP control program via encoder interface. Measured rotor position serves as an input signal for the control program. Outputs from the control program are switching signals for the inverter. These are sent to the inverter via bit I/O unit. Hence, switching states can be detected by measuring the output of bit I/O unit. It is required to check the switching states before connecting the motor with the inverter circuit to protect malfunction of the inverter switching sequences.

4.4.2 Measuring back-emf

Measurement of the back-emf in BLDC motor mostly uses prime mover such as DC motor or stepper motor which is directly mounted with the test motor. The test motor is allowed to run the rated speed and then measures the induced voltage within the motor winding (back-emf) via oscilloscope or other data acquisition units. In most cases, HDD spindle motors used in PC computers are designed to run two disc platters. Mounting both encoder and prime mover in this type of spindle motor may lead to improper running condition because encoder has its own mass moment of inertia and prime mover motor has holding torque itself. Motor will be overloaded and sometimes it may not start because of high holding torque. In order to overcome these shortcomings and difficulties, a simple method is implemented in this experiment. Firstly, motor is allowed to run the rated speed to few minutes and then switch off the motor power supply. Although there is no current in the stator winding, the motor will be run few milliseconds at this instant because of the rotor high inertia. Therefore, induced voltage in stator winding which is called Back-emf can be measured at this instant. When the motor speed goes down to zero, the measured bacemf signals will be distorted and go down to zero. However, only a few cycle is enough for measuring back-emf since it is repeated for every 360 electrical degree cycle.

4.4.3 Measuring stator current

Sufficiently accurate measurements of the motor phase currents are essential to ensure high-performance in the BLDC drive system. In this experimental set-up, two simple and reliable current sensing methods: (a) measuring by using clamp meter and (b) by using shunt resistors, are utilized to measure the phase-A and phase-B currents. In current sensing by clamp meter, the measured currents from the clamp meter are converted into voltage signals scaled to the range 10V by using resistors of appropriate resistance values. These voltage signals are then fed into the A/D converters of the DS1104.

4.4.4 Measuring motor speed

Motor speed is measured using the encoder interface of the DS1104 controller board. The speed is calculated by the encoder line count. Both transient and steady state conditions can be measured easily. For disk drive motor, starting time to reach the rated motor speed is one of the important parameters for drive precisions and implementation. In this experiment, motor speed vs. time under the following conditions

- motor starting with different supply voltages
- motor starting with different rotor inertias
- motor starting with drive limits.

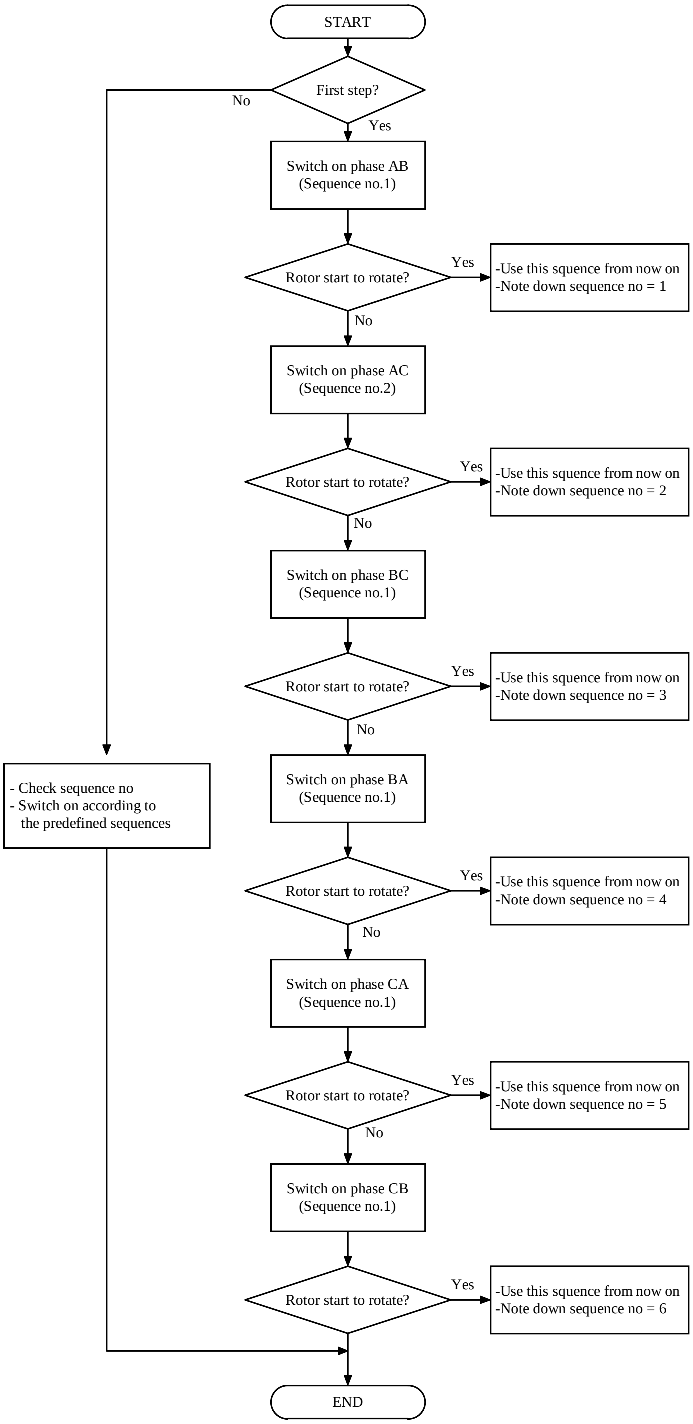

Figure 4.8: Flow chart of switching sequences control program

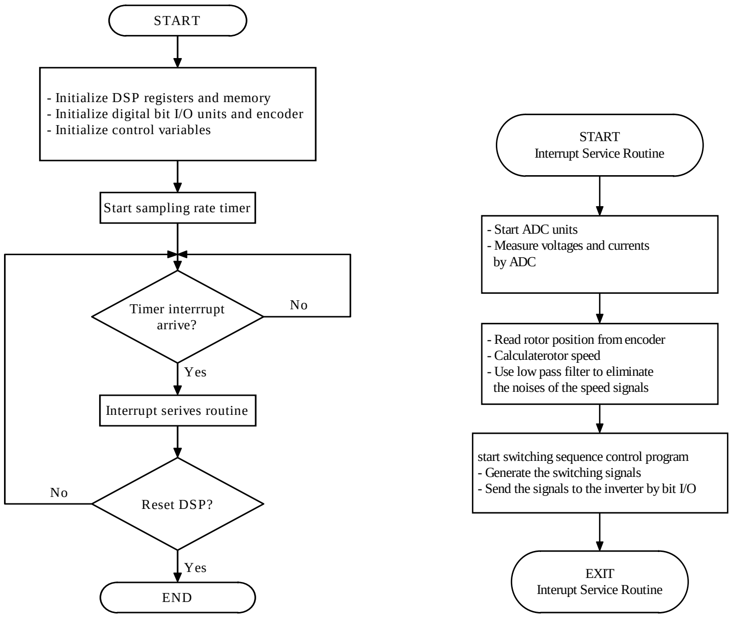

Figure 4.9: Main control program and interrupt service routing flow charts

Chapter 5

Performance Analysis of the BLDC Motor

5.1 Introduction

Detailed formulations of mathematical models and experimental methods for exterior rotor BLDC motor have been developed in the previous chapters. In this chapter, the investigations of steady state operations and dynamic behaviours of the BLDC motor under no-load and loaded conditions are presented. In the time stepping FEM simulation, time step sizes are adjusted as mentioned in Section 3.10. In order to validate the numerical models, experimental results are described and compared with simulation results obtained from FEM analysis.

5.2 Steady State Analysis of the BLDC Motor

Normally, the transient solver begins with a flat start by initializing all state variables to zero. This results in a large DC components of current and several hundred integral time steps are needed before reaching its steady state [109]-[110]. While only the steady state solutions may be of interest, it may take many cycles of computation before starting transient disappear. This excessive computation time required to reach the steady state solution has prompted an interest in the traditional current fed two dimensional magneto-static FEM. One motivation in this work is that the steady state solution from the two dimensional magneto-static FEM model is used as an initial condition for the time stepping solver. The steady state model of the BLDC motor includes four main parts.

1. Mesh generation
2. Pre-computation by two dimensional magneto-static FEM
3. Computation in time domain by time stepping FEM
4. Post processing

Detailed descriptions for each of these parts are discussed in the next sections. The program structure is given in Appendix G.

5.2.1 Mesh generation

FEM mesh is generated according to the procedures which have been described in Section 3.4. For the static analysis, the rotor is assumed to be psuedo-stationary. Stator mesh and rotor mesh are generated separately and connected by periodic boundary condition. After mesh generation, pre-computation by two dimensional magneto-static FEM is started.

5.2.2 Pre-computation using two dimensional magneto-static FEM

Pre-computation of initial conditions for the time domain solver is carried out by using current fed two dimensional magneto-static FEM which has been developed in Chapter 2.

Recall the non-linear electromagnetic field equation (2.18), which is

$$\frac{\partial}{\partial x}\left(\nu\frac{\partial A}{\partial x}\right)+\frac{\partial}{\partial y}\left(\nu\frac{\partial A}{\partial y}\right)=-J_0+J_m \tag{5.1}$$

where ν is the reluctivity of the material, J_0 is the applied source current density and J_m is the equivalent current density of the permanent magnet. Galerkin's method is employed for finite element formulation. Detailed procedures of Galerkin's formulation for the above two-dimensional eddy complex eddy current equation (5.1) have been discussed in Chapter 2. Hence, the final global system element matrix equation for the electromagnetic field equation (5.1) is

$$\begin{aligned} &\frac{1}{4\mu^e\Delta}\begin{pmatrix} b_i^2+c_i^2 & b_ib_j+c_ic_j & b_ib_k+c_ic_k \\ b_ib_j+c_ic_j & b_j^2+c_j^2 & b_jb_k+c_jc_k \\ b_ib_k+c_ic_k & b_jb_k+c_jc_k & b_k^2+c_k^2 \end{pmatrix}\begin{pmatrix} \hat{A}_i \\ \hat{A}_j \\ \hat{A}_k \end{pmatrix} \\ &= J_0^e\frac{\Delta}{3}\begin{pmatrix} 1 \\ 1 \\ 1 \end{pmatrix} + \frac{\nu\mu_o}{2\Delta}\left(M_x\begin{pmatrix} c_i \\ c_j \\ c_k \end{pmatrix} - M_y\begin{pmatrix} b_i \\ b_j \\ b_k \end{pmatrix}\right) \end{aligned} \tag{5.2}$$

Newton Raphson's method is used to linearize the non-linear equations. ICCG algorithm is used to solve the global system of equations. After obtaining a solution (magnetic vector potential A) from magneto-static FEM, an instant of time is chosen and the time stepping solver is started.

5.2.3 Computation in time domain by time stepping FEM

In this step, time domain models of the BLDC motor which have been developed in chapter 3 are used. Computational analysis in time stepping FEM includes modelling of the electromagnetic field, circuit and motion equations in time domain, finite element formulation, time discretization, linearization of the nonlinear field equations, simulation of rotor rotation and solving the global system of equations as discussed before. At the first time step, the initial values are the solutions got from the previous magneto-static FEM.

5.2.4 Post processing

The post processing is the process to compute the desired parameters of motor performances. Post processing includes computation of magnetic flux density, stator current, torque, force, motor speed etc., with various time frames. Evaluations of steady state performances in a BLDC motor using the proposed steady state model are discussed in the next section.

5.3 Evaluation of Steady State Performances

This section describes the methods of computation of important steady state performance indicators such as determination of electromagnetic torque, back-emf, stator current, torque-speed characteristics and computation of cogging torque using proposed steady state FEM model. Experimental results are given to compare with the computational results in order to verify the validity of the proposed steady state model.

5.3.1 Calculation of stator current

In time stepping model, the field equations, the circuit equation and the motion equation are solved simultaneously. The inputs are the stator voltages and rotor positions whereas the outputs are magnetic vector potentials and stator currents. Hence, no extra step is needed to calculate the stator current. Fig. 5.1 shows the input stator voltage waveforms and Fig. 5.2 is the corresponding output stator current waveform at no load condition computed in time domain. Fig 5.2 shows the computation and experimental results of the stator current waveforms at no load condition. It can be seen that the simulation and experimental results are in good agreement. According to the Fig. 5.2, the transient time stepping solver can also be started with the initial conditions quite close to the steady state solution.

There is still a transient at the first cycle due to the fact that the 2D static FEM does not correctly account for eddy current effect and ignores the motion effects.

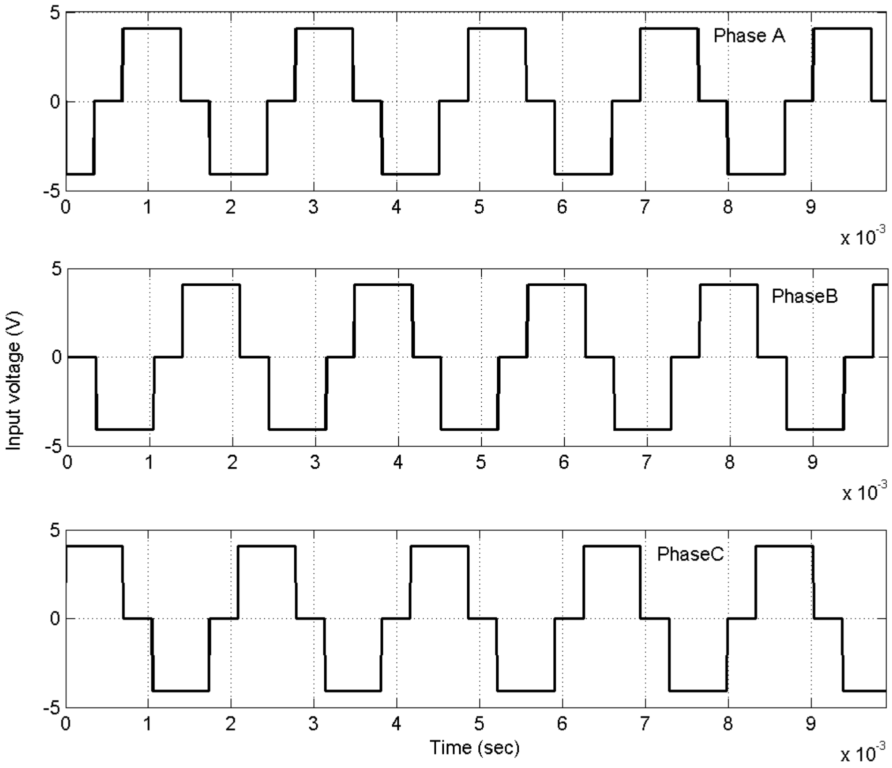

Figure 5.1: Input voltage waveform against time

5.3.2 Computation of electromagnetic force and torque

To predict the performance of an electrical machine, precise knowledge of force and torque is important. Electromagnetic forces and torques can be computed in a variety of ways. The three basic methods often employed with finite element analysis are Lorentz force, Maxwell's stress tensor and Energy methods [111]-[112]. Each method has its own merits. In this work, Maxwell's stress tensor method is used to calculate the torque and force of the BLDC motor. Maxwell's stress tensor method is based on the fact that the field distribution inside a closed surface in along the air gap remains unchanged even if the external sources are removed and replaced by a distribution of currents [113]. For a ferromagnetic material of volume

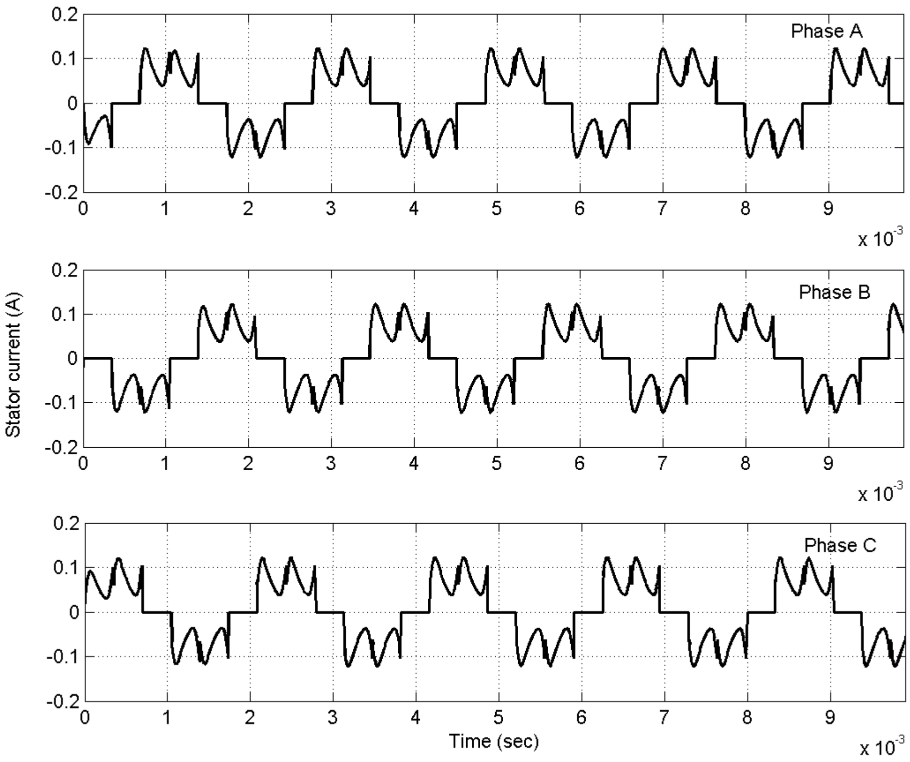

Figure 5.2: Computed stator current waveforms at no load condition

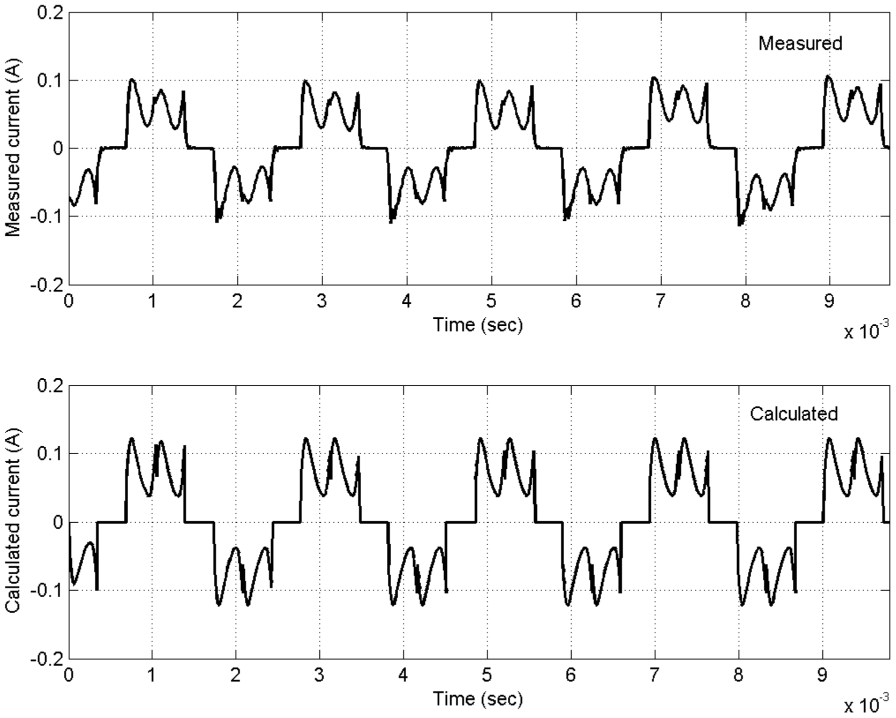

Figure 5.3: Experimental and computational results of stator current

v, the volume current J_v can be defined by

$$J_v = \frac{\nabla \times M}{\mu_0} \tag{5.3}$$

And then the force density can be found by

$$f_v = J_v \times B \tag{5.4}$$

The force density can be represented as follow by using Ampere's law $\nabla \times H = J$ and constitutive relationship $B = \mu_0 H$, therefore

$$f_v = \left(\nabla \times \frac{B}{\mu_0}\right) \times B \tag{5.5}$$

After performing a few mathematical calculations, the force density can be expressed as the divergence of the Maxwell tensor σ,

$$f_v = \nabla . \sigma \tag{5.6}$$

where the Maxwell tensor σ is

$$\sigma = \frac{1}{\mu_0}\left(B.\vec{n}\right) B - \frac{1}{2\mu_0}\left(B^2 \vec{n}\right) \tag{5.7}$$

Since

$$B = B_n \vec{n} + B_t \vec{t} \tag{5.8}$$

and

$$B^2 = B_n^2 + B_t^2 \tag{5.9}$$

Substitute equations (5.8) and (5.9) into equation (5.7) yields

$$\sigma = \frac{1}{\mu_0}\left(B_n B_t\right)\vec{t} + \frac{1}{2\mu_0}\left(B_n^2 - B_t^2\right)\vec{n} \tag{5.10}$$

where B_n and B_t are the normal and tangential components of flux density respectively.

From Maxwell formulation, the electromagnetic force acting on the rigid body can be calculated by

$$\vec{F} = \int\limits_v \vec{f_v} dv = \int\limits_v \nabla . \sigma dv \tag{5.11}$$

According to the Divergence theorem, the volume integral can be changed into surface integral as

$$\vec{F} = \oint_{s} \sigma.dS \tag{5.12}$$

where S is the surface surrounding the ferromagnetic material where forces are exerting. Substitute the tensor equation (5.10) to the electromagnetic force equation (5.12) we get,

$$\vec{F} = \oint_{S} \left[\frac{1}{\mu_0} \left(B_n B_t \right) \vec{t} + \frac{1}{2\mu_0} \left(B_n^2 - B_t^2 \right) \vec{n} \right] dS \tag{5.13}$$

When equation (5.13) is applied to the calculation of the torque of a BLDC motor, a closed integration surface that surrounds the stator in free space along the air gap must be chosen. For a two dimensional case, the surface integral is reduced to a line integral along the air gap. If a circle of radius r is taken as the integration path, the force is obtained from the following:

$$\vec{F} = \int_{0}^{2\pi} \left[\frac{1}{\mu_0} \left(B_r B_\theta \right) \vec{\theta} + \frac{1}{2\mu_0} \left(B_r^2 - B_\theta^2 \right) \vec{r} \right] r d\theta \tag{5.14}$$

Since, for the two dimensional case,

$$B_r = B_n \tag{5.15}$$

$$B_\theta = B_t \tag{5.16}$$

$$dS = r d\theta \tag{5.17}$$

If the solution would be exact, the force would be independent of the integration radius r when r varies within the air gap. However, the calculated force depends greatly on the choice of the integration radius, and to achieve satisfactory accuracy, the force is calculated over the closed integration circular path that surrounds the rotor in free space along the air gap [112]. Due to the fact that the true force is independent of the radius we obtain by integrating (5.22)

$$\begin{aligned}\vec{F}\left(r_s - r_r\right) &= \int_{r_r}^{r_s}\int_{0}^{2\pi}\left[\frac{1}{\mu_0}\left(B_r B_\theta\right)\vec{\theta} + \frac{1}{2\mu_0}\left(B_r^2 - B_\theta^2\right)\vec{r}\right] r d\theta dr \\ &= \int_{S_{ag}}\left[\frac{1}{\mu_0}\left(B_r B_\theta\right)\vec{\theta} + \frac{1}{2\mu_0}\left(B_r^2 - B_\theta^2\right)\vec{r}\right] dS\end{aligned} \tag{5.18}$$

$$\vec{F} = \frac{1}{\left(r_s - r_r\right)}\int_{S_{ag}}\left[\frac{1}{\mu_0}\left(B_r B_\theta\right)\vec{\theta} + \frac{1}{2\mu_0}\left(B_r^2 - B_\theta^2\right)\vec{r}\right] dS \tag{5.19}$$

where r_r and r_s are the outer and inner radii of the circular ring; S_{ag} is the cross-sectional area of the integration path; B_r and B_θ are the components of the flux density respectively. In the two dimensional electromagnetic field, the electromagnetic force for the rotation of rotor is generated by the tangential component of force. Hence the electromagnetic force acting on the rotor is

$$\begin{aligned}F_\theta &= \frac{1}{r_r - r_s}\int_{r_s}^{r_r}\sum_{m=1}^{M} l_m \int_{0}^{2\pi}\left(\frac{1}{\mu_0}B_r B_\theta\right) r d\theta dr \\ &= \frac{1}{\mu_0\left(r_r - r_s\right)}\sum_{m=1}^{M} l_m \iint_{S_{ag}} B_r B_\theta dS\end{aligned} \tag{5.20}$$

where M is the triangular elements on the integration path of the air gap, l_m is the axial length of the machine.

Finally, the electromagnetic torque can be obtained by integration along the circular path

$$T_e = \frac{1}{\mu_0(r_r - r_s)}\int_{r_s}^{r_r}\sum_{m=1}^{M} l_m \int_{0}^{2\pi}(r B_r B_\theta) ds \tag{5.21}$$

Calculated flux plot at static and after rotation 1000 step are given in Fig. 5.4 and Fig. 5.5. The calculated electromagnetic torque computed using Maxwell's stress tensor method at no load and loaded conditions at each time step is shown in Fig. 5.6.

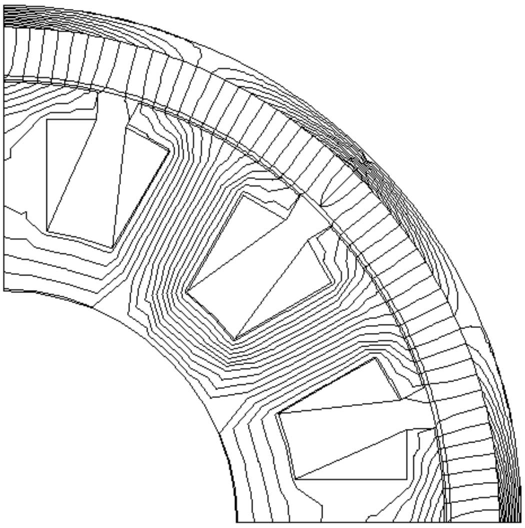

Figure 5.4: Calculated flux plot at static position

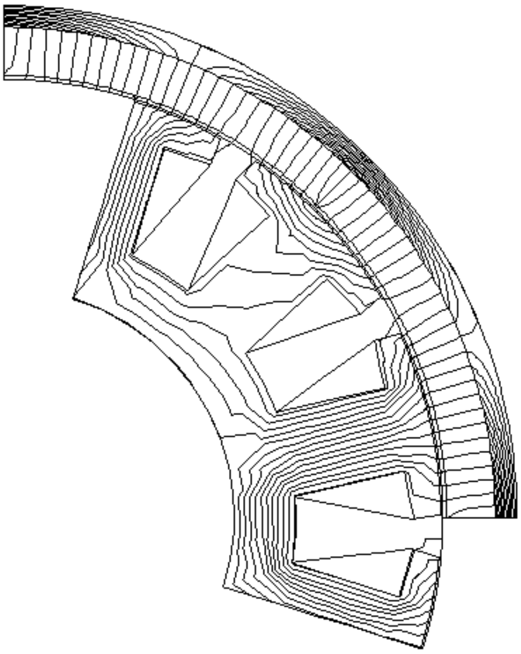

Figure 5.5: Calculated flux plot after rotor is rotated 1000 steps

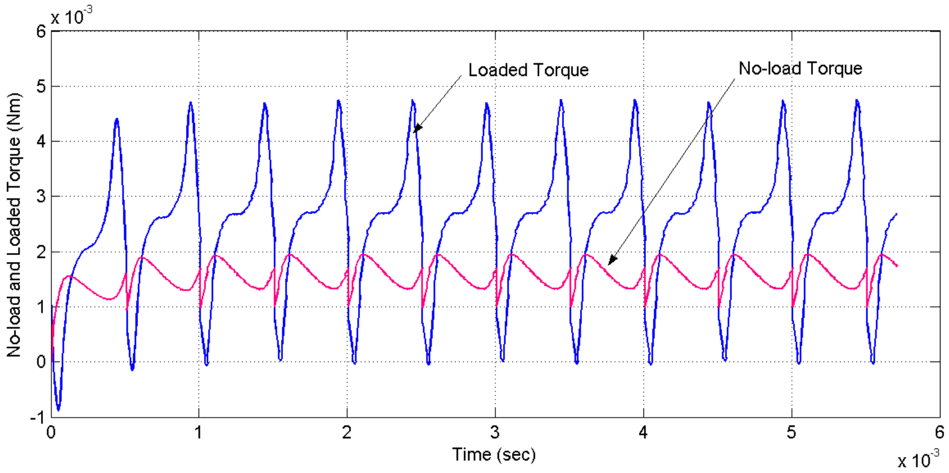

Figure 5.6: Electromagnetic torques at no load and loaded conditions

5.3.3 Determination of torque-speed characteristics

BLDC motors are used in many constant and adjustable speed control applications, because their speed and torque can be easily controlled. Hence, the best way to gain an understanding of the performance characteristics of a BLDC motor is to study the speed and torque relationship. This curve can represent the steady state capability of the motor in driving various types of loads. The most basic functional requirement is to ensure that the motor has enough torque at all speeds, from zero to full speed, to accelerate the load from standstill and maintain full speed without exceeding any thermal or electrical limits.

Torque vs. speed characteristic of the proposed BLDC motor with 4V and 6V supply voltage is presented in Fig. 5.7. It can be seen that the torque-speed curve is merely straight line; when torque is increased, the speed is decreased. This phenomena can be explained by the following steady state equations of the motor. The equivalent circuit equation of the BLDC motor in steady state condition is

$$V = IR + e \tag{5.22}$$

Where V is the supply voltage, I is the stator current, R is the stator conductor resistance and e is the back-emf and can be represented as

$$e = k\phi\omega \tag{5.23}$$

Motor torque in steady state can be expressed as

$$T = k\phi I \tag{5.24}$$

In equations (5.15) and (5.16), $k\phi$ is the back-emf constant and torque constant. If the motor is operating at no load, very small current is drawn from the supply and generally it is neglected for analysis. According to the equation (5.12), if there is no voltage drop in the stator resistance and the motor will accelerate until the back-emf equals to the supply voltage. This occurs at the no load speed which is the highest speed of the motor. Torque speed characteristic of the proposed BLDC motor is shown in the Fig. 5.7. When load torque is applied, current is drawn from the supply, resulting in a voltage drop in the stator conductor resistance. This voltage drop is possible only if the back-emf, falls to the value $(V - IR)$, and according to the equation (5.13), the speed must fall. The drop in e is proportional to the current, and therefore to the torque because motor torque is directly proportional to the current according to the equation (5.22).

The results of torque-speed characteristic curve (Fig. 5.7) and current vs. torque curve (Fig. 5.7) show the relationship between motor speed and the torque is linear and motor speed is directly proportional to the supply voltage in this type of BLDC motor. In addition, torque and current are directly proportional to each other. Based on these results it can be seen clearly that controlling of these two parameters (torque and speed) is straightforward. Motor speed can be controlled just simply by varying the supply voltage where the back-emf is kept constant. On the other hand, motor torque can be controlled by varying both supply voltage and back-emf. This results are used as the application of simple torque and speed cascaded control for BLDC motor drive system in the next chapter.

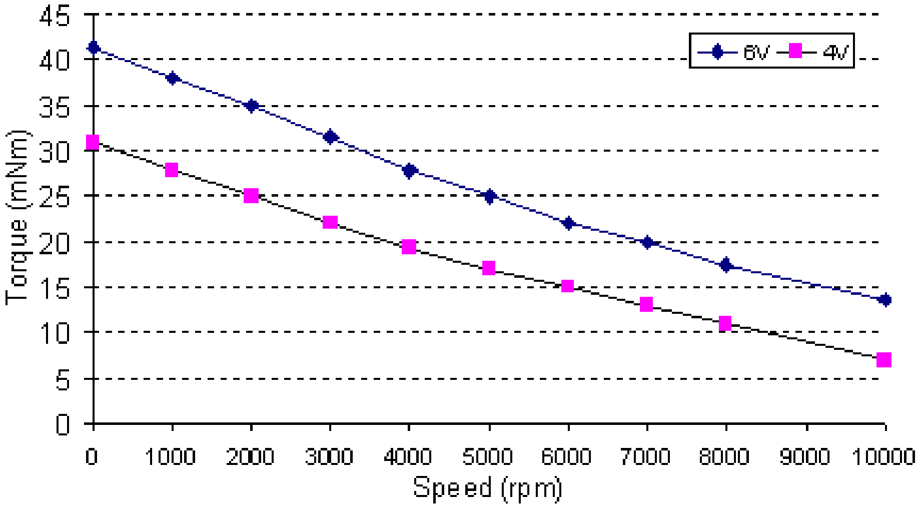

Figure 5.7: Torque-speed curve of the motor

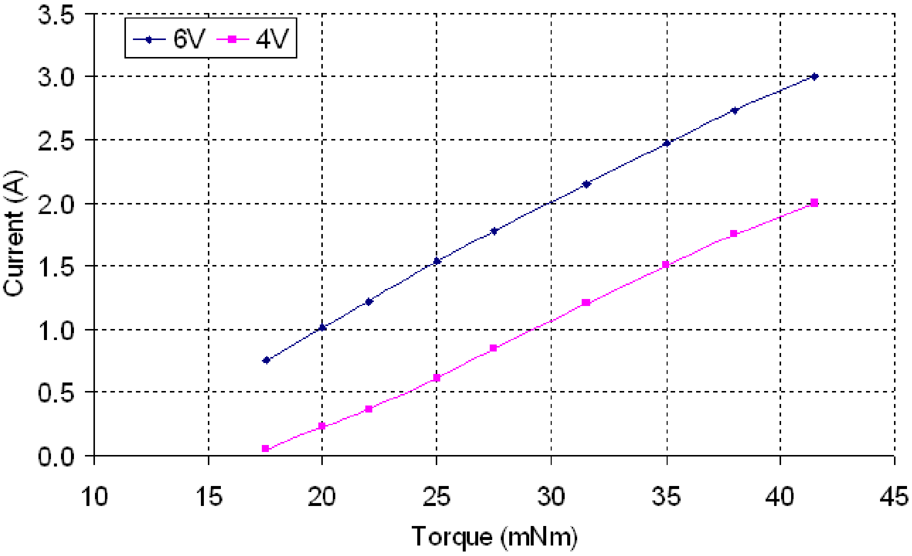

Figure 5.8: Current and torque relationship

5.3.4 Computation of cogging torque

In a slotted permanent magnet motor, cogging torque is one of the key components of torque pulsations. High cogging causes not only variations in motor speed and torque but they are also a source of motor vibration and noises [114]-[116]. It is well known that cogging torque is a magneto-static effect. It is caused by the air-gap permeance variation due to slotting effect; the rotor magnet is attracted to certain positions where the effective permeance is maximum. This torque component is typically independent of stator current excitation. The precise determination of the cogging torque is of great importance for the design of a slotted permanent magnet motor especially for disk drive spindle motor where constant motor torque is highly demanded [117].

Generally, cogging torque is computed according to the magnetic field computations when there are no armature currents and no magnetic field excitation, respectively. However, this method cannot take into account the effect of the saturation of iron.

In this work, a new approach has been used for computation of cogging torque including the effect of iron saturation. The proposed algorithm to compute the cogging torque synchronously with the time stepping solver is: in the time domain solver, after the normal time stepping computation has been done, the reluctivity of the materials are fixed and the currents in stator winding are set to zero. And then, the time stepping computation is simulated again. Cogging torque is computed by Maxwell's stress tensor method and the same function block is used for computing the electromagnetic torque. However, the motor current is zero within cogging torque computation process. Hence, cogging torque obtained by this method has included saturation effect. No other field computation is required. This method can be applied for back-emf and inductance computation.

Fig. 5.9 shows the results of computation of cogging torque profiles with various magnet strengths. It is found that varying the magnet strength with the remanent flux density (7.0T, 6.5T, 6.0T, 5.5T, 5.0T, 4.5T as shown in Fig. 5.9) affects only the peak value of cogging torque. Since there is no change in the physical geometry of the motor, the shape of cogging torque profiles remain unchanged. Although reducing the magnet strength lowers the cogging torque, it can also degrades the performance of the motor at the same time because the electromagnetic torque of a motor is directly proportional to the amount of flux produced by the permanent magnets.

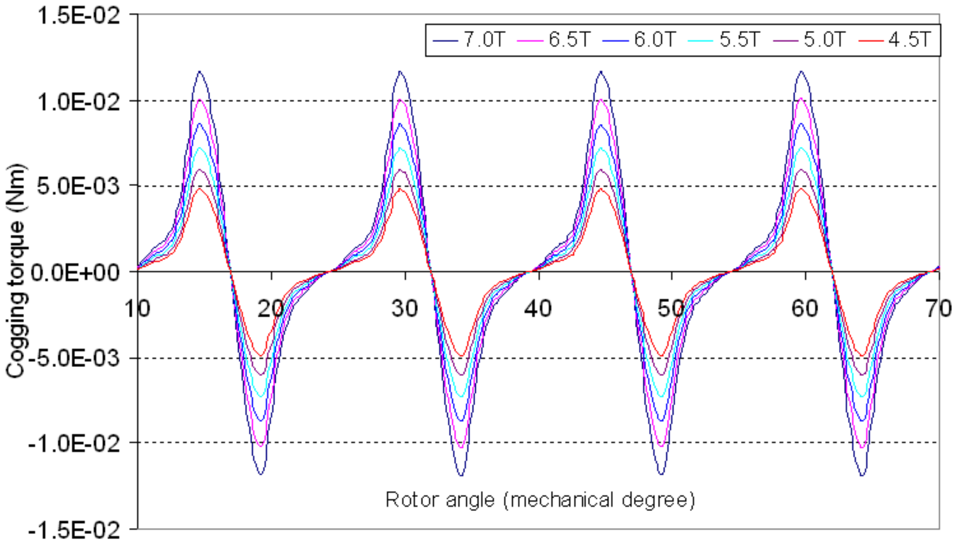

Figure 5.9: Cogging torque profiles for 8p 12s spindle motor with different magnet strengths

5.3.5 Calculation of back-emf

A good estimate of back-emf is required because it is an important indicator of the ability of the motor to produce torque and speed. It also requires for accurate simulation of the motor operating with its controller, and also for the determination of the current waveform for the correct control strategy. In time stepping solver, back-emf is computed while stator current is set to zero at each time step as mentioned in Section 5.3.4. The back-emf as shown in equation (3.30) is given by

$$e = -\frac{lN}{S} \iint\limits_{S} \frac{\partial A}{\partial t} ds. \tag{5.25}$$

And the back-emf equation after time discretization is given by equation (3.92)

$$e = \frac{l}{s} \{Q\} \left(\frac{\{A\}^{t+\Delta t} - \{A\}^{t}}{\Delta t} \right)_{\Omega+} - \frac{l}{s} \{Q\} \left(\frac{\{A\}^{t+\Delta t} - \{A\}^{t}}{\Delta t} \right)_{\Omega-} . \tag{5.26}$$

According to the equation (5.26), back-emf can be calculated after the magnetic vector potential values at each time step have been determined in each nodes of the elements. Fig. 5.10 shows the computed back-emf values where input voltage is 4V and motor speed is 7200 rpm. It can be seen that there is not much difference between the magnitude of input voltage and motor back-emf when the motor is in its steady state condition. This is one of the spindle motor characteristics, it requires very small current at normal running conditions. The voltage drop across the motor resistance is very small and the supply voltage is nearly the same as its induced voltage of stator winding when the motor is running in steady state condition.

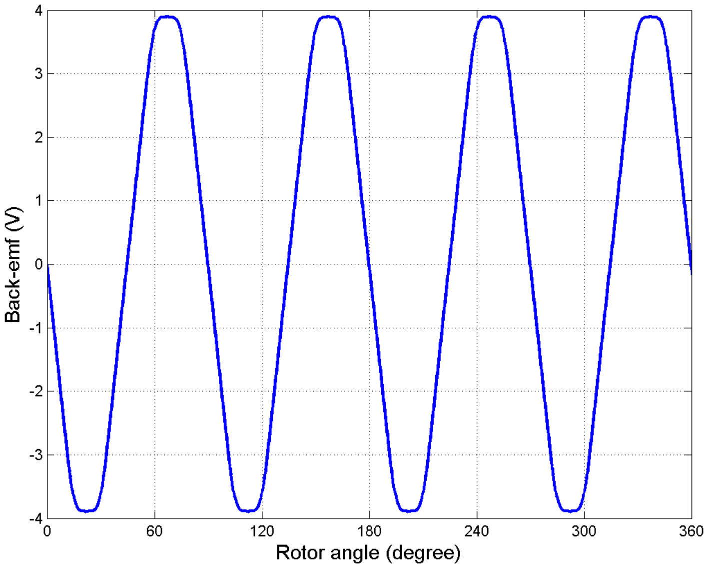

Figure 5.10: Calculated back-emf with corresponding rotor angle

5.4 Performance Evaluation with and without the Time Steps Adjustment Scheme

In the time stepping FEM, the system equations are solved at specific time t_1, t_2... etc. step by step. The computation precision is directly dependent on the step size δT. If the step size is too small, a lot of computing time is required. In turn, if the the step is too large, the error will be unacceptable. Hence, the step size should be adjusted to compromise between CPU time and acceptable errors. Adjusting the time step based on local truncation error is adapted in this work. Detail procedures have been described in Section 3.10. Fig. 5.11 shows the comparison of simulated cogging torque waveforms with and without using the time adjustment scheme. In the computation of Fig. 5.11(a), the minimum step size is 0.006 ms and the average step size is 0.0125 ms. If all other conditions are the same and the step size is fixed at 0.0125 ms, the computed cogging torque waveform is as shown in Fig. 5.11(b). The same condition is tested to calculate the electromagnetic torques on load condition of the motor and simulated results are shown in Fig. 5.12. It is observed that if the number of time step sizes in the integration time is the same, the error caused by the fixed step size method is significantly greater.

5.5 Transient Analysis of the BLDC Motor

Transient behaviours of the BLDC motor are simulated by using the the time stepping FEM model. Using the proposed transient time stepping FEM solver, motor dynamics in step voltage variation, changing of the mechanical load torque and locked rotor conditions are analyzed. Experimental results at transient conditions are described and compared with simulation results for validation of the proposed model.

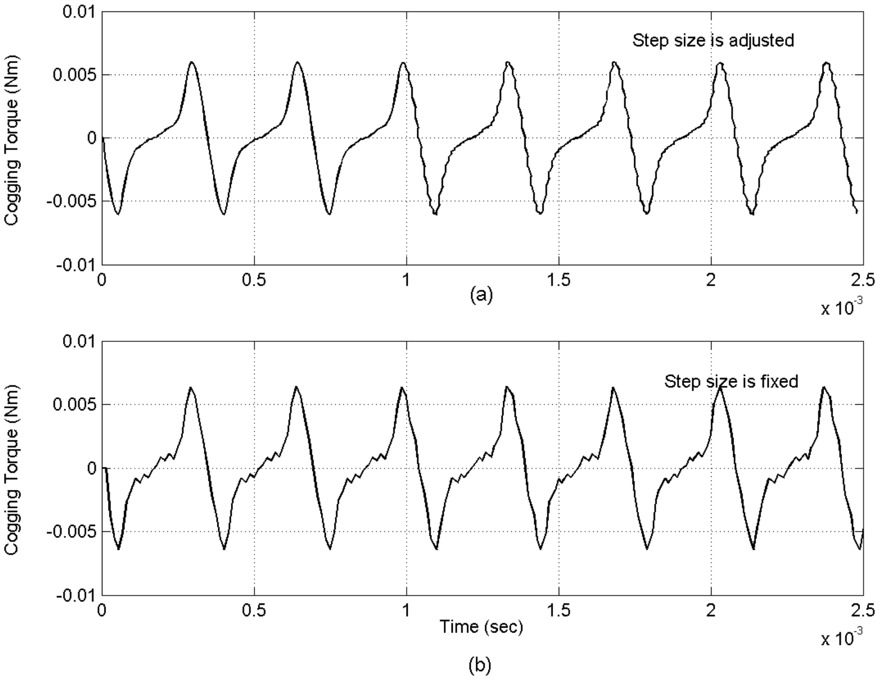

Figure 5.11: Simulated cogging torque with and without step size adjustment scheme

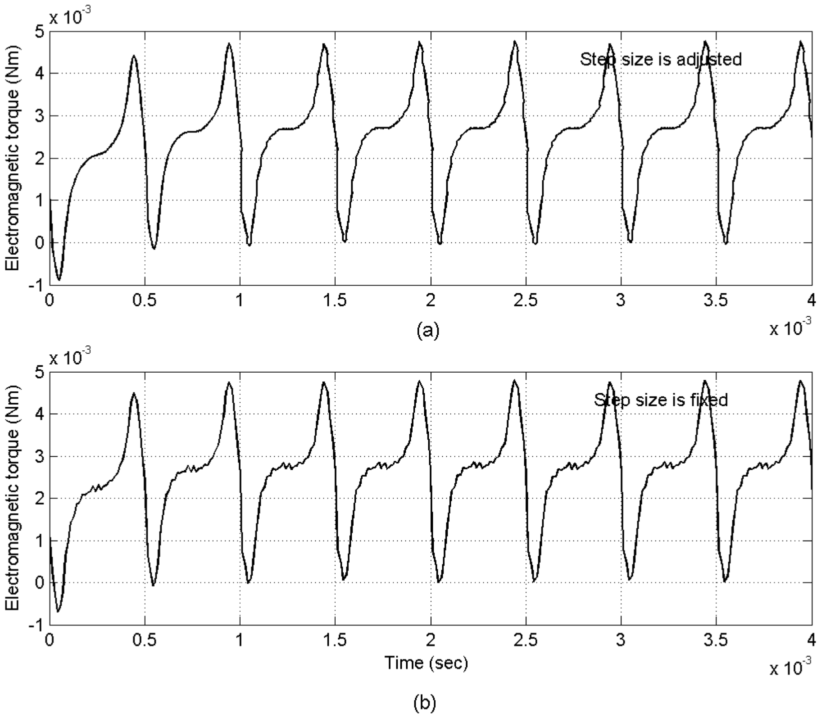

Figure 5.12: Simulated load torque with and without step size adjustment scheme

5.5.1 Step voltage variation

Step voltage variation could arise when the motor speed is controlled through supply voltage. Fig. 5.13 - Fig. 5.17 show the current, torque and speed transients when the motor is loaded and an excessive drop in the applied voltage occurs; a drop from 4.5 V to 2.5 V at 5 ms is being assumed.

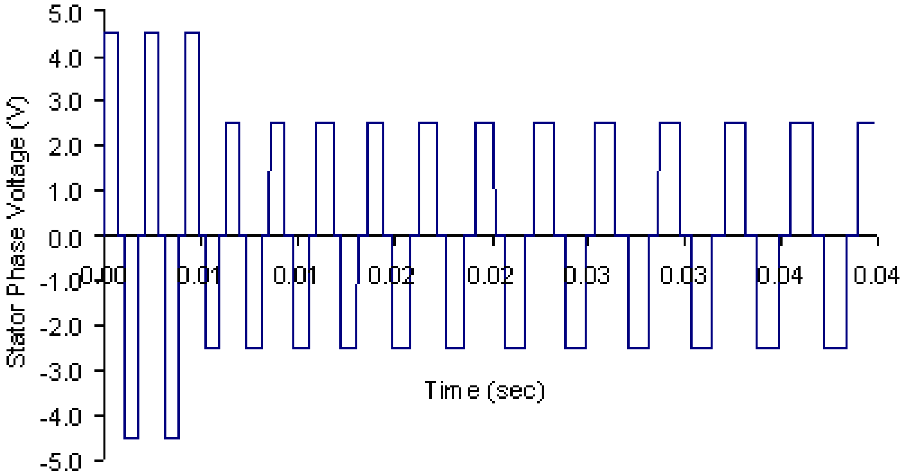

Figure 5.13: Step voltage change

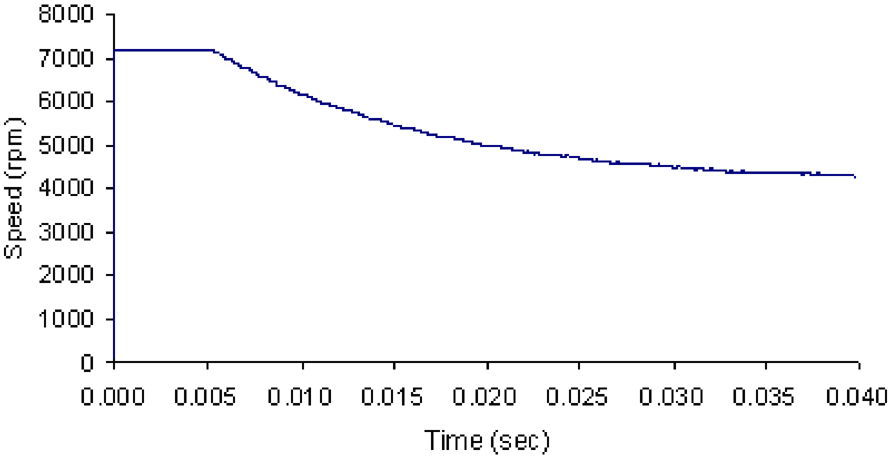

Figure 5.14: Speed response during step voltage change

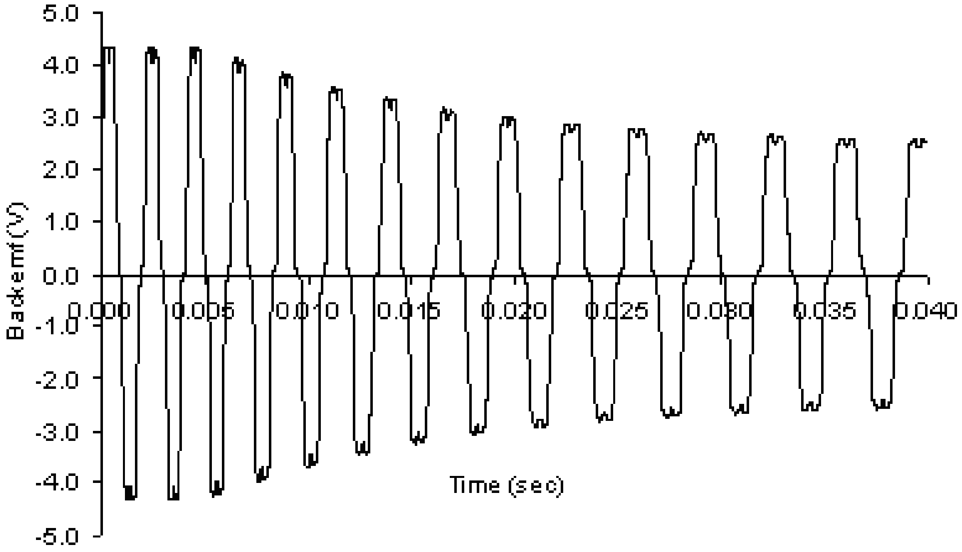

Figure 5.15: Simulated back-emf during step voltage change

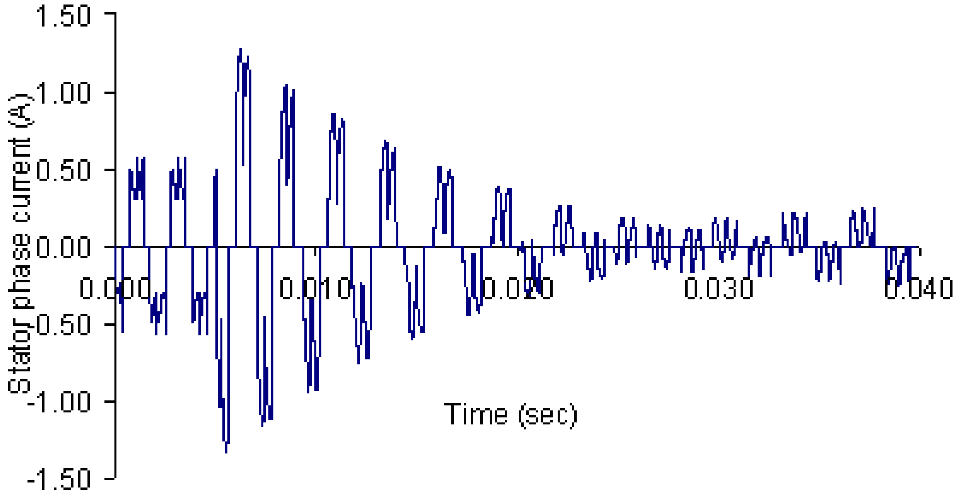

Figure 5.16: Stator current transient during step voltage change

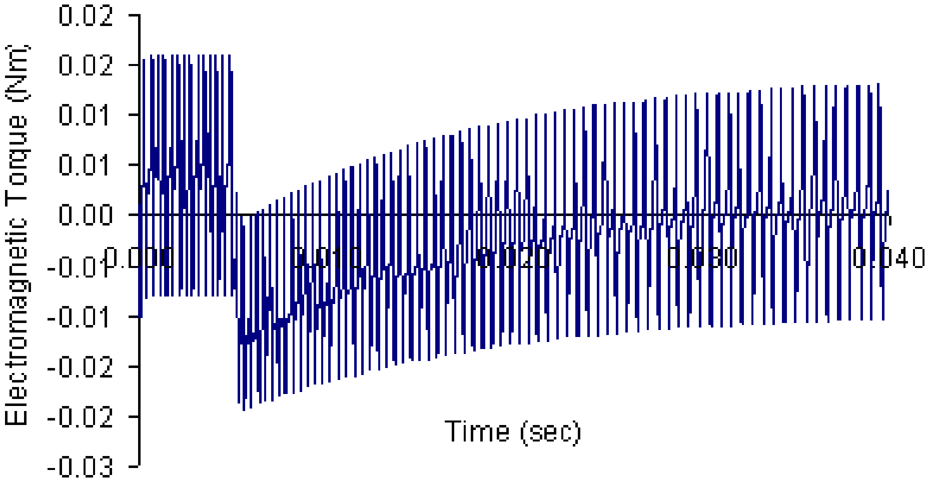

Figure 5.17: Developed torque during step voltage change

From Fig. 5.16, it can be seen that the stator current goes up from 0.5 A to 1.45 A in reverse direction at this instant and then it slowly goes down to zero. It takes 30 ms to reach to zero value. After that it goes up again from 30 ms onwards. The motor speed also drops exponentially from the rated speed, 7200 rpm to 5800 rpm within 35 ms.

Possible reason for this phenomenon is that although the supply voltage drops suddenly, the generated back-emf could not be adjusted simultaneously at this instant (Fig. 5.15) because of the magnetic saturation as well as the rotor inertia, so that according to the stator circuit equation (5.14), the stator current will be increased from 0.5A to 1.45 A in magnitude. However, the supply voltage is lower than the back-emf at this instant and therefore the motor current will be negative flowing in the reverse direction. A few seconds later, the generated back-emf is decreased corresponding with the speed reduction and at 25 ms the back-emf is equal to the supply voltage where the current will be zero. When the back-emf is lower than the supply voltage, the current will be increased to positive direction again. This can be seen clearly within the time period between 30 ms to 40 ms in Fig. 5.15. The result in Fig. 5.14 shows that the motor speed drops exponentially, because of the effects of the rotor inertia and stator winding inductance, which causes distortion at low speed, and the magnetic saturation coupled with the demagnetizing effect of the phase currents at low torque.

When the motor current flows in reverse direction, the motor will be generated negative torque as shown in Fig. 5.17). It can be seen clearly that when the motor current suddenly increased up to 1.45A in reverse direction, the motor torque also decreased to negative value simultaneously at this instant. It is likely due to the linear relationship between the motor torque and speed in BLDC motor. In addition, the reversal of the torque eventually decelerates the motor to a speed which is needed to match the new level of the supply voltage. The case shown is for the motor driving a load requiring constant torque. This is why the current eventually recovers its original value before the change in the supply voltage occurs.

It needs to be mentioned here that, any drop in voltage results in a negative current. The drop has to be such magnitude that the new voltage level is lower than the generated back-emf. The transient responses where the supply voltage is dropped from 4.5 V to 3.5 V are shown in Fig. 5.18. The time instant when the motor voltage drop from 4.5V to 3.5V, motor back-emf is lower than the supply voltage as shown in Fig. 5.19, therefore, the motor current drops exponentially from 1.5 A to 0.5A within 40 ms as in Fig. 5.19 and motor speed also drops from rated value 7200 rpm to 5000 rpm again in exponential form. Experimental results for this transient condition are shown in Fig. 5.20. It can be seen that experimental results are a little difference with the simulating results. Possible reason is that for the drive system in practical condition, it is difficult to send back the current from the motor to inverter circuit. Therefore, in adjusting the speed drop from high speed to low speed, the motor is difficult to work in generator state. In the FEM simulation, it is assumed that the motor drive operates in ideal condition therefore speed drops exponentially corresponding with back-emf as shown in Fig. 5.19.

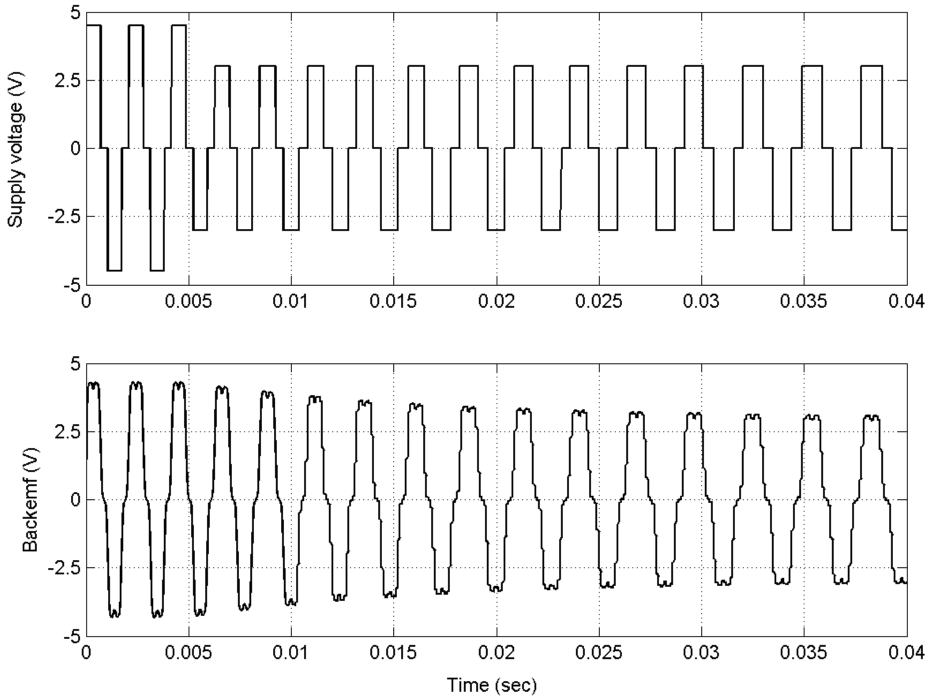

Figure 5.18: Input simulated step voltage waveform and output back-emf waveform

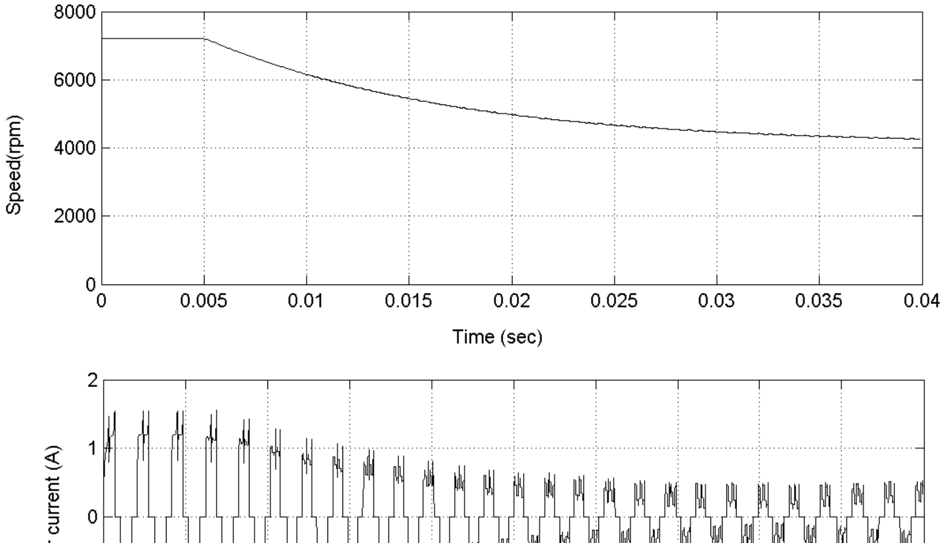

Figure 5.19: Calculated transient speed and stator current waveform

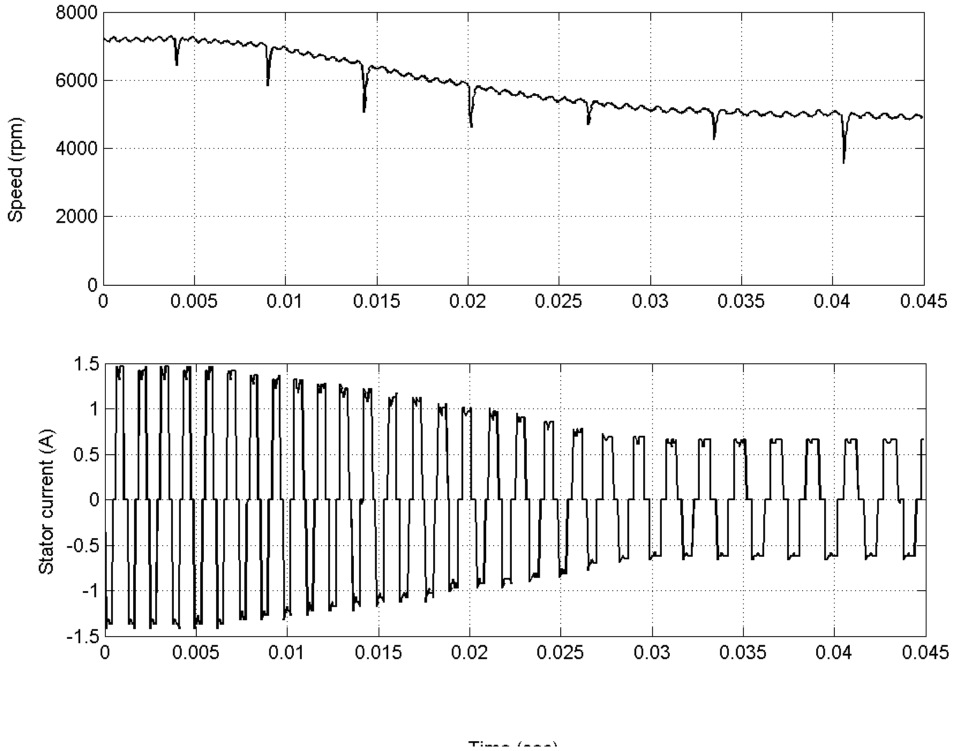

Figure 5.20: Measured transient speed and stator current waveform

5.5.2 Step change variation in mechanical load torque

The transient response for this condition was verified for a step increase of the mechanical load torque from 0.002Nm to 0.01 Nm when the stator phase voltage is 4.5 V and the rated speed is 7200 rpm. The simulation results are shown in Fig. 5.21and Fig. 5.22. Speed versus time graph shows that the motor speed decreases from rated speed of 7200 rpm to 6000 rpm within 30ms. Stator current and electromagnetic torque increase two times of the rated conditions respectively. The results show that the dynamic behaviour of the motor adjusts its operating conditions to the change of the load by decreasing the rotor speed and increasing the motor torque to counter-balance the load torque. It is known that the torque is directly proportional to the stator current if the motor is operated with constant magnetic field. Hence the stator current increases up to 2.5A in this transient condition.

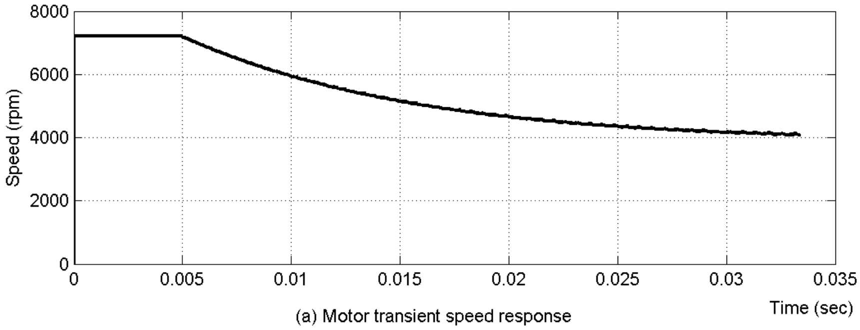

(a) Motor transient speed response

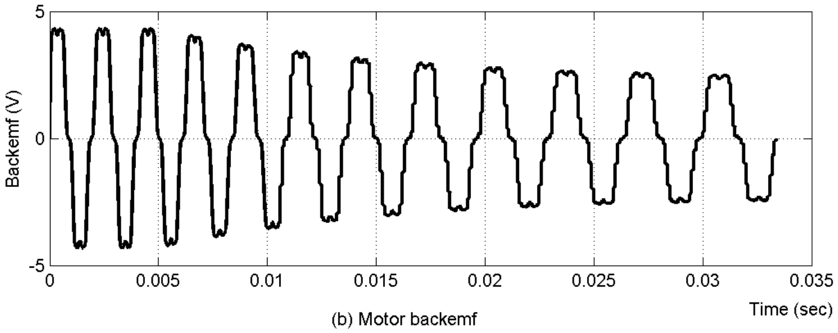

(b) Motor backemf

Figure 5.21: Speed and back-emf transients due to an increase in load torque

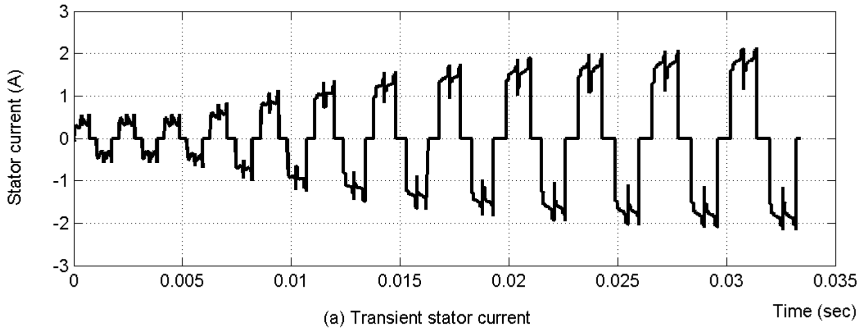

(a) Transient stator current

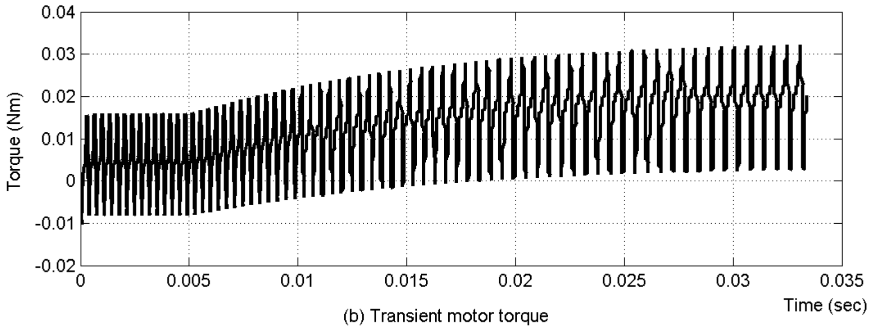

(b) Transient motor torque

Figure 5.22: Current and torque transient due to an increase in load torque

5.5.3 Locked rotor condition

When a load torque is applied, current is drawn from the supply, resulting a voltage drop in the motor resistance. This voltage drop is possible only if the back-emf falls to the value equal to the difference between the supply voltage and the voltage drop in the motor resistance, and hence the speed falls. If a sufficient load torque is applied, the speed falls to zero and the motor is then stalled [103]. Then back-emf is zero and the supply voltage is drop across the motor resistance. Since the motor resistance is very small, the resulting stall current is extremely large. It is not normally permissible to allow the full locked rotor current to flow, even for a short time, because it would either demagnetize the magnets or destroy the power transistors or burn the winding insulation. Therefore, locked rotor current is one of the important parameters for motor designers and operators.

In this work, motor stall condition is simulated by using the transient time stepping model. The motor is loaded from 0.002 Nm to 0.05 Nm suddenly at 2.48 ms where the supply voltage is 4.5 V and the rated speed is 7200rpm. Fig. 5.23 and Fig. 5.24 show the transient response of the motor at stall conditions. It can be seen that motor speed falls sharply from its rated speed to zero speed within a very short time interval in about 16.30 ms. The current goes up to 4.1 A, nearly 27 times of the rated current. Attention needs to be drawn to the rapid response of current to the change in the voltage in this type of motors. This is due to the very low value of the inductance of the winding.

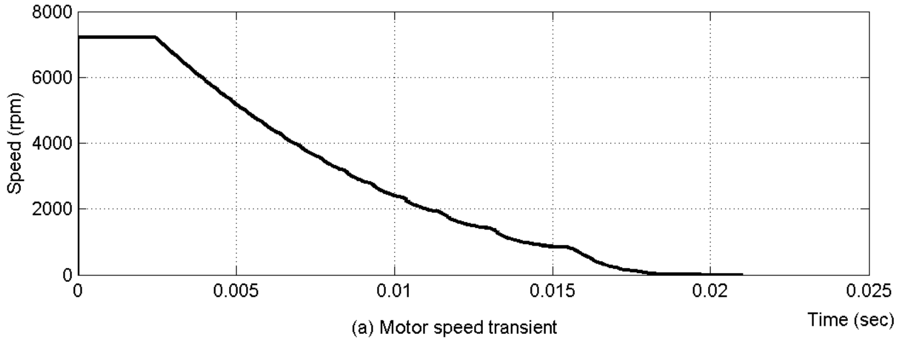

(a) Motor speed transient

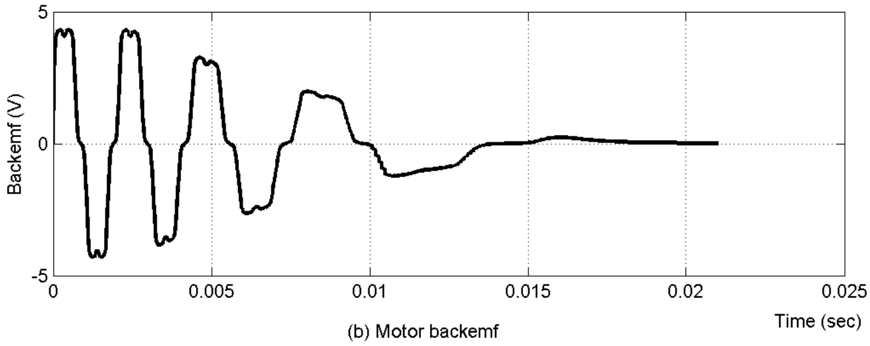

(b) Motor backemf

Figure 5.23: Speed and back-emf transient at locked rotor conditions

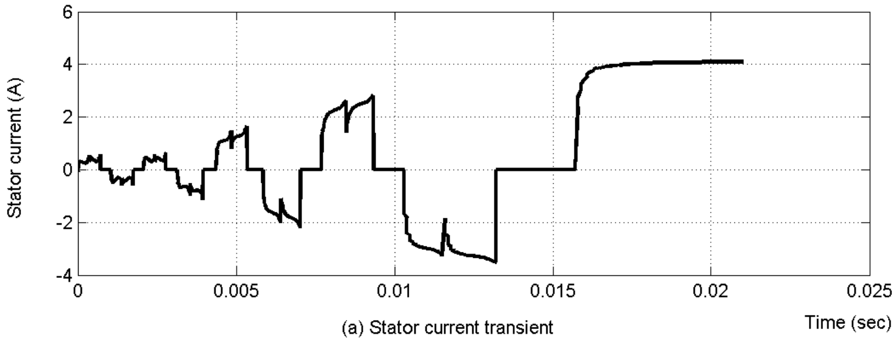

(a) Stator current transient

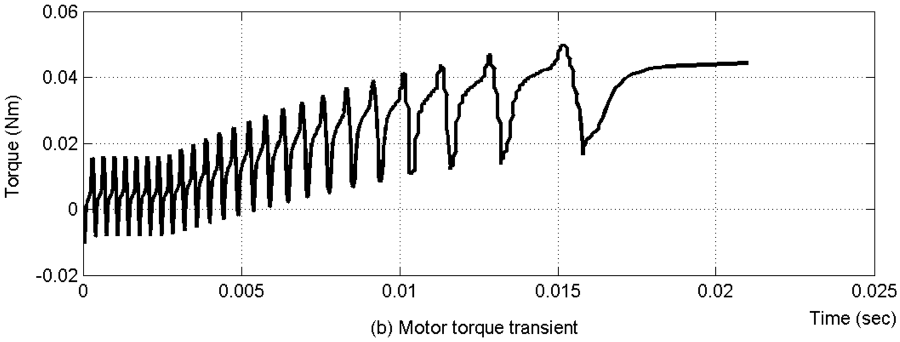

(b) Motor torque transient

Figure 5.24: Current and torque transient at locked rotor conditions

5.6 Conclusion

This chapter attempted to analyze the steady state and dynamic performances of the BLDC motor using the current fed 2D magneto-static FEM model and time stepping FEM model. In steady state analysis, a new approach to overcome the extensive computation time to reach the steady state was implemented. In this approach, magneto-static FEM model was developed prior to the time domain model and the solutions (magnetic vector potential A) obtaining from magneto-static FEM were used for the initial conditions for the time domain analysis. Results showed that the computation time is greatly reduced to reach to a steady state and the time domain solver can also be started with the initial conditions quite close to the steady state solution. Moreover, the proposed model had been successfully simulated the steady state performance of the motor such as the computation of the stator current, electromagnetic torque, back-emf, determination of the torque-speed characteristic, and computation of cogging torque. To validate the proposed steady state model, experimental results for the steady state conditions were presented and compared with computation results. It was shown that these two sets of results agreed closely.

Dynamic conditions of step voltage variation, change of load torque and locked rotor condition were also investigated. Experiments for these dynamic conditions were carried out and compared with computational results. Results showed that the time stepping FEM model can be used to investigate the static and transient responses of the motor under various time steps.

Chapter 6

Application Characteristics of BLDC Motors for Hard Disk Drives

6.1 Introduction

The need for large storage capacity and increased data access performance of modern hard disk drive technology over the passed decade has meant the continuous development of small spindle motors. The spindle motor is one of the important elements in a computer hard disk drive (HDD) system and in many ways determines the drive capacity and performance through its configuration, operating speed, mechanical and electrical performances like run-out, resonance, starting torque, run-current etc [118]-[120].

The spindle motor rotates the disk and media while recording heads are stationary and positioned by an actuator. An accurate assessment of requirement of starting torque in a spindle motor is vital [121]-[123]. The starting torque can be 20 times as high as the the running torque while the starting current is severely limited by the computer power supply and other electronics limitations. In addition, the starting time, otherwise called spin-up time (the amount of time that is required for the disk platters to get up to full operational speed from a stationary start) is largely determined by the drive specifications and has to be very fast.

Therefore, the starting torque, the starting current and the starting time are the important quality indexes for the HDD spindle motor. An accurate evaluation of these quantities is always very challenging.

In addition, some of the requirements of the motor run-up performances are conflicting and difficult to meet. For example, spin-up time is the important parameters of the HDDs using power management scheme. Power management is a set of protocols used to allow HDDs to reduce the amount of power consumption especially when they lie idle. Spindle motor is allowed to spin down after a couple of minutes of idle time and then spin up to operational speed whenever one uses the disk again. Users increasingly want hard disk that will spin up from a stationary position to operating speed quickly, which also requires faster spin-up time. However, to achieve faster spin up time generally required higher the supply voltage which can result in higher starting current demand and higher running current at normal running condition. The consequences are increased in power consumption in both starting and running. Power consumption is an area of concern for PCs especially for the system of multiple storage drives and certainly for laptop users. Modern PCs use very limited power packs such as the PC/XT, AT, Baby AT and LPX form factors power supplies for PCs can provide maximum 12A for 12V output voltage level whereas the ATX/NLX, SFX AND WTX form factors can provide only 8A for 12V voltage level. Generally, 25% is taken by the actuator assembly and the rest 75% of the 12V power can be taken by the spindle motor. Therefore, the starting current and the supply voltage are limited in practical case. It is needed to calculate accurately the motor run-up performances in the design stages.

An attempt is made in this work to study the starting process of a HDD spindle motor and analyze the run-up characteristics of the spindle motor with different drive constraints such as limited starting current and supply voltage, lower power consumption for both starting and running states by computational means. Time stepping FEM coupled with closed loop feed back controller is used.

6.2 Coupling with the Control Loop

Spindle motors are outer rotor type brushless permanent magnet DC motors and require electronic controllers. The phase windings of the motor are energized in sequence by switching elements in the inverter. In order to simulate precisely the performances of the motor, characteristic of the inverter circuit and its control loop feature is needed to include as a coupled system. Moreover, in the hard disk drive system, fast and accurate control of disk spinning speed is vital for error free read and write operations. This requires a sophisticated controller for the purpose of rapid response. In this model, a simple and cascaded speed and current control structure, based on the current hysteresis PWM switching strategy, is proposed to couple the time stepping FEM model. Detailed control system block diagram is shown in Fig. 6.1.

In the control loop simulation, the required feedback signals, rotor speed and stator current are determined from the time stepping FEM model. In the outer speed loop simulation, the reference speed is 7200 rpm where actual motor speed is calculated from the time stepping FEM model. In the inner current loop, reference current for the current hysteresis loop is determined from the PI controller of the speed loop. The feedback current signal is determined from the time stepping FEM model. The output of the current hysteresis loop is the firing signal for the inverter circuit and again these are the input voltage for the time stepping FEM model. Detailed modeling technique for the current hysteresis control is as follows. The reference current is determined by the PI controller of the speed loop;

$$I_s^* = \begin{cases} K_p\left(\omega^* - \omega\right) + I_k^* & -I_m \leqslant I_s^* \leqslant I_m \\ I_m & I_s^* > I_m \\ -I_m & I_s^* > -I_m \end{cases} \tag{6.1}$$

where

$$I_k^* = \begin{cases} I_{k(0)}^* = 0 \\ I_k^* = I_{k-1}^* + \dfrac{\omega^* - \omega}{T_s}\Delta T \end{cases} \tag{6.2}$$

Therefore, the reference current is

$$i_s^* = I_s^* i^* \tag{6.3}$$

In equation (6.1), (6.2) and (6.3), ω^* is the reference speed, ω is the speed feedback from the time stepping FEM model, K_p is the proportionality factor, T_s is the integral factor; ΔT is the time step size; I_m is the maximum allowable value of stator current and i^* is the expected current waveform with unity value of 0 and 1. Finally, the stator voltage is controlled by the following current loop when $i_s^* \neq 0$;

$$V_{s(k)} = \begin{cases} +V_s & i_s < i_s^* - \Delta i \\ -V_s & i_s < i_s^* + \Delta i \\ V_{s(k-1)} & i_s^* - \Delta i \leqslant i_s \leqslant i_s^* + \Delta i \end{cases} \tag{6.4}$$

By coupling the closed loop speed and current control with the time stepping FEM, the stator windings could be fed with the actual output voltage from the inverter to FEM model. As mentioned before, in the time stepping FEM, the magnetic field equations, the stator circuit equations and the motion equation are all solved simultaneously according to the time step. The effects of high order harmonic, the non-sinusoidal quantities, the eddy current, the saturation and the rotor rotation can be directly included into the whole modeling system. This model is not so difficult for implementation, and accurate to a great extent. Starting characteristics of the BLDC motor using the developed cascaded control loop structure with time stepping FEM model are analyzed in the next sections.

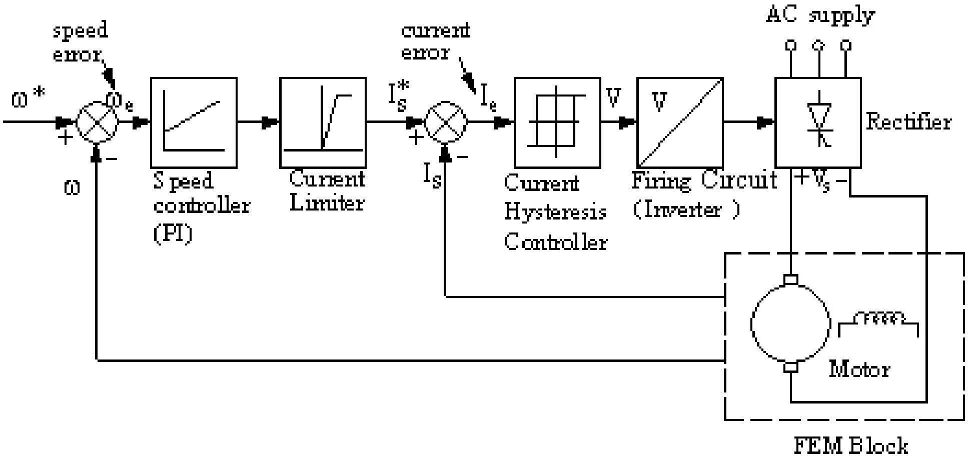

Figure 6.1: Control system block diagram

6.3 Analysis of the Starting Process of a HDD Spindle Motor

Starting characteristics of a HDD spindle motor are analyzed under the following different conditions.

1. Starting without drive limits
2. Starting with current limits and
3. Starting with speed limits

6.3.1 Motor starting without drive limits

The starting processes of the motor without drive limits are analyzed using the time stepping FEM model. This is an open loop simulation. Closed loop control structure is not included in this process. Both no-load and loaded conditions are considered.

No-load condition: Firstly, it is assumed that the motor runs freely without any platters and spacer rings. Fig. 6.2 shows the input voltage waveform for the FEM block. The calculated starting characteristics of speed, back-emf, current and torque with motor starting time are shown in Fig. 6.3 - Fig. 6.6.

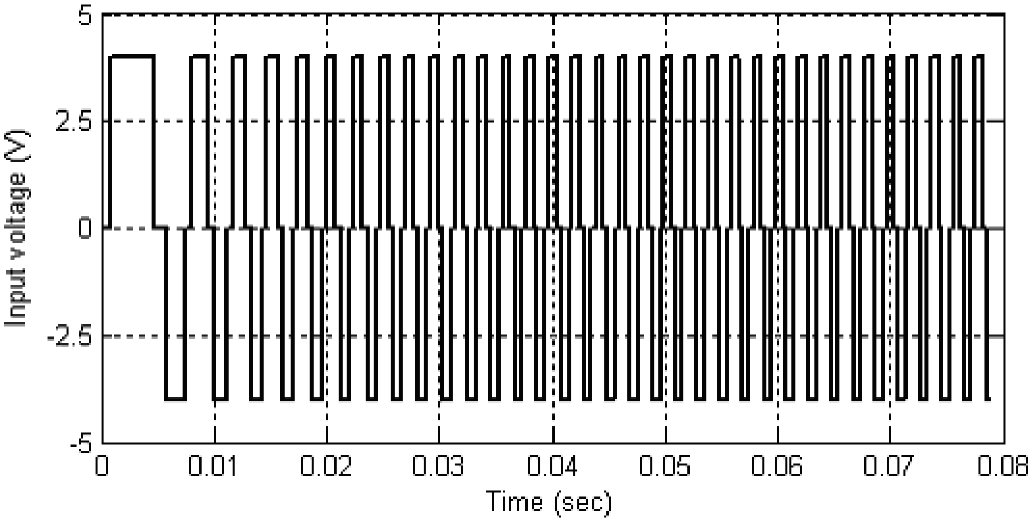

Figure 6.2: Input voltage waveform against time

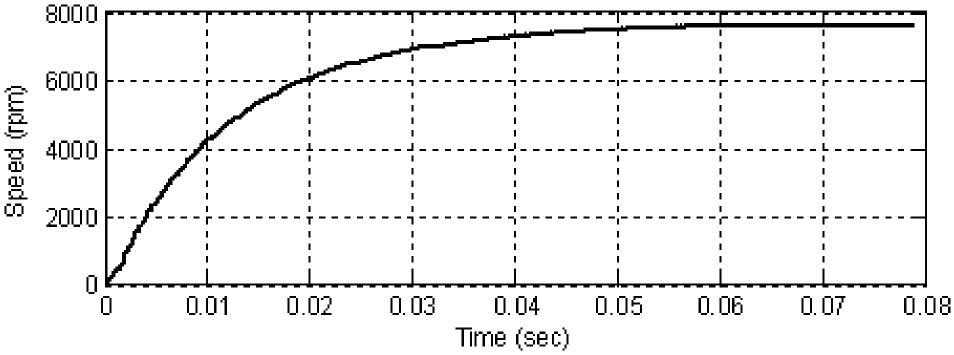

Figure 6.3: Motor starting speed without limits

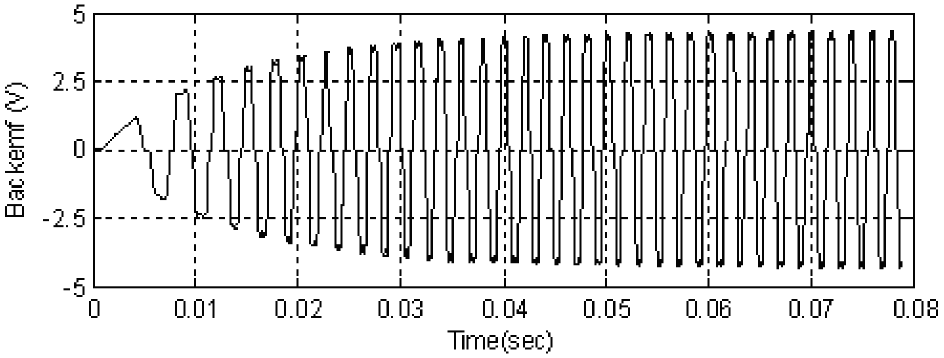

Figure 6.4: Back-emf waveform without limits

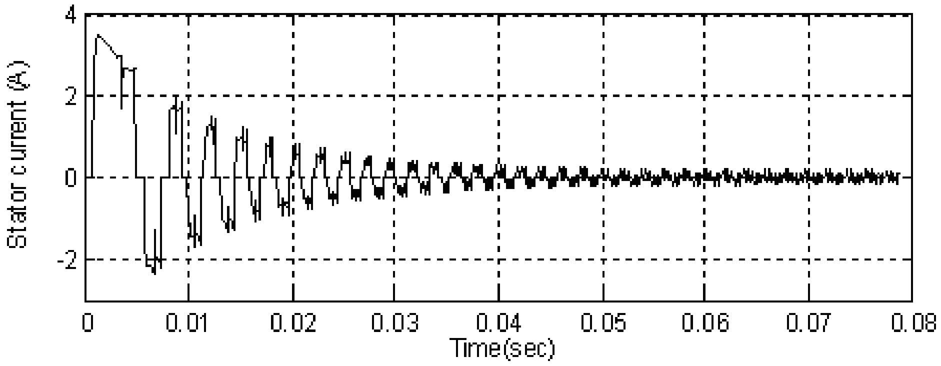

Figure 6.5: Starting current without limits

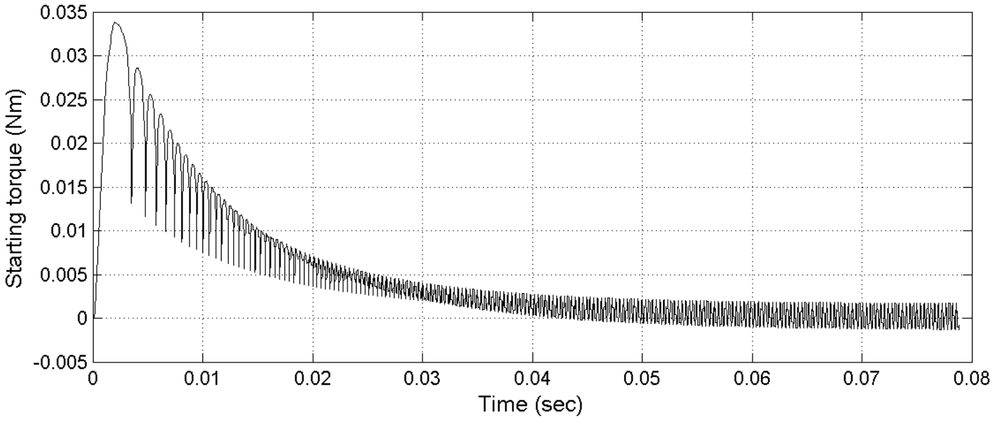

Figure 6.6: Starting torque without limits

From speed vs. time graph (Fig. 6.3), the motor takes 40 ms to reach the rated speed of 7200 rpm and the motor speed keeps on increasing. There is no voltage limit in this simulation process so that the motor is operated over-speed region. The back-emf also keeps on increasing since it is directly proportional to the motor speed. In the over-speed region, the back-emf is a little higher than the motor supply voltage as shown in Fig. 6.4. In a practical case, the supply voltage has to be regulated using voltage control mechanism in this over-speed condition.

Fig.6.5 shows the starting stator current profile of the motor without any limit. The stator current goes up to 3.5A at starting which is more than nearly 10 times larger than the rated value, but the current goes down to its normal running current, 0.36 A, within 40ms. The stator current keeps on decreasing nearly to zero within the next 40 ms. The results show that when the motor speed increases, the motor current also decreases proportionately. In addition, motor torque is also very high at starting as shown in Fig 6.6. However, when the motor speed goes up, torque decreases proportionately.

When motor reaches to a steady state condition, the developed torque is very small as shown in Fig.6.6. A very small torque is required in normal running condition in this type of drives. At starting, the motor speed goes up, the back-emf also increases and the voltage overhead (the difference between the supply voltage and the back-emf) decreases proportionally so that the motor current decreases. When the motor speed reaches to the rated value of 7200 rpm in 40 ms, the motor current also hits its rated value, 0.36A, and the motor torque is also at its rated value, 0.01Nm. The controller needs to maintain this rated condition in order to keep machine stability and reliability. Voltage control is needed to regulate the motor speed and current control is required to stabilize the motor current. However, in this simulation, the motor is running without voltage and current limiters so that the motor spins up to 7600 rpm whereas the stator current and developed torque becomes nearly zero.

Loaded with one platter: The next step is to study the motor starting characteristic under loaded conditions. The motor is loaded with a 3.5 inch platter and a spacer ring as shown in Fig. 6.7. Loaded condition means the inertia of platter and spacer ring are added to the mechanical equation in the FEM simulation. The supply voltage is 4V. Fig. 6.8, Fig. 6.9, Fig. 6.10 and Fig. 6.11 show the simulation results.

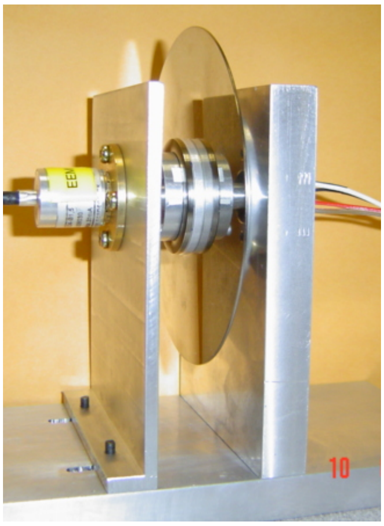

Figure 6.7: Motor loaded with one platter

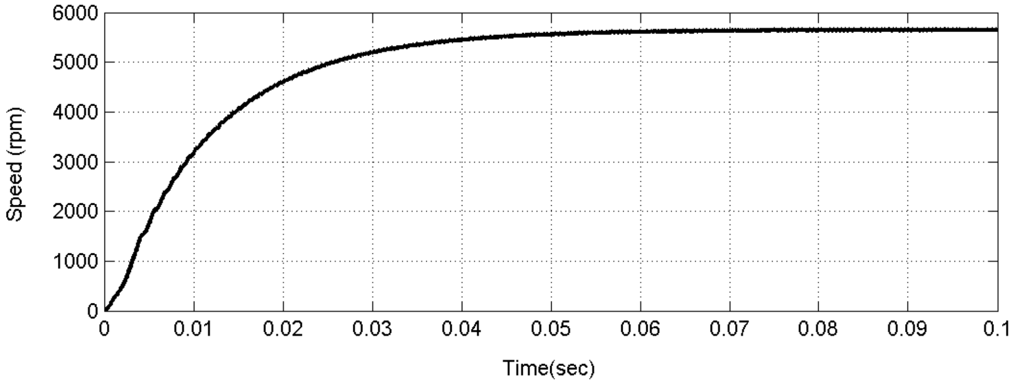

Figure 6.8: Speed against time waveform when motor is loaded with one platter

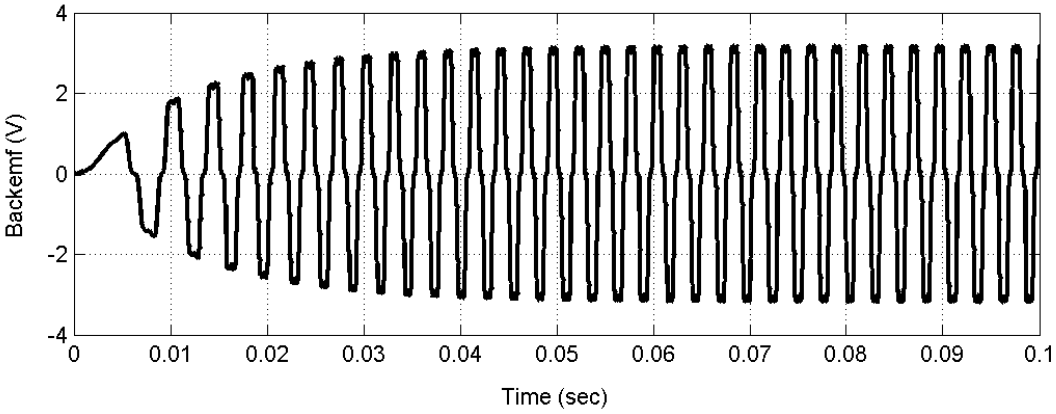

Figure 6.9: Back-emf waveform when motor is loaded with one platter

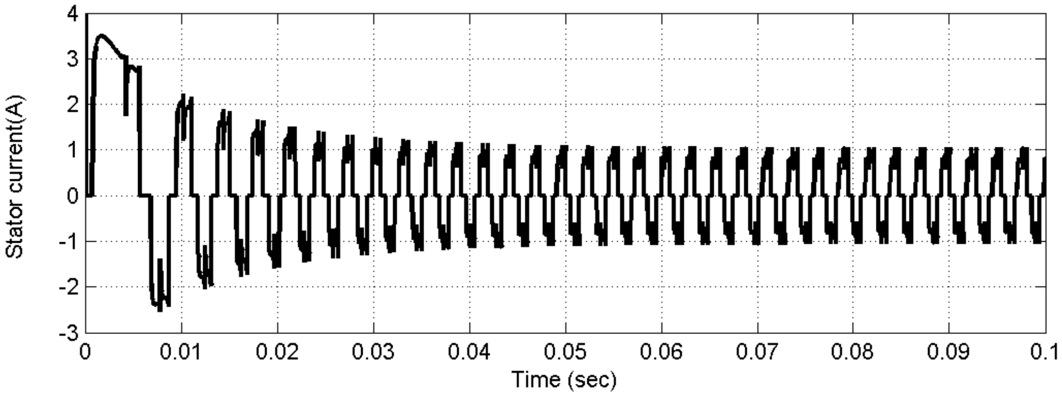

Figure 6.10: Stator current waveform when motor is loaded with one platter

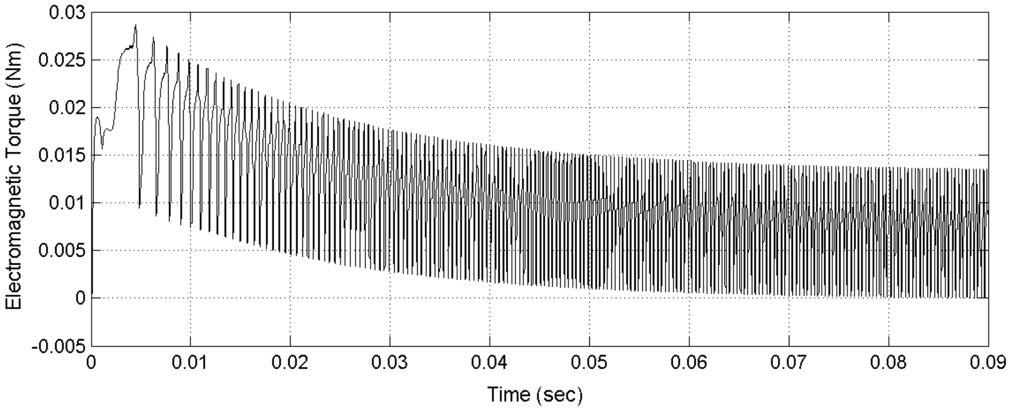

Figure 6.11: Torque against time graph where motor is loaded with one platter

Loaded with two platters: For a second experiment, the spindle motor is loaded with two platters and a spacer ring as shown in Fig. 6.12. The simulation results are shown in Figs. 6.13, 6.14, 6.15 and 6.16. The speed against spin up time for loaded and no-load conditions from the simulation results are shown in Fig. 6.17. Results from measurement are presented in Fig. 6.18. It is found that as the number of spindle platters increases, the motor speeds are decreased accordingly. This generally means that the spin-up speed and power consumption of a drive with four platters is much higher than those figures for the same drive with one or two platters. In practice, the number and the size of the platters vary in different hard disk drive designs and have an important impact on performance in several ways. The trend is towards smaller platter sizes.

Based on these results, we can conclude that precise computation of the starting process of the BLDC motor is one of the important issues for studying the motor performance and control implementation. Moreover, fast and accurate control for spinning speed is vital for error free operation in BLDC motor. Evaluation of motor starting performance using the developed model including speed and current controls are presented in the next section.

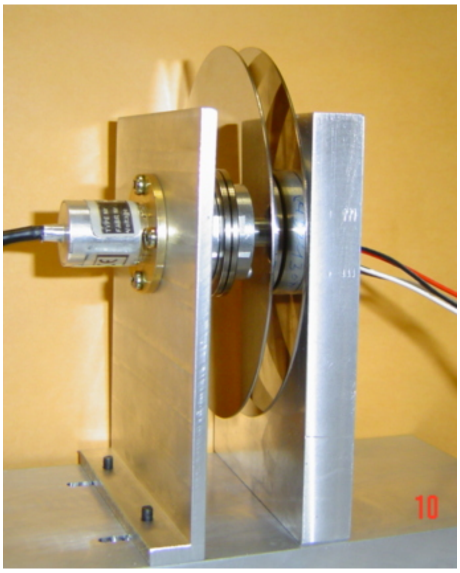

Figure 6.12: Motor loaded with two platters

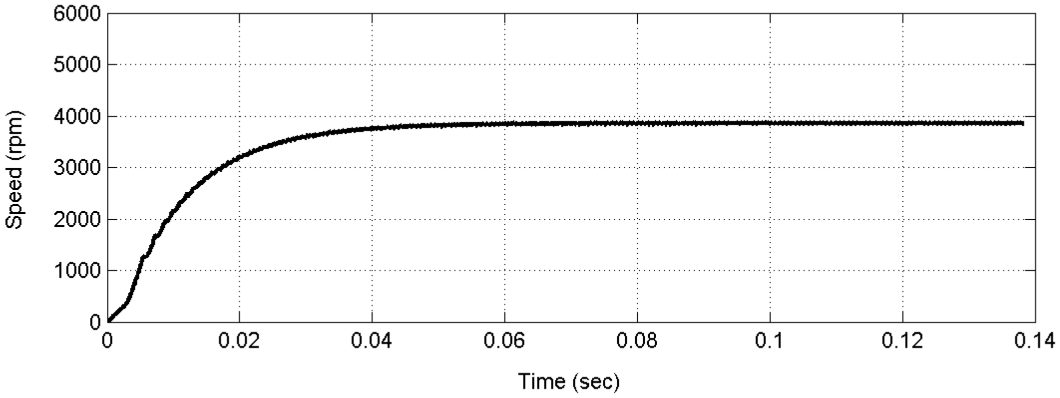

Figure 6.13: Speed against time waveform when motor is loaded with two platters

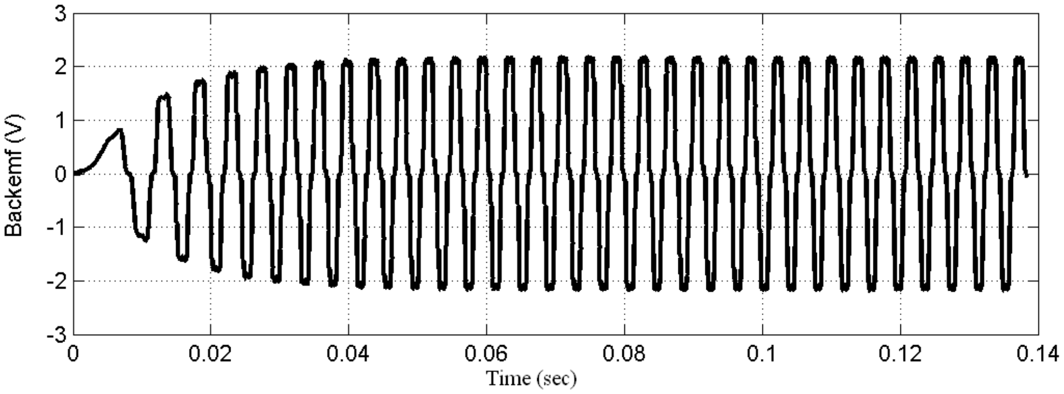

Figure 6.14: Back-emf waveform when motor is loaded with two platters

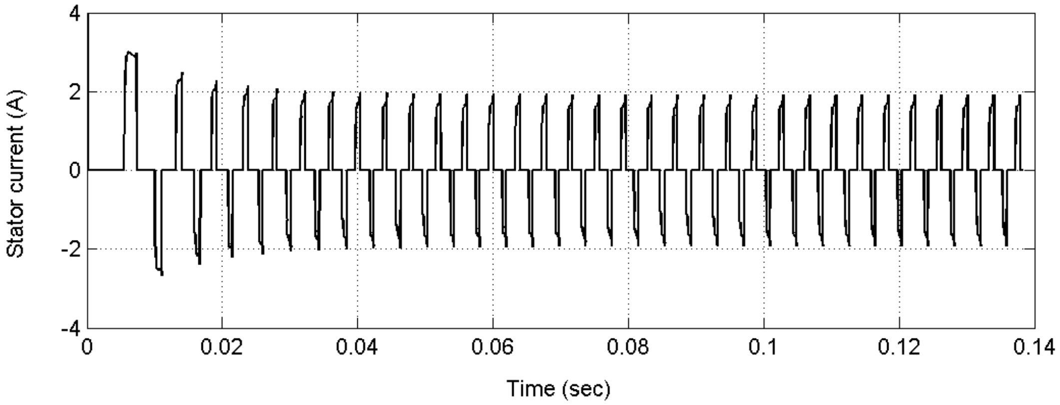

Figure 6.15: Stator current waveform when motor is loaded with two platters

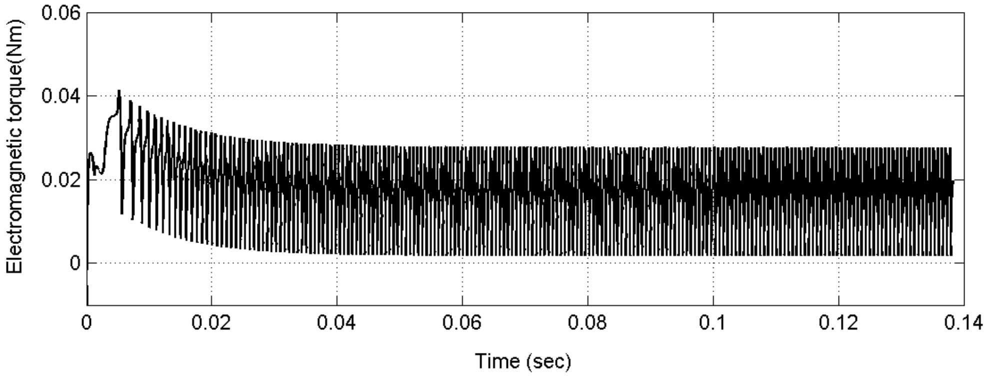

Figure 6.16: Torque against time graph where motor is loaded with two platters

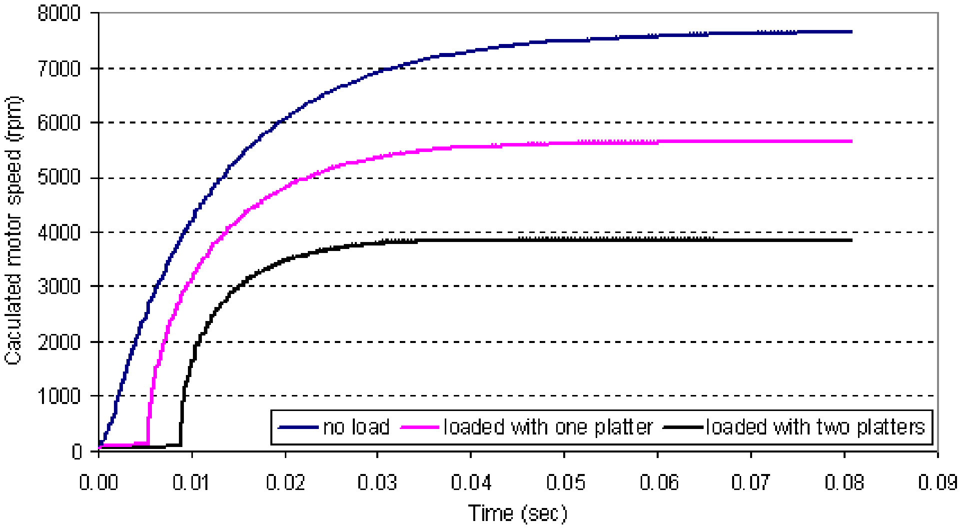

Figure 6.17: Calculated motor speed under no load and loaded conditions

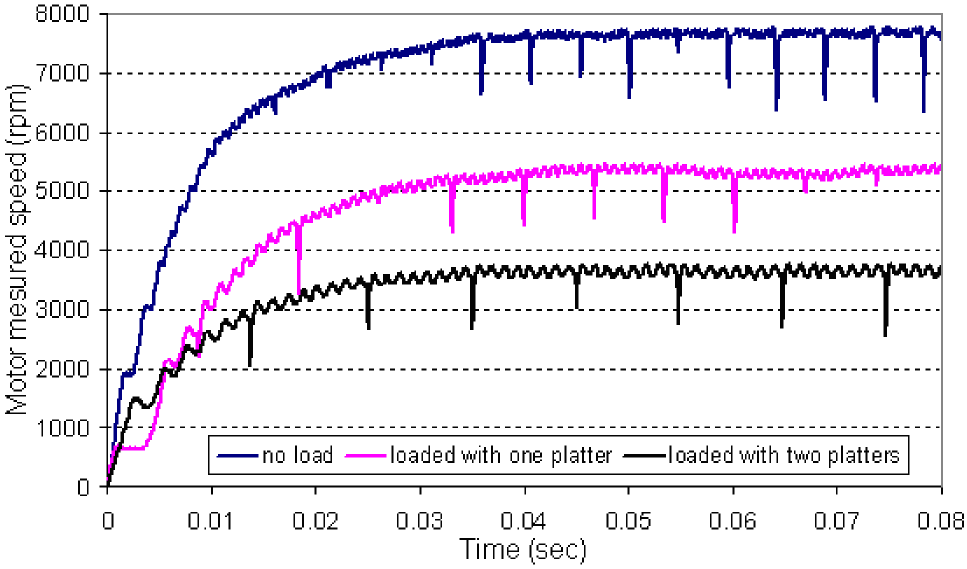

Figure 6.18: Measured motor speed under no load and loaded conditions

6.3.2 Motor starting with current limits

The power supply for hard disk drive for PC computer is +12V for the spindle motor and actuator; and +5V for drive circuits respectively. Roughly, 75% of the +12V power is taken by the spindle motor and the rest 25% by the actuator assembly.

As shown in Fig.6.5, if there is no limit, motor starting current can be as high as 3.5A. The higher the motor starting current is concerned with drive power consumption, heat and temperature; and must be given special consideration in systems with multiple storage drives. The ratings of the power supply, particularly at the +12V level, sometimes may not be sufficient for starting conditions. Therefore, the motor starting current is limited by the controller in practice.

In this work, the cascaded closed loop control structure which was given in Section 6.1 is used to control the motor current. In the current control loop, a current limiter is used to set the current limit and a current hysteresis controller is used to control the current in keeping within the required limit. Fig. 6.19 shows the motor voltage from the current hysteresis controller. The motor starting current with 1.5 A current limit is shown in Fig. 6.20. It can be seen that the motor starting current is within the limits of 1.5A. However, the motor speed is slower to reach to the rated speed compared with the first case- without limits (Fig. 6.3). It takes 57 ms which is 17ms longer, to spin up to the rated speed of 7200 rpm (Fig. 6.22). The motor torque is also lower compared to that in the first case as shown in Fig. 6.23 because torque is directly proportional to the current.

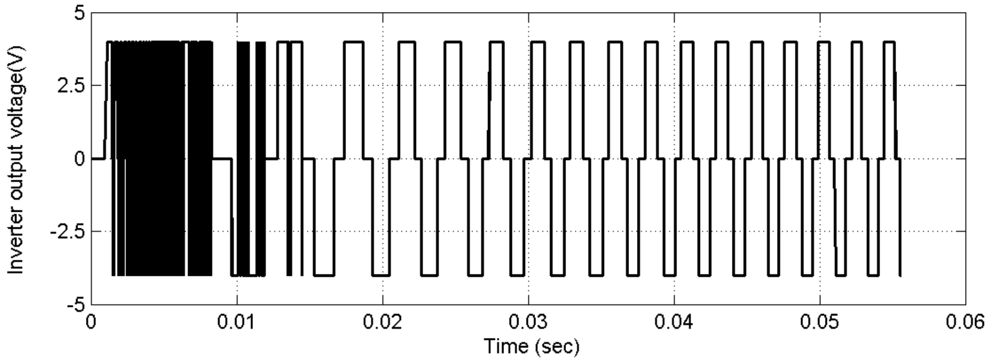

Figure 6.19: Voltage comes from the hysteresis controller

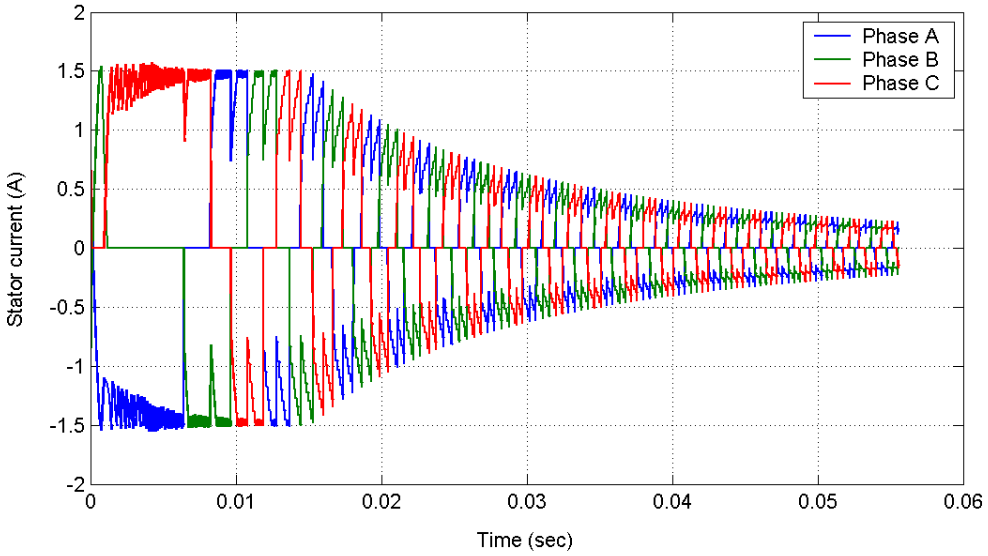

Figure 6.20: Motor starting current with 1.5A current limit

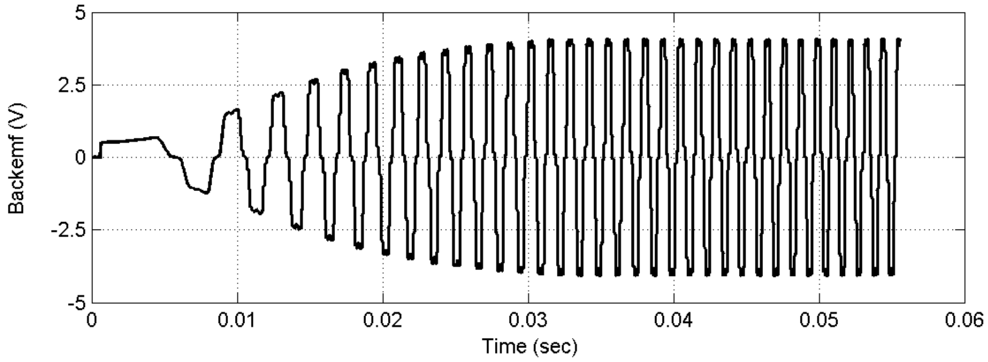

Figure 6.21: Motor back-emf waveform when current is limited at 1.5A

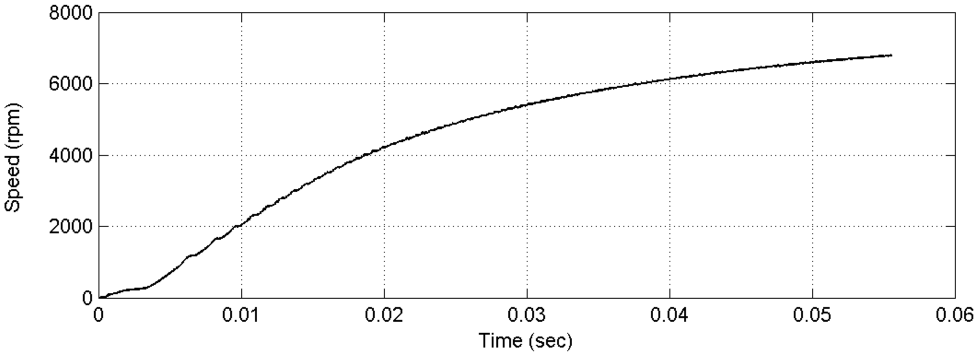

Figure 6.22: Speed profile with 1.5A current limit

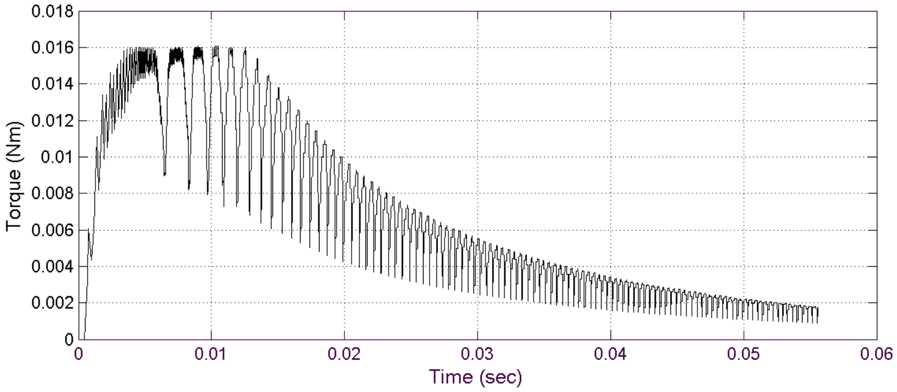

Figure 6.23: Starting torque profile with 1.5A current limit

6.3.3 Motor starting with speed limit

When the motor is running with no speed limits as discussed in the previous section, where motor supply voltage was fixed so that the motor speed keeps on increasing to over speed region with a higher back-emf value. In order to avoid this condition, a speed limit is needed. In this work, cascaded closed loop control which has been proposed in a previous section 6.1, can be used to implement the speed limits of the motor. In the outer speed loop, we set the motor reference speed to the rated speed 7200 rpm. If the speed is more than its rated value, the controller adjusts the speed to its rated value again.

The simulated results are shown in Fig. 6.24- Fig. 6.27. Motor speed profiles with and without speed limits are also compared and results are shown in Fig. 6.28. The point where motor speed reaches to its rated value, speed controller maintains the speed in its rated speed 7200rpm. According to Fig. 6.24, the motor speed reaches to its rated value at 40 ms and from that point speed is limited to 7200 rpm. When the speed is constant, motor back-emf is constant as shown in Fig. 6.26. Motor current is also in a steady state in this instant as shown in Fig. 6.27, since the motor input voltage is constant.

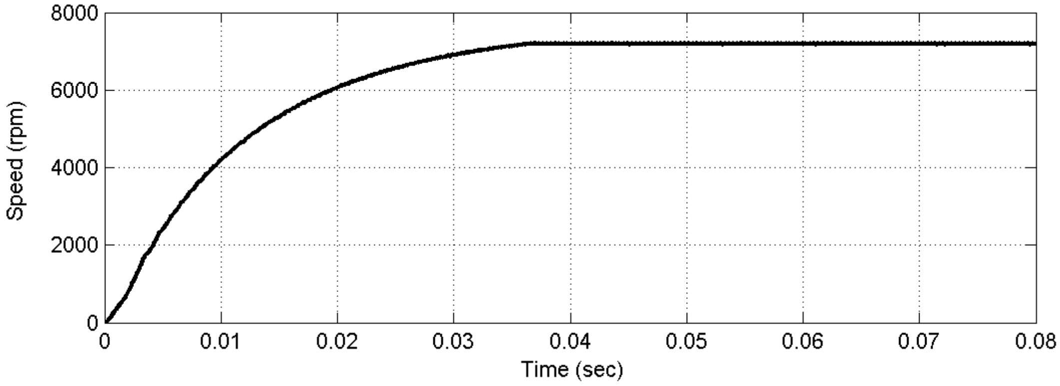

Figure 6.24: Starting speed profile with speed limit

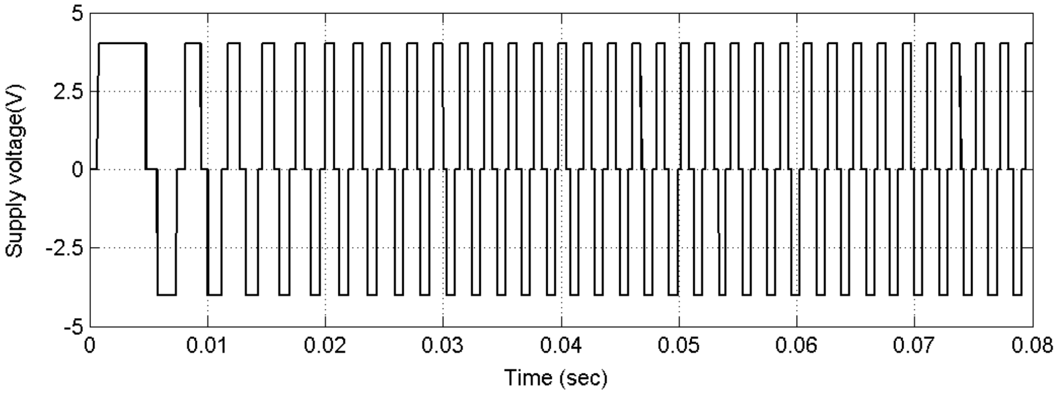

Figure 6.25: Motor supply voltage

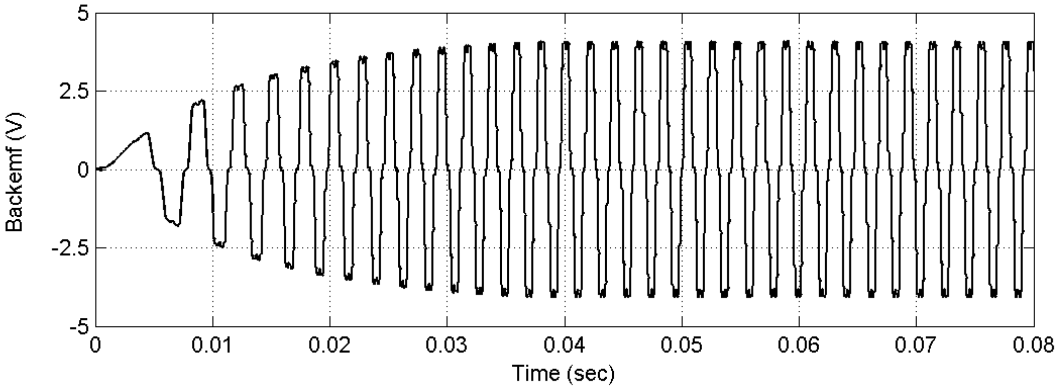

Figure 6.26: Motor back-emf profile with speed limit

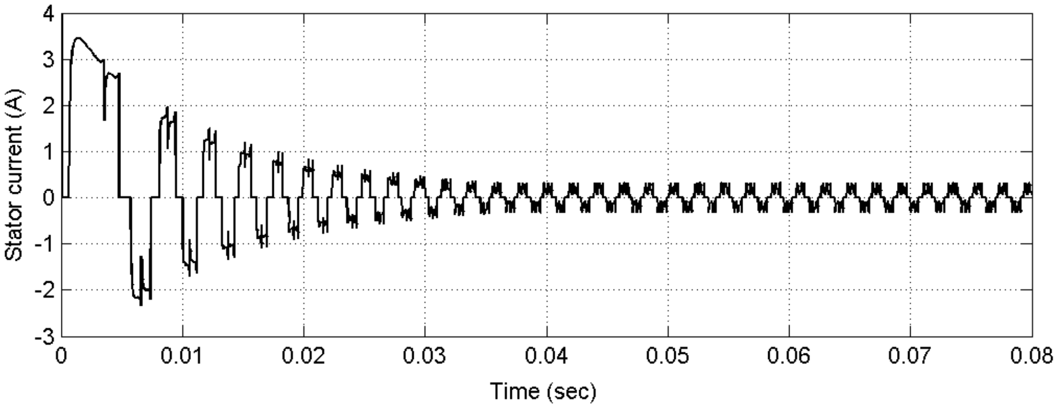

Figure 6.27: Stator current profile with speed limit

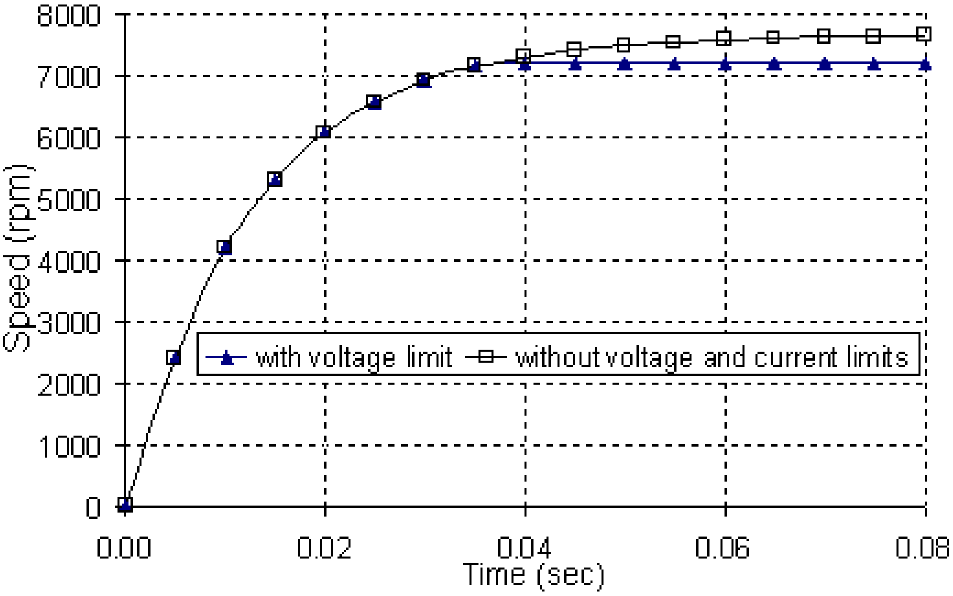

Figure 6.28: Speed with speed limit and without limits

6.4 Computational Analysis of the Run-up Performances of a HDD Spindle Motor

In this section, the run-up characteristics of the spindle motor with various supply voltages and limited starting currents, which are the practical constraints in motor design stages, are analyzed. Possible Conditions are justified to optimize the spin-up time and power consumptions in both starting and running conditions. Time stepping FEM coupled with closed loop feedback controller is used.

6.4.1 Case I: Motor runs freely under various stator phase supply voltages

In this condition, motor is allowed to run freely up to its rated condition. Feedback control adjusts the speed to rated speed 7200 rpm. Simulated results are shown in Fig. 6.29 and listed in Table 6.1. The stator phase supply voltages are 6V, 5V, 4.5V and 4V whereas the spin-up times to reach the rated speed 7200rpm are 12.7ms, 16.8ms, 21.0ms and 32.1ms respectively as shown in Fig. 6.29. The highest the stator phase supply voltage 6V resulted the fastest the spin-up time of 12.7ms to reach the rated speed and the lowest the stator phase supply voltage 4V resulted the slowest spin-up time of 32.1ms. However, if the supply voltage is high, the spin-up time is fast, at the same time the starting current is also high as shown in Fig. 6.30 and in many cases the current may go beyond the cut-off point. As a result, the motor power consumption is high in both starting and running conditions. Simulated data are summarized in Table 6.1.

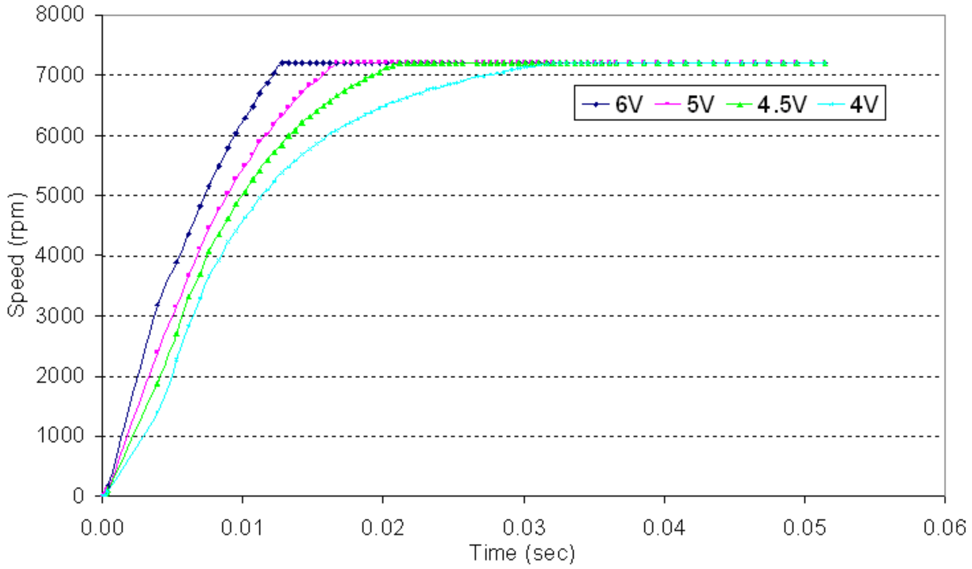

Figure 6.29: Motor speed vs. spin-up time with different supply stator phase voltages

6.4.2 Case II: Motor running with current limiter

Starting current is limited at 1.5A using the current limiter in the feedback closed loop control. Fig. 6.31 shows the spin-up times against the speed with different supply voltages. Motor power consumptions with current limit under different supply voltages are listed in Table 6.2. The power consumption for the 6V is also the highest. Comparison of spin-up time with and without current limits are shown in Fig. 6.32 and listed in Table 6.3. It is found that the spin-up times for each voltage level with current limits for Case II are slower than compared with Case

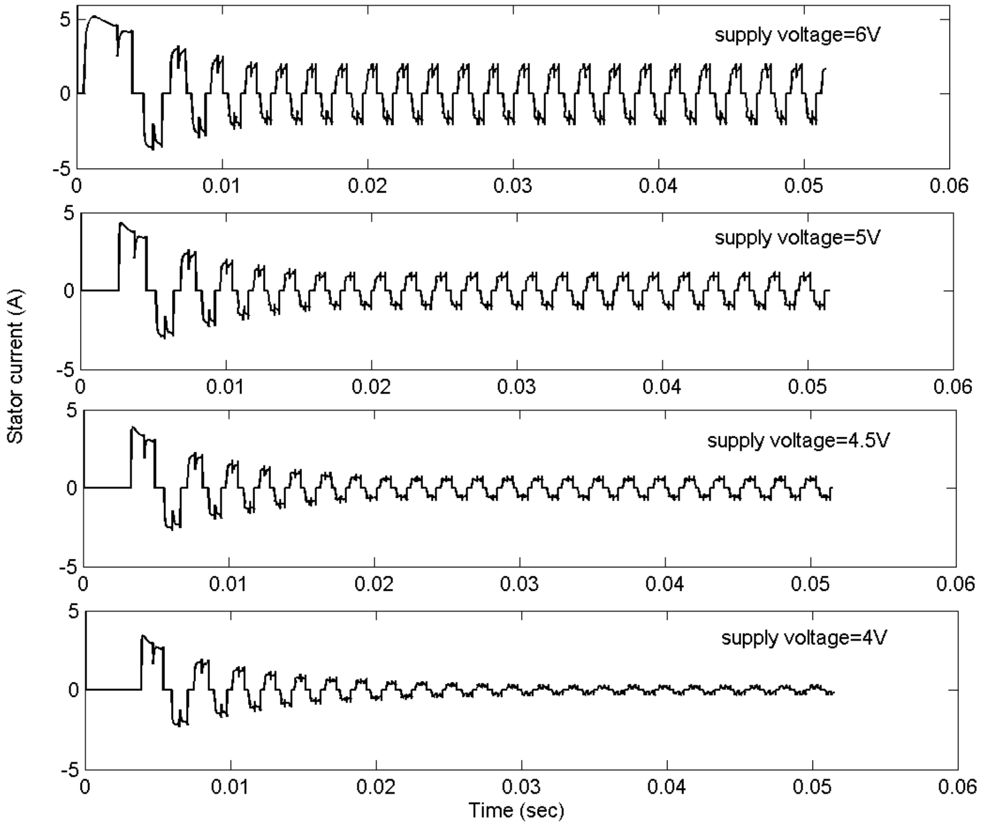

Figure 6.30: Starting current profiles with different supply stator phase voltages

Table 6.1: Power consumptions with different supply phase voltages at no load condition

Supply voltage (V)	*Spin−time (ms)*	*starting current (A)*	*steady state current(A)*	*Power consumption at starting(W)*	*Power consumption at steady state(W)*
6	12.7	5.19	2.06	31.14	12.36
5	16.8	4.32	1.19	21.60	5.95
4.5	21.0	3.89	0.75	17.50	3.38
4	32.1	3.45	0.32	13.80	1.28

I without current limits. Power consumptions for the operation models with and without current limit are also compared in two different conditions: (1) starting (2) running (steady state). Comparisons data are listed in Table 6.4 and shown in Fig. 6.33. It is found that the power consumption for Case I is lower than that in case II for all supply voltage levels both at starting and running states. Based on these results, it can be concluded that, one can use the higher supply voltage to get the faster spin-up time if the current is in the limited range so that the power consumption is estimated.

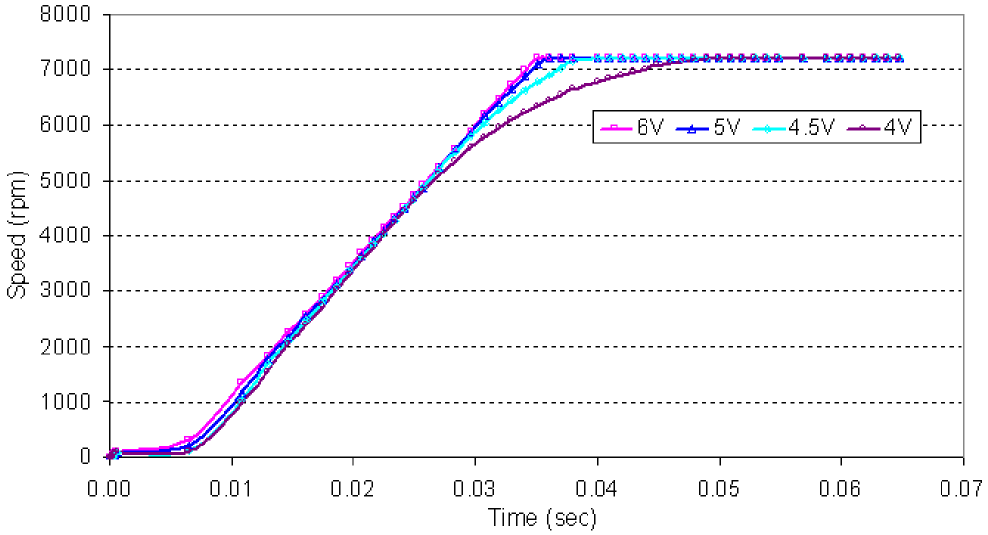

Figure 6.31: Speed vs. spin-up time with different supply voltages where current is limited at 1.5A

Table 6.2: Motor power consumptions with current limits

Supply voltage (V)	*Spin−time* (ms)	*starting current* (A)	*steady state current*(A)	*Power consumption at starting*(W)	*Power consumption at steady state*(W)
6	34.9	1.5	1.5	9.0	9.0
5	35.7	1.5	1.19	7.50	5.95
4.5	38.5	1.5	0.75	6.75	3.38
4	48.7	1.5	0.32	6.0	1.28

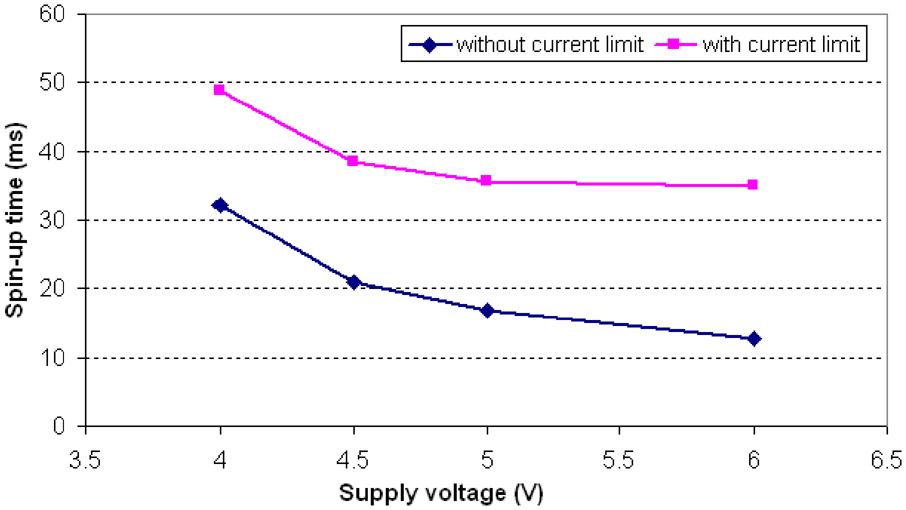

Figure 6.32: Supply voltage vs. spin-up time with and without current limit

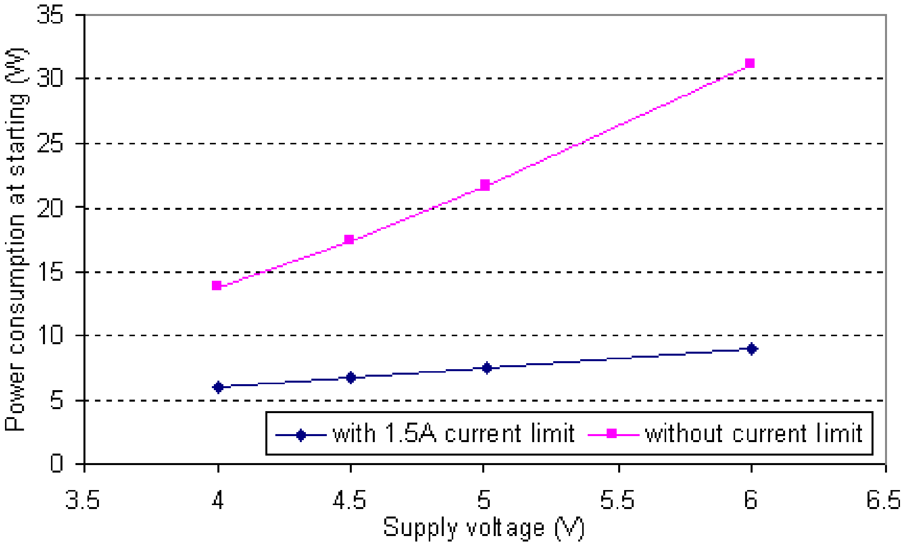

Figure 6.33: Comparison of power consumption with and without current limit at starting

Table 6.3: Spin-time with and without current limits

$Supply$ $voltage(V)$	$Spin - time$ $without\ current\ limit(ms)$	$spin - time$ $with\ current\ limit(ms)$
6	12.7	34.9
5	16.8	35.7
4.5	21.0	38.5
4	32.1	48.7

Table 6.4: Comparison of power consumption with and without current limits

$Supply$ $voltage$ (V) .	$Power$ $consumption\ at$ $starting\ with$ $limits(W)$	$Power$ $consumption\ at$ $starting\ without$ $limits(W)$	$Power$ $consumption\ at$ $steady\ state$ $with\ limits(W)$	$Power$ $consumption\ at$ $steady\ state$ $without\ limits(W)$
6	9.0	31.14	9	12.36
5	7.5	21.6	5.95	5.95
4.5	6.75	17.5	3.38	3.38
4	6.0	13.8	1.28	1.28

6.4.3 Case III: Motor running with voltage adjusting scheme

Although the spindle motor requires high power at start up, the power consumption at normal running is very low. Therefore, we can reduce the supply voltage to optimize the motor power when the motor reaches its rated speed. The closed loop model which has been developed in Section 6.1 is used to implement the voltage control. In the simulation program, the flag is set to check whether the speed reaches to its rated value. When the speed reaches to the rated value, the motor current starts to reduce to its rated value by adjusting the voltage. Hysteresis controller is used to adjust the supply voltage. For example, if the rated current for this prototype motor is 0.2A, set the reference current of the current loop in the proposed controller to 0.2A. Outer speed loop also adjust the motor speed into its rated value 7200rpm. Therefore motor supply voltage has been adjusted by controller to maintain these drive requirements.

Calculated results are shown in Fig. 6.35. Results without voltage limits are also shown to compare with the results using adjusting supply voltage scheme. The current profiles are shown in Fig. 6.34 and Fig. 6.35. It can be seen clearly that the motor current is reduced to its rated value 0.2A starting from the motor speed reaches to its rated value 7200 rpm by using voltage adjusting scheme. By using the proposed voltage adjusting scheme, the motor power consumption at motor running condition can be saved.

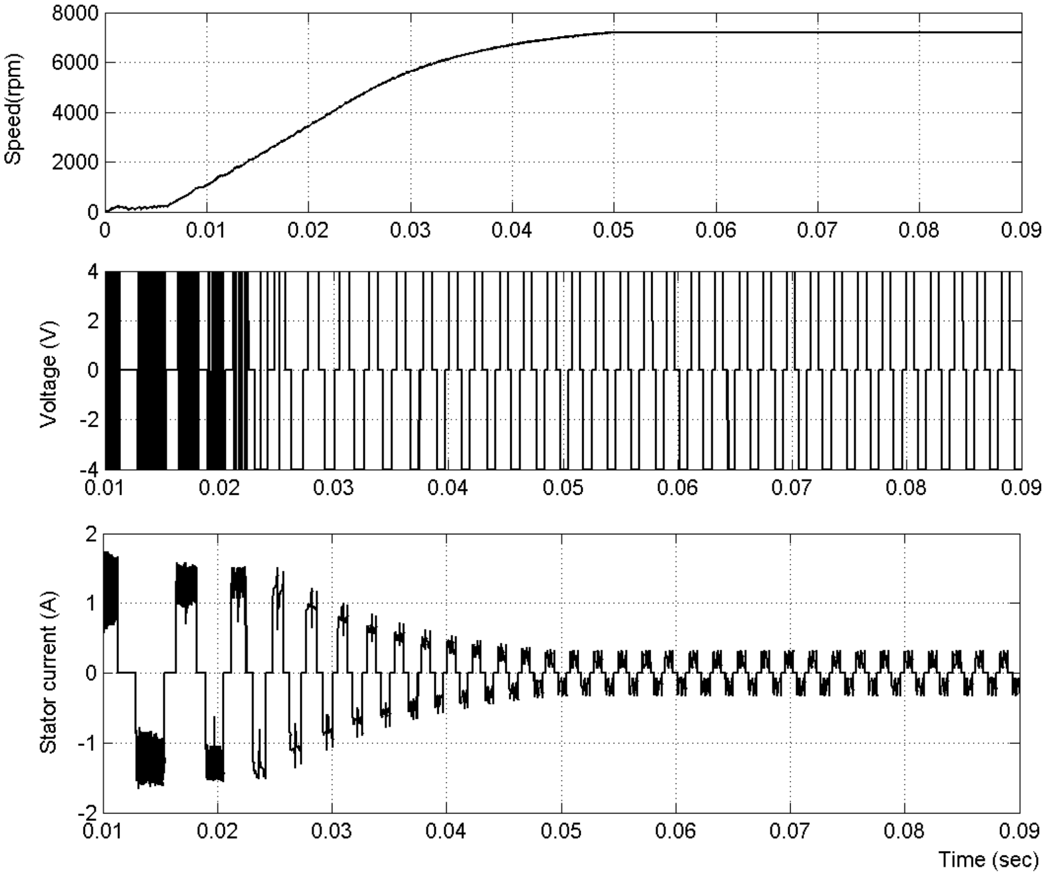

Figure 6.34: Motor transient responses without voltage adjusting scheme

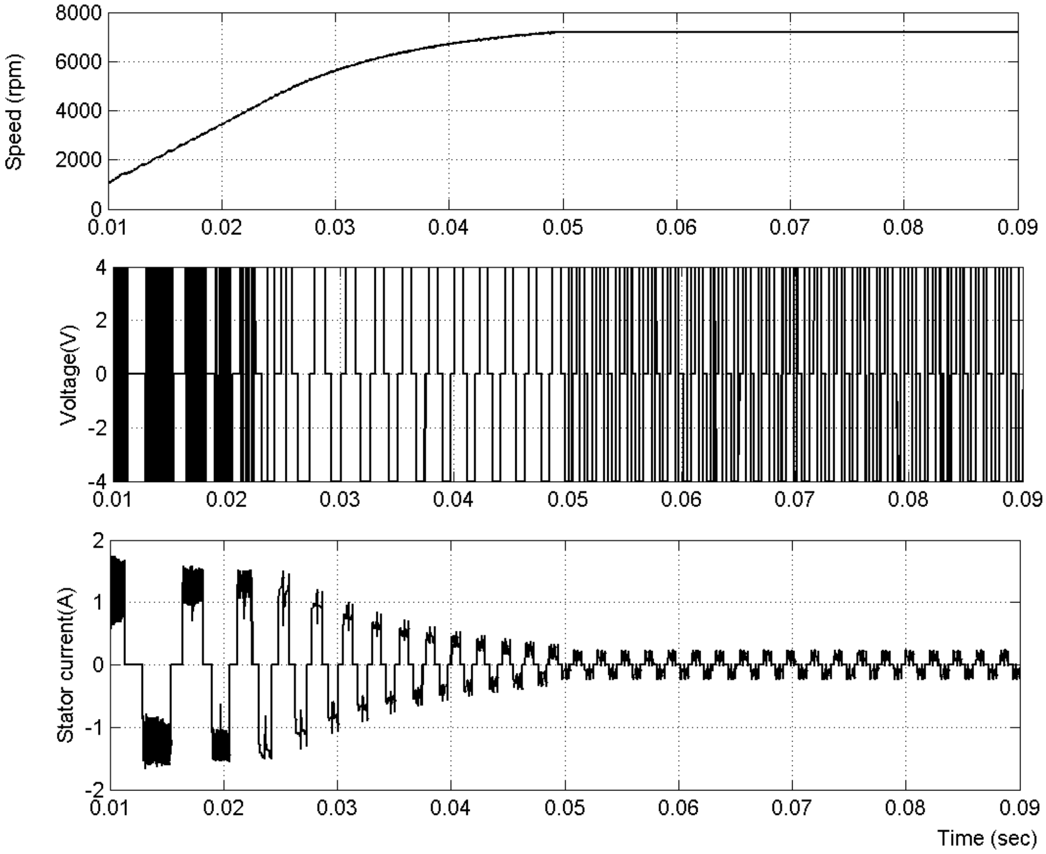

Figure 6.35: Motor transient responses with voltage adjusting scheme

6.5 Conclusion

In this chapter, efforts were made in order to investigate the important quality indexes of the spindle motor such as an accurate assessment of the requirement of starting torque, spin-time and starting current. Starting performances of the spindle motor with drive current limits, speed limits and without limits were determined.

In order to analyze the motor with a controller as an actual system, a new approach to couple the time stepping FEM with closed loop control structure was implemented. Cascaded speed and current hysteresis control loop structures was used. By coupling the control loop features with the time stepping FEM, the stator windings could be fed with the actual input voltages to the time stepping FEM model. In addition, motor performances under transient conditions can be controlled instantaneously as an actual motor-controller system. Using this new scheme, simple and efficient techniques to analyze the spindle motor performance using time stepping FEM couple with cascaded control loop were developed. Computational analysis of run-up performances of HDD spindle motor under starting and normal running conditions were investigated.

Chapter 7

Discussions and Conclusions

This thesis attempted to investigate the computation and analysis of steady state and dynamic performances of BLDC motor. Modelling, simulation and performance analysis of the BLDC motor using numerical methods were presented.

An accurate analysis of a real machine would call upon three dimensional analysis. However, comparing with 2D FEM, the 3D FEM requires much computing power, storage and computer time usage especially in transient analysis where rotor movement has to be included in field simulation. In order to study dynamic performances of the motor, external circuit and rotor rotation should be coupled with the electromagnetic field in time domain and time stepping technique is a practical solution for this problem. If one uses 3D time stepping FEM, rotor meshes are required to move according to the rotor rotation at each time steps. It may take very long computing time and require very large amount of memory. It is often neither practical nor always possible in real world applications. In addition, 3D effects such as end winding effect can, however, be taken into account using empirical formulae and the validity of the formulae have been well proven with experiments and analytical techniques. In this work, numerical models for studying the steady state and dynamic performances are formulated in two dimensional and 3D effects such as end winding effects are approximated and included. The validity of 2D FEM model is verified by the experiments. Good agreements in experimental and simulation results show that 2D FEM is validated to study the steady state as well as the transient performance of the BLDC motor.

In addition, spindle motor is used as a working example in this work. The axial length of the spindle motor is quite short and it is seemed that 3D FEM is necessary. However, the air gap length of the spindle motor is very small (0.05mm $\sim$ 0.15mm). Hence, 2D FEM is good enough to use in performance analysis of this particular case.

Dynamic model of the BLDC motor was developed based on the 2D time stepping FEM. This model was the numerically strong coupling model whereas the system equations are solved simultaneously at each time steps in time varying electromagnetic solver. Due to the direct coupling of transient electromagnetic field, the electric circuits and the motion in this dynamic model, the solution could be taken into account the eddy current effect, the saturation effect, the rotor movement, high order harmonic of the electromagnetic fields and the non-sinusoidal quantities which are very difficult to include in conventional finite element method coupled with equivalent circuit models. 3D effects i.e end winding effects are taken into account using empirical formulae. Dynamic model was used in studying the transient analysis of the BLDC motor at step voltage variations, load torque changing and locked rotor condition. Results shows that the proposed model can investigate the transient responses of the motor under various motor operating conditions. It can give a clear representation of the motor performances such as stator current, torque, motor back-emf, speed with its operating times respectively. In addition, the model can be used to simulate dynamic characteristics of the motor under various time steps. These are the important features for the machine designers to do simple simulation of the dynamic performance of the motor with desired motor parameters. Proposed dynamic model was also used to investigate the starting processes of the BLDC motor. It has been observed that the important motor starting parameters such as starting currents; motor spin up time with various supply voltages; required starting torques for given motor parameters etc., can be calculated precisely under time frames.

The analysis of the steady state performance of nonlinear electromagnetic systems using time stepping FEM requires very long computational times. Normally, the transient solver begins with a flat start by initializing all state variables to zero. This results in a large DC components of current and several hundred integral time steps are needed before reaching its steady state. An improved steady state model of the BLDC motor was implemented using time stepping FEM coupled with two dimensional magneto-static FEM. In this steady state model, magneto-static FEM was used as a pre-computation stage for time stepping FEM. It is found that using this improved method, the transient solver can be started with initial conditions quite close to the steady state solutions.The first few cycles are almost free of direct current. It can reduce the time spent in reaching a steady state solution is cut by roughly a factor of three. The model can take into account the non-sinusoidal quantities, stator harmonics and rotor movement which are very difficult to simulate instantaneously in the steady state analysis using traditional finite element method. Using the proposed model, calculation of the steady state current, cogging torque, back-emf and determination of torque-speed characteristics of the BLDC motor were analyzed. Results show that the torque was directly proportional to the winding currents and speed of the motor can be controlled by measuring the stator phase voltage applied to the motor. These results were used to implement the application of simple speed and current control for BLDC motor drive system.

In order to determine the accuracy and validation of the proposed dynamic and steady state model, DSP based BLDC motor test stand was implemented. Simple and reliable methods of motor performance measurements were presented. A new approach for detecting the motor starting sequences for controller was developed. Based on the experience of hardware set up in this experiment, it is recommended that very low rotor inertia incremental encoder is necessary in order to couple with this type of small capacity HDD spindle motor. Since the motor is designed to run two 3.5 inch disc platters, it is needed to calculate prior the inertia of the whole coupling hardware components such as shaft inertia, coupler inertia, encoder inertia and platters inertia in order to avoid the motor to run the overloaded conditions.

BLDC motors cannot work without the electronic controllers. In order to analyze the motor with controller as an actual system, a new approach to couple the time stepping FEM with closed loop control structure was implemented. Cascaded speed and current hysteresis control loop structures were used. By coupling the control loop features with the time stepping FEM, the stator windings could be fed with the actual input voltages to the time stepping FEM model. In addition, motor performances under transient conditions can be controlled instantaneously as an actual motor-controller system. Using this new scheme, application characteristics of the HDD spindle motors were investigated. Important features of the spindle motor at starting conditions under no load and loaded conditions were analyzed. It is found that the proposed model worked satisfactorily when used in simulation for motor under real transient cases with voltage, current and speed limits. This analysis provides assistance to implement the power management scheme especially for the notebook PCs and investigations of spin up times under drive limits such as current limits, voltage limits and speed limits. Results are verified with experiments. It is found that the simulation results of the motor have little discrepancies with experimental results especially in transient conditions. This is because although the control loop structure is included in the FEM model, the transient characteristics of the controller cannot be taken into account in this work. It is another big issue to analyze the dynamic behaviour of control system. Further work is needed to develop a controller dynamic model such as by using Matlab simulink in order to couple the fully dynamic behaviour of motor-controller drive system.

Computational analysis of run-up performances of the HDD spindle motor performances under starting and normal running conditions were investigated. These studies are demonstrated that motor performances can be optimized at normal running conditions by adjusting the supply voltages in order to maintain the motor with its rated conditions. Current hysteresis control is suitable for fast and accurate response.

Bibliography

[1] Essam S. Hamdi, "Design of small electrical machines," John Wiley and Sons, 1996.

[2] Jacek F. Gieras and Michell Wing, "Permanent magnet motor technology-Design and application," Marcel Dekker, Inc. 1997.

[3] J. R. Hendershot Jr. and T. J. E Miller, "Design of brushless permanent-magnet motors," Magan Physis Publishing and Calerndon Press, Oxford 1994.

[4] Cho, Chahee Peter, " Analysis and design considerations of a high-power density, dual air gap, axial-field, brushless, permanent magnet motor," Ph.D thesis, University of New Hampshire, May 1995.

[5] N. Ertugrul, P. P. Acarnley, "Indirect rotor position sensing in real-time for BLDC motor drives," IEEE Trans. on Power Electronics, vol.13, No.4, pp. 608-616, July 1998.

[6] Remigius C. Okonkwo, " Design and investigation of linear brushless dc motors with high energy permanent magnets," Verlag Dr. Kster, 1999.

[7] Takashi Kenjo, "Permanent magnet and brushless DC motors," Sogo Electronic Publishing Company, Tokyo, 1984.

[8] Pei Bai Zhou, "Numerical analysis of electromagnetic fields," Springer-Verlag, 1993.

[9] K. Hameyer and R. Belmans, "Numerical Modelling and design of electrical machines and devices," WIT Press, 1999.

[10] S. J. Salon, "Finite element analysis of electrical machines," Kluwer, 1995.

[11] N. A. Demerdash and D. H. Gillot, "A new approach for determination of eddy currents and flux penetration in on-linear ferromangetic material," IEEE Trans. on Magn., vol. 74, pp. 682-685, march 1974.

[12] A. G. Jack and B. C. Mecrow, "Methods for magnetically non-linear problems involving significant hyeteresis and eddy currents," IEEE Trans. on Magn., vol. 26, no. 2, pp. 424-429, march 1990.

[13] David Meeker, "Finite element method magnetics - User Manual(Version 3.4)," http://www/femm.berlios.de, December 2004.

[14] G. R. Slemon, A. V. Gumaste, "Steady-state analysis of a permanent magnet synchronous motor drive with current source inverter," IEEE Trans. on Industry Applications, vol. IA-19, no. 2, pp. 190-197, 1983.

[15] Thomas M. Jahns, Gerald B. Kliman and Thomas W. Neuman, "Interior permanent magnet synchronous motors for adjustable speed drives," IEEE Trans. on Industry Applications, vol. IA-22, no. 4, July/August 1986.

[16] Pillay, Pragasen, "Modeling Simulation and Analysis of Permanent Magnet Synchronous and Brushless DC Motor Drives," Ph.D thesis, Virginia Polytechnic Institute and State University, 1987.

[17] C. C. Hwang, S. B. Jhon, S. S. Wu, "Reduction of cogging torque in spindle motors for CD-ROM drive," IEEE Trans on Magn., vol.34, No.2, pp.468-470, March 1998.

[18] Francis Piriou and Adel Razek, “Finite element analysis in electromagnetic systems accounting for electric circuits,” IEEE Trans. on magnetic, vol.29, no.2, March 1993.

[19] Zhou P., Rahman M. A and Jabbar M. A, “Field circuit analysis of permanent magnet motors,” IEEE Trans. on magnetics, vol.30, pp.1350-1359, July 1994.

[20] M. A. Rahman, Ping Zhou, “Analysis of brushless permanent magnet synchronous motors,” IEEE Trans. on Magnetics, vol. 43, no. 2, pp. 250-267, April 1996.

[21] Andrew M. Knight, John C. Salmon, “Modeling the dynamic behavior of single phase line-start permanent magnet motors,” IEEE Industry Society, 54th meeting, session 59, pp. 2582-2588, 1999.

[22] Shailesh Waikar, Tilak Gopalarathnam and Hamid A. Toliyat, “ Evaluation of multiphase brushless permanent magnet (BPM) motors using finite element method (FEM) and experiments,” IEEE Trans. on Industry Appl. Vol.2, no.1, pp.396-401, May 1999.

[23] C. Bi, Z. J. Liu and S. X. Chen, “Estimation of back emf of PM BLDC motors using derivative of FE solutions,” IEEE Trans. on Magnetics, vol. 36, no.4, July 2000.

[24] M. V. K. Chari and S. J. Salon, “Numerical methods in electromagnetism,” Academic Press, A Harcourt Science and Technology Company, 2000.

[25] K. Hameyer, J. Driesen, H. D. Gersem and R. Belmans, “The classification of coupled field problems,” IEEE Trans on magnetics, vol.35, no.3, pp.1618-1620, May 1999.

[26] S. J. Salon, R. Palma and C. C. Hwang, "Dynamic modeling of an induction motor connected to an adjustable speed drive," IEEE Trans on magnetics, vol.25, no.4, pp. 3061-3063, July 1989.

[27] Z. Q. Zhu, G. W. Jewell and D. Howe, "Finite element analysis in the design of permanent magnet machiens," IEE Seminar on Current Trends in the Use of Finite Elements in electrmechanical Design and Analysis, pp. 1-7, January 2000.

[28] S. L. Ho and W. N. Fu, "A comprehensive approach to the solution of direct couple multislice model of skewed rotor induction motors using time stepping eddy current finite element method," IEEE Trans on Magnetics, vol.33, no.3, pp. 2265-2273, May 1997.

[29] S. Wang, J. Kang, K. Park, H. Yoon and G. Jang, "2D and 3D FEA of a BLDC motor," The international journal of Computation and Mathematics in Electrical and Electronics Eng., vol.19, no.2, pp. 529-537, 2000.

[30] T. W. Nehl, F. A. Fouad, N. A. Demerdash and E. A. Maslowski, " Dynamic simulation of radially oriented permanent magnet electronically operated synchronous machines with parameters obtained from finite element field solutions," IEEE Trans. Vol.IA-18, no.2, pp.172-181, March/April 1982.

[31] T. W. Nehl, F. A. Fouad and N. A. Demerdash, "Digital simulation of power conditioner-machine interaction for electronically commutated DC permanent magnet machines," IEEE Trans on magnetics, vol.MAG-17, no.6, pp.3284-3286, November 1981.

[32] N. A. Demerdash and T. W. Nehl, "Dynamic modeling of brushless DC motors in electric propulsion and electromechanical actuation by digital techniques," IAS annual meeting, pp.570-578, 1980.

[33] N. A. Demerdash and T. W. Nehl, “Dynamic modeling of brushless DC motors for aerospace actuation,” IEEE Trans., vol.AES-16, no.6, pp. 811-821, November 1980.

[34] R. H. Miller, T. W. Nehl, N. A. Demerdash, B. P. Overton and C. J. Ford, “An electronically controlled permanent magnet synchronous machine conditioner system for electric passenger vehicle propulsion,” IAS Annual meeting, pp.506-510, 1982.

[35] P. F. Muir and C. P. Neumann, “Pulsewidth modulation control of brushless DC motors for robotic applications,” IEEE Trans., vol.IE-32, no.3, pp.222-229, August 1985.

[36] D. M. Erdman and H. B. Harms, “Estimating speed-torque profiles of the brushless DC motor,” Proceedings of the Motorcon Conference, pp.1-8, 1985.

[37] A. K. Wallace and R. F. Spee, “The effect of motor parameters on the performance of brushless DC drives,” IEEE PESC, pp. 591-597, 1987.

[38] P. Pillay and R. Krishnan, “Modelling, simulation and analysis of a permanent magnet brushless DC motor drive,” IAS Annual meeting, pp.7-14, 1987.

[39] R. Spee and A. Wallace, “Performance characteristics of brushless DC drives,” IAS Annual meeting, pp.1-6, 1987.

[40] P. Pillay and R. Krishnan, “Modeling, Simulation, and analysis of permanent magnet motor drives, Part II: The Brushless DC Motor Drive,” IEEE Trans on Industry applications, vol. 25, no.2, pp.274-279,March/April 1989.

[41] Y. P. Liu, D. Howe, T. S. Birch and D. M. H. Matthews, “Dynamic Modeling and Performance Prediction of Brushless Permanent Magnet Drive System,”

Electrical Machines and Drives, Fourth International Conference, pp. 95-99, 1989.

[42] M. M. Elmissiry and S. Chari, “Dynamic Performance of a Permanent Magnet, Axial Flux, Toroidal Stator, Brushless D.C.Motor,” 3rd Africon Conference, pp. 400-403, 1992.

[43] Liuchen Chang, “An improved FE inductance calculation for electrical machines,” IEEE Trans on magnetics, vol.32, no.4, pp.3232-3245, July 1996.

[44] D. Howe and Z. Q. Zhu, “The influence of finite element discretisation on the prediction of cogging torque in permanent magnet excited motors,” IEEE Trans on magnetic, vol.28, no.2, pp.1080-1083, March 1992.

[45] Z. J. Liu, C. Bi, H. C. Tan and T. S. Low, “Modeling and torque analysis of permanent magnet spindle motor for disk drive system,” IEEE Trans on magnetics, vol.30, no.6, pp.4317-4319, November 1994.

[46] Z. Q. Zhu, P. J. Hor, D. Howe and J. Rees-Jones, “Calculation of cogging force in a slotted linear tubular brushless permanent magnet motor,” IEEE Trans on magnetic, vol.33, no. 7, pp.4098-4100, September 1997.

[47] S. X. Chen, T. S. Low, B. Brhsul, “The robust design approach for reducing cogging torque in permanent magnet motor,” IEEE Trans on magnetics, vol.34, no.4, pp. 2135-2137, July 1998.

[48] C. Bretn, J. Bartolom, J. A. Benito, G. Tassinario, I. Flotats, C. W. Lu, and B. J. Chalmers, “Influence of machine symmetry on reduction of cogging torque in permanent magnet brushless motors,” IEEE Trans on magnetics, vol.36, No. 5, pp.3819-3823, September 2000.

[49] M. A. Jabbar, Win Lai Aye, Z. J. Liu and M. A. Rahman, “Computation of forces and torques in electric machines,” Canadian Conference on Electrical and Computer Engineering, vol.1, pp.370-374, May 2000.

[50] C. Bi, Z. J. Liu and S. X. Chen, “Estimation of back-emf of PM BLDC Motors using derivative of FE solutions,” IEEE Trans on magnetics, vol.36, no.4, pp.697-699, July 2000.

[51] K. Atallah, Z. Q. Zhu and D. Howe, “An improved method for prediction iron losses in brushless permanent magnet DC drives,” IEEE Trans on magnetics, vol.28, no.5, pp. 2997-2999, September 1992.

[52] Z. J. Liu, C. Bi, and T. S. Low, “Analysis of iron loss in hard disk drive spindle motor,” IEEE Trans on magnetics, vol.33, no.5, September 1997.

[53] Z. Q. Zhu, K. Ng and D. Howe, “Design and analysis of high speed brushless permanent magnet motors,” EMD 97, conference publication no. 444, pp. 381-385, September 1997.

[54] M. S. N. AI-Din, A. F. Kader and J. AI-Samarai, “A new method to compute eddy current losses by the finite elements method,” IEEE Industry Applications Society Annual Meeting, New Orleans, Louisiana, pp.3-9, October5-9, 1997.

[55] G. W. Jewell and D. Howe, “Computer-aided design of magnetizing fixtures for the post-assembly magnetization of rare-earth permanent magnet brushless DC motors,” IEEE Trans on magnetics, vol.28, no.5, pp. 3036-3038, September 1992.

[56] C. C. Chan, K. T. Chau, J. Z. Jiang, “Novel permanent magnet drive for electric vehicles,” IEEE Trans on Industrial Electronics, vol.43, no.2, April 1996, pp.331-339.

[57] Gyu-Hong Kang, Jung-Pyo Hong and Gyu-Tak Kim, “Design and analysis of slotless-type permanent magnet linear brushless motor by using equivalent magnetizing current,” IEEE Trans on Industry Applications, vol.37, no.5, September/October 2001, pp. 1241-1247.

[58] S. Williamson, “Induction motor modeling using finite element,” Int. Conf. Electrical Machines, Paris, France, pp. 1-8, September 5-8 1994.

[59] A. Arkkio, “Analysis of induction motors based on the numerical solution of the magnetic field and circuit equations,” Helsinki Acta Polytechnica Scandinavica, Electrical Engineering Series, no. 59, 1987.

[60] T. H. Pham, P. F. Wendling, S. J. Salon and H. Acikgoz, “Transient finite element analysis of an induction motor with external circuit connections and electromechanical coupling,” IEEE Trans. Energy conversion, vol. 14, no.4, pp.1407-1414, December 1999.

[61] M. J. DeBortoli, S. J. Salon, D. W. Burow and C. J. Slavik, “Effects of rotor eccentricity and parallel windings on induction machine behaviour: a study using finite element analysis,” IEEE Trans. Magn. Vol. 29, No. 2, pp.1676-1682, March 1993.

[62] S. L. Ho, W. N. Fu, and H. C. Wong, “Estimation of stray losses of skewed induction motors using coupled 2-D and 3-D time stepping finite element models,” IEEE Trans. on Magnetics, vol. 34, pp. 3102-3105, Sept. 1998.

[63] S. L. Ho, H. Li, and W. N. Fu, “Inclusion of interbar currents in a network-field coupled time-stepping finite element model of skewed-rotor induction motors,” IEEE Trans. on Magnetics, vol. 35, no. 5, pp. 4218-4225, Sept. 1999.

[64] R. De Weerdt, E. Tuinman and K. Hameyer, "Finite element analysis of steady state behaviour of squirrel cage induction motors compared with measurements," IEEE Trans. on Magnetics, vol.33, no.2, pp2093-2096, March 1997.

[65] S. L. Ho, H. L. Li, "Dynamic modeling of permanent magnet synchronous machines using direct-coupled time stepping finite element method," Electric machines and drives Conference, Seattle, WA, USA, pp.113-115, May 9-12, 1999.

[66] Jinyun Gan, K. T. Chau, Yong Wang, C. C. Chan and J. Z. Jiang, "Design and analysis of a new permanent magnet brushless DC machine," IEEE Trans on magnetics, vol.36, no.5, September 2000.

[67] Seung-Chan Park, Byung I1 Kwon, Hee-Soo Yoon, Sung-Hong Won and Young-Gyu Kang, "Analysis of exterior-rotor BLDC motor considering the eddy current effect in the rotor steel shell," IEEE Trans on magnetics, vol.35, no.3, May 1999.

[68] Yong Wang, K. T. Chau, C. C. Chan and J. Z. Jiang, "Transient analysis of a new outer-rotor permanent magnet brushless DC drive using circuit-field-torque coupled time stepping finite element method,"IEEE Trans. on magnetics, vol.38, no.2, pp.1297-1330, March 2002.

[69] C. W. Chan and H. L. Li, "Simulation of rotor rotation in electromagnetic field problem using time stepping finite element technique," IEEE Trans. on Magnetics, vol.40, no.6, pp 1204-1209, September, 1997.

[70] B. I. Kwon, K. I. Woo, D. J. Kim, and S. C. Park, "Finite element analysis for dynamic characteristics of an inverter-fed PMLSM by a new moving mesh technique," IEEE Trans. on Magnetics, vol.36, no.4, pp 1574-1577, July 2000.

[71] S. J. Salon, M. J. Lee, "Coupling of finite element and analytical solution in the airgap of electric machines," IEEE Trans. on Magnetics, vol.27, no.5, September 1991.

[72] Chunt Mi, Gordon R. Slemon and Richard Bonert, "Modeling of iron loss of surface-mounted permanent magnet synchronous motors," 36th IAS Annual meeting, vol.4, pp.2585-2591, Oct 2001.

[73] S. L. Ho and W. N. Fu, "A comprehensive approach to the solution of direct couple multislice model of skewed rotor induction motors using time stepping eddy current finite element method," IEEE Trans on Magnetics, vol.33, no.3, May 1997.

[74] Hui Tan, W. N. Fu and Jianzhong Jiang, "A multi-pole brushless DC motor and its analysis using time stepping finite element method," Proceeding of the 3rd. International Power Electronic and Motion Control Conference (PIEMC 2000), vol.3,pp.1308-1311, August 15-18, 2000.

[75] W. N. Fu, Z. J. Liu and C. Bi,"A dynamic model of disk drive motor and its applications," IEEE Trans on Magnetics, vol.38, no.2, pp.973-976, March 2002.

[76] G. H. Jang, J. H. Chang, D. P. Hong and K. S. Kim, " Finite element analysis of an electromechanical field of a BLDC motor considering speed control and mechanical flexibility," IEEE Trans on Magnetics, vol.38, no.2, pp.945-948, March 2002.

[77] P. P. Silvester, R. L. Ferrari, " Finite elements for electrical engineers (2nd. edition)," Cambridge University Press, 1990.

[78] M. V. K. Chari, P. P. Silvester, " Finite elements in electrical and magnetic field problems," Jhon Wiley, 1980.

[79] H. R. Schwarz, " Finite element methods," Academic Press, 1988.

[80] S. S. Rao, " The Finite element method in engineering (2nd. edition)," Pergamon Press, 1989.

[81] K. H. Huebner, E. A. Thronton, " The Finite element method for engineers," Jhon Wiley and Sons, 1982.

[82] Ping Zhou, "Field and circuit combined analysis of permanent magnet synchronous motors," Ph.D Thesis, Memorial University of Newfoundland, Canada, May 1994.

[83] S. R. Hoole, "Computer-aided analysis and design of electromagnetic devices," Elsevier Science Publishing Co., Inc, 1989.

[84] D. A. Lowther, "Computer Aided Design in Magnetics," 1986.

[85] Nay Lin Htun Aung, "Computation and analysis of performance of small PM motors," Master Thesis, National University of Singapore, 2002.

[86] Matthew N. O. Sadiku, "Numerical techniques in electromagnetics," CRC press, 1992.

[87] M. V. K. Chari, S. J. Salon, "Numerical methods in electromagnetism," Imprint San Diego : Academic Press, 2000.

[88] R. L. Stoll, "The analysis of eddy currents," Oxford University Press,1974.

[89] D. C. Jites and D. L. Atherton, "Model of ferromagnetic hysteresis," J. Apply Physics, vol.75, No.5, pp.2594-2597, March 1994.

[90] T. F. Pirious, A. Razek, "Finite element analysis in electromagnetic systems accounting for electric circuits," IEEE Trans on Magnetics, vol.29, No.2, pp.1669-1675, March 1993.

[91] A. Demenko, “Time-stepping FE analysis of electric motor drives with semiconductor converters,” IEEE Trans on Magnetics, vol.30, No.5, pp.3264-3267, September,1994.

[92] T. H. Kim, J. H. Choi, K. C. Ko and J. Lee, “Finite element analysis of brushless DC motor considering freewheeling diodes and DC link voltage ripple,” IEEE Trans on Magnetics, vol.39, No.5, pp.3274-3276, September,2003.

[93] F. Pirious, A. Razek, “Coupling of saturated electromagnetic systems to nonlinear power electronic devices,” IEEE Trans on Magnetics, vol.24, No.1, pp.274-277, January 1988.

[94] T. J. E. Miller, M. I. McGilp, D. A. Staton and J. J. Bremner, “Coupling of saturated electromagnetic systems to nonlinear power electronic devices,” IEE Proc. Electr. Power Appl., vol.146, No.2, pp.129-137, March 1999.

[95] frederick W. Grover, “Inductance calculation: Working formulas and tables,” Dover Publications Inc.,1946.

[96] J. Engstrom, “Inductance of slotless machines,” IEE Proc. Electr. Power Appl., vol.146, No.2, pp.129-137, March 1999.

[97] P. Salminen,“Fractional slot permanent magnet synchronous motors for low speed applications,”Thesis for the degree of Doctor of Science (Technology) Lappeenranta University of Technology, December 2004.

[98] S. L. Ho and W. N. Fu, “A fully automatic mesh generation method for the movement field modeling,”The second Chinese Int. Conf. Electrical Machines, Hangzhou, China, pp. 624-630, 31st August- 2nd September 1995.

[99] Richard M. Crowder,“Electric drives and their controls,” Oxford Science Publications, Claredon Press, 1995.

[100] P. L. George, "Automatic mesh generation: Application to finite element methods," John Wiley and Sons, England, 1991.

[101] D. T. Lee and B. J. Schachter, "Two algorithms for constructing a Delaunay Triangulation," International Journal of Computer and Information Sciences, vol. 9, No.3, pp. 219-242, 1980.

[102] D. A. Lindholm, "Automatic triangular mesh generation on surfaces of polyhedra," IEEE Trans. Magn. Vol.19, no.6, pp. 2539-2542, November 1983.

[103] P. P. Silvester, "Advances in electrical engineering software," Computational mechanics publications, Springer-Verlag, 1990.

[104] Y. Lauze, "Interactive generation of structure/unstructured surface meshes using adaptivity," The Third Inter. Conf. on Numerical Grid in Computational Fluid Dynamics and Related Fields, North -Holland, pp. 491-502, 1991.

[105] S. L. Ho, W. N. Fu and H. C. Wong "Application of automatic choice of step size for time stepping finite element method to induction motor," IEEE Trans. Magn., vol.33, no.2, pp. 1370-1373, March 1997.

[106] C. William Gear, "Numerical initial vluse problems in ordinary differential equations," Prentice-Hall, Inc., Englewood Cliffs, 1971.

[107] S. L. Ho and W. N. Fu, "Computation of harmonics stray losses of induction motors using adaptive time stepping finite element method coupled with circuits," Seventh International Electric Machines and Drives Conference,pp. 93-97, September 11-13, 1995.

[108] S. L. Ho, H. L. Li "Adjustment of step size for time stepping finite element analysis to skewed rotor induction motors fed by SPWM source," IEEE International Electric Machines and Drives Conference, Seattle, Washington, pp. 679-681, May 9-12, 1999.

[109] S. J. Salon, D. W. Burow, R. E. Ashley III, L. Ovacik and M. J. DeBortoli, "Finite element analysis of induction machines in the frequency domain," IEEE Trans. Magn., vol.29, no.2, pp. 1438-1441, March 1993.

[110] R. Palma, S. J. Salon and M. J. DeBortili, "Dynamic electromechanical analysis of induction machines using finite elements," Proceedings of the International Conference on Electric Machines, pp.952-958, 1990.

[111] W. Muller, "Comparison of different methods of force calculations," IEEE Trans., Magn., vol.26, no.2, pp.1058-1061, 1990.

[112] M. Antila, E. Lantto and A. Arkkio, "Determination of forces and linearized parameters of radial active magnetic bearings by finite element technique," IEEE Trans., Magn., vol.34, pp. 684-694, May 1998.

[113] M. Marinescu, N. Mainescu, "Numerical computation of torques in permanent magnet motors by Maxwell's stresses and energy method," IEEE Trans., Magn., vol.24, no.1, January 1988.

[114] C. C. Hwang, S. B. John and S. S. Wu, "Reduction of cogging torque in spindle motors for CD-ROM drive," IEEE Trans., Magn., vol.34, no.2, pp. 468-770, March 1998.

[115] G. H. Jang and J. W. Yoon, "Torque and unbalanced magnetic force in a rotational unsymmetric brushless DC motors," IEEE Trans., Magn., vol.32, no.5, pp. 5157-5159, 1996.

[116] C. S. Koh, H. S. Yoon, K. W. Nam and H. S. Choi, "Magnetic pole shape optimization of permanent magnet motor for reduction of cogging torque," IEEE Trans., Magn., vol.33, no.2, pp.1822-1827, January 1988.

[117] T. S. Low, S. X. Chen and X. Gao, "Robust torque optimization for BLDC spindle motors", IEEE Trans. on Industrial Electronics, vol.48, No.3, pp.656-663, June 2001.

[118] M. A. Jabbar, "Some novel ideas for disk drive spindle motors," Motion control proceedings, Asia-Pacific workshop on advances in Singapore, pp.171-176, July 1993. '

[119] S. X. Chen, T. S. Low, H. Lin and Z. J. Liu, "Design trends of spindle motors for high performance hard disk drives," IEEE Trans. Magn, vol.32,No.5, pp. 3848-3850, September 1996.

[120] M. A. Jabbar, "Disk drive spindle motors and their controls," IEEE Transs Industrial Elec., vol.43, No.2, pp. 271-350, April 1996.

[121] M. A. Jabbar, T. S. Tan and K. J. Binns, "Recent developments in disk drive spindle motors," Int. Conf. on Electrical Machines (ICEM'92), Manchester, UK, vol.2, pp. 381-385, 1992.

[122] M. A. Jabbar, T. S. Low and M. A. Rahman, "Permanent magnet motors for brushless operation," IAS annual meeting, pp. 15-19, 1988.

[123] T. S. Low, C. S. Soh, C. Bi and K. T. Chang, "Identity control for spindle motors in hard disk drives," IEEE Trans. Magn. vol.31, No.5, pp.3117-3119, November 1995.

List of Publications

1. H. N. Phyu, M. A. Jabbar and Z. J. Liu, "Numerical Modelling and Analysis of a Brushless Permanent Magnet DC Motor using Circuit-Field Coupled Time Stepping FEM,"The 15th Conference on the Computation of Electromagnetic Fields (COMPUMAG 2005), China, 26th - 30th June, 2005.
2. H. N. Phyu, M. A. Jabbar and Z. J. Liu, "Computational Optimization of the Run-up Performance of a HDD Spindle Motor," International Electrical Machines and Drives Conference (IEMDC'05), San Antonio, TX, USA, 15th-18th May, 2005.
3. H. N. Phyu, M. A. Jabbar and Z. J. Liu, "Numerical Modelling and Analysis of a Brushless Permanent Magnet DC Motor using Circuit-Field Coupled Time Stepping FEM," IEEE Trans. On Magnetics. (Under Review)
4. M. A. Jabbar, H. N. Phyu, Z. J. Liu and C. Bi, "Modelling and Numerical Simulation of Brushless Permanent Magnet DC Motors in Dynamic Conditions by Time Stepping Techniques," IEEE Transaction on Industry Applications, vol.40, No.3, pp. 763-770, May/ June 2004.
5. M. A. Jabbar, H. N. Phyu and Z. J. Liu, "Analysis of the Starting Process of a Disk Drive Spindle Motor by Time Stepping Finite Element Method," IEEE Transaction on Magnetic, vol.40, No.4, pp. 3204-3206, July 2004.
6. M. A. Jabbar, H. N. Phyu and Z. J. Liu, "Analysis of the Starting Process

of a Disk Drive Spindle Motor by Time Stepping Finite Element Method," The 9th MMM-Intermag 2004, Anaheim, California, USA, January 2004.

7. H. N. Phyu, M. A. Jabbar, Z. J. Liu and C. Bi, "Modelling and Simulation of Brushless Permanent Magnet DC Motors in Dynamic Conditions by Time Stepping Techniques," IEEE International Electric Machines and Drives Conference (IEMDC'03), Madison, Wisconsin, USA, Vol. 1, pp. 376-381, June 1- 4 2003.

8. M. A. Jabbar, H. N. Phyu and Z. J. Liu, "Modelling and Simulation of Steady State Performance of Brushless Permanent Magnet DC Motors," International Conference on Applied Electromagnetics and Mechanics (ISEM 2003), Versailles, France, May 2003.

9. M. A. Jabbar, H. N. Phyu and Z. J. Liu, "Dynamic Modelling of Brushless Permanent Magnet DC Motors using Time Stepping Finite Element Method," International Conference on Evolutionary Computation (ICEC 2002), Dhaka, Bangladesh, December 2002.

Appendix A

Motor Specification

Table A.1: Motor specifications

voltage	12V
No of poles	8
No of slots	12
Rated speed	7200rpm
Stator outside diameter	28mm
Rotor outside diameter	30mm
Stack length	4.5mm
Air gap	0.2mm
Magnet	$NdFeB$

Appendix B

Newton Raphson Algorithm

The Newton Raphson method is based on derivatives of the function or quantity to be updated, and the procedure yields rapid convergence, with the error in a given step decreasing as the square of the error in the previous step. Therefore, it is one of the quadratic methods. Consider, for example, the following non-linear equation

$$Ax = B \tag{B.1}$$

Where x is unknown and A is the function of x. B is a constant. Define

$$f(x) = A(x).x \tag{B.2}$$

Fig. B.1 shows the relationship between $f(x)$ and B. The solution of equation (B.1)is the intersection of the curve $f(x)$ and the line B. Expand the equation (B.2) by using the Taylor series

$$f(x) = f(x^{(0)}) + f'(x^{(0)})(x - x^{(0)}) \tag{B.3}$$

where $x^(0)$ is the initial value of the solution. We have

$$f(x) = A(x).x = B \tag{B.4}$$

And

$$B = f(x^{(0)}) + f'(x^{(0)})(x - x^{(0)}) \tag{B.5}$$

Therefore

$$f'(x^{(0)})(x - x^{(0)}) = B - f(x^{(0)}) \tag{B.6}$$

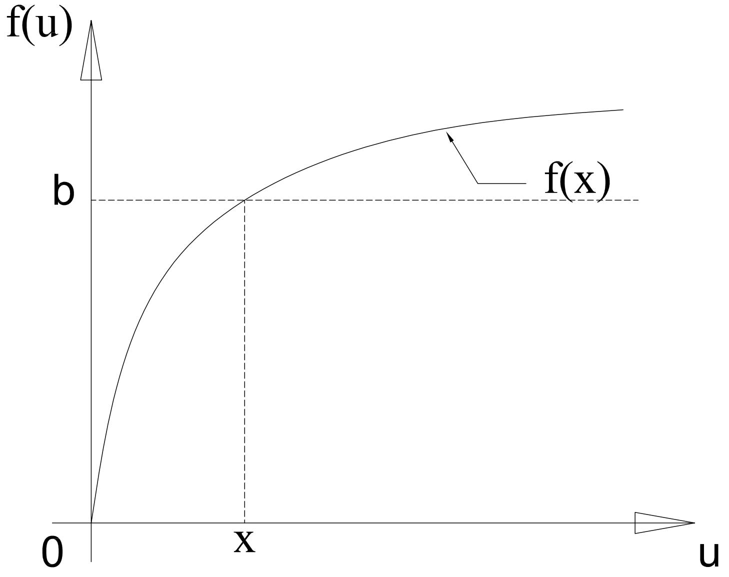

Figure B.1: Relationship between $f(x)$ and B

From the initial estimate, $x^(0)$, we can find

$$f'(x^{(1)})(x^{(0)} - x^{(1)}) = B - f(x^{(1)}) \tag{B.7}$$

and so forth.

$$f'(x^{(2)})(x^{(1)} - x^{(2)}) = B - f(x^{(2)}) \tag{B.8}$$

The similar computation can be done continually to k times iterations as follow

$$f'(x^{(k)})(x^{(k+1)} - x^{(k)}) = B - f(x^{(k)}) \tag{B.9}$$

The procedure is illustrated graphically in Fig. B.2. After several iterations, the right hand side of the equation (2.96) will close to zero. That is, the sequence of points converges to the solution. It can be shown that if the function $f(x)$ is monotonic, the solution converges quadratically. However, if the function is not monotonic, the derivative will change sign. This can lead to non-convergence as illustrated in Fig. B.3. Caution is advised if the electrical machine is operated in saturation region, the magnetic permeability vs flux density is not a monotonic function. In order to guarantee convergence the permeability in the low flux density region is usually approximated as a constant. Since most electrical machines are not designed to operate in this region, therefore the approximation is acceptable.

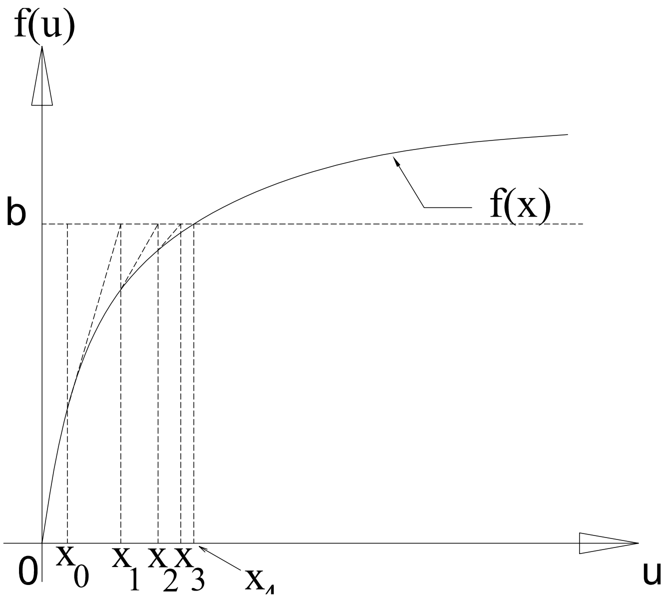

Figure B.2: Newton Raphson procedure

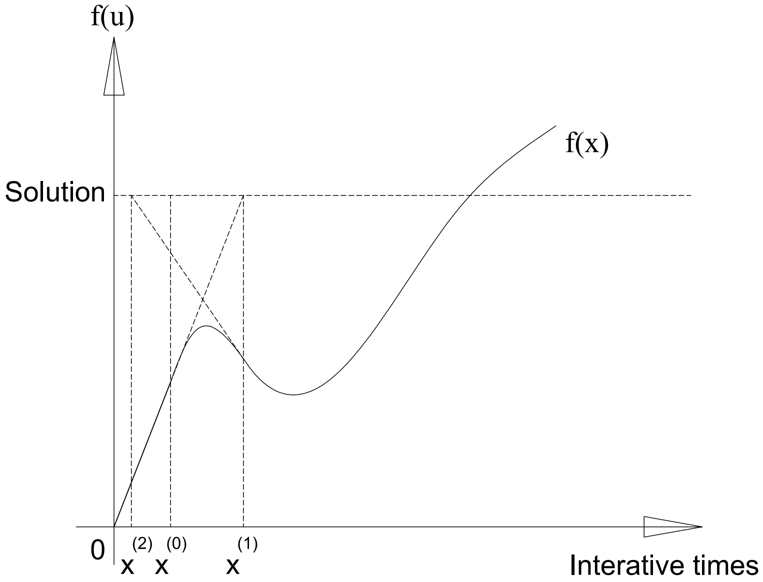

Figure B.3: Effect of non-monotonic function on Newton's method

Appendix C

Cubic Spline Interpolation

The development of cubic spline algorithm is as follow. Consider a set of sample points, , i = 1(1) n on an interval $[a, b]$ of a real line with the corresponding values of the real function, y_i , I = 1(1)n. The arrangement of the sample points is monotonous, i.e.:

$$a = x_1 < x_2 < x_3 < .... < x_n = b \tag{C.1}$$

The function is to be approximated with and interpolating cubic spline function, S(x). The spline function should fulfill the following conditions:

- S(x) is continuous within the interval $[a, b]$ along with derivative up to the second derivative.
- On every interval $[x_i, x_{i+1}]$, S(x) is identical to a cubic polynomial called a subspline.
- At the sample points,x_i, i = 1(1)n, the points of of S(x) are $y(x_i)$.
- The boundary conditions, $s''(a) = s''(b) = 0$ or are valid.

Using the approach,

$$S(x) = y(x) = a_i.y_i + b_i.y_{i+1} + c_i.y''_i + d_i.y''_{i+1} \tag{C.2}$$

In which:

$$h_i = x_{i+1} - x_i \tag{C.3}$$

$$a_i = \frac{x_{i+1} - x}{x_{i+1} - x_i} \tag{C.4}$$

$$b_i = \frac{x - x_i}{x_{i+1} - x_i} \tag{C.5}$$

$$c_i = \frac{\left(a_i^3 - a_i\right)\left(x_{i+1} - x_i\right)^2}{6} \tag{C.6}$$

$$d_i = \frac{\left(b_i^3 - b_i\right)\left(x_{i+1} - x_i\right)^2}{6} \tag{C.7}$$

The first derivative with respect to x of the interpolating function is

$$\frac{dS\left(x\right)}{dx} = \frac{dy}{dx} = \frac{y_{i+1} - y_i}{x_{i+1} - x_i} - \frac{3a_i^2 - 1}{6}(x_{i+1} - x_i)y_i'' + \frac{3b_i^2 - 1}{6}(x_{i+1} - x_i)y_{i+1}'' \tag{C.8}$$

while the derivative is

$$\frac{d^2S\left(x\right)}{dx^2} = \frac{d^2y}{dx^2} = a_i y_i'' + b_i y_{i+1}'' \tag{C.9}$$

With this, the requirement of the continuity of the second derivative over the boundaries of the interval $[x_i, x_{i+1}]$ and $[x_{i-1}, x_i]$ is satisfied. Because of a required continuous derivative of first order of the interpolating spline function, the values of dS/dx at the point $x = x_i$ for $x \in [x_{i-1}, x_i]$ and $x \in [x_i, x_{i+1}]$ must be equal. Employing for both interval yields

$$\frac{h_{i-1}}{6}.y_{i-1}'' + \frac{h_i + h_{i-1}}{3}.y_i'' + \frac{h_i}{6}.y_{i+1}'' = \frac{y_{i+1} - y_i}{h_i} - \frac{y_i - y_{i-1}}{h_{i-1}} \tag{C.10}$$

This equation can be evaluated with $i = 2(1)n - 1$ for every interval. This results in $n - 2$ linear independent equations for the n unknown $y_1'' = y_n'' = 0$ yields two additional constraints. This is a symmetric diagonal system of equations and is easy to solve. With the derivatives known, the coefficients of the interpolating spline function are now determined.

Appendix D

Demagnetization Curve for Permanent Magnet

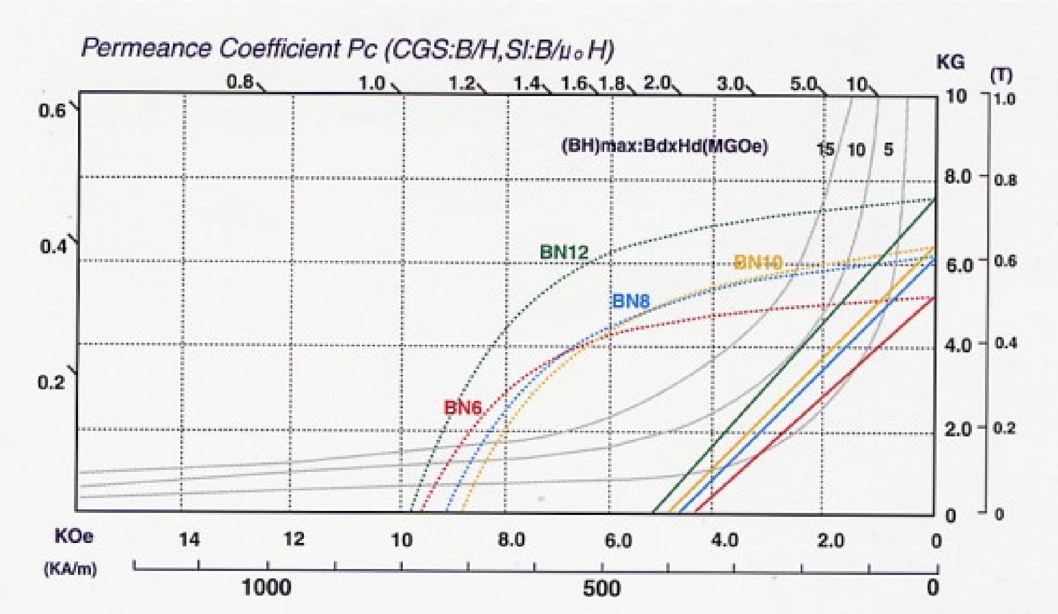

Figure D.1: Demagnetization curve for bonded NdFeB magnet

Appendix E

Specifications of Inverter Circuit Components

Inverter circuit for the experimental set up consists of the following two main components.

1. High speed switching MOSFETs IRF620 and
2. IR2110 high side and low side drivers.

E.1 MOSFET IRF620

Detailed specifications sheets of MOSFET IRF620 are shown in Fig. E.1, Fig. E.2 and Fig. E.3

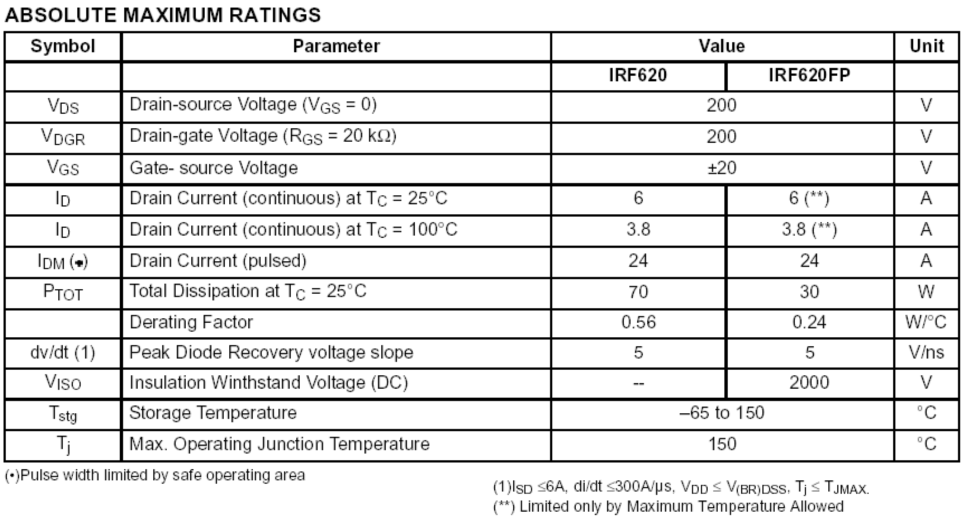

ABSOLUTE MAXIMUM RATINGS

Symbol	Parameter	Value		Unit
		IRF620	**IRF620FP**	
V_{DS}	Drain-source Voltage (V_{GS} = 0)	200		V
V_{DGR}	Drain-gate Voltage (R_{GS} = 20 kΩ)	200		V
V_{GS}	Gate- source Voltage	±20		V
I_D	Drain Current (continuous) at T_C = 25°C	6	6 (**)	A
I_D	Drain Current (continuous) at T_C = 100°C	3.8	3.8 (**)	A
I_{DM} (•)	Drain Current (pulsed)	24	24	A
P_{TOT}	Total Dissipation at T_C = 25°C	70	30	W
	Derating Factor	0.56	0.24	W/°C
dv/dt (1)	Peak Diode Recovery voltage slope	5	5	V/ns
V_{ISO}	Insulation Winthstand Voltage (DC)	--	2000	V
T_{stg}	Storage Temperature	–65 to 150		°C
T_j	Max. Operating Junction Temperature	150		°C

(•)Pulse width limited by safe operating area

(1)$I_{SD} \leq 6A$, di/dt ≤300A/μs, $V_{DD} \leq V_{(BR)DSS}$, $T_j \leq T_{JMAX}$.

(**) Limited only by Maximum Temperature Allowed

Figure E.1: Date sheets of absolute maximum ratings

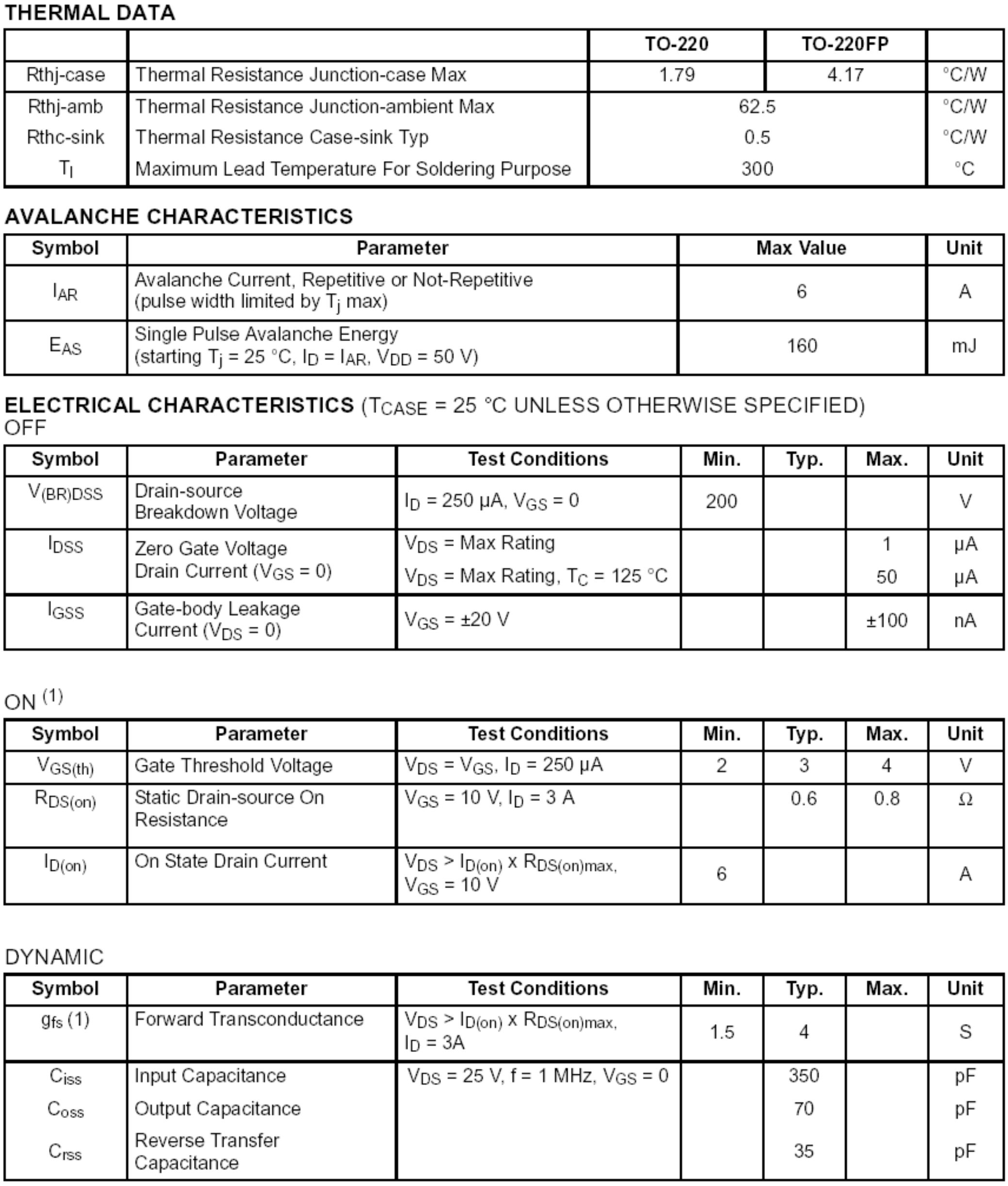

THERMAL DATA

		TO-220	TO-220FP	
Rthj-case	Thermal Resistance Junction-case Max	1.79	4.17	°C/W
Rthj-amb	Thermal Resistance Junction-ambient Max	62.5		°C/W
Rthc-sink	Thermal Resistance Case-sink Typ	0.5		°C/W
T_l	Maximum Lead Temperature For Soldering Purpose	300		°C

AVALANCHE CHARACTERISTICS

Symbol	Parameter	Max Value	Unit
I_{AR}	Avalanche Current, Repetitive or Not-Repetitive (pulse width limited by T_j max)	6	A
E_{AS}	Single Pulse Avalanche Energy (starting T_j = 25 °C, $I_D = I_{AR}$, V_{DD} = 50 V)	160	mJ

ELECTRICAL CHARACTERISTICS (T_{CASE} = 25 °C UNLESS OTHERWISE SPECIFIED)

OFF

Symbol	Parameter	Test Conditions	Min.	Typ.	Max.	Unit
$V_{(BR)DSS}$	Drain-source Breakdown Voltage	I_D = 250 µA, V_{GS} = 0	200			V
I_{DSS}	Zero Gate Voltage Drain Current (V_{GS} = 0)	V_{DS} = Max Rating			1	µA
		V_{DS} = Max Rating, T_C = 125 °C			50	µA
I_{GSS}	Gate-body Leakage Current (V_{DS} = 0)	V_{GS} = ±20 V			±100	nA

ON (1)

Symbol	Parameter	Test Conditions	Min.	Typ.	Max.	Unit
$V_{GS(th)}$	Gate Threshold Voltage	$V_{DS} = V_{GS}$, I_D = 250 µA	2	3	4	V
$R_{DS(on)}$	Static Drain-source On Resistance	V_{GS} = 10 V, I_D = 3 A		0.6	0.8	Ω
$I_{D(on)}$	On State Drain Current	$V_{DS} > I_{D(on)} \times R_{DS(on)max}$, V_{GS} = 10 V	6			A

DYNAMIC

Symbol	Parameter	Test Conditions	Min.	Typ.	Max.	Unit
g_{fs} (1)	Forward Transconductance	$V_{DS} > I_{D(on)} \times R_{DS(on)max}$, I_D = 3A	1.5	4		S
C_{iss}	Input Capacitance	V_{DS} = 25 V, f = 1 MHz, V_{GS} = 0		350		pF
C_{oss}	Output Capacitance			70		pF
C_{rss}	Reverse Transfer Capacitance			35		pF

Figure E.2: Thermal and electrical characteristics sheet (1)

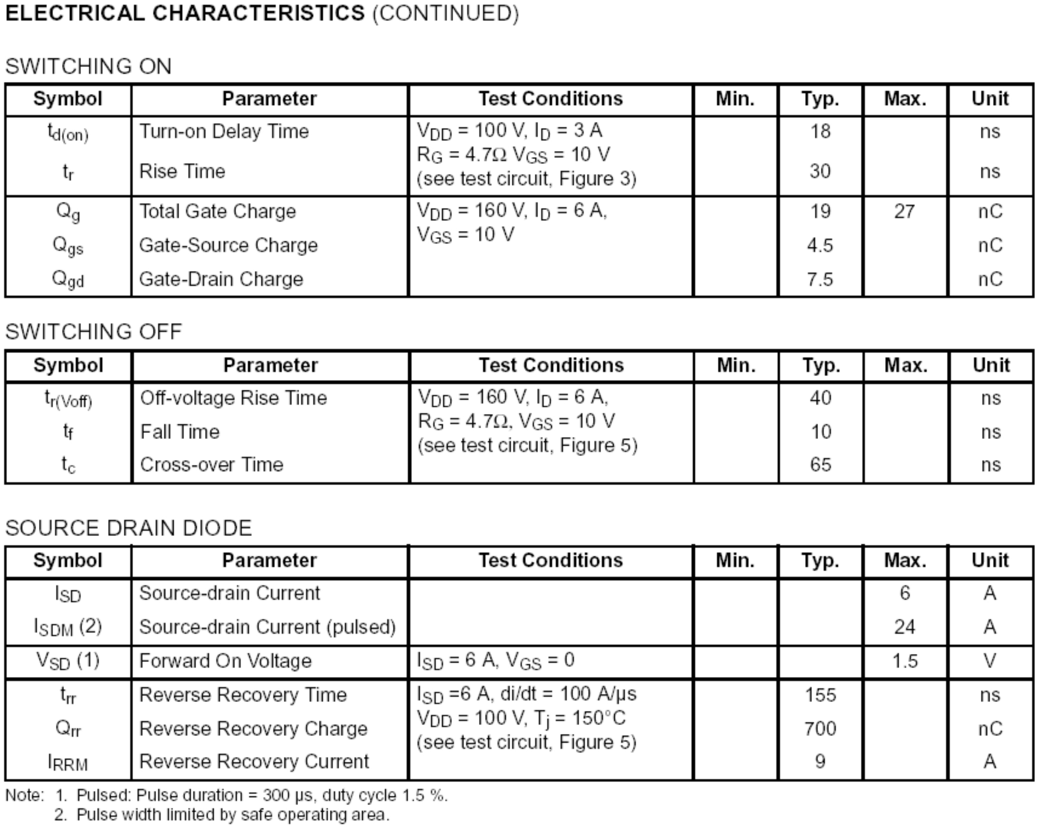

ELECTRICAL CHARACTERISTICS (CONTINUED)

SWITCHING ON

Symbol	Parameter	Test Conditions	Min.	Typ.	Max.	Unit
$t_{d(on)}$	Turn-on Delay Time	V_{DD} = 100 V, I_D = 3 A R_G = 4.7Ω V_{GS} = 10 V (see test circuit, Figure 3)		18		ns
t_r	Rise Time			30		ns
Q_g	Total Gate Charge	V_{DD} = 160 V, I_D = 6 A, V_{GS} = 10 V		19	27	nC
Q_{gs}	Gate-Source Charge			4.5		nC
Q_{gd}	Gate-Drain Charge			7.5		nC

SWITCHING OFF

Symbol	Parameter	Test Conditions	Min.	Typ.	Max.	Unit
$t_{r(Voff)}$	Off-voltage Rise Time	V_{DD} = 160 V, I_D = 6 A, R_G = 4.7Ω, V_{GS} = 10 V (see test circuit, Figure 5)		40		ns
t_f	Fall Time			10		ns
t_c	Cross-over Time			65		ns

SOURCE DRAIN DIODE

Symbol	Parameter	Test Conditions	Min.	Typ.	Max.	Unit
I_{SD}	Source-drain Current				6	A
I_{SDM} (2)	Source-drain Current (pulsed)				24	A
V_{SD} (1)	Forward On Voltage	I_{SD} = 6 A, V_{GS} = 0			1.5	V
t_{rr}	Reverse Recovery Time	I_{SD} =6 A, di/dt = 100 A/µs V_{DD} = 100 V, T_j = 150°C (see test circuit, Figure 5)		155		ns
Q_{rr}	Reverse Recovery Charge			700		nC
I_{RRM}	Reverse Recovery Current			9		A

Note: 1. Pulsed: Pulse duration = 300 µs, duty cycle 1.5 %.
2. Pulse width limited by safe operating area.

Figure E.3: Thermal and electrical characteristics sheet (2)

E.2 IR2110 high side and low side driver

The IR2110 are high voltage, high speed power MOSFET and IGBT drivers with independent high and low side referenced output channels. Proprietary HVIC and latch immune CMOS technologies enable ruggedized monolithic construction. Logic inputs are compatible with standard CMOS or LSTTL output, down to 3.3V logic. The output drivers feature a high pulse cur- rent buffer stage designed for minimum driver cross-conduction. Propagation delays are matched to simplify use in high frequency applications. The floating channel can be used to drive an N-channel power MOSFET or IGBT in the high side configuration which operates up to 500 or 600 volts. Typical connection diagram and functional block diagram are shown in Fig. E.4 and Fig. E.5. Data sheet of absolute maximum ratings from the supplier is shown in Fig. E.6.

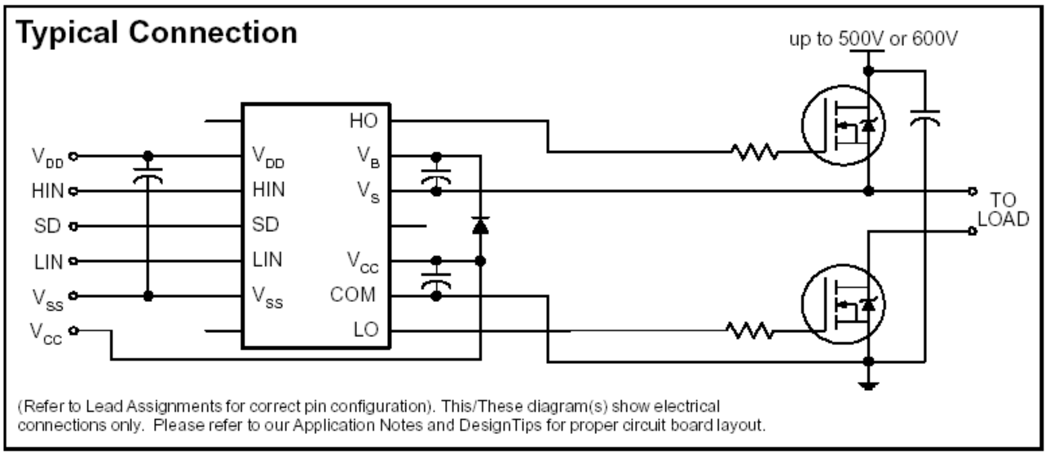

Figure E.4: Typical connection diagram

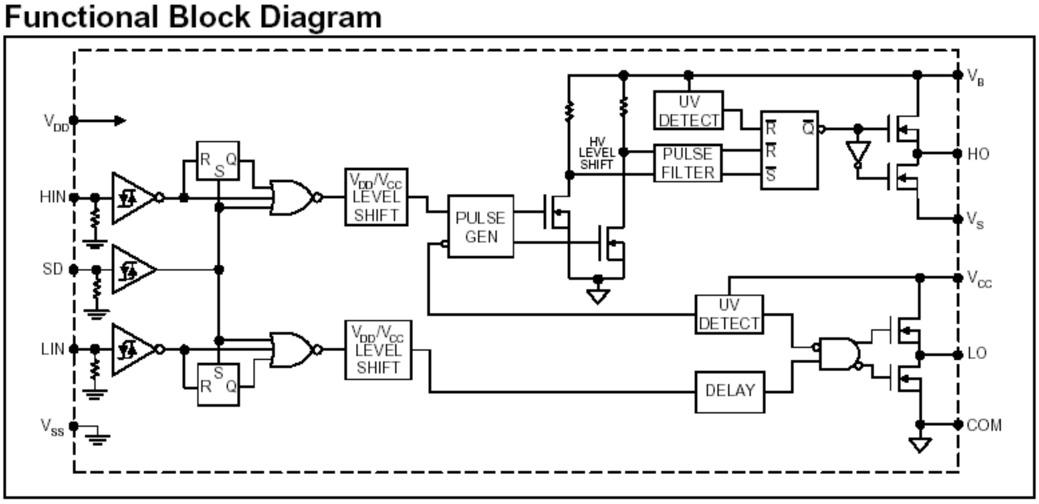

Figure E.5: Functional block diagram

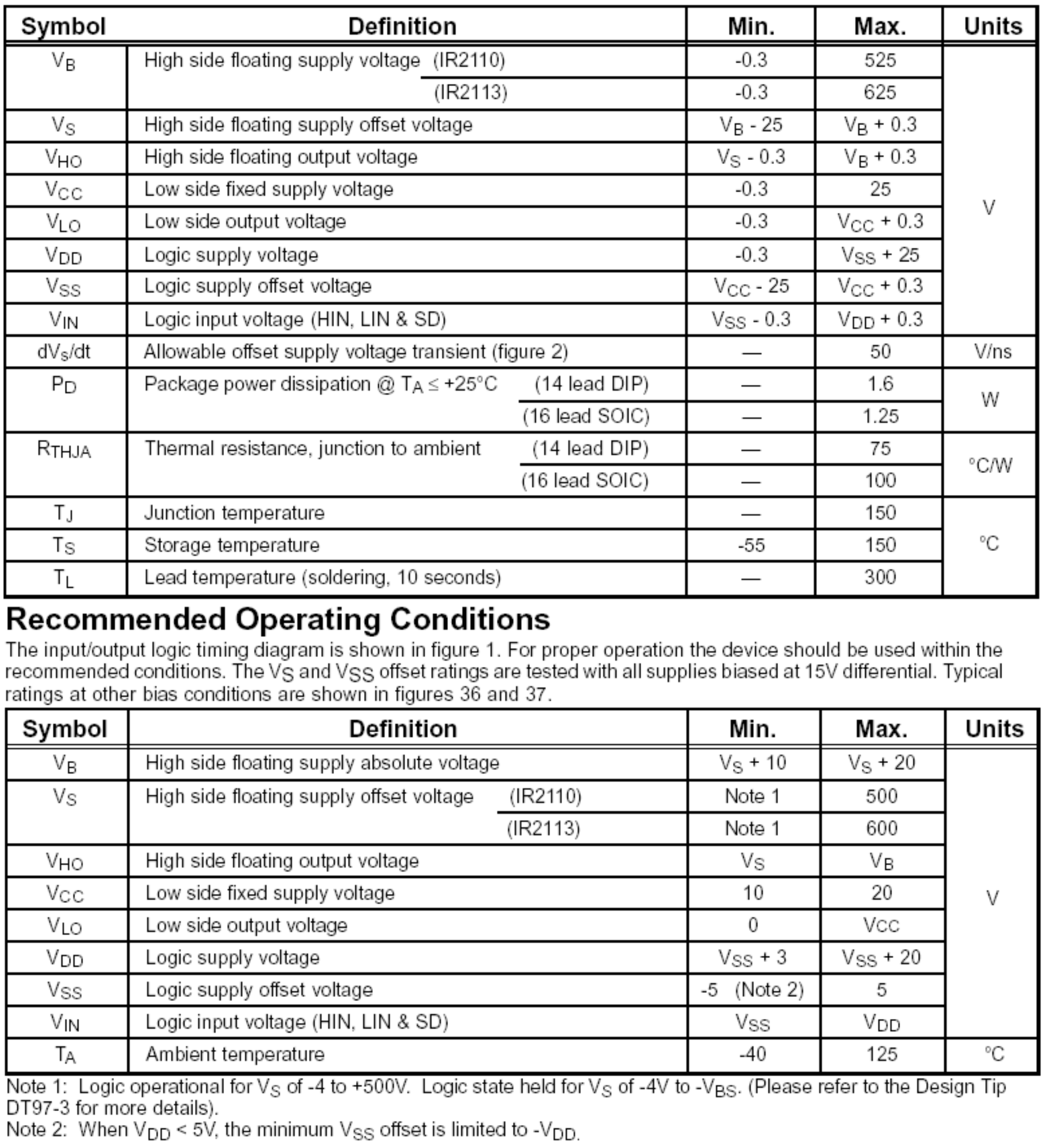

Symbol	Definition		Min.	Max.	Units
V_B	High side floating supply voltage	(IR2110)	-0.3	525	V
		(IR2113)	-0.3	625	
V_S	High side floating supply offset voltage		V_B - 25	V_B + 0.3	
V_{HO}	High side floating output voltage		V_S - 0.3	V_B + 0.3	
V_{CC}	Low side fixed supply voltage		-0.3	25	
V_{LO}	Low side output voltage		-0.3	V_{CC} + 0.3	
V_{DD}	Logic supply voltage		-0.3	V_{SS} + 25	
V_{SS}	Logic supply offset voltage		V_{CC} - 25	V_{CC} + 0.3	
V_{IN}	Logic input voltage (HIN, LIN & SD)		V_{SS} - 0.3	V_{DD} + 0.3	
dV_s/dt	Allowable offset supply voltage transient (figure 2)		—	50	V/ns
P_D	Package power dissipation @ $T_A \le +25°C$	(14 lead DIP)	—	1.6	W
		(16 lead SOIC)	—	1.25	
R_{THJA}	Thermal resistance, junction to ambient	(14 lead DIP)	—	75	°C/W
		(16 lead SOIC)	—	100	
T_J	Junction temperature		—	150	°C
T_S	Storage temperature		-55	150	
T_L	Lead temperature (soldering, 10 seconds)		—	300	

Recommended Operating Conditions

The input/output logic timing diagram is shown in figure 1. For proper operation the device should be used within the recommended conditions. The V_S and V_{SS} offset ratings are tested with all supplies biased at 15V differential. Typical ratings at other bias conditions are shown in figures 36 and 37.

Symbol	Definition		Min.	Max.	Units
V_B	High side floating supply absolute voltage		V_S + 10	V_S + 20	V
V_S	High side floating supply offset voltage	(IR2110)	Note 1	500	
		(IR2113)	Note 1	600	
V_{HO}	High side floating output voltage		V_S	V_B	
V_{CC}	Low side fixed supply voltage		10	20	
V_{LO}	Low side output voltage		0	V_{CC}	
V_{DD}	Logic supply voltage		V_{SS} + 3	V_{SS} + 20	
V_{SS}	Logic supply offset voltage		-5 (Note 2)	5	
V_{IN}	Logic input voltage (HIN, LIN & SD)		V_{SS}	V_{DD}	
T_A	Ambient temperature		-40	125	°C

Note 1: Logic operational for V_S of -4 to +500V. Logic state held for V_S of -4V to $-V_{BS}$. (Please refer to the Design Tip DT97-3 for more details).

Note 2: When V_{DD} < 5V, the minimum V_{SS} offset is limited to $-V_{DD}$.

Figure E.6: Absolute maximum ratings

Appendix F

Specifications of Incremental Encoder

Figure F.1: Photograph of Scancon incremental encoder

Basic characteristics are listed below.

- Micro hollow shaft encoder
- Strong compact electronics
- Std. IP 54 (with IDC; IP 50)
- To be connected directly to PLC'S and counters
- Thermal shut down at 155C

- $5V \pm 10\%$

- Based on 2 precision ball bearings for industrial environment

Electrical and mechanical characteristics are shown in Fig. F.2 and Fig. F.3.

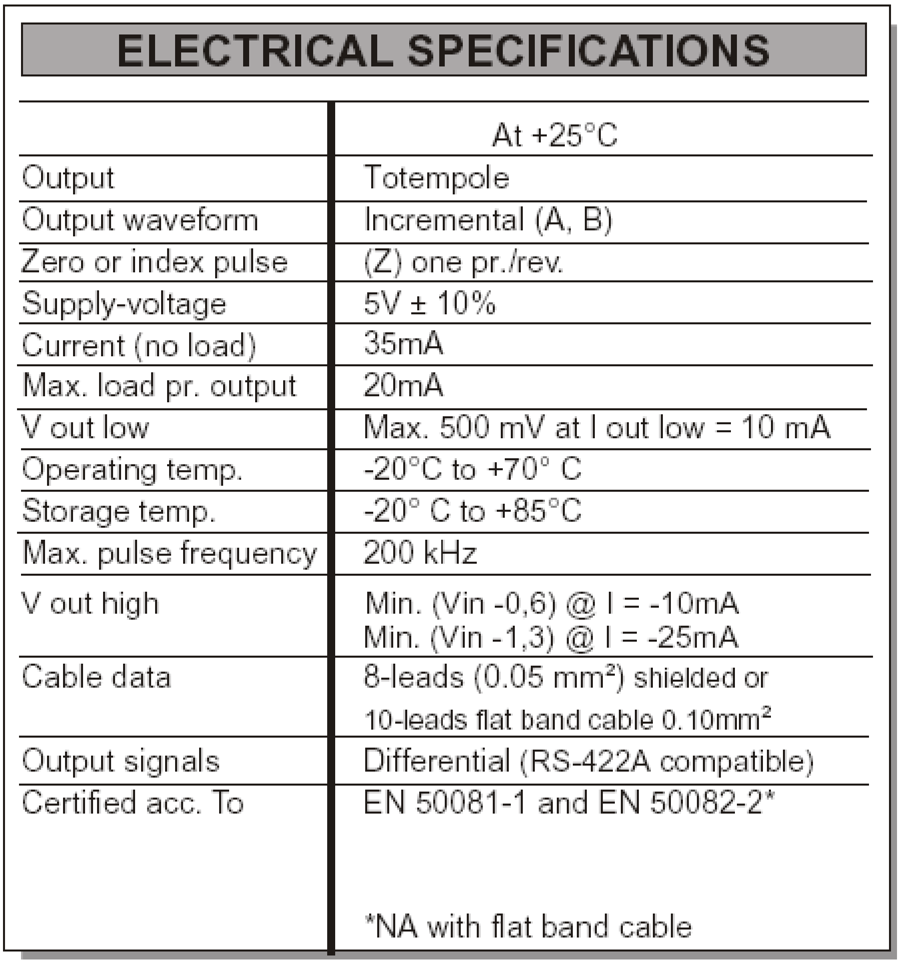

ELECTRICAL SPECIFICATIONS

	At +25°C
Output	Totempole
Output waveform	Incremental (A, B)
Zero or index pulse	(Z) one pr./rev.
Supply-voltage	5V ± 10%
Current (no load)	35mA
Max. load pr. output	20mA
V out low	Max. 500 mV at I out low = 10 mA
Operating temp.	-20°C to +70° C
Storage temp.	-20° C to +85°C
Max. pulse frequency	200 kHz
V out high	Min. (Vin -0,6) @ I = -10mA Min. (Vin -1,3) @ I = -25mA
Cable data	8-leads (0.05 mm²) shielded or 10-leads flat band cable 0.10mm²
Output signals	Differential (RS-422A compatible)
Certified acc. To	EN 50081-1 and EN 50082-2* *NA with flat band cable

Figure F.2: Electrical specifications

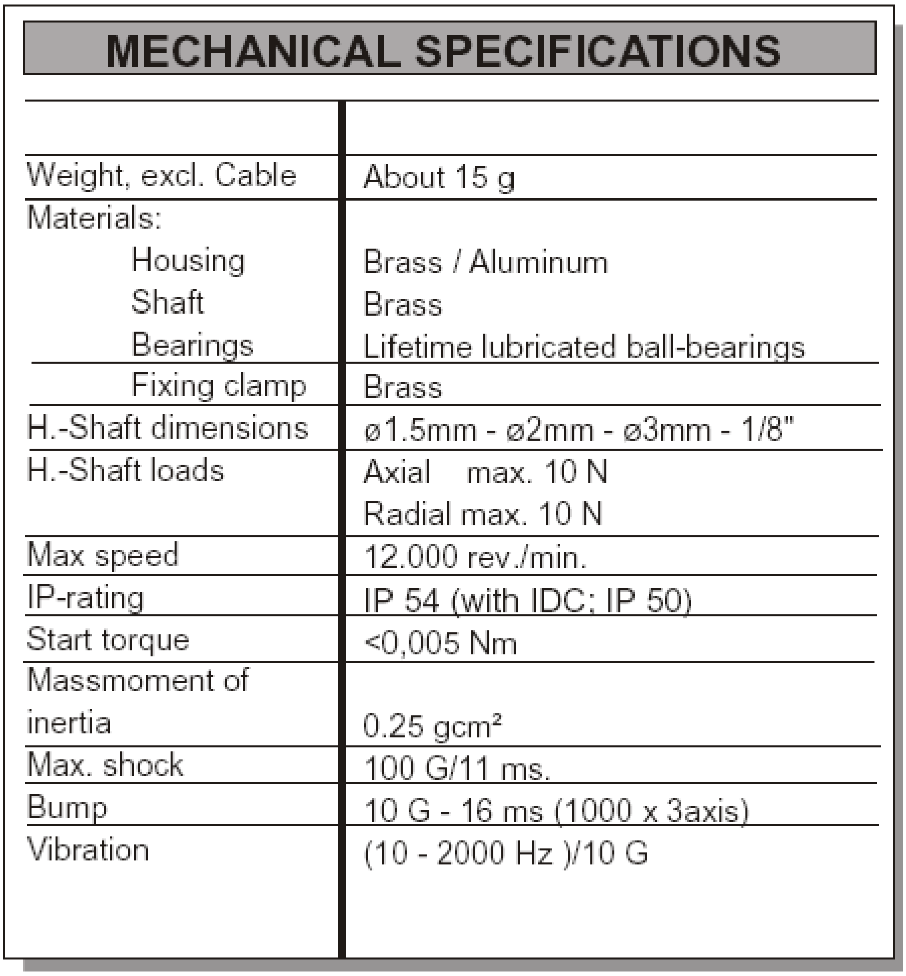

MECHANICAL SPECIFICATIONS

Weight, excl. Cable	About 15 g
Materials:	
Housing	Brass / Aluminum
Shaft	Brass
Bearings	Lifetime lubricated ball-bearings
Fixing clamp	Brass
H.-Shaft dimensions	ø1.5mm - ø2mm - ø3mm - 1/8"
H.-Shaft loads	Axial max. 10 N Radial max. 10 N
Max speed	12.000 rev./min.
IP-rating	IP 54 (with IDC; IP 50)
Start torque	<0,005 Nm
Massmoment of inertia	0.25 gcm²
Max. shock	100 G/11 ms.
Bump	10 G - 16 ms (1000 x 3axis)
Vibration	(10 - 2000 Hz)/10 G

Figure F.3: Mechanical specifications

Appendix G

Program Structure for Steady State Analysis

There are four main parts in the program.

1. Mesh Generation
2. Pre-computation by frequency domain analysis
3. Time stepping FEM computation
4. Post processing

1. **Mesh Generation**

Main input file : motor.dat

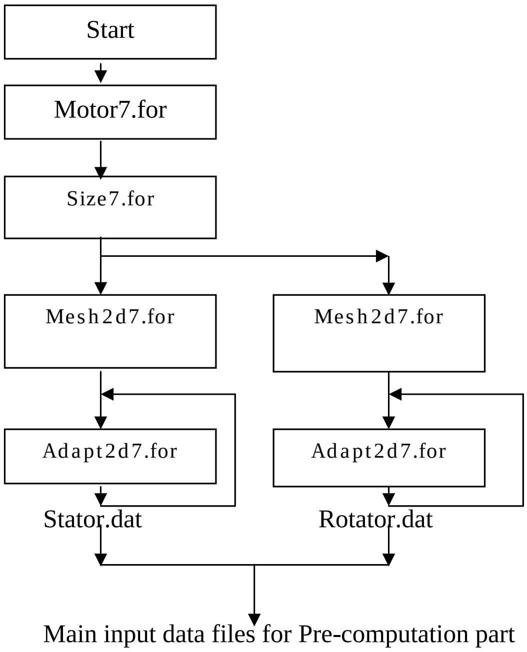

Produce input data files
For the whole program

Prepare geometric data
For the mesh2d7.for

Mesh generation using
Eating nodes algorithm

Refine FEM mesh by
using Delaunay method

Main input data files for Pre-computation part

2. **Pre-computation**

Main input data files : motor.dat ,stator.dat ,rotor.dat

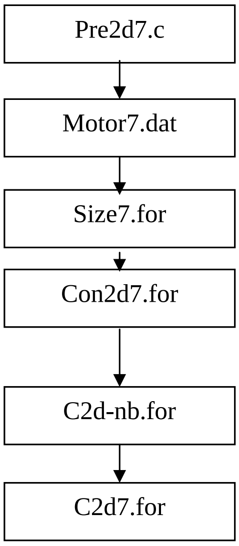

Main control program for
The pre-computation

Produce data files for other programs

Prepare geometric data

Connect the stator mesh
and the rotor mesh

Pre-processor for generating
address matrixes

FEM computation using complex model

3. Time stepping FEM computation

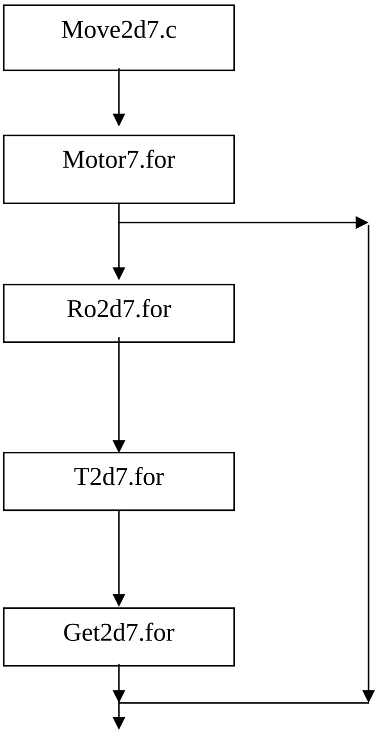

Main control program for time stepping FEM

Produce data files for the whole program

Rotate FEM mesh

Time stepping FEM computation

Post computation

4. Post Processing

Compute desired parameters by using the output data come from the time stepping FEM computation.

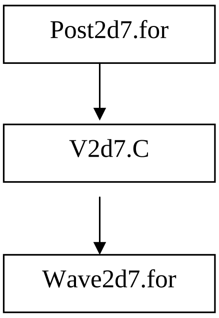

Prepare data for V2d7.C
(Compute magnetic flux density)

Show 2D FEM results such flux plot, flux density.

Show waveforms against time
(stator current, torque, speed, etc.)